Bulletin 55
(Part 3 of 3 Parts)

THE SHOCK AND VIBRATION BULLETIN

Part 3
Machinery Dynamics, System Identification and Structural Analysis

JUNE 1985

A Publication of
THE SHOCK AND VIBRATION INFORMATION CENTER
Naval Research Laboratory, Washington, D.C.

Office of
The Under Secretary of Defense
for Research and Engineering

DISCLAIMER NOTICE

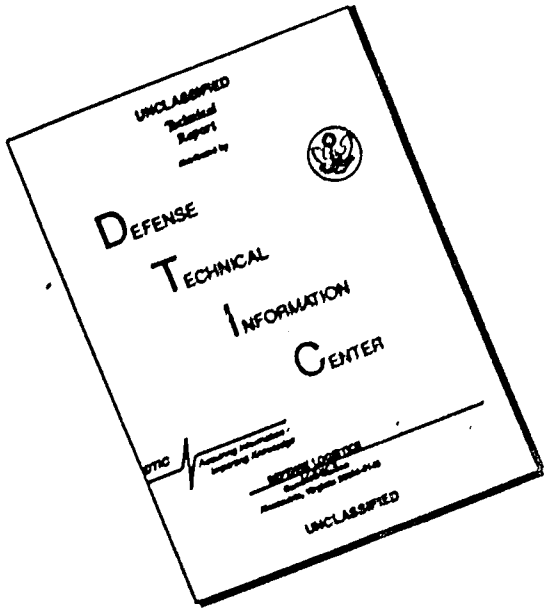

THIS DOCUMENT IS BEST QUALITY AVAILABLE. THE COPY FURNISHED TO DTIC CONTAINED A SIGNIFICANT NUMBER OF PAGES WHICH DO NOT REPRODUCE LEGIBLY.

SYMPOSIUM MANAGEMENT

THE SHOCK AND VIBRATION INFORMATION CENTER

J. Gordan Showalter, Acting Director

Rudolph H. Volin

Jessica Hileman

Elizabeth A. McLaughlin

Mary K. Gobbett

Bulletin Production

Publications Branch, Technical Information Division,
Naval Research Laboratory

Bulletin 55
(Part 3 of 3 Parts)

THE SHOCK AND VIBRATION BULLETIN

JUNE 1985

A Publication of
THE SHOCK AND VIBRATION INFORMATION CENTER
Naval Research Laboratory, Washington, D.C.

The 55th Symposium on Shock and Vibration was held in Dayton, Ohio, October 22-24, 1984. The Aeronautical Systems Division, Wright-Patterson Air Force Base, Ohio, was the host.

Office of
The Under Secretary of Defense
for Research and Engineering

CONTENTS

PAPERS APPEARING IN PART 3

PAPERS APPEARING IN PART I

Welcome

WELCOME
Keith Collier, Deputy Director, Air Force Wright Aeronautical Laboratories, Wright-Patterson AFB, OH

Keynote Address

KEYNOTE ADDRESS
Colonel Craig O. Schaum, Deputy for Engineering, Aeronautical Systems Division, Wright-Patterson AFB, OH

Invited Papers

AVIP AIR FORCE THRUST FOR RELIABILITY
Dr. John C. Halpin, Assistant for Product Assurance, Deputy for Engineering, Aeronautical Systems Division, Wright-Patterson AFB, OH

DYNAMICS R&D IN THE AFWAL STRUCTURES AND DYNAMICS DIVISION
Dr. James J. Olsen, Assistant for Research and Technology, AFWAL/FIB, Wright-Patterson AFB, OH

A DECADE OF RELIABILITY TESTING PROGRESS
Robert N. Hancock, LTV Aerospace and Defense Company, Vought Missiles and Advanced Programs Division, Dallas, TX

CERT – WHERE WE HAVE BEEN – WHERE WE ARE GOING
Dr. Alan Burkhard, Air Force Wright Aeronautical Laboratories, Wright-Patterson AFB, OH

FACTORS AFFECTING THE FATIGUE LIFE OF TURBINE BLADES AND AN ASSESSMENT OF THEIR ACCURACY
Dr. Neville R. Rieger, Stress Technology, Inc., Rochester, NY

Damping Practices

SPIN PIT TEST OF BLADED DISK WITH BLADE PLATFORM FRICTION DAMPERS
R.J. Dominic, University of Dayton, Research Institute, Dayton, OH

A DIFFERENT VIEW OF VISCOUS DAMPING
P.J. Torvik, Department of Aeronautics and Astronautics, Air Force Institute of Technology, Wright-Patterson AFB, OH and Major R.L. Bagley, 4950th Test Wing, Aeronautical Systems Division, Wright-Patterson AFB, OH

SESSION CHAIRMEN AND COCHAIRMEN

Date	Session Title	Chairmen	CoChairmen
Tuesday, 23 October, A.M.	Opening Session	Mr. Jerome Pearson, Air Force Wright Aeronautical Laboratories, Wright-Patterson Air Force Base, OH	Dr. J. Gordan Showalter, The Shock & Vibration Information Center, Naval Research Laboratory, Washington, DC
Tuesday, 23 October, P.M.	Dynamic Testing	Mr. Edwin M. Rzepka, Naval Surface Weapons Center, Silver Spring, MD	Mr. Frederick Anderson, U.S. Army Missile Command, Redstone Arsenal, AL
Tuesday, 23 October, P.M.	Fluid-Structure Interaction	Mr. Arthur D. Carlson, Naval Underwater Systems Center, New London, CT	Dr. Y. S. Shin, Naval Post Graduate School, Monterey, CA
Wednesday, 24 October, A.M.	Plenary A	Mr. Henry Caruso, Westinghouse Electric Corporation, Baltimore, MD	
Wednesday, 24 October, A.M.	Flight Vehicle Dynamics	Mr. Joseph J. Popolo, Grumman Aerospace Corporation, Bethpage, NY	Mrs. Phyllis Bolds Air Force Wright Aeronautical Laboratories, Wright-Patterson Air Force Base, OH
Wednesday, 24 October, A.M.	Damping and Isolation	Dr. John P. Henderson, Air Force Wright Aeronautical Laboratories, Wright-Patterson Air Force Base, OH	Dr. David I. G. Jones, Air Force Wright Aeronautical Laboratories, Wright-Patterson Air Force Base, OH
Wednesday, 24 October, P.M.	Seismic Loads	Mr. James P. Ballard, U.S. Army Engineer Waterways Experiment Station, Vicksburg, MS	Mr. Donald Bettge, Federal Emergency Management Agency, Washington, DC
Wednesday, 24 October, P.M.	Damping Practices	Dr. Lynn C. Rogers, Air Force Wright Aeronautical Laboratories, Wright-Patterson Air Force Base, OH	Mr. Michael Parin, Anatrol Corporation, Cincinnati, OH
Thursday, 25 October, A.M.	Plenary B	Dr. Ronald L. Eshleman, Vibration Institute, Clarendon Hills, IL	

Thursday, 25 October, A.M.	Machinery Dynamics	Dr. Ronald L. Eshleman, Vibration Institute Clarendon Hills, IL	Mr. Robert Leon, Liberty Technology Center, Inc. Conshohocken, PA
Thursday, 25 October, A.M.	System Identification	Dr. H. Joseph Weaver, Lawrence Livermore Laboratory, Livermore, CA	Dr. David Brown University of Cincinnati, Cincinnati, OH
Thursday, 25 October, P.M.	Structural Analysis	Mr. Tommy L. Dobson, 6585 Test Group, Holloman, Air Force Base, NM	
Thursday, 25 October, P.M.	Short Discussion Topics	Mr. James Bair, Aeronautical Systems Division, Wright-Patterson Air Force Base, OH	

AN INTEGRATED GEAR SYSTEM DYNAMICS ANALYSIS OVER A BROAD FREQUENCY RANGE

L. K. H. Lu, W. B. Rockwood, P. C. Warner
Westinghouse Electric Corporation
Sunnyvale, California

and

R. G. DeJong
Cambridge Collaborative, Incorporated
Boston, Massachusetts

An integrated analytical scheme for Marine Gear System Dynamics is presented in this paper. The work can be divided into three parts: Gear excitation source prediction, response calculation in the low frequency range, and average response estimation in the high frequency range.

Various sources of gear mesh excitation are considered by Mark in his excellent analysis (1). However, for modern precision ground gears, the source of primary interest is likely to be that portion of the static transmission error whose frequency is the tooth meshing frequency. This is the case treated herein. In this work, the steady component of static transmission error and the first harmonic of mesh tone component of static transmission error are calculated from a solution of the mesh contact problem. A simplex algorithm proposed by Conry & Seireg (2) is used to solve the gear contact problem.

Marine gear-turbine systems are comprised of individual components connected by bearings, mounts and gear tooth contacts. Methods best suited for response calculation of such a complex structure depend on the frequency range of interest as well as the properties of the methods. In the low frequency range, finite-element analysis, FEA, may be used. For intermediate and high frequencies when many modes participate in the response, our experience (3,4) indicates that Statistical Energy Analysis (5), SEA, offers a preferred solution. In order to demonstrate the feasibility and validity of the above procedure, a simplified gear-turbine problem is analyzed. The results are presented and discussed.

INTRODUCTION

Associated with the operation of most machines are variable forces which cause vibration. These vibrations are generally transmitted to the surfaces of the machines from which they radiate sound as illustrated in Figure 1.

The principal source of vibratory excitation of many accurate gears is the unsteady component of the relative angular motion of pairs of meshing gears. A pair of meshing gears with rigid, perfect, uniformly spaced involute teeth would transmit exactly uniform angular motion. However, the teeth of real gears contain machining errors, elastic deformation, tooth wear, profile modifications and other nonidealities. Such effects give rise to fluctuations in the angular motion.

The dynamic properties of a structure can influence noise generation, noise transmission, and noise radiation. The input forces may have their effect amplified by structural resonance. Structural characteristics and isolation design also determine the amount of vibrational energy which flows from one element to another in a structure.

If the dynamics of a structure are understood, structural modifications or damping treatments can often be made to reduce the noise transmission or radiation. Traditionally, the techniques used to solve dynamics problems in complex mechanical equipment include finite-element analysis, and lumped-mass methods. At low frequencies, where the modes are well spaced, both the lumped-mass and the finite-element (FEA) methods can work well.

Because of the complexity of many practical structures, however, the use of a sufficiently detailed FEA model of the structure, for use over an appreciable frequency range, can become cumbersome and expensive.

As the frequency of interest increases, more local modes appear, and the mesh size must decrease to maintain accuracy. As a consequence, conventional FEA methods often are very expensive to use, or fail to provide a satisfactory solution.

An alternative to conventional methods for frequency ranges with high modal density is Statistical Energy Analysis (SEA) (5). SEA calculates the average and standard deviation of RMS response of structural subsystems in a frequency band. Because it does not seek to calculate discrete-point response, SEA is not succeptable to degration of accuracy at high frequencies. In fact, the accuracy increases with modal density. In addition, the detailed peaks and toughs of high modal density frequency response functions are typically variant from one unit to the next, which makes a statistical description of the vibration more meaningful, as well as easier to interpret (Figure 2)

A gear system analysis scheme has been developed which utilizes the relative merits of both the FEA and SEA techniques. The stretegy involves calculating mesh tone excitation by a quasi-static simplex solution to the nonlinear gear contact problem. Subsequently, this excitation is applied to a NASTRAN FEA model of the system, employing substructural modal synthesis at low frequencies, and an SEA model at intermediate and high frequencies. The scheme is illustrated in Figure 3. In this way, gear system dynamics may be analyzed across a broad frequency range.

The excellent analysis of transmission error by Mark (1) is extremely useful, particularly for identification of source for the various components of excitation. To actually perform the complete analysis implied, however, requires a comprehensive, detailed description of tooth surface geometry under load, and the actual thermal and centrifugal environment. To acquire these data is an onerous experimental and analytical task. Fortunately, for a modern precision ground gear, the noise signature is dominated by vibration due to a small number of sources. The principal source is usually that causing mesh tone vibration and its harmonics.

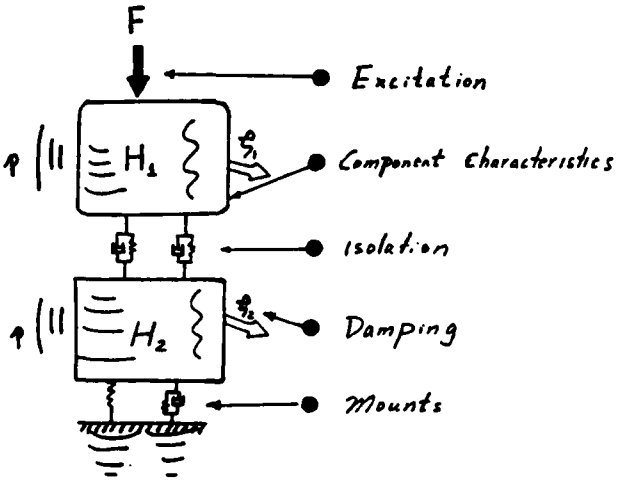

Figure 1: Structureborne and Airborne Noise Generation

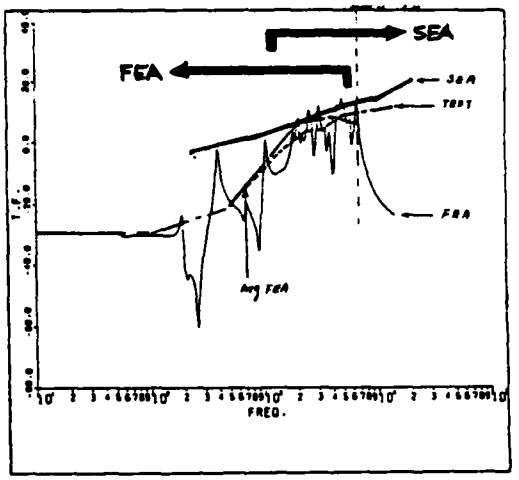

Figure 2: Analysis Method Applicable Frequency Range

SOURCE PREDICTION

In modern gears, manufacturing accuracy has improved to the point where, with proper control of manufacturing errors, gear mesh tone is the dominant component of gear noise.

Gear mesh load distribution is obviously a dominating factor in gear design. It is the basis of accurate stress calculation, and hence, is required to insure failure prevention. It is also required for precise noise estimation, and is the basis for prediction of the amount of profile modification and end relief necessary to obtain optimum performance on both counts.

For a gear mesh load distribution analysis to be used as a design tool, the calculation procedure must not only be sufficiently accurate, but must also be affordable, since design iterations are often needed before a gear is finalized.

Due to the complexity in geometry (tooth, root, helical angle, etc.) and the requirement for small element sizes in solving Hertzian contact stresses, a full three-dimensional finite-element analysis can be costly, time consuming, and will not necessarily suit the purpose.

In this study, an influence coefficient approach is used to solve the helical gear tooth deflection and load distribution problem. The required "compliance matrix", deflections due to unit load in a discretized tooth contact zone, is obtained by separating the effects of tooth, gear rim, pinion, and local contact deflections, and analyzing each separately. The procedures follow closely those used by Seireg and Conry (2,7). They are also similar to those in Refs. (8-11) for helical gears and Ref. (12) for spur gears. These works are extended by applying finite-elements to evaluate major components of the compliance matrix.

Because the areas of contact are unknown before the problem is solved, discretization at the contact points involve more unknowns than simultaneous equations. A simplex-type algorithm was devised by Conry and Seireg to handle this problem, and was found to be very effective.

The method is described briefly in the following.

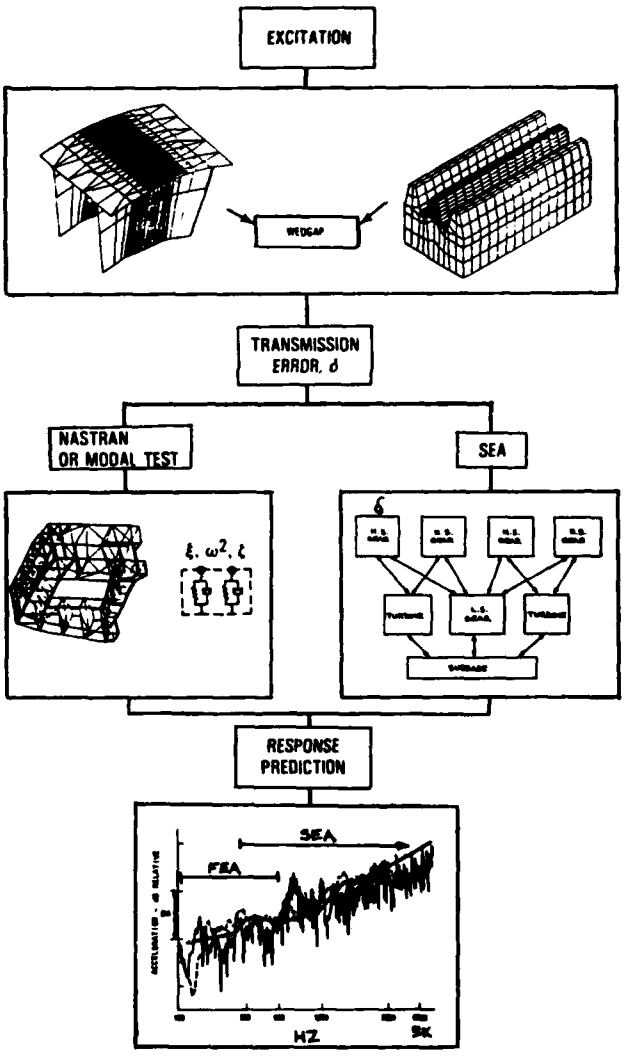

Figure 3: Integrated Gear System Dynamics Analysis

EQUILIBRIUM EQUATIONS

When two gears are in mesh, the following conditions exist:

1. Geometrical compatibility at each contact point; i.e. initial separation + elastic deformation - rigid body approach = final separation.
2. Load compatibility, i.e. Summation of contact forces = applied load.
3. When there is separation at a point, there is no load.

The above conditions can be expressed mathematically in the following manner:

$$-[K]\{F\} + \{e\}\Delta + [I]\{Y\} = \{\delta\}$$

$$\{e\}^T\{F\} = W$$

Either $F_j = 0$ or $Y_j = 0$

and $F_j \geq 0,\ Y_j \geq 0,\ \Delta \geq 0$

where:
- $[K]$ is the total influence coefficient matrix.
- $\{e\}$ is a column matrix of elements unity.
- $[I]$ is an identity matrix.
- $\{\delta\}$ is the initial separation vector.
- Δ is the mesh transmission error.
- $\{Y\}$ is a vector of "slack" variables.
- $\{F\}$ is a vector of forces.
- W is the total applied load.

Equation (1) is written for N discretized contact points in the contact zone as shown in Figure 4.

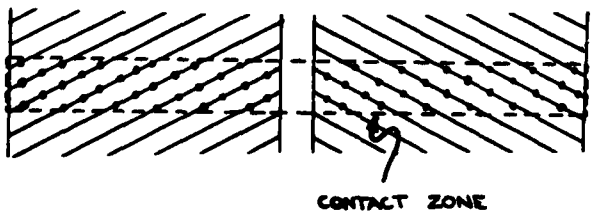

Figure 4: Tooth Contact Zone

INFLUENCE COEFFICIENTS

Equation (1) is solved by a modified simplex algorithm. The general method may be found in the literature (2). The most difficult part of gear mesh excitation prediction is the calculation of the influence coefficients. When two gears are in contact, the deformation of the teeth due to loads can be summarized by four influence coefficients.

They are K_T = Tooth deflection relative to the rim.
K_R = Gear rim deflection
K_P = Pinion deflection
K_H = Hertzian deformation at the load point.

Each is illustrated in Figure 5.

TOOTH FLEXIBILITY

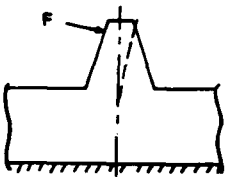

RIM DEFLECTION

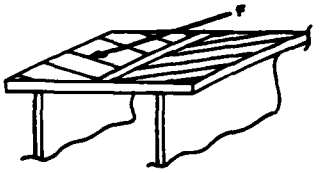

PINION DEFLECTION

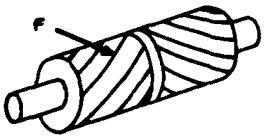

HERTZIAN DEFORMATION

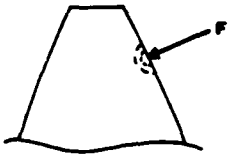

Figure 5: Influence Coefficient Components

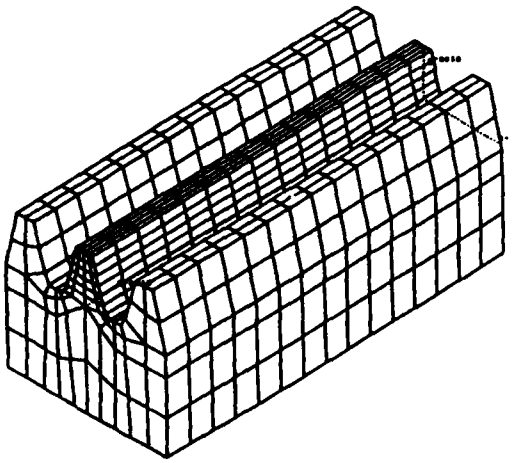

Figure 6: Tooth Compliance FEA Model

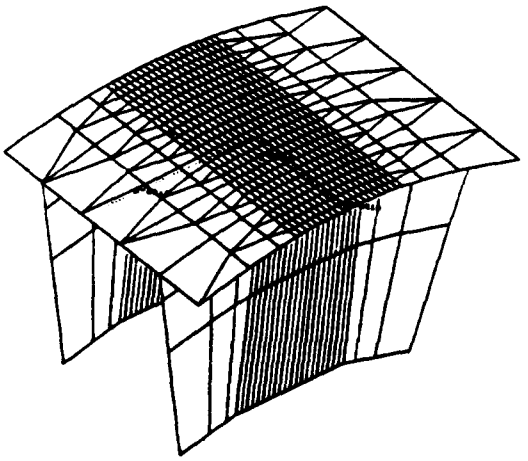

Figure 7: Gear Rim Compliance FEA Model

Due to the complexity of the geometry, three-dimensional finite-element analysis is employed to determine accurately the required influence coefficients (Figures 6 and 7). Other effects such as thermal distortion, gear rim centrifugal "flyout", and tooth modifications may be estimated separately and input as separations between the teeth (Figure 8).

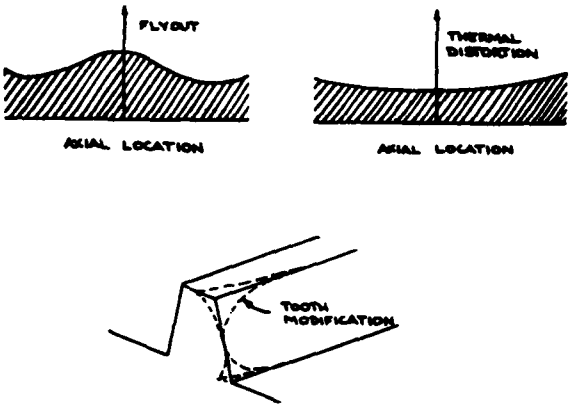

Figure 8: Initial Separations

STATIC TRANSMISSION ERROR

A computer program, WEDGAP (Westinghouse Electric Dynamic Gear Analysis Program), has been developed to solve equation (1) at several increments of gear rotation angle. Load distribution and mesh transmission error in the contact zone are obtained at each increment (Figure 9a,b). The load distribution is desirable for fatigue, pitting, and scuffing calculations.

If the "roll-angle" sequence of mesh transmission error is Fourier-transformed into the frequency domain, average (DC), as well as tooth mesh-harmonic (AC) components of the mesh transmission error are obtained. This quasi-static estimation of dynamic response yields vibratory excitation levels of the gear mesh at the tooth mesh harmonics.

Figure 9a: Mesh Force Distribution

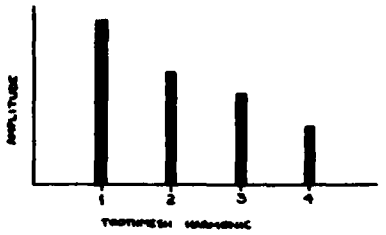

Figure 9b: Toothmesh Harmonics

SYSTEM RESPONSE IN THE LOW FREQUENCY RANGE BY FEA

For marine structures, FEA models on the order of thousands of degrees-of-freedom are not unusual. However, in rotating machinery, due to the characteristics of the bearings, isolators, and damping treatments, we encounter nonproportional damping. That is, the modes are complex quantities. For a large model, the cost of solving such a large eigenvalue problem is prohibitive, if not impossible. In addition, since effects such as static transmission error, rotation unbalance, and shaft out-of-round can best be expressed in terms of rotational frequency, the solution becomes a complex frequency response problem. In order to reduce the cost of computation, substructural modal synthesis appears appropriate.

The mathematical background of modal synthesis can be found in the literature (13), hence is not repeated here. Essentially, a complex structure is divided into a convenient number of substructures. For each component, the undamped free vibration modes are calculated. In gear rotating machinery, the true displacements of the components often resemble those in free vibration. Therefore, fre constraint modes of the component are usually sought. As each component is simpler than the total structure, the risk and cost of modelling error are minimized. The component modes of each substructure are then combined via their boundary compatability conditions to obtain the total system response. A major advantage of the method is its ability to employ a limited number of modes to model a substructure possessing many degrees of freedom, thus reducing the computational cost.

Substructural modal synthesis lends itself well to the design of vibration reduction treatments. The effects of constrained-layer or free-layer damping treatments may be estimated by the modal strain energy method (14), and incorporated as modal damping of individual components. Isolators may also be conveniently applied between subsystems. The effectiveness of vibration isolation is not only influenced by the stiffness of the isolator, but also by the dynamical characteristics of the structures they connect (5). The isolator can be selected while the structure is being designed. However, very often isolators are chosen after the main components are determined. To achieve the best vibration attenuation, the dynamical characteristics of all the major parts of the structure must be carefully considered. Usually, the design procedure is iterative. Therefore, the method used to design the isolator must include an efficient evaluation of the total system. Substructural modal synthesis offers an ideal solution to this problem. Physical properties of the isolator and bearings are inserted between each component, along with the component modes. The forced vibration response thereby employs an accurate model of each influence.

SYSTEM RESPONSE IN THE HIGH FREQUENCY RANGE BY SEA

Why SEA?

When the frequency of interest increases, the number of modes which contribute to the response increases. Eventually, local modes begin to participate, and the number of modes can increase sharply. This is especially true for a complex structure such as a gearcase.

In these circumstances, a coarse-mesh finite-element model can be too stiff to represent the true structural behavior. The mesh size must be reduced to the order of a quarter-wavelength. Therefore, at high frequencies, it becomes increasingly difficult to discretize a structural model sufficiently. A further difficulty is that the detail of the structure is undetermined in the initial design stages. A problem inherent in a discrete response calculation, such as FEA, is that it can be unreliable when oversimplifications are made in modelling complex structures. At frequencies where the modal density is high, the simple model can only account for the activity of a small number of global modes. Thus, in basing a conceptual design on a discrete response model, errors may be made. The designer needs a method for estimating intermediate to high frequency response before the design is solidified.

The SEA procedure involves modelling groups of similar modes as individual "subsystems" in a given structure. Power balance equations are then developed for the entire system. The sample case of two-subsystem interaction is illustrated in Figure 10. Power in input to subsystem 1, and is output either as dissipation, or to subsystem 2, where it must be dissipated.

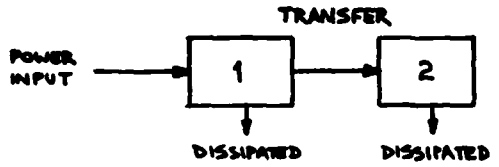

Figure 10: SEA Power Transfer

The parameters controlling the balance are "dissipation" and "coupling" loss factors, which indicate the strength of each power flow path. The equations may be expressed in the following matrix form for the general case:

$$\begin{vmatrix} \eta_1 + \sum_{j=2}^{N} \eta_{1j} & -\eta_{21} & \cdots & -\eta_{N1} \\ -\eta_{12} & \eta_2 + \sum_{\substack{j=1 \\ j=2}}^{N} \eta_{N2j} & \cdots & -\eta_{N2} \\ \vdots & \ddots & \vdots & \vdots \\ \eta_{1N} & \cdots & \cdots & \eta_N + \sum_{j=1}^{N-1} \eta_{Nj} \end{vmatrix} \begin{vmatrix} E_1 \\ E_2 \\ \vdots \\ E_N \end{vmatrix} = \begin{vmatrix} \pi_{in}^1 / \omega \\ \pi_{in}^2 / \omega \\ \vdots \\ \pi_{in}^N / \omega \end{vmatrix}$$

Where

η_i = The loss factor of the subsystem i

η_{ij} = Coupling loss factor

E_i = Energy stored in the subsystem

π_{in}^i = Input power

ω = Radian frequency

Given the resultant internal energy associated with each subsystem, time-average response is obtained for a desired frequency band.

SEA BENCHMARKS

Because the application of SEA to marine structures is relatively recent, an effort to benchmark SEA against test data and other analytical techniques is ongoing. Although a compilation of all such projects is outside the scope of this report, two examples serve to illustrate the results of the study.

As marine structures are largely groups of connected flat plates, it was felt that a comparison of SEA with the closed form plate solution would provide a reasonable result. The thin-plate, simply supported form was chosen to obtain a classical calculation of the special and frequency average response which SEA seeks to estimate. A rectangular plate of typical dimensions was divided into nine segments, and the center of a corner segment was driven. For each segment, the classical point vibration levels were spatially averaged for the low, center, and upper frequencies of a third octave band. These results were compared with SEA for several frequency bands and levels of damping (Figure 11). They show that SEA yields a good average response estimate, differences being on the order of a few dB.

A benchmark of SEA against test data for a marine structure was established for a reduction gearcase. Vibration levels from an actual unit are compared with those given by SEA and a quarter-scale model in Figure 12. The results show SEA closely following the full-scale data, which are also accurately modeled by the precision quarter-scale model.

These and other efforts (Figure 13) to benchmark SEA show it to be a powerful tool for intermediate and high frequency calculations. At low frequencies, SEA generally gives a good estimate of the average response. However, when the modes are well spaced, the average response is dominated by the peaks. There, the discrete-frequency response is often needed.

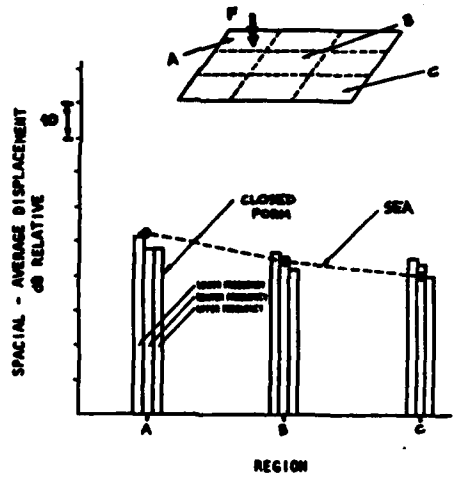

Figure 11: Flat-plate SEA Prediction

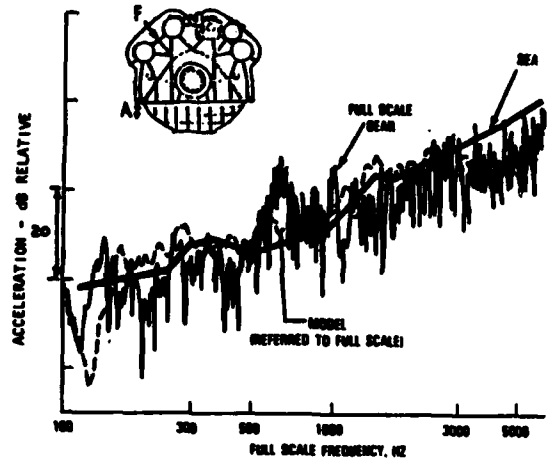

Figure 12: Reduction Gear SEA Prediction

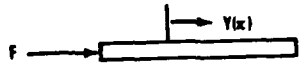

A) ROD

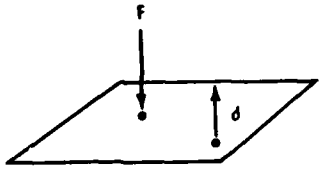

B) PLATE

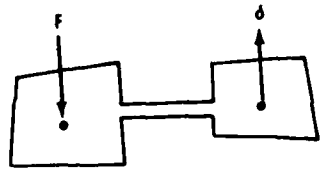

C) CONNECTED PLATES

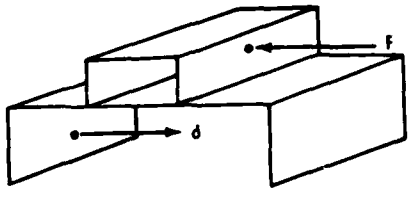

D) FRAME STRUCTURE

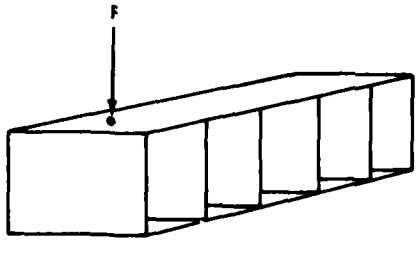

E) BOX BEAM

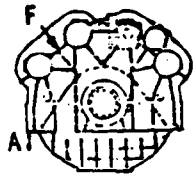

F) 1/4 SCALE GEAR

Figure 13: SEA Benchmarks

DESIGN EXAMPLE

The concept of integrated gear system dynamics analysis is applied to a marine propulsion unit. The system under investigation consists of a double reduction gear train (Figure 14) driven by two turbines, and the supporting subbase. Twenty-two bearings serve to mount the gears and turbines to the subbase structure, which itself is spring-mounted to the ship's foundation structure.

A simplified finite-element model is shown in Figure 15. The gearcase and bull gear are modelled by plate elements, while the first reduction gears and shafts appear as concentrated masses on beams. The subbase is modelled by plates and beams, and the turbine shafts are represented by beams. The 138 plate, 110 beam, and 40 elastic elements are believed to adequately account for the essential dynamical features of a typical propulsion unit.

The FEA is carried out in two steps. First, the natural frequencies and mode shapes of the bull gear, turbines, and subbase are extracted. The resulting 72 eigenvalues and eigenvectors, plus each of the bearing and support stiffnesses and damping, are recombined via modal synthesis. The low speed gear static transmission error, $\delta(\omega)$, calculated by WEDGAP, is input as relative displacement excitation at eight tooth mesh locations. The problem is solved by the complex direct frequency response method of NASTRAN SOL 71 (6).

The SEA model is comprised of 79 subsystems and 148 junctions, schematically represented in Figure 16. $\delta(\omega)$ is again input at the second reduction mesh. The SEA code SEAM* is used to compute the response at the subbase mounting points.

Typical FEA and SEA responses are compared in Figure 17. They show agreement to within 10 dB from 80 to 500 HZ. In this range, the FEA and SEA results can be used as cross-checks of both models. At low frequencies, before the structure "breaks up" into a large number of modes, the SEA model overpredicts the response. Above 500 Hz, the FEA response drops dramatically, indicative of saturation.

* Copyright Cambridge Collaborative, Inc.

CONCLUSION

The integrated gear analysis procedure has been shown to provide complex turbine-gear system response over a broad frequency range. Intermediate frequencies serve to confirm consistency between FEA and SEA models, while low and high frequency calculations utilize the strengths of each. The procedure permits maximum flexibility in designing vibration isolation and damping treatments, so that optimization can be more readily achieved.

ACKNOWLEDGEMENT

The authors wish to acknowledge the contributions of Dr. D. H. Keefe, of Cambridge Collaborative, to the mesh transmission error calculation, and those of Dr. W. C. Gibson, of CSA Engineering, to the finite-element analysis.

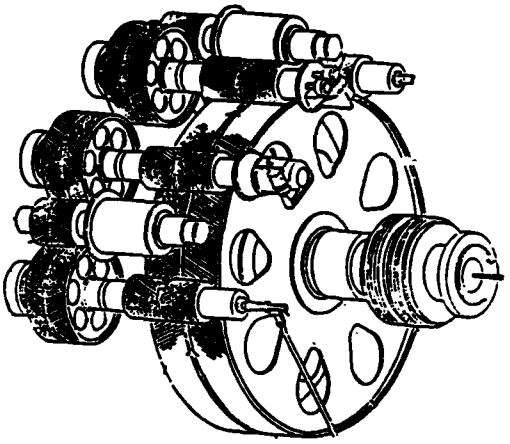

Figure 14: Reduction Gear

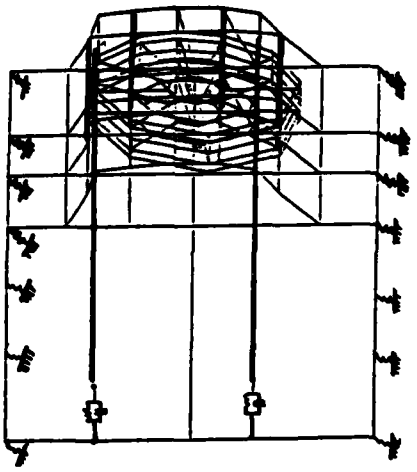

Figure 15: FEA Model of Propulsion Unit

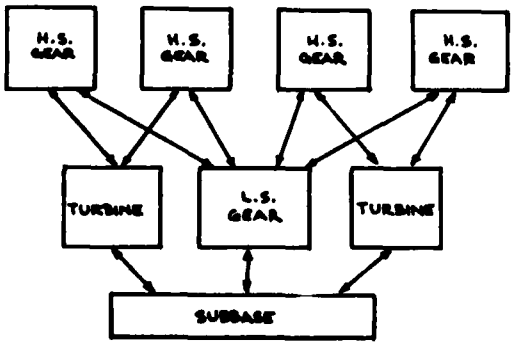

Figure 16: SEA Model Schematic

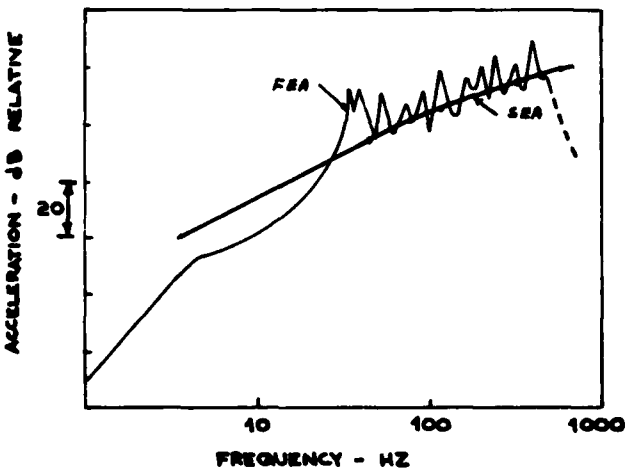

Figure 17: Typical Subbase Mount Point Response

REFERENCES

(1) W. D. Mark "Analysis of the Vibratory Excitation of Gear Systems," Journal of Acoustic Society of America, May 1978.

(2) T. F. Conry and A. Seireg, "A Mathematical Programming Technique for the Evaluation of Load Distribution and Optimal Modification for Gear System", ASME Journal of Engineering for Industry, November 1973.

(3) L. K. H. Lu, W. J. Hawkins, D. F. Downard and R. G. DeJong, "Comparison of Statistical Energy Analysis and Finite-Element Analysis Vibration Prediction with Experimental Results". Shock and Vibration Bulletin (53), 1978.

(4) L. K. H. Lu and P. C. Warner, "Vibration Analysis of a Large Naval Gear", ASME paper No. 81-DET-142.

(5) R. H. Lyon, "Statistical Energy Analysis of Dynamical Systems," MIT Press, 1976.

(6) "MSC/NASTRAN Users Manual", MacNeal-Schwender Corp., Los Angeles, CA 1980.

(7) T. F. Conry, "The Use of Mathematical Programming in Design for Uniform Load Distribution in Non-Linear Elastic Systems", Ph.D. Thesis, University of Wisconsin, 1969.

(8) A. Kubo, "Strength Calculation of Large Helical Gears", Bulletin of JSME, Vol. 22, No. 166, April 1979.

(9) A. Kubo, "Initiation and Progress of Scoring Failure on Cylindrical Involute Gears", Bulletin of JSME, Vol. 24, No. 187, Jan. 1981.

(10) A. Kubo and S. Kiyono, "Vibrational Excitations of Cylindrical Involute Gears Due to Tooth Form Errors", Bulletin of JSME, No. 183, Sept. 1980.

(11) G. R. Schmidt, W. Primekamp and A. Wunder, "Optimum Tooth Profile Correction of Helical Gears", ASME Paper No. 80-C2/DET-110.

(12) R. W. Cornell, "Compliance and Stress Sensitivity of Spur Gear Teeth", ASME J. of Meshanical Design, April, 1981.

(13) W. C. Hertz, "Introduction to Modal Synthesis Techniques", Synthesis of Vibration System, ASME, 1971.

(14) C. D. Johnson and D. A. Kienholz, "Finite-Element Prediction of Damping in Structures with Constrained Viscoelastic Logers", AIAA 2nd Structures, Structural Dynamics and Matrial Conf. 1981.

COUPLED TORSIONAL-FLEXURAL VIBRATION OF A GEARED SHAFT SYSTEM USING FINITE ELEMENT ANALYSIS

S.V. Neriya, R.B. Bhat, T.S. Sankar
Department of Mechanical Engineering
Concordia University
Montreal, Quebec H3G 1M8 Canada

The coupled torsional-flexural vibration due to unbalance and geometrical eccentricity in the gears is studied. The coupling action is identified through the analysis of the gear motion and this effect is included in the finite element model of the system. The free vibration problem is solved to obtain the natural frequencies and mode shapes. Normal mode analysis is employed to obtain the dynamic response of the system to excitations arising from the mass unbalance and geometrical eccentricity in the gears. The response exhibits peaks not only at the system natural frequencies, but also at those frequencies which are related to the system natural frequencies through the gear ratio. The response spectra for various parametric combinations are presented and discussed. The finite element formulation in which the effect of torsional-flexural coupling due to gear pairs are included is found to be a very convenient method to study complex geared shaft systems.

NOMENCLATURE

$\bar{c}_t$	average flexural damping of the gear tooth
$[C]$	generalized global damping matrix
c_m	lumped torsional damping at the motor
c_d	lumped torsional damping at the dynamo
d	diameter of the beam element
E	modulus of elasticity of the beam element
F	transmitted force
$\{F\}$	generalised force vector
G	modulus of rigidity of the beam element

NOMENCLATURE (cont'd)

I_1	moment of inertia of the driving gear
I_2	moment of inertia of the driven gear
J_1	moment of inertia of the motor
J_2	moment of inertia of the dynamo
$\bar{k}_t$	average flexural stiffness of the gear tooth
K_{yy}	stiffness of the rolling contact bearing in the y-direction
K_{zz}	stiffness of the rolling contact bearing in the z-direction
$[K]$	generalised global stiffness matrix
ℓ	length of the beam element
m_1	mass of the driving gear
m_2	mass of the driven gear
m_{t1}	mass of the driving gear tooth
m_{t2}	mass of the driven gear tooth
$[M]$	generalised global mass matrix
$\bar{m}$	mass per unit length of the beam element
$\{p_s\}_k, \{p_c\}_k$	principal coordinates corresponding to the k^{th} sine and cosine excitations
$\{q\}$	generalised displacement vector

NOMENCLATURE cont'd.

r_1	base circle radius of the driving gear
r_2	base circle of the driven gear
U_1	mass unbalance in the driving gear
U_2	mass unbalance in the driven gear
$[\gamma]$	diagonal damping matrix
ε_1	geometrical eccentricity in the driving gear
ε_2	geometrical eccentricity in the driven gear
θ_{f1}	angle between the directions of the eccentricity and unbalance for the driving gear
θ_{f2}	angle between the directions of the eccentricity and unbalance for the driven gear
$[\kappa]$	diagonal stiffness matrix
λ_i	ith eigenvalue
$[\mu]$	diagonal mass matrix
$\{\psi_i\}$	ith eigenvector

INTRODUCTION

Noise and vibration are serious problems in the operation of a geared shaft system. The problem is complicated by the fact that the torsional and flexural vibrations are coupled which makes the analysis more difficult. The system is excited during the operation by the forces originating from incorrect mounting, unbalance in the gears and profile errors. Mahalingam and Bishop [1] determined the dynamic load due to excitation from a static transmission error which encompassed all forms of error in the geared system.

Mahalingam and Bishop [1] determined the dynamic load due to excitation from a static transmission error which encompassed all forms of error in the geared system. Lund [2] considered coupling in the torsional-flexural vibrations in a geared system of rotors. He analysed a system with high damping and obtained the system dynamic response in terms of the complex eigenvalues and eigenvectors. He also studied the stability of the rotor system. Iida et al [3] studied a geared shaft system including the effects of torsional-flexural coupling. The geared shaft system was described as a 4 DOF lumped mass model where the driven shaft is considered flexible in bending and the driving shaft is considered rigid. He obtained the response due to mass unbalance and geometrical eccentricity. Neriya et al [4] extended this study considering both the driving and driven shafts flexible in bending. The flexibility of the mating teeth was considered in the analysis. The frequency response and subsequently the dynamic tooth load were obtained by normal mode analysis.

In this paper, the geared shaft system is modelled by using the finite element method. The effect of coupling between torsional and flexural motions is identified by analysing the gear motion and is included in the finite element formulation. The flexibility of the bearings supporting the shafts is considered in this investigation and the frequency response is then obtained using the normal mode analysis. The finite element method offers significant advantages in extending the simple geared system considered into a train of geared rotors as well as the case of introducing flexibility and damping in the bearing supports.

ANALYSIS

A schematic representation of a simple geared shaft system is shown in Fig. 1. A sectional view at the gear pair location [see Fig. 1] is shown in Fig. 2 and it shows the relative positions of the driving and driven gears, θ. There exists a "force" coupling between the translational motion of the gear center y, z; and the rotational motion of the gear. At the gear location they correspond to the flexural motion of the shaft carrying the gear and its torsional motion. Fig. 3(a) shows the spring mass representation for the driving gear. The mass of the driving gear m_1 is denoted by the mass of the gear m_{t1} tooth in contact. The coordinate z_{t1} describes the gear tooth motion and is in a direction parallel to the line of action of the gears. The time average stiffness and damping of the gear tooth are denoted by $\bar{k}_t$ and $\bar{c}_t$ respectively. The tooth stiffnesses are very high compared to the shaft stiffness and their variation with time does not significantly affect the natural frequencies of the rotor system. k_{b1} and c_{b1} denote the stiffness and damping of the shaft carrying the driving gear. The driven gear is similarly modelled and is shown in Fig. 3(b). Tooth separation is not considered in this analysis and this is incorporated through the constraint equation $z_{t1} = z_{t2}$. The motion of the pair of gears described above is analysed and it reveals the terms coupling the torsional and flexural displacements at the gear locations and the forces occuring at the gear pair. [Refer the Appendix.] The contact ratio for the gear pair is assumed to be unity.

The finite element discretisation of the geared shaft system under study is shown in

Fig. 4. The driving and driven shafts are both divided into beam elements 1 to 6 as shown. The eight nodes of the system denoted by a to h, each have 5 degrees of freedom after excluding motion in the axial direction. As seen above, the contact point of the mating gear teeth has one DOF in the z direction, which accounts for the tooth flexibility. The system thus has 41 degrees of freedom. The generalised displacement vector for the beam element described in Fig. 5 is given by

$$\{y_1, z_1, \theta_{x1}, \theta_{y1}, \theta_{z1}, y_2, z_2, \theta_{x2}, \theta_{y2}, \theta_{z2}\}^T$$

The element mass and stiffness matrices obtained from the consistent formulation are then assembled to form the global mass and stiffness matrices. The concentrated masses and inertia (including transverse moment of inertia) due to the motor, dynamo gears and gear teeth are introduced into the appropriate locations in the global mass matrix. The stiffnesses of the rolling contact bearings are included in the analysis. The terms arising from the coupling between the torsional and flexural motions [Ref(4)] are now introduced into the appropriate locations in the global stiffness matrix. The global force vector is also formulated on the basis of [4]. These are given in the Appendix along with the notations used for the corresponding degrees of freedom as illustrated in Fig. 4.

The equations of motion of the 41 DOF geared shaft system can now be written as

$$[M]\{\ddot{q}\} + [C]\{\dot{q}\} + [K]\{q\} = \{F\} \qquad (1)$$

The homogenous part of Eq. 1 neglecting damping is given by

$$[M]\{\ddot{q}\} + [K]\{q\} = 0$$

and is solved to obtain the eigenvalues λ_i and the eigenvectors $\{\psi_i\}$ of the system.

The force vector $\{F\}$ in Eq. 1 has the excitation consisting of frequencies ω_1 and ω_2 as:

$$\{F\} = \{F_s\}_1 \sin \omega_1 t + \{F_s\}_2 \sin \omega_2 t + \{F_c\}_1 \cos \omega_1 t + \{F_c\}_2 \cos \omega_2 t \qquad (2)$$

where θ_{10}, θ_{20}, θ_{f1} and θ_{f2} have been assumed to be zero. The corresponding response also can be expressed in a form involving the two frequencies as

$$\{q\} = \{q_s\}_1 \sin \omega_1 t + \{q_s\}_2 \sin \omega_2 t + \{q_c\}_1 \cos \omega_1 t + \{q_c\}_2 \cos \omega_2 t \qquad (3)$$

Using Eqs. 2 and 3, Eq. 1 can be written as four separate equations.

$$[M]\{\ddot{q}_s\}_k + [C]\{\dot{q}_s\}_k + [K]\{q_s\}_k = \{F_s\}_k$$

$$[M]\{\ddot{q}_c\}_k + [C]\{\dot{q}_c\}_k + [K]\{q_c\}_k = \{F_c\}_k$$

$$; k = 1, 2 \qquad (4)$$

Expressing the response $\{q\}$ in terms of the modal coordinates $\{p\}$ as

$$\{q_s\}_k = [\psi]\{p_s\}_k$$

$$\{q_c\}_k = [\psi]\{p_c\}_k \; ; k = 1, 2 \qquad (5)$$

where $[\psi]$ is the modal matrix formed by using the eigenvector $\{\psi_i\}$, and $\{p_s\}_k$ and $\{p_c\}_k$, are the principal coordinate vectors corresponding to the sine and cosine components. Using Eqs. 5 in Eqs. 4 and premultiplying by $[\psi]^T$ results in uncoupled equations in the modal coordinates of the form,

$$\mu_i(\ddot{P}_{si})_k + \gamma_i(\dot{P}_{si})_k + \kappa_i(P_{si})_k = (\sigma_{si})_k$$

$$\mu_i(\ddot{P}_{ci})_k + \gamma_i(\dot{P}_{ci})_k + \kappa_i(P_{ci})_k = (\sigma_{ci})_k \qquad (6)$$

where $k = 1, 2$
$i = 1, 2, \ldots 41$

where μ_i and κ_i are the elements of diagonal matrices $[\mu]$ and $[\kappa]$ given by

$$[\mu] = [\psi]^T [M] [\psi]$$

$$[\kappa] = [\psi]^T [K] [\psi]$$

and γ_i is the equivalent damping coefficient in each mode. $(\sigma_{si})_k$ and $(\sigma_{ci})_k$ are the elements of the generalised force vectors $\{\sigma_s\}_k$ and $\{\sigma_c\}_k$, given by

$$\{\sigma_s\}_k = [\psi]^T \{F_s\}_k$$

$$\{\sigma_c\}_k = [\psi]^T \{F_c\}_k \; ; k = 1, 2,$$

The solution of Eq. (6) yields

$$(p_{si})_k = \frac{(\sigma_{si})_k}{(-\omega_k^2 \mu_i + \kappa_i) + j(\gamma_i \omega_k)}$$

$$(p_{ci})_k = \frac{(\sigma_{ci})_k}{(-\omega_k^2 \mu_i + \kappa_i) + j(\gamma_i \omega_k)} \qquad (7)$$

$k = 1, 2$
$i = 1, 2, \ldots 41$

Using Eqs. (7), (5) and (3) we obtain the system dynamic response $\{q\}$. Since the response involves two frequencies ω_1 and ω_2, the total response has the form

$$q_j = q_{1j}\sin(\omega_1 t + \psi_{1j}) + q_{2j}\sin(\omega_2 t + \psi_{2j})$$

$$= q_{1j}\sin\lambda_1 + q_{2j}\sin\lambda_2$$

$$= (q_{1j}+q_{2j})\sin\left(\frac{\lambda_1-\lambda_2}{2}\right)\cos\left(\frac{\lambda_1-\lambda_2}{2}\right)$$

$$+ (q_{1j} - q_{2j})\cos\left(\frac{\lambda_1+\lambda_2}{2}\right)\sin\left(\frac{\lambda_1+\lambda_2}{2}\right) \quad (8)$$

Hence, the response is an amplitude modulated harmonic phenomenon. If ω_1 and ω_2 are close to each other, this will result in beats.

NUMERICAL RESULTS

The details of the geared shaft system used the stiffnesses are to obtain the numerical results are given in Table. 1. The pedestals are assumed to be flexible in both y and z directions and the stiffnesses are denoted by k_{yy} and k_{zz} respectively. The details of the beam elements comprising the finite element model are given in Table 2. The system natural frequencies and their gear ratio multiples in the range 0-80 Hz are given in Table 3. The zero natural frequency corresponds to a torsional rigid body mode.

The time domain response at two individual frequencies are plotted in Fig. 6 and Fig. 7. Fig. 6(a) shows the time domain response at the driven gear location at a frequency of 37 Hz which is very close to a system natural frequency. Fig. 6(b) shows the same at the driving gear location. Fig. 7(a) shows the time domain response at the driven gear location at a frequency of 50 Hz which is away from a system natural frequency. Fig. 7(b) shows the same at the driving gear location.

The frequency domain response is plotted for the flexural responses at the gear locations. Fig. 8 shows the response in the z direction at the driven gear location. The system shows peak responses at the system natural frequencies corresponding to modes 2, 4, 6 and 8, and also at the frequencies related to the modes 2, 4 and 6 by the gear ratio (Table 3). The natural frequency of mode 8 when multiplied by the gear ratio is found to be outside the frequency range of interest. Three cases corresponding to varying unbalance and eccentricity are plotted.

The response in the z direction at the driving gear location is shown in Fig. 9. The system shows peak responses at the system natural frequencies corresponding to modes 2, 4, 6 and 8, and also at frequencies related to the modes 2, 4, and 6 by the gear ratio (Table 3). The natural frequency of mode 8 when multiplied by the gear ratio is found to be outside the frequency range of interest. Three cases corresponding to varying unbalance and eccentricity are plotted.

ACKNOWLEDGEMENTS

The work reported was partially supported by grants A1375 and A7104 from Natural Sciences and Engineering Research Council of Canada.

REFERENCES

1. Mahalingam, S. and Bishop, R.E.D., "Dynamic Loading of Gear Teeth", Journal of Sound and Vibration, pp. 179-189, 1974.

2. Lund, J.W., "Critical Speed, Stability and Response of a Geared Train of Rotor", Journal of Mechanical Design, Vol. 100, pp. 535-539, July 1978.

3. Iida, H., Tamura, A., Kikuch, K. and Agata, H., "Coupled Torsional-Flexural Vibration of a Shaft in a Geared System of Rotors", Bulletin of the JSME, Vol. 23, No. 186, pp. 2111-2117, December 1980.

4. Neriya, S.V., Bhat, R.B. and Sankar, T.S., "Effect of Coupled Torsional-Flexural Vibration of a Geared Shaft System on the Dynamic Tooth Load", 54th Shock and Vibration Bulletin, June 1984.

APPENDIX

a. STIFFNESS MATRIX

$$\begin{bmatrix} q_{27} \\ q_{11} \\ q_{21} \\ q_{29} \\ q_{13} \end{bmatrix} \rightarrow \begin{bmatrix} \bar{k}_t & 0 & -\bar{k}_t & \bar{k}_t r_1 & 0 \\ 0 & \bar{k}_t & -\bar{k}_t & 0 & \bar{k}_t r_2 \\ -\bar{k}_t & -\bar{k}_t & 2\bar{k}_t & -\bar{k}_t r_1 & -\bar{k}_t r_2 \\ -\bar{k}_t r_1 & 0 & -\bar{k}_t r_1 & \bar{k}_t r_1^2 & 0 \\ 0 & \bar{k}_t r_2 & -\bar{k}_t r_2 & 0 & \bar{k}_t r_2^2 \end{bmatrix}$$

b. FORCE VECTOR

$$\begin{bmatrix} F_{28} \\ F_{27} \\ F_{12} \\ F_{11} \\ F_{21} \\ F_{29} \\ F_{13} \end{bmatrix} \rightarrow \begin{bmatrix} -\bar{c}_t\varepsilon_1\omega_1\cos(\omega_1 t + \theta_{10}) - \bar{k}_t\varepsilon_1\sin(\omega_1 t + \theta_{10}) + \\ +u_1\omega_1^2\sin(\omega_1 t + \theta_{10} + \theta_{f1}) \\ u_1\omega_1^2\cos(\omega_1 t + \theta_{10} + \theta_{f1}) \\ -\bar{c}_t\varepsilon_2\omega_2\cos(\omega_2 t + \theta_{20}) - \bar{k}_t\varepsilon_2\sin(\omega_2 t + \theta_{20}) + \\ +u_2\omega_2^2\sin(\omega_2 t + \theta_{20} + \theta_{f2}) \\ u_2\omega_2^2\cos(\omega_2 t + \theta_{20} + \theta_{f2}) \\ \bar{c}_t\{\varepsilon_2\omega_2\cos(\omega_2 t + \theta_{20}) + \varepsilon_1\omega_1\cos(\omega_1 t + \theta_{10}) \\ +\bar{k}_t\{\varepsilon_2\sin(\omega_2 t + \theta_{20}) + \varepsilon_1\sin(\omega_1 t + \theta_{10})\} \\ -\bar{c}_t r_1\varepsilon_1\omega_1\cos(\theta_{10} + \omega_1 t) - F_o\varepsilon_1\cos(\theta_{10} + \omega_1 t) \\ -\bar{k}_t r_1\varepsilon_1\sin(\theta_{10} + \omega_1 t) \\ -\bar{c}_t r_2\varepsilon_2\omega_2\cos(\theta_{20} + \omega_2 t) + F_o\varepsilon_2\cos(\theta_{20} + \omega_2 t) \\ -\bar{k}_t r_2\varepsilon_2\sin(\theta_{20} + \omega_2 t) \end{bmatrix}$$

TABLE 1

E	1.96×10^{11} N/m^2
G	7.84×10^{16} N/m^2
I_1	3.0×10^{-2} kgm^2
I_2	6.28×10^{-3} kgm^2
J_1	4.59×10^{-1} kgm^2
J_2	5.49×10^{-1} kgm^2
k_t	2.45×10^{9} N/m
k_{yy}	8.83×10^{8} N/m
k_{zz}	8.83×10^{8} N/m
m_1	16.96 kg
m_2	5.65 kg
mt_1, mt_2	4.9×10^{-3} kg
r_1	0.1 m
r_2	0.05 m
ε_1, ε_2	120 μm (variable)
u_1, u_2	2.8×10^{-4} kgm (variable)

TABLE 2

Element No.	Length ℓ mm	Diameter d mm	Mass per unit length - m kg/mm
1	300	15	1.41 E-3
2	300	20	2.15 E-3
3	600	20	2.51 E-3
4	600	30	5.655 E-3
5	300	30	5.655 E-3
6	300	25	3.93 E-3

TABLE 3

System Natural Frequencies and their Gear Ratio Multiples in the Range

0 - 80 Hz

Mode No.	System Natural Frequency	System Natural Frequency Gear Ratio
1	zero	zero
2	7.78	15.56
3	21.27	42.54
4	22.96	45.92
5	29.22	58.44
6	35.46	70.92
7	36.57	73.14
8	44.09	--
9	71.39	--
10	71.57	--
11	72.24	--

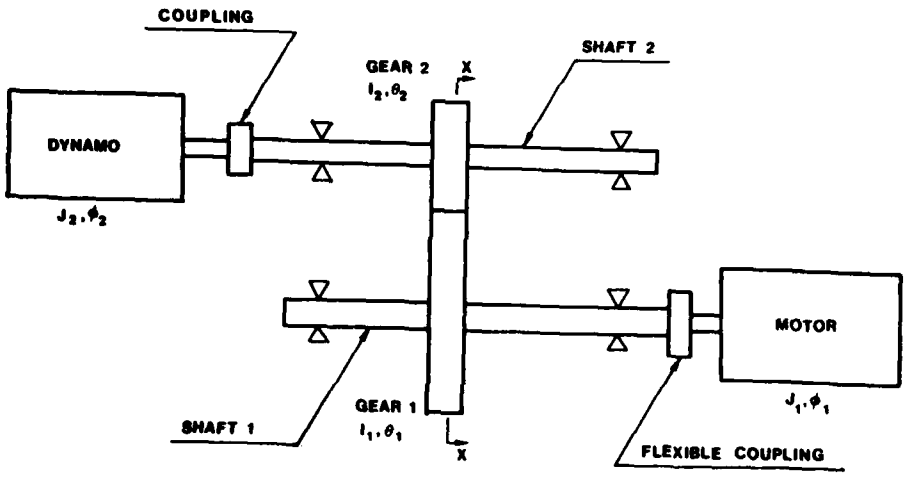

Fig. 1 Simple Geared Shaft System

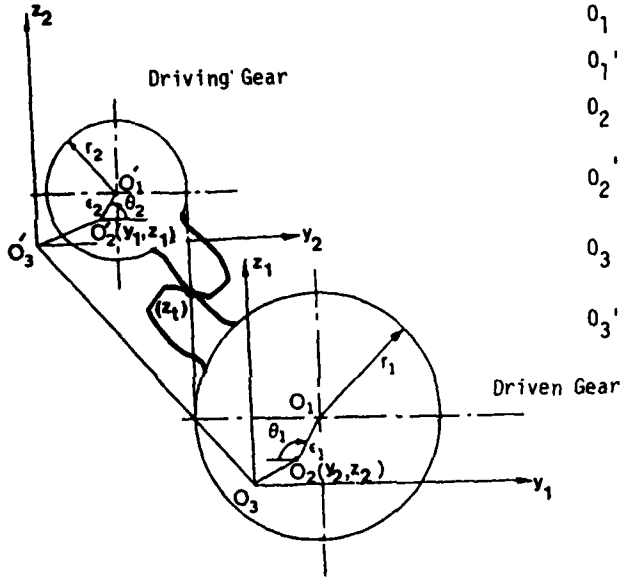

O_1 geometric center of the driving gear

O_1' geometric center of the driven gear

O_2 center of the driving shaft when it is rotating

O_2' center of the driven shaft when it is rotating

O_3 center of the driving shaft when it is stationary

O_3' center of the driven shaft when it is stationary

Fig. 2 Sectional view at the gear location

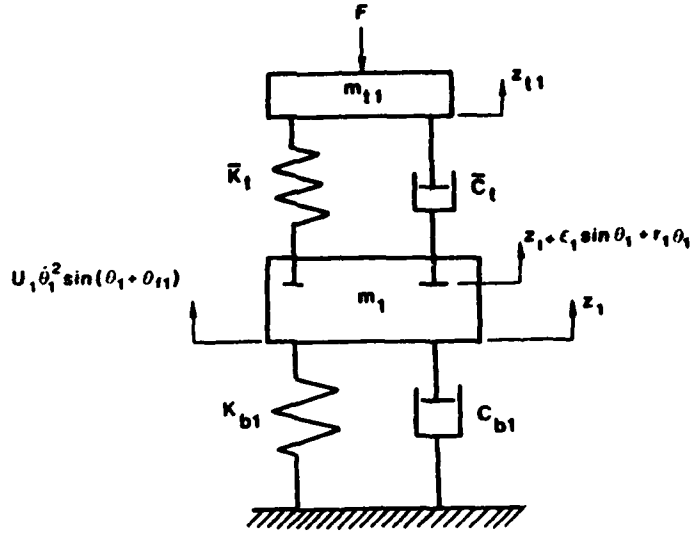

Fig.3a Driving Gear Model

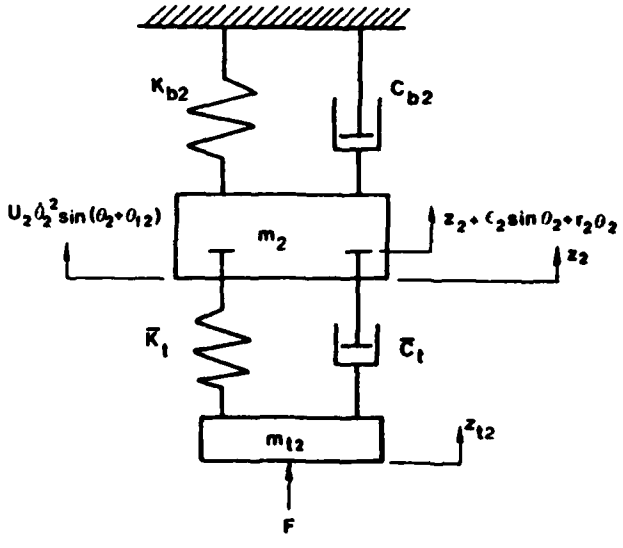

Fig.3b Driven gear model

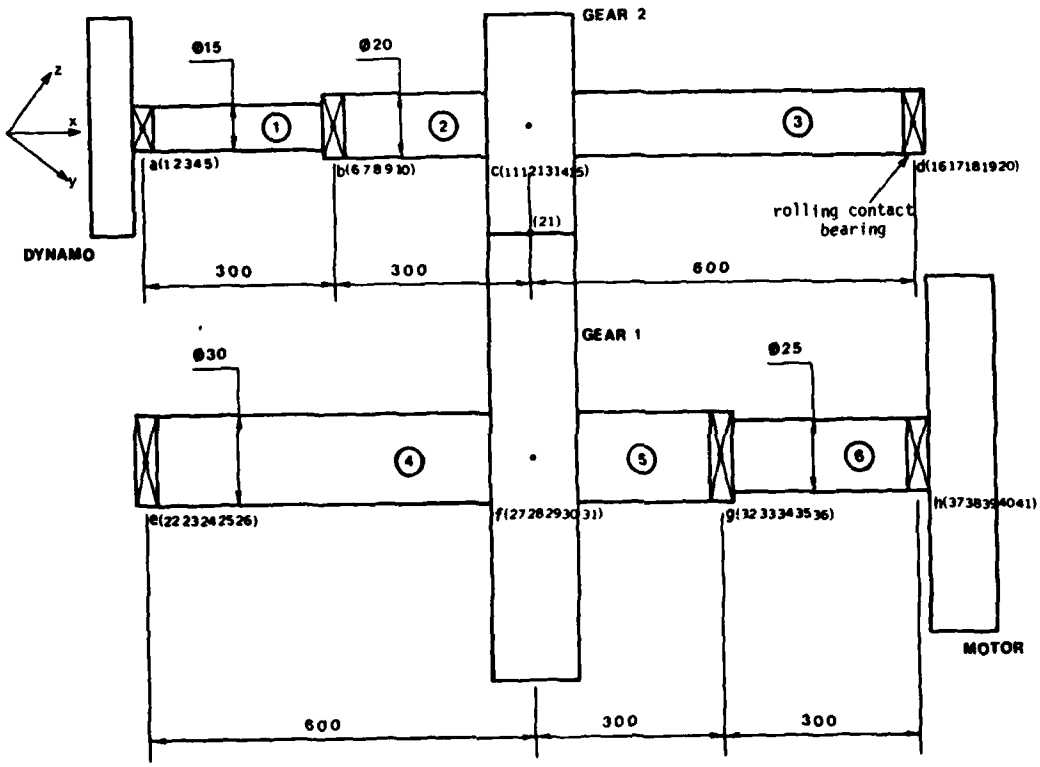

Fig. 4 Geared shaft system and its finite element discretisation

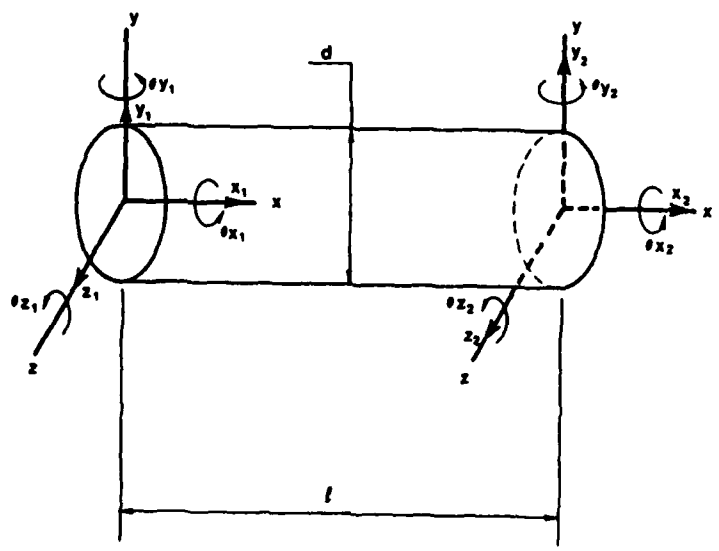

Fig. 5 Typical beam element

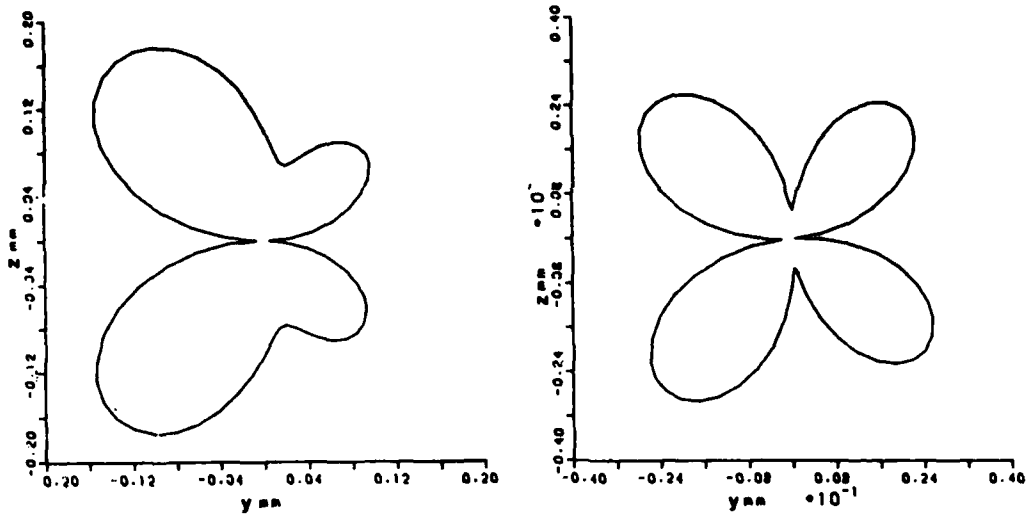

a) Driven Gear Location b) Driving Gear Location

Fig. 6 Time Domain Response at 38 Hz.

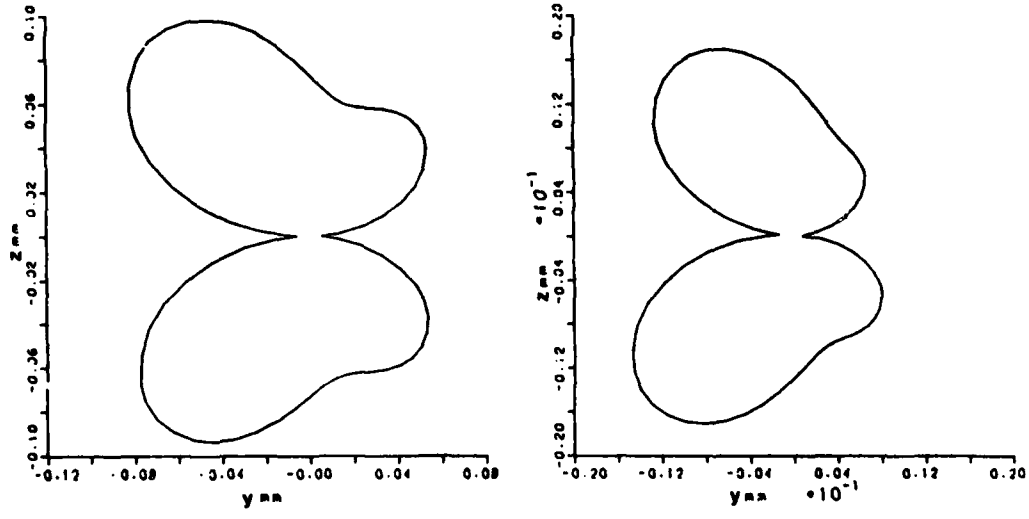

a) Driven Gear Location b) Driving Gear Location

Fig. 7 Time Domain Response at 50 Hz.

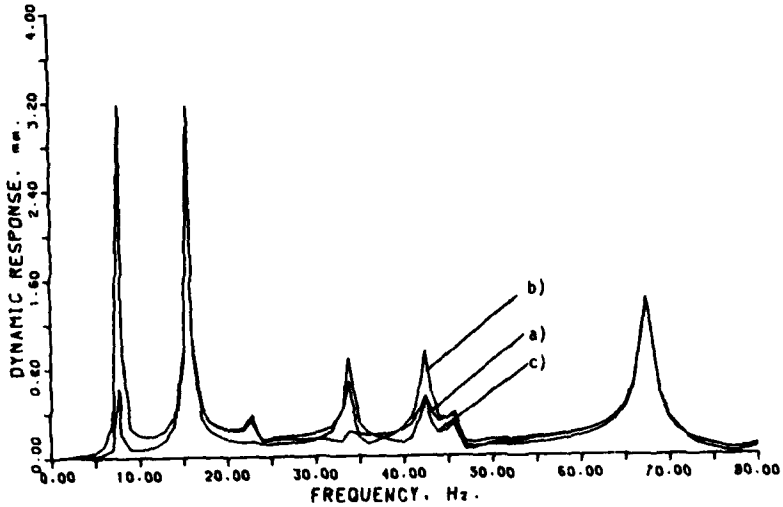

Fig. 8 Frequency Domain Response in the z Direction at the driven gear location (DOF #12)

a) ε_1 = 120 μm, ε_2 = 20 μm, u_1 = 2.8x10^{-4} kgm, u_2 = 2.8x10^{-4}kgm

b) ε_1 = 120 μm, ε_2 = 120μm, u_1 = 2.8x10^{-4} kgm, u_2 = 0.78x10^{-4}kgm

c) ε_1 = 120 μm, ε_2 = 120μm, u_1 = 2.8x10^{-4} kgm, u_2 = 2.8x10^{-3} kgm

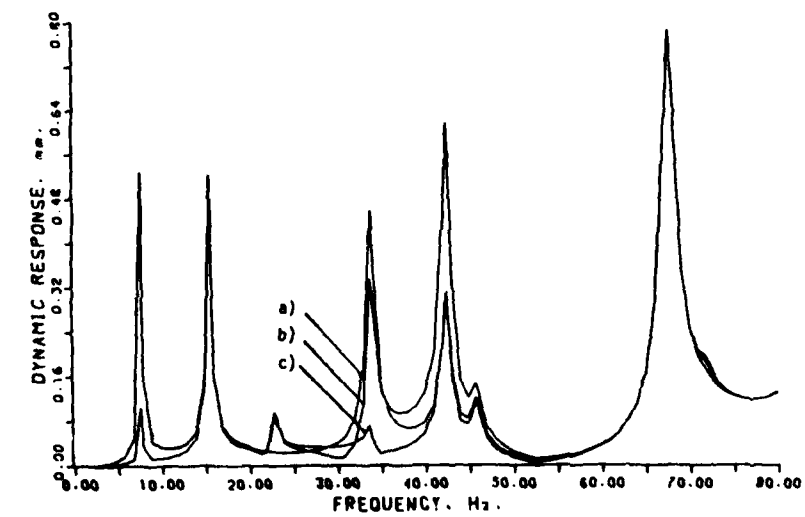

Fig. 9 Frequency Domain Response in the z Direction at the Driving Gear Location (DOF #28)

a) ε_1 = 120 μm, ε_2 = 20 μm, u_1 = 2.8x10^{-4} kgm, u_2 = 2.8x10^{-4}kgm

b) ε_1 = 120 μm, ε_2 = 120μm, u_1 = 2.8x10^{-4} kgm, u_2 = 0.78x10^{-4}kgm

c) ε_1 = 120 μm, ε_2 = 120μm, u_1 = 2.8x10^{-4} kgm, u_2 = 2.8x10^{-3} kgm

DISCUSSION

Mr. Rieger (Stress Technology, Inc.): What kind of bearings were you talking about? Were they rolling element bearings with low damping?

Mr. Neriya: That is correct.

INFLUENCE OF AN AXIAL TORQUE ON THE DYNAMIC BEHAVIOR OF ROTORS IN BENDING

R. Dufour, J. Der Hagopian, M. Lalanne
I.N.S.A.
Laboratoire de Mécanique des Structures
U.A. C.N.R.S. 862
20, avenue Albert Einstein
69621 Villeurbanne - France

Today it is necessary to predict with great accuracy the dynamic behavior of rotating machinery components at the design stage. This paper focuses on the secondary effect on the dynamic characteristics of rotors in bending, introduced by axial torque. The influence of a constant and an harmonic exciting torque has been studied both experimentally and theoretically in this work.

INTRODUCTION

The dynamic characteristics of rotating machinery must at this time be predicted quite accurately. The main effects of rotor dynamics are now well known and taken into account in the equations and the corresponding computer programs. This paper considers the secondary effect of an axial torque in view of including its influence systematically in the analysis of a rotor.

Eshleman and Eubanks |1| have presented the equations of motion for rotors in bending subjected to several secondary effects such as constant axial torque. The solution of the equations shows that the stiffness of the shafts decreases as the axial torque increases. This effect is predominant over the other secondary effects if the slenderness ratio $r = R/2L$ is < 0.0025. Zorzi and Nelson |2| have calculated the virtual work of the components of the axial torque and deduced a matrix to be used in a finite element formulation. This matrix is non-symmetric and must be added to the stiffness matrix. They have applied that formulation to simple examples : i.e. a simple beam with boundary conditions either simply-supported or clamped at both ends. Ziegler |3| has dealt with nonconservative systems and given for different boundary conditions the values of critical torques leading to buckling. Willems and Holzer |4| have published results on the critical speeds of a rotating shaft subjected to a constant torque and a constant axial force.

Eshleman and Eubanks |5| have built and tested an original apparatus. They have shown the difficulties in obtaining a pure axial torque and have observed, with a pulsating harmonic torque, zones with instabilities.

Unger and Brull |6| have obtained theoretical results, using a quasi-analytical Galerkin type method. They consider both a constant axial torque and an harmonic pulsating torque at the same time. As did Hsu |7| they prove the existence of three kinds of instabilities for coupled Mathieu's equations. In the type P the system vibrates with period P. In the type 2P the system vibrates with period P, the excitation period being 2P. The last kind of instability is $(\omega_i+\omega_j)/k$ with $i,j,k = 1,2,\ldots$ where the system vibrates at frequency ω_i or ω_j for the excitation $(\omega_i+\omega_j)/k$. The work presented in what follows is mostly devoted to an experimental set up in which the influences of a constant axial torque and of a pulsating torque can be simulteanously observed. Solutions of equations have also been presented. A matrix for a constant axial torque has been included in a finite element computer program |8|.

EQUATIONS

The dynamic behavior of a constant circular cross-section Euler-Bernoulli beam, Figure 1, subjected to an axial torque T is defined in absence of other external forces by the two following equations presented in |1|, |4| :

$$\rho S \frac{\partial^2 w}{\partial t^2} + EI \frac{\partial^4 w}{\partial y^4} + T \frac{\partial^3 u}{\partial y^3} = 0$$
$$\rho S \frac{\partial^2 u}{\partial t^2} + EI \frac{\partial^4 u}{\partial y^4} - T \frac{\partial^3 w}{\partial y^3} = 0 \qquad (1)$$

with

S, cross section area
I, diametral area moment of inertia of the cross section
E, Young's modulus
ρ, mass per unit volume
u,w, displacement components of the center of inertia of the beam cross section.

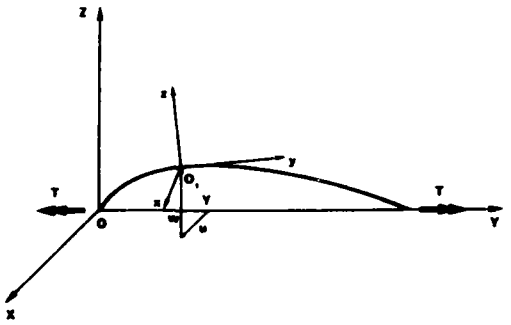

Fig.1 - Beam reference axis

The two equations can be written more compactly. Introducing the new variable :

$$z = w + iu \quad ; \quad (i = \sqrt{-1}) \qquad (2)$$

it comes

$$\rho S \frac{\partial^2 z}{\partial t^2} + EI \frac{\partial^4 z}{\partial y^4} - iT \frac{\partial^3 z}{\partial y^3} = 0 \qquad (3)$$

For convenience equation (3) has been written in a non dimensionnal form :

$$p^2 \frac{\partial^2 f}{\partial t} + \frac{\partial^4 f}{\partial \xi^4} - iH \frac{\partial^3 f}{\partial \xi^3} = 0 \qquad (4)$$

with

$$\xi = \frac{y}{L} \quad ; \quad f = \frac{z}{L} \quad ; \quad H = \frac{TL}{EI} \quad ; \quad p^2 = \frac{\rho S}{EI} L^4 \qquad (5)$$

The non dimensionnal torque H will be :

$$H = H_0 + H_1 \cos \eta t \qquad (6)$$

where H_0 and $H_1 \cos \eta t$ are respectively the constant and the harmonic pulsating torque.

EXPERIMENTAL SET-UP

The set up has been designed for the dynamic study without inclusion of the rotation effect in order to have well known boundary conditions, (see Figures 2-5). The experiments have been performed with a beam clamped at both ends (C-C) to have a better control of the axial torque. With those boundary counditions the torque remains axial during the experiments.

Constant torque experiment ($H = H_0$)

The torque effect corresponds to the last term of equation (4). The larger H_0 the higher is the influence of T_0. Equation (5) shows that for a given T_0 it is necessary to have a long beam (L) with a small cross section (I). A high stress steel is thus used, whose characteristics in SI are :

$E = 2.06\ N/m^2$
$\rho = 7850\ kg/m^3$

The dimensions of the beam experimented are
L, length = 1.845 m
D, diameter = 3.10^{-3} m.

The maximum torque imposed is $T_{0_{max}} \simeq 2.68$ N.m and $H_{0_{max}} \simeq 6$.

In order to avoid the influence of gravity the experimental set-up presented in Figure 2 is vertical. A force gage ⑦ is fixed at the upper end of the beam, Figure 3. That gage allows the measure of any axial force which can thus be eliminated. At the lower end, Figure 4, the beam is fixed in a parallelepipedic steel support ③ whose only motion is axial, (to avoid axial force and keep the beam clamped). The axial torque is obtained by rotating ②. The resonant frequencies of the system are then obtained by a conventional way, magnetic excitation and detection by proximity probes, for H_0 varying from 0 to 6.

Constant torque and harmonic axial torque ($H = H_0 + H_1 \cos \eta t$).

An electrodynamic shaker, Figure 5, is used to impose the harmonic torque. Needle bearings are used, see part ④, the beam is thus clamped at $L_1 = 1.435$ m from the upper part ⑦. The amplitude of this torque is such that $H_1 \leq 0.02$. The instability zones are obtained by a point by point frequency sweep between 0 to 60 Hz.

SOLUTION OF THE EQUATIONS ($H = H_0$)

Equation (4) has previously been solved |1| by the method of separation of variables. The frequencies are then obtained from the zero values of the determinant associated with the boundary conditions. This paper presents a simple method which makes the phenomena i.e. frequencies and mode shapes, easier to understand. The method is a Galerkin type method and is used for two kinds of boundaries.

Simply supported beam (SS).

The solution is sought using the hypothesis of separation of variables :

$$f_n = \phi_n(\xi).\psi_n(t) \qquad (7)$$

with, n being an integer

$$\phi_n(\xi) = \sin n\pi\xi . e^{iH_0\xi/k} \qquad (8)$$

$\sin n\pi\xi$ is the well known mode shape for SS beams. Here $e^{iH_0\xi/k}$ takes into account the rotation due to the torque. The coefficient k is obtained by

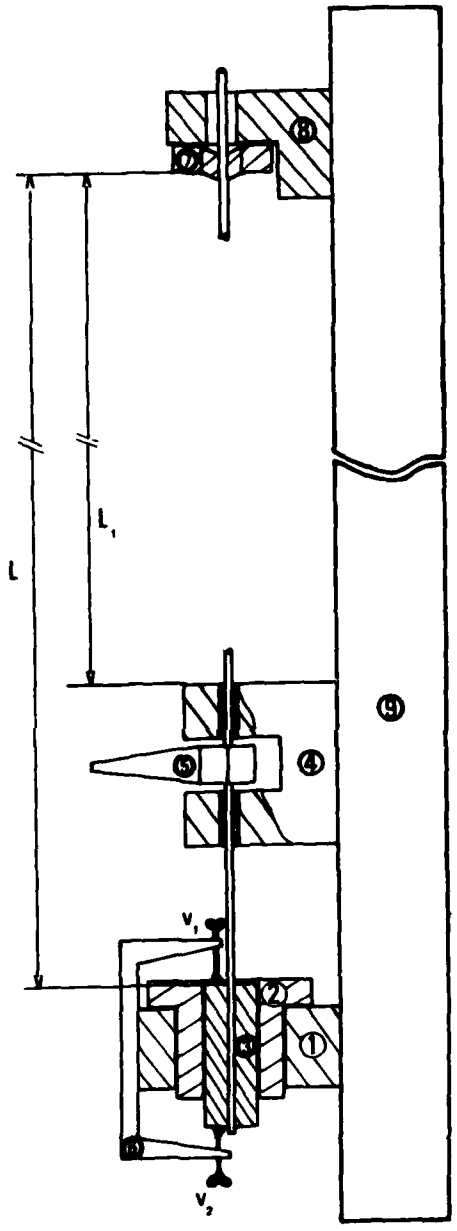

Fig. 2 : Experimental set up

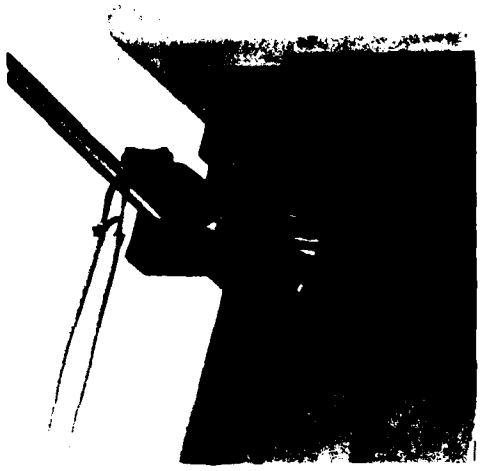

Fig. 3 : Upper support

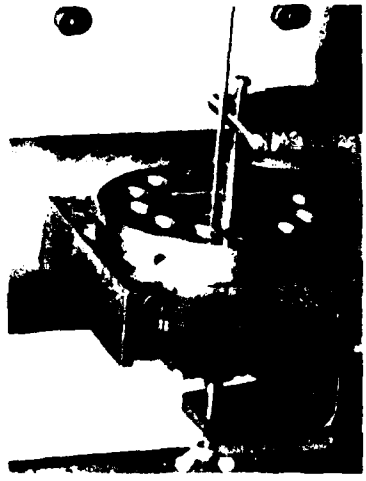

Fig. 4 : Constant axial torque system

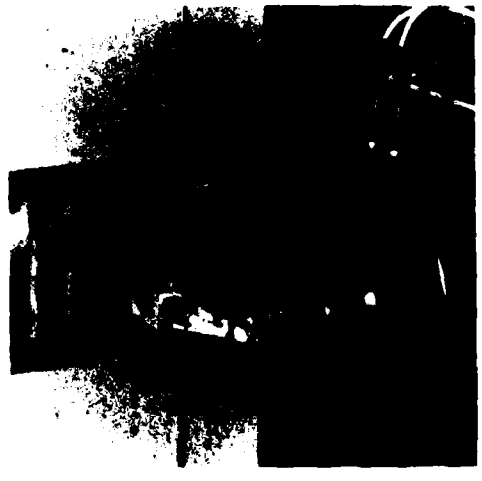

Fig. 5 : Harmonic excitation

the application of the boundary conditions : bending moments and displacements equal to zero for $\xi = 0$, $\xi = 1$. The conditions on the displacements are directly included in equation (8). The bending moments are :

$$m_z = EI \frac{\partial^2 u}{\partial y^2} - T_0 \frac{\partial w}{\partial y} \quad (9)$$

$$m_x = - EI \frac{\partial^2 w}{\partial y^2} - T_0 \frac{\partial u}{\partial y} \quad (10)$$

Equations (9) and (10) can be combined into :

$$m = - m_x + i m_z \quad (11)$$

This gives :

$$\frac{\partial^2 f}{\partial \xi^2} - i H_0 \frac{\partial f}{\partial \xi} = 0 \quad (12)$$

Equation (12) must be valid for $\xi = 0$ and $\xi = 1$, the only solution is $k = 2$. Thus equation (7) becomes :

$$f_n = \text{Sin } n\pi\xi \; e^{iH_0\xi/2} \; \psi_n(t) \quad (13)$$

The solution to equation (13) is introduced in the equations of the motion (4) and the factors of the sine and cosine functions are set equal to zero. This leads to :

$$p^2 \psi^{\circ\circ}_n + (n^4\pi^4 - \frac{H_0^4}{16}) \psi_n = 0 \quad (14)$$

$$n\pi H_0 \; (\frac{H_0^2}{4} - n^2\pi^2) \; \psi_n = 0 \quad (15)$$

From (14) one has :

$$\psi_n = a_n \text{ Sin } \omega_n t + b_n \text{ Cos } \omega_n t \quad (16)$$

with the frequency

$$\omega_n = \frac{1}{p} \sqrt{n^4\pi^4 - \frac{H_0^4}{16}} \quad (17)$$

Due to (5), (17) is :

$$\omega_n = \sqrt{n^4\pi^4 - \frac{H_0^4}{16}} \; \frac{1}{L^2} \; \sqrt{\frac{EI}{\rho S}} \quad (18)$$

$$\omega_n = \frac{X_n^2}{L^2} \sqrt{\frac{EI}{\rho S}} \quad (19)$$

With

$$X_n^2 = \sqrt{n^4\pi^4 - \frac{H_0^4}{16}} \quad (20)$$

$$(n^4\pi^4 \geq \frac{H_0^4}{16})$$

The frequencies ω_n are zero for $H_0 = \pm 2n\pi$, which are the exact values of the buckling torque. Equation (15) shows that solution (13) is the exact solution for : $H_0 = 0$ and $H_0 = \pm 2n\pi$.

Clamped-clamped beam (CC)

The CC beam is more difficult to compute than the SS beam, as it is not easy to suggest a very convenient hypothesis for the displacement. For a CC beam with $H_0 = 0$ it can be observed that :

$$\phi_n(\xi) = \text{Sin } \pi\xi . \text{Sin } n\pi\xi \quad (21)$$

gives a convenient value for the first frequencies. The X_n values, see (19), are shown Table 1.

$H_0 = 0$	EXACT VALUE	APPROXIMATE VALUE
X_1^2	22.37	22.79
X_2^2	61.67	63.2
X_3^2	120.9	115.1
X_4^2	199.8	185.4

Table 1 : - C-C beam - Exact and approximate values of beam coefficients.

As a consequence of these results the following displacement function is defined :

$$\phi_n(\xi) = \text{Sin}\pi\xi . \text{Sin } n\pi\xi . e^{iH_0\xi/k} \quad (22)$$

where $e^{iH_0\xi/k}$ takes into account the rotation due to the torque.

The calculations are performed on a slightly different way from the SS case. Equation (22) is used with equation (4). This gives a second order differential equation in time. The Galerkin procedure is then used. The equation is multiplied by $\text{Sin}\pi\xi . \text{Sin } n\pi\xi \; d\xi$ and integrated between 0 and 1. In order to avoid lengthy developpment only the results are given :

The frequencies obtained are :

$$\omega_1 = \frac{\pi^2 \sqrt{[\lambda_1^2(1-k_1) + 4\lambda_1(2-k_1) + 16/3]}}{L^2} \sqrt{\frac{EI}{\rho S}} \quad (23)$$

$$\omega_1 = \frac{X_1^2}{L^2} \sqrt{\frac{EI}{\rho S}}$$

$$\omega_n = \frac{\pi^2 \sqrt{[\lambda_n^2(1-k_n) + 3\lambda_n(n^2+1)(2-k_n) + (n^4+6n^2+1)]}}{L^2} \sqrt{\frac{EI}{\rho S}} \quad (24)$$

$$\omega_n = \frac{X_n^2}{L^2} \sqrt{\frac{EI}{\rho S}}$$

with

$$\lambda_1 = \frac{H_0^2}{K_1^2\pi^2} \; , \; k_1 = \frac{43}{15} \; , \quad (25)$$

$$\lambda_n = \frac{H_0^2}{k_n^2\pi^2} \; , \; k_n = \frac{8n^4+12n^2+1}{n^2(4n^2+3)} \qquad n = 2,3,\ldots$$

The axial torque is non conservative [3] and its introduction in the finite element method is obtained from the virtual work of the torque. It is easy to introduce the correspon-

ding nonsymmetric matrix $T.K_T$, whose expression is given in |2|, in a finite element computer program.

SOLUTION OF THE EQUATIONS ($H = H_0 + H_1 \cos \eta t$)

As in the case where $H = H_0$, a simple method limited to the types P and 2P is proposed to obtain instabilities. The calculations based on Galerkin's method are presented only for SS beams. For a CC beam the conclusions are identical and the developments are not presented. It is supposed that the mode shapes are not significantly modified by the pulsating torque, then equation (13) is used and equation (4) becomes :

$$p^2 \psi^{\circ\circ}_n(t) + \left[(n^4\pi^4 + \frac{3}{2} H_0^2 n^2 \pi^2 + \frac{H_0^4}{16}) - (H_0 + H_1 \cos \eta t) \frac{H_0}{2} (3n^2\pi^2 + \frac{H_0^2}{4})\right] \psi_n(t) = 0 \quad (26)$$

Let

$$\tau = \eta t \quad (27)$$

$$\delta_n = \frac{\omega_n^2}{\eta^2} \quad (28)$$

$$\varepsilon_n = - \frac{H_0 H_1}{2p^2\eta^2} (3n^2\pi^2 + \frac{H_0^2}{4}) \quad (29)$$

then (26) may be written :

$$\psi^{\circ\circ}_n(\tau) + (\delta_n + \varepsilon_n \cos \tau)\, \psi_n(\tau) = 0 \quad (30)$$

Equation (30) is a Mathieu's equation. Strutt's diagram shows the instability zones corresponding to equation (30) with the most dangerous zones identified for $\delta_n = 1/4$ and $\delta_n = 1$, i.e. $\eta = 2\omega_n$ and $\eta = \omega_n$, |3|, |9|.

APPLICATIONS

Constant axial torque H_0

The results presented are either analytical |4|, |6| or experimental. They include also the formulas proposed here : equations (18) for the SS beam and equations (23), (24) for the CC beam, (Tables 2-3). The mode shapes depicted are from (13) and (22) and given for three values of H_0. They are presented in a plane perpendicular to the Oy axis, (Figures 6-7). The finite element results obtained with 9 elements are in satisfactory agreement with the frequencies and mode shapes and are thus not given. It has been observed that the agreement between experimental and analytical results is satisfactory for the frequencies, Figure 8. Mode shapes have been computed, they have been experimentally observed but not measured.

		$H_0 = 0$	1	2	3	4	5	6
X_1^2	|6|	1	0.99	0.96	0.90	--	0.65	0.33
π^2	|4|	1	0.99	0.96	0.90	0.81	0.66	0.36
	(13)	1	1	0.99	0.97	0.91	0.77	0.41
X_2^2	|6|	4	3.98	3.94	3.86	--	3.59	3.39
π^2	|4|	4	3.99	3.95	3.88	3.78	3.67	3.53
	(13)	4	4	4	3.99	3.98	3.95	3.89
X_3^2	|6|	9	8.98	8.93	8.85	--	8.58	8.38
π^2	(13)	9	9	9	9	8.99	8.98	8.95

Table 2 : - S-S Beam - X_n^2/π^2 versus torque

		$H_0 = 0$	1	2	3	3.5	4	5	6
X_1^2	|6|	1	---	0.98	---	0.94	---	0.87	0.79
22.37	(22)	1.02	1.01	1	0.98	---	0.94	0.89	0.82
X_2^2	|6|	2.76	---	2.73	---	2.68	---	2.59	2.51
22.37	(22)	2.83	2.82	2.81	2.79	---	2.77	2.73	2.69
X_3^2	|6|	5.40	---	5.38	---	5.32	---	5.23	5.15
22.37	(22)	5.15	5.14	5.14	5.13	---	5.11	5.09	5.06

Table 3 : - C-C Beam - $X_n^2/22.37$ versus torque

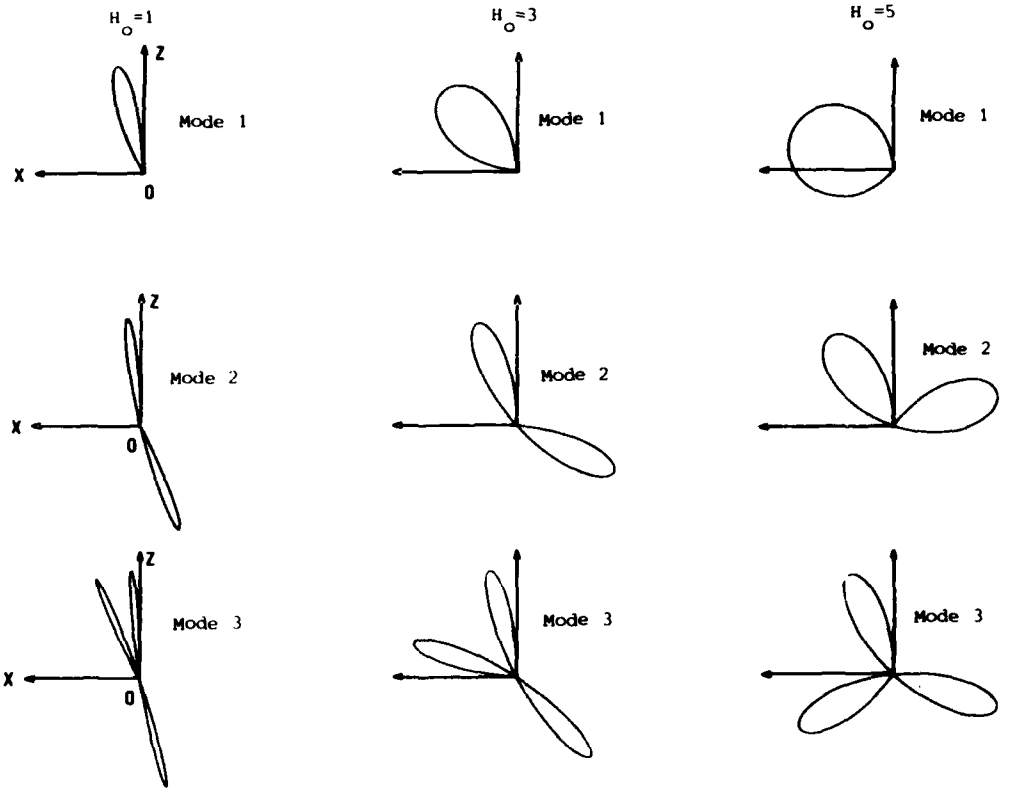

Fig. 6 : S-S Beam - Mode shapes

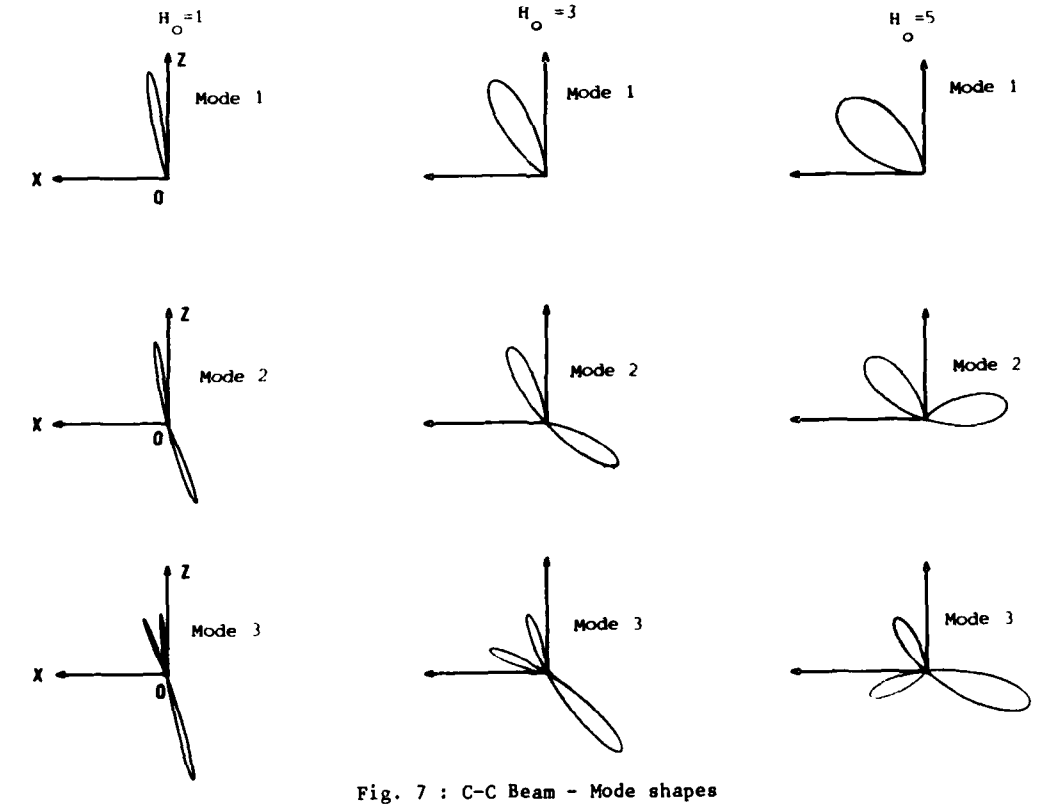

Fig. 7 : C-C Beam - Mode shapes

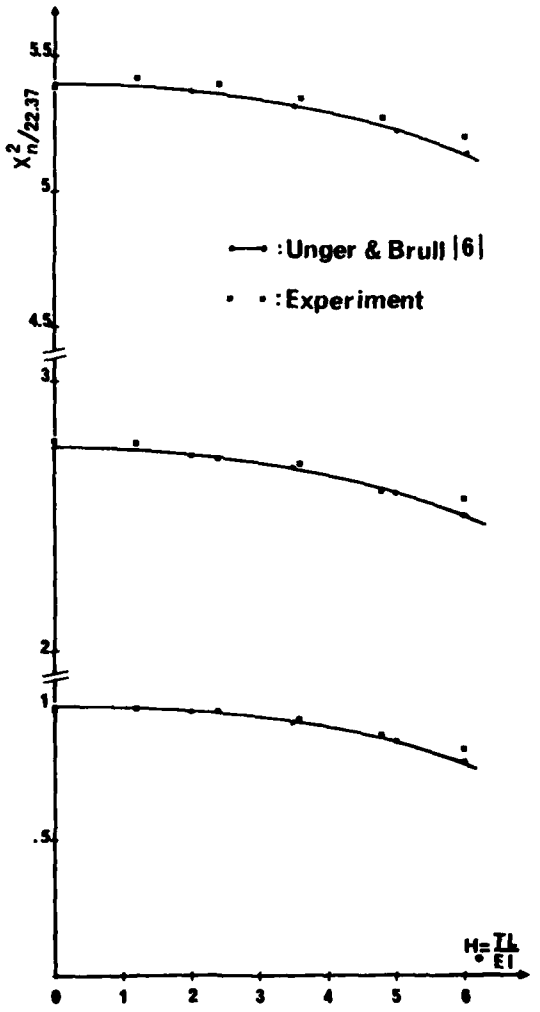

Fig.8 : C-C Beam coefficients

Constant axial torque H_0 and pulsating torque H_1 Cos ηt.

The experiment has been performed with $H_0 = 3.75$ and $H_1 \simeq 0.02$. The experimental natural frequencies in rd/s are :

$\omega_1 = 37.7$; $\omega_2 = 110.6$; $\omega_3 = 216.1$; $\omega_4 = 364.4$

The beam was excited by a torque whose frequency in rd/s is η, as shown in [5] the beam vibrates with the frequency η.

On the other hand during the frequency sweep between 0 and 60 Hz zones of instabilities were observed. The results of this experiment are presented in Table 4. The instabilities are detected by a two channel oscilloscope, where η and η_i could be easily compared. In addition a spectral analysis of a signal given by a non contact probe is performed, this analysis is very useful to detect the nature of the instability.

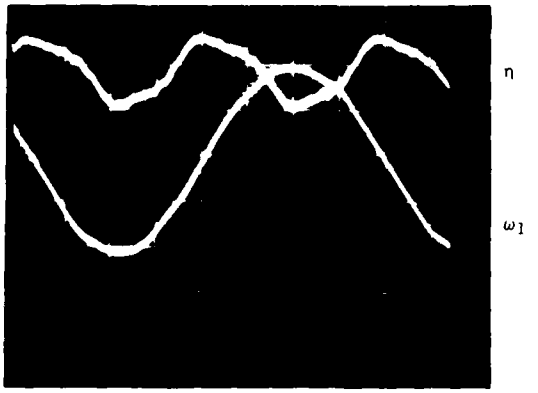

Fig.9 : 2P instability ($\eta = 2\omega_1$)

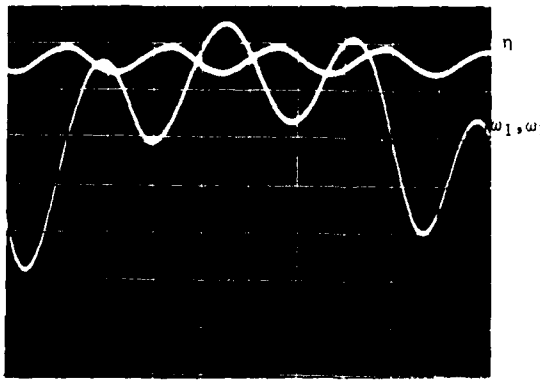

Fig.10 : Combined resonances instability
$\eta = \omega_1 + \omega_3$

For instabilities of type P, $\eta = \omega_n$ the beam vibrates at the same frequency as the excitation. For instability of type 2P, $\eta = 2\omega_n$, the zone of instability is wide (Fig.9). The modes are noted visually. For combined instabilities two frequencies are observed for $\eta = (\omega_1+\omega_2)/2$ the beam vibrates with frequencies ω_1 and ω_2 and for $\eta = \omega_1+\omega_3$ the beam vibrates with frequencies ω_1 and ω_3, (Fig.10). The instability zones of this type are also wide.

No other instabilities have been seen in the range considered. The instabilities of type P and 2P have been simply explained by the calculations presented. The combined resonances are predicted in [6] and [7], they could also certainly be predicted by the method given here. To achieve this, equation (13) would be a sum of expressions corresponding to $n = 1,2,3$. When $H_1 = 0$ the instability of type 2P is neither predicted and not observed.

TORQUE FREQUENCY η rd/s	ZONE	BEAM FREQUENCY rd/s	CONCLUSION	INSTABILITY TYPE
$\eta \simeq 37.7$	narrow	ω_1	$\eta = \omega_1$	P
$73. \leq \eta \leq 81.7$	wide	ω_1 or ω_1 and ω_2	$\eta = 2\omega_1$ or $\eta = (\omega_1+\omega_2)/2$	2P and or combined resonances
$\eta \simeq 110.6$	narrow	ω_2	$\eta = \omega_2$	P
$\eta \simeq 216$	narrow	ω_3	$\eta = \omega_3$	P
$221. \leq \eta \leq 228$	wide	ω_2	$\eta = 2\omega_2$	2P
$254. \leq \eta \leq 270.$	wide	ω_1 and ω_3	$\eta = \omega_1+\omega_3$	combined resonances
$\eta \simeq 364$	narrow	ω_4	$\eta = \omega_4$	P

Table 4 : - C-C Beam - Pulsating torque influence

CONCLUSIONS

The influence of a constant axial torque on the dynamic of rotors can be significant and is easily included in any computer program.

The harmonic exciting torque, which can also be important in turbomachinery and reciprocating compressors can be very dangerous. The instability zones seem at present impossible to predict for a real rotor because the stiffness matrix would have to include periodic coefficients.

BIBLIOGRAPHY

|1| - R.L. Eshleman, R.A. Eubanks, "On the critical speeds of a continous rotor", A.S.M.E. J. Eng. Ind., pp.1180-1188, (1969).

|2| - E.S. Zorzi, H.D. Nelson, "The dynamics of rotor-bearing systems with axial torque. A finite element approach", A.S.M.E. J. Mech. Des., pp.158-161, (1980).

|3| - H. Ziegler, "Principles of structural stability", 2nd Ed. Basel, Stuttgart, Birkhaüser, (1977).

|4| - N. Willems, S.M. Holzer, "Critical speeds of rotating shaft subjected to axial loading and tangential torsion", A.S.M.E. J. Eng. Ind., pp.259-264, (1967).

|5| - R.L. Eshleman, R.A. Eubanks, "Effects of axial torque on rotor response : an experimental investigation", A.S.M.E. Paper No.70-WA/DE 14.

|6| - A. Unger, M.A. Brull, "Parametric instability of a rotating shaft due to pulsating torque", A.S.M.E. J. Applied Mech., pp.948-958, (1981).

|7| - C.S. Hsu, "On the parametric excitation of a dynamic system having multiple degrees of freedom", A.S.M.E. J. Applied Mech., pp.367-372, (1963).

|8| - P. Berthier, G. Ferraris, M. Lalanne, "Prediction of critical speeds, unbalance and nonsynchronous forced response of rotors", Shock and Vib. Bull., n°53.

|9| - C.H.R. Wehrli, "Uber Kritische Drehzohlen Unter Pulsierender Torsion", Ing. Arch., XXXIII Band, (1963).

DISCUSSION

Mr. Rieger (Stress Technology, Inc.): Has any research been done on those instability bounds to determine the critical value of the damping which is likely to suppress the bound altogether?

Mr. Eshleman: No. There has not been. Some analytical work was done by Ziegler, in Switzerland, on the effect of damping to show how the bounds decrease. But, as far as experimental work is concerned, I did some experimental work on those bounds, and I showed some of the bounds in it. However, I am afraid the damping wasn't quantified to determine what they were.

Mr. Rieger: It would seem that the post-buckling behavior would be quite promising because a shaft would deform, and if it continued to rotate, it then would begin to develop quite substantial damping because you have a torque effect. The shaft, which is bowed out and rotating, would have a very substantial vector. Has anybody done any work in the post-buckling region?

Mr. Eshleman: No. They have not.

Mr. Rieger: That is something new to think about.

SENSITIVITY ANALYSIS OF THE LOCATIONS OF THE BALANCING PLANES OF AN UNBALANCED ROTOR-BEARING SYSTEM USING DYNAMIC CONDENSATION TECHNIQUE

S. Ahuja, A. M. Sharan
Faculty of Engineering, Memorial University
St. John's, Newfoundland, Canada, A1B 3X5

An analytical procedure for the dynamic balancing of multi-rotor systems supported on fluid-film bearings is presented. The model is developed based on the finite element method which includes the effects of translational, and rotational inertia, and gyroscopic moments, using the consistent matrix approach in conjunction with the dynamic matrix reduction technique, the modal analysis, and the least-square balancing technique. The use of the matrix reduction technique for determining an equivalent reduced system for balancing, provides subsequent saving of both, the computational time and space, on the digital computer. Three distinct practical conditions are investigated in the present work which are:

(1) The balancing of rotor disks at and below the critical speeds.
(2) The effect of the location of the balancing planes on the rotor response.
(3) The effect of the number of balancing planes on the rotor response.

The balancing method is found to be quite effective, permitting safe rotor operation over the speed range covering the three critical bending speeds.

1. INTRODUCTION

There has always been a demand for greater power output per unit-weight in the design of turbomachinery. This requires higher operating speeds. The key factor in achieving this objective is the control of vibrations of the rotor as it goes through the critical speeds.

The turbomachinery can be modelled as several rotor-disks mounted on hydrodynamic bearings. The stiffness and damping coefficients of such bearings are speed dependent, hence the dynamic analysis is more involved as compared to the systems which are supported on ball bearings, where these coefficients can be considered as isotropic. The precision modes, in case of isotropic bearings, are circular, whereas, for the fluid film bearings, it is elliptical [1].

There have been various techniques used in the dynamic analysis of the rotor-bearing systems such as (a) the lumped parameter method, (b) the transfer matrix method, and (c) the finite element method. Ruhl [2] analysed the rotor vibrations using the finite element method and concluded that the results are more accurate than those obtained using the transfer matrix method. Nelson and McVaugh [3] studied the dynamics of a rotor-disk supported on isotropic and orthotropic bearings using the finite element analysis. The damping in the bearings was not included in the results.

In rotor-balancing through the criticals, one has to have a reasonable number of balancing runs around each critical speed, which is costly and time consuming. It would be ideal if the balancing can be done at the critical speeds only.

In the present work, a mathematical model to control the vibration of several disks supported on fluid-film bearings including damping, has been developed. The response at the various locations on the rotor, is obtained using the finite element analysis in conjunction with the modal analysis [4]. The size of the system matrices is reduced using the dynamic reduction technique [5]. This reduction technique yields sufficient accuracy due to the lower vibrational modes. The balancing weights are obtained using the least square analysis [6-8]. The system in the present work is balanced exactly at the

critical speed, whereas, in other balancing techniques, runs at several speeds have to be carried out. Further, by varying the number and location of the balancing planes, better balancing conditions are achieved.

2. THE SYSTEM CONFIGURATION AND THE COORDINATES

In modelling a rotor bearing system, important consideration must be given to the set of reference axes utilized to describe its motion. A typical rotor-bearing system is illustrated in Fig. 1. The motion studied can be in a rotating or a fixed frame of reference. The rotating frame is particularly useful, when analyzing systems with isotropic bearings. In this case the motion in two normal planes can be treated separately. The fixed frame provides the generality of handling problems with nonsymmetric bearing stiffness, and damping effects. The only disadvantage of the fixed frame finite element formulation is that the order of the system matrices is large. This disadvantage can be overcome by using the dynamic matrix reduction technique.

A cross section of a rotor in its deformed state as defined in the fixed frame of reference system (XYZ:Θ), is shown in Fig. 1, and a typical finite rotor element is shown in Fig. 2. The various stiffness and the damping coefficients of the fluid film bearings are shown in Fig. 3. The triad is fixed with the x axis coinciding with X. The cross-section of the element, located at a distance (s) from the left end point, translates and rotates during the general motion of the element. The translations V(x,t) and W(s,t) in the Y and Z directions respectively locate the elastic centerline, and small angle rotations B(s,t) and Γ(s,t) respectively, represents the orientation of the cross-sectional plane. The cross-section also spins at a constant speed ω about the X axis defined by (x,y,z: T) triad.

3. MATHEMATICAL MODEL

3.1 The System Equation

The finite element modelled equation of motion of a rotor-disk system can be written as [3]

$$[M]\{\ddot{q}(t)\} - \omega[G]\{\dot{q}(t)\} + [C]\{\dot{q}(t)\} + [K]\{q(t)\} = \{Q(t)\} \quad (1)$$

The equation is obtained by considering the kinetic and potential energies of each of the components of this system. The details of the derivation are given in the Appendix A. The number of degrees of freedom in Eqn. (1) can be quite large. In order to carry out the modal analysis, any transformation matrix which can be used for the matrix reduction, must retain the lower modes for controlling the vibrations through the critical speeds.

3.2 The Dynamic Matrix Reduction Technique

The reduction process is most simply described as a transformation, relating condensed degrees of freedom in terms of retained ones. The computation of the transformation matrix, can proceed by a number of approaches; the most straight forward approach is to minimize the potential energy of the deformed structure, ignoring inertial effects and forces on the condensed degrees of freedom, thereby retaining the lower modes, for controlling the vibrations through the critical speeds. This is done by defining a transformation matrix [T], and writing the relation [5]

$$\{q\}_{nx1} = \begin{bmatrix}\{q_m\}\\ \{q_s\}\end{bmatrix}_{nx1} = [T]_{nxm}\{q_m\}_{mx1}, \quad (2)$$

where,

$$[T] = \begin{bmatrix} I \\ \hline -[K_{ss}]^{-1}[K_{ms}]^T \end{bmatrix} \quad (3)$$

The submatrices $[K_{ss}]$ and $[K_{ms}]$ are obtained by partitioning the stiffness matrix [K] in Eqn. (1) which can be written as

$$[K]_{nxn} = \left[\begin{array}{c|c} [K_{mm}] & [K_{ms}] \\ \hline [K_{ms}]^T & [K_{ss}] \end{array}\right] \quad (4)$$

In Eqns. (2) to (4) 'm' refers to the number of master degrees of freedom, and 's' to the slaves. The master degrees of freedom are retained, whereas the slaves are removed. Using this transformation matrix, the condensed matrix equation can be written as

$$[M_m]_{mxm}\{\ddot{q}_m(t)\} - \omega[G_m]_{mxm}\{\dot{q}_m(t)\}_{mx1} + [C_m]_{mxm}\{\dot{q}_m(t)\}_{mx1} + [K_m]_{mxm}\{q_m(t)\}_{mx1} = \{Q_m(t)\}_{mx1} \quad (5)$$

where, the condensed matrices are given by

$$[M_m]_{mxm} = [T]^T[M]_{nxn}[T], \quad (7)$$

$$[K_m]_{mxm} = [T]^T[K]_{nxn}[T], \quad (8)$$

$$[G_m]_{mxm} = [T]^T[G]_{nxn}[T], \quad (9)$$

$$[C_m]_{mxm} = [T]^T[C]_{nxn}[T], \quad (10)$$

and $$\{Q_m(t)\}_{mx1} = [T]^T\{Q\}_{nx1}.$$

The eigenvalues of the condensed system as represented by Eqn. (5) are higher than that of the original system because of the imposed constraints. The selection of the master and slave degrees of freedom is automated so as to ensure that the lower modes are retained as the masters. The diagional coefficients of [K] and [M] are scanned, and the degree of freedom i for which K_{ii}/M_{ii} is the smallest, is selected as the first master, and the rows and columns of the system matrices are rearranged accordingly. This is repeated, till the system matrices are arranged in an ascending manner, based on the K_{ii}/M_{ii} ratio of the diagional elements.

3.3 The Modal Response Analysis

The modal analysis [4] of the condensed system can then be carried out, after rearranging Eqn. (5), into a system of first order differential equation of the form

$$[\bar{M}]\{\dot{x}(t)\} + [\bar{K}]\{x(t)\} = \{\bar{F}\}, \tag{11}$$

where,

$$[\bar{M}] = \left[\begin{array}{c|c} [0] & [M_m] \\ \hline [\bar{M}_m] & -(-\omega[\bar{G}_m] + [\bar{C}_m]) \end{array}\right] \tag{12}$$

$$[\bar{K}] = \left[\begin{array}{c|c} [M_m] & [0] \\ \hline [0] & [\bar{K}_m] \end{array}\right] \tag{13}$$

$$\{\bar{F}\} = \left[\begin{array}{c} \{0\} \\ \hline \{Q_m\} \end{array}\right] \tag{14}$$

$$\{\dot{X}(t)\} \left[\begin{array}{c} \{\ddot{q}_m(t)\} \\ \hline \{\dot{q}_m(t)\} \end{array}\right], \text{ and } \{X(t)\} = \left[\begin{array}{c} \{\dot{q}_m(t)\} \\ \hline \{q_m(t)\} \end{array}\right] \tag{15}$$

The damped natural frequencies of the system are then obtained, by finding the eigenvalues of the dynamical matrix [D] which is given by

$$[D] = [\bar{M}]^{-1}[\bar{K}] \tag{16}$$

The transformation of Eqn. (11) is carried out by using the relation

$$\{X(t)\} = [\phi]\{\eta(t)\} \tag{17}$$

where $[\phi]$ contains the eigenvectors of the reduced system represented by Eqn. (11). Introducing Eqn. (17) into Eqn. (11) and premultiplying the result by $[\phi^*]^T$, which is the transpose of the eigenvectors of the transposed system, leads to the following:

$$[\phi^*]^T[\bar{M}][\phi]\{\dot{\eta}(t)\} + [\phi^*]^T[\bar{K}][\phi]\{\eta(t)\} = [\phi^*]^T\{\bar{F}\} \tag{18}$$

representing the dynamics of the system in the normal coordinates. Because of nonsymmetric nature of the stiffness and damping matrices, a conventional normal mode analysis is not possible, where $[\phi]^T$ is used instead of $[\phi^*]^T$. Eqn. (18) can be rewritten as

$$[\mu^*]\{\dot{\eta}(t)\} + [\kappa^*]\{\eta(t)\} = \{\sigma\} \tag{19}$$

where $[\mu^*]$ and $[\kappa^*]$ are diagional matrices respectively. The steady state solution for Eqn. (19) can be written as [4]

$$\eta_i(t) = N_i \exp(j\omega t) + \bar{N}_i \exp(-j\omega t) \tag{20}$$

and

$$\sigma_i(t) = E_i \exp(j\omega t) + \bar{E}_i \exp(-j\omega t)$$

$$i=1,2,\ldots,2m \tag{21}$$

Substitution of Eqn. (20) and (21) into Eqn. (19) leads to

$$(\kappa_i + j\omega\mu_i) N_i \exp(j\omega t) + (\kappa_i - j\omega\mu_i)\bar{N}_i \exp(-j\omega t) = E_i \exp(j\omega t) + \bar{E}_i \exp(-j\omega t) \tag{22}$$

Equating coefficients of $\exp(j\omega t)$ and $\exp(-j\omega t)$ respectively, one can write

$$N_i = \frac{E_i}{(\kappa_i + j\omega\mu_i)} \text{ and } \bar{N}_i = \frac{\bar{E}_i}{(\kappa_i - i\omega\mu_i)} \tag{23}$$

where E_i and $\bar{E}_i$ represent the forces due to mass unbalance in the normal coordinates.

Eqn. (19) can be solved on a mode-by-mode basis and Eqn. (17) can be used to obtain $\{X\}$. The nodal displacements, which represent the elements of the vector $\{q_m\}$, are obtained using Eqn. (15) by taking the real part of the lower submatrix of the vector $\{X\}$. The displacement vector $\{q\}$ is obtained using Eqn. (2).

3.4 The Least-Square Balancing

The magnitude of the elements of the vector thus obtained, is reduced using the least square method [6-8]. As the first step, the rotor is run at its first critical speed without making any changes to it. Next, a known trial weight is placed in each of the balancing planes, and the resulting vibration

calculated at each of the measuring planes. By subtracting from these results, the corresponding results for the uncorrected rotor, and dividing the difference by the value of the trial weight, a series of influence coefficients are obtained one for each measuring plane. This is mathematically writen as

$$\alpha_{ij} = \frac{R_{ij} - R_{io}}{T_j} \qquad (24)$$

where α is the complex influence coefficient, T the trial weight, R_{ij} and R_{io} the elements of the response vector $\{R\}$, and i, j represent the measuring and balancing plane numbers respectively. Once all the influence coefficients are evaluated, the correction weights required to minimize the unbalance vibrations of the rotor can be computed by using the relation [6]

$$\{R\}_{qx1} = [A]_{qxp}\{U\}_{px1} \qquad (25)$$

where [A] is the influence matrix coefficient whose elements are α_{ij}, $\{U\}$ is a complex vector defining the correction weights and the subscripts q and p represent the available number of measuring and balancing planes respectively.

In exact point method [7], the number of balancing planes are equal to the number of measuring planes i.e. p=q. The least-square method although based on the same principles, permits the condition where the number of measuring planes can exceed the number of balancing planes. This allows an increase in the input data (more measuring planes than balancing planes), whereby the consequence of a single error in the data tend to decrease. The analytical procedure for the least-square method is given in [8].

In general case, where the number of measuring planes exceed the number of balancing planes, the unbalance is reduced by minimizing the square of the residual amplitudes. The expression for the correction weights vector $\{U\}$ in this case, can be written as

$$\{U\} = -[[\bar{A}]^T [A]]^{-1} \cdot [\bar{A}]^T \cdot \{R_o\} \qquad (26)$$

The final equation yields that particular combination of correction weights which minimizes the residual vibrations of the rotor in the least-square sense.

3.5 The Sensitivity Analysis

To provide further flexibility in rotor balancing, the effect of varying the location of the balancing planes within an element, is incorporated in the system. For a typical uniform element shown in Fig. 4, the variable balance plane is located at distance (a) along the axis of the element, the end planes of the element are shown as b_1 and b_2 respectively. The displacement shape functions are given by

$$\psi_1 = 1 - 3(\tfrac{s}{\ell})^2 + 2(\tfrac{s}{\ell})^3, \qquad (27)$$

$$\psi_2 = \ell[1 - 2(\tfrac{s}{\ell}) + (\tfrac{s}{\ell})^2], \qquad (28)$$

$$\psi_3 = 3(\tfrac{s}{\ell})^2 - 2(\tfrac{s}{\ell})^3, \quad \text{and} \qquad (29)$$

$$\psi_4 = \ell[-(\tfrac{s}{\ell})^2 + (\tfrac{s}{\ell})^3], \qquad (30)$$

The forces due to the addition of the trial weight in a plane are given by

$$F_y = (m\rho\omega^2 \sin\theta)\cos\omega t + (-m\rho\omega^2 \cos\theta) \sin\omega t \qquad (31)$$

$$F_z = (m\rho\omega^2 \cos\theta)\cos\omega t + (m\rho\omega^2 \sin\theta)\sin\omega t \qquad (32)$$

Referring to Fig. 2, the forces at a joint of a given element, due to a trial weight located at a distance (a) can be obtained by combining Eqns. (31) and (32). The expression for these (joint) forces can be written as

$$F_i = \int_0^{\ell} [(m\rho\omega^2 \sin\theta)\,\delta(s-a)\,\psi_i \cos\omega t + (m\rho\omega^2 \cos\theta)\,\delta(s-a)\,\psi_i \sin\omega t]ds \qquad i=1,2,3,4 \qquad (33)$$

These forces at the joints of the elements are assembled into the global force vector for the dynamic response calculations.

4. THE NUMERICAL EXAMPLE

To demonstrate the application of the finite element model, a typical rotor bearing system with six elements as illustrated in Fig. 5, is analyzed. The details of the rotor are provided in Table 1. It consists of a shaft, with a uniform diameter of 0.050 m, and an overall length of 0.76 m. The rotor is symmetrical with most of its mass concentrated in the two disks. A density of 7806 kg/m^3 and elastic modulus of 2.078×10^{11} N/m^2 are used to model the rotor shaft. The two disks, with a mass of 20.45 kg, polar moment of inertia of 0.0020 kg-m^2 and diametrial inertia of 0.0010 kg-m^2 are located 0.254 m in from the ends. The rotor was supported on plain cylindrical fluid-film bearing with a L/D ratio of 1 and a bearing clearance of 0.000635 m. The unbalance condition was represented by the two disks with an in-line, in-phase mass centre eccentricity of 0.000635 m. This configuration is common to impellers keyed to the shaft with the same key. The stiffness and the damping coefficients of the bearings, which are speed dependent, were obtained from [1] where these values are given in a graphical form.

5. THE RESULTS AND DISCUSSIONS

5.1 The Dynamic Matrix Reduction Technique

In the dynamic reduction technique, the original system matrices were reduced to smaller sizes by using a transformation matrix obtained by using Eqn. (3). In this reduction process, care was taken that the properties of the original system, such as the natural frequencies, did not alter significantly. The greater is the degree of reduction, more is the deviation of properties such as the natural frequencies.

For the present system, the number of degrees of freedom were 28. This had to be reduced as much as possible. Trial runs on the computer for the calculation of the natural frequencies using Eqn. (16), were made by varying the degrees of freedom between 12 to 25. Some of the results obtained are shown in Table 2. In this table, the first five natural frequencies were computed by varying the number of master degrees of freedom. As the number of master degrees were increased, the natural frequencies decreased. However, this rate of decrease in the frequency value with respect to the increase in the degree of freedom, became very small when the degrees of freedom were 16. Therefore, the reduced system, for further analysis, was chosen to have 16 degrees of freedom, which represents 42 percent reduction in the each of the system matrix sizes.

5.2 The Variations of the Natural Frequencies of the System with the Operating Speed

The first three damped natural frequencies of the system are given in Fig. 6. The critical speeds are frequencies when the system natural frequencies are equal to the operating speed. The abrupt changes in the frequency map are because of the speed dependent fluid-film bearing coefficients. The rotor, light in weight, has a Sommerfeld number ranging between 1.0 to 10.0, within the operating speed range. The response at the first three critical speeds for the original and reduced system are shown in Table 3. The location of the measuring planes are shown in Fig. 7. A maximum deviation of 1.05 percent as given in this table indicates the effectiveness of the matrix reduction technique.

5.3 The Effect of Gyroscopic Moment on the Rotor Response

To study the effect of gyroscopic moments on the rotor-bearing response, the unbalance damped response values for the three critical speeds were calculated. The response values obtained are shown in Table 4. As can be seen from this table, the gyroscopic moments have very little effect on the overall response of the system. This is due to the damping in the system, which tends to mask the gyroscopic effects of the shaft and the two disks. Although the gyroscopic effects were small for this system, they were included in the overall system analysis.

5.4 The Dynamic Response as a Function of Rotor Speed

The unbalance response at the middle of the rotor, for various operating speeds, is shown in Fig. 8. The three critical speeds are clearly indicated by the peaks in the curve. The response is very high at the first critical whereas it is almost equal at the second and the third critical speeds.

It is obvious from this study that the vibration levels at the criticals must be controlled. The maximum whirl amplitude at the measuring planes, at various criticals, are shown in Table 3. It can be clearly seen that 16 master degrees of freedom are sufficient for the dynamic response study because the deviations from the original system are very small. In addition, the deflections are symmetrical along the rotor as shown in Fig. 9. This is because the measuring planes (refer to Fig. 7) have been located in a symmetrical manner, and the deflection of the corresponding points on either ends, are equal. For example, the measuring plane numbers 2, and 6 are equi-distant from the ends and their respective response values are equal.

5.5 The Dynamic Balancing of the Rotor-Bearing System

The dynamic balancing can be carried out by selecting equal number of measuring and balancing planes. For rotors, which are symmetrically located, it often leads to large correction weights at the middle [6]. On the other hand, one can use the least-square method, where the rotor amplitude response, can be minimized without adding excessive weights, and where the number of measuring planes can be greater than the number of balancing planes. Another advantage of this method is that there can be several measuring planes and even if there is some error in the measurement in one or more than one plane, still the computed values yield very good results. In other words, by increasing the number of the measuring planes, the influence of a measurement error in any one of these planes, is diminished. The greater the number of balancing planes, the better will be the balancing of the system. Unfortunately, due to the limitations of the accessibility and other constraints, the balancing planes can not be increased beyond certain number, for a given system. However, in these situations, the best one can do is to increase the number of measuring planes and carry out the balancing using the least-square analysis.

The rotor was then balanced at the first

critical speed using three fixed balancing planes as shown in Fig. 10. In order to present a meaningful comparison of the balance improvement as a result of balancing at the critical speeds, two balancing methods were considered.

Method 1 involves a commercially used balancing technique [6]. In it, the rotor is first balanced at little above half its first critical speed to stabilize the higher modes, and then balanced at 1190 rpm., a speed close to the first critical without actually balancing the rotor at its critical speed.

Method 2 involves balancing the rotor at its critical speed only. The results for the two methods, are presented in Table 5. In method 1, the unbalance response at various measuring planes was calculated using Eqn. (5) and is shown in column 3. The response at various speeds after balancing at 760 rpm, is shown in column 4. Similarly, the response at various speeds after balancing at 1190 rpm, is shown in column 6. The percentage improvements, due to the first and the second balancing are shown in columns 5 and 7 respectively. Referring to this table, it can be easily seen that the major reduction in the response is carried out by the first balancing at 760 rpm. The second balancing is more effective at higher speeds such as 1190 or 1253 rpm (percentage reduction in response is higher).

In method 2, the balancing is done only at the critical speed and the results after this balancing, are shown in column 8. The percentage reduction due to this balancing is the percent difference of the results given in columns 3 and 8 respectively.

The results obtained either by method 1 or 2 are quite good, but method 2 yields better results. The balance results, along the length of the rotor, are shown in Fig. 11. As stated earlier, the deflections are symmetrical. The curve obtained using method 2, shows a slight dip at the middle of the rotor. This is due to the presence of the balancing plane at this location.

After balancing the rotor for the first critical speed, method 2 was selected for further balancing. The rotor response at the second and third critical speeds were obtained and the corresponding correction weights were calculated. The system unbalance and balance response values at the three criticals are given in Table 6. The magnitude of the correction weights and their phase angles at these criticals, are given in Table 7.

The maximum reduction in the unbalance response is attained under the first balance run. The effect of the second critical balance results in an increase in the overall balance condition. The increase is probably because the balance plane locations are not properly spaced. Similar results are reported by Tessarzik [6].

Next, the rotor response at the third critical speed with the first set of correction weights, was calculated and the corresponding correction weights at this critical speed, were determined. The response values, with the first and the third sets of correction weights, are shown in column 8. The results in column 9, indicate that the response, after the first and the third critical balancing, decreases at most of the locations except at and near the bearings. This is possibly due to the balancing planes locations which are away from the bearings. The dynamic response along the length of the rotor due to these balancing are shown in Fig. 9 to 11. Referring to Fig. 9, there is quite significant reduction in the unbalance response due to the correction weights. The deflection curve along the rotor, is symmetrical even after the balancing, in all of these three figures. This is because the balancing planes have been symmetrically located along the length of the rotor. However, the percentage decrease in the rotor response, after the balancing at the second and the third critical, is much less than that at the first critical. For example, at a distance of 0.15 m along the rotor, the difference in the unbalance and balance response in Fig. 12, is much more than a similar difference in Figs. 13 and 14.

Referring to the Table 7, the angular location of the correction weights is approximately opposite to the disk mass centre eccentricity, which is 45°.

It must be added here that the overall saving of CPU time for a balancing run was 38 percent.

5.6 The Effect of the Location of the Balancing Planes on the Rotor Response

In the previous section, three balancing planes were used; one located at the middle and the other two symmetrically located away from the first one. Since the rotor disks are symmetrically located on the rotor shaft, it appears logical to place these two balancing planes also symmetrically. Therefore, in order to study the effect of the location of these planes on the response of the system, the locations of the two outer planes and the location of the third plane, have been chosen as variables for the parametric study.

The effect of balancing plane location, for reducing the system response, is studied using three balancing planes, as shown in Fig. 15, where a_1 and a_2 represent the location of the two outer and inner planes, respectively.

At first, a_1 was varied with a_2 fixed corresponding to the middle of the rotor. The

resulting response values are shown in Table 7 and correction weights in Table 8. It is evident from Table 9 that as the balancing planes are moved towards the disks, the residual response value decrease. This is because of the flexibility in the rotor shaft, the greater is the spacing between the unbalance forces at the disk and the correcting forces in the balancing planes, the less is the effectiveness of the correcting forces in reducing the response. Table 9 shows that as these measuring planes are moved in towards the disk, the magnitude of the correction weights in these planes also increase. When these two planes are located close to the disks, most of the correction weights are needed in these variable balancing planes; the weight in the fixed balancing plane is negligibly small.

Tables 10 and 11 show the effect of varying the center balancing plane while keeping the other two fixed. It can be seen in these tables, that as the center balancing plane is moved, both the response as well as the magnitude of the correction weights, increase. In addition, the maximum deflection curve along the length of the rotor, is no longer symmetrical. The best balance condition, using the locations of the measuring planes (a_1, a_2) as the variable parameters, is achieved when a_1 = 0.228 m and a_2 = 0.381 m. Fig. 13 shows the unbalance response along the rotor; the balance response with a_1 = 0.127 m, a_2 = 0.381 m; the best balance response after the parametric variation, with a_1 = 0.228 m, and a_2 = 0.381 m. It clearly shows that significant benefits can be realized by this parametric variation study as shown in Fig. 16.

5.7 The Effect of the Number of Balancing Planes on the Rotor Response

In carrying out balancing using the least-square method, an important consideration is the ratio of the number of measuring planes to the balancing planes. In the previous section this ratio used was 7 to 3. The effect of the variation of this ratio on the response, has been studied in this section. The number of the balancing planes have been varied between 3 and 7 while keeping the number of the measuring planes equal to 7. The various plane configurations are shown in Fig. 17. The rotor response, as a result of these variations, are shown in Table 12 and the corresponding correction weights in Table 13.

Fig. 17 shows that when the total number of balancing planes are 5, or 7, there is a balancing plane on the either side of a disk at equal distance besides a plane at the middle. The results in Table 12 show that the odd number of balancing planes yield better results than the even number of these planes. Among the odd number of planes, the best results are obtained when the number of balancing planes are equal to 5. The results shown in Table 13 indicate that for odd number of balancing planes, the correction weight in the middle balancing plane, is very small. This indicates that the forces generated due to the correction weights located near the disks, are mainly responsible for the balance condition. It was also reported by Tessarzik [6] that increasing the number of balancing planes does not necessarily lead to better balance results.

CONCLUSIONS

The finite element approach provides a convenient and accurate means of balancing a multi-rotor system, supported on fluid-film bearings. The use of matrix reduction technique in calculation of the reduced set of system matrices, enabled subsequent saving in computational memory storage of 42 percent, and that of computational time for a balancing run of almost 38 percent. Besides, in the reduction process, the retained degrees were the translational degree of freedom, therefore one could work with the reduced system only. There was no necessity of recovering all the degrees of freedom where the rotational degrees were also included. The modal analysis gives an effective means of determining the unbalance force response, and the relevant mode information. The use of least-square method, for the case investigated, provided good results, whereby balancing at the first critical speed was sufficient to bring the rotor amplitude down over the other critical speeds also. Further, by varying the number and location of balancing planes, better balance conditions were achieved. The results revealed that when using the least-square method, the odd number of balancing planes yield better results than even number of balancing planes.

REFERENCES

1. Rao, J. S., "Rotor Dynamics", Wiley Eastern, New Delhi, India, 1983, Chapter 6.

2. Ruhl, R., "Dynamics of Distributed Parameter Rotor Systems: Transfer Matrix and Finite Element Techniques", Ph. D. Thesis, Cornell University, 1970.

3. Nelson, H. D. and McVaugh, J. N., "The Dynamics of Rotor Bearing System Using Finite Elements", Journal of Engineering for Industry, Vol. 98, 1976, pp. 593-602.

4. Bhat, R. B., Subbiah, R., Sankar, T. S., "Dynamic Behaviour of a Simple Rotor with Dissimilar Hydro-Dynamic Bearings by Modal Analysis", Paper No. 83-Det-75, ASME.

5. Cook, R. D., "Concepts and Applications of Finite Element Analysis", John Wiley and Sons, New York, p. 313, 1981.

6. Lund, J. W., Tonnesen, J., "Analysis and Experiments on Multi-Plane Balancing of a Flexible Rotor", Journal of Engineering for Industry, Feb. 1972, pp. 233-241.

7. Tessarzik, J. M., Badgley, R. H., and Anderson, W. J., "Flexible Rotor Balancing by Exact Point-Speed Influence Coefficient Method", Journal of Engineering for Industry, TRANS. ASME, Feb. 1972, p. 148.

8. Tessarzik, J. M., Badgley, R. H., "Experimental Evaluation of the Exact Point-Speed and Least Square Procedures for Flexible Rotor Balancing by Influence Coefficient Method", Journal of Engineering for Industry, May 1974, pp. 633-643.

9. Timonshenko, S., "Vibration Problems in Engineering", 3rd ed., in collaboration with D. H. Young, D. Van Nostrand Company, Inc., Princeton, N. J., 1955.

APPENDIX A

The Component Equations of a Rotor-Bearing System

The rotor bearing system is comprised of a set of interconnecting components, consisting of uniform rotor segments with rigid disks, and fluid film bearings.

The shaft portion of the rotor is modelled as beam elements, by specifying spatial shape functions, and then treating the rotor element as an integration of a infinite set of differential disks. A typical rotor element is shown in Fig. 2. The cross-sectional displacements within the element are defined relative to a fixed frame of reference $\mathbb{E}$, by translations V(s,t) and W(s,t) and rotations B(s,t) and Γ(s,t). The finite rotor element coordinates are indicated by eight degrees of freedom (q_1^e, q_2^e, ..., q_8^e), four at each end, with two for translation, and two for rotation.

The rigid disks representing the impellers, coupling, flywheels, are convieniently described by a single plane, with only four degrees of freedom, two for the translation and two for the rotation.

The equation of motion for the elements are derived, by writing the expressions for the kinetic and the potential energies, of the components. The kinetic energy consists of both translational and rotational modes. The rotation terms also include gyroscopic effects associated with the spining of the shaft. The potential energy consists of the elastic bending effects of the shaft. The formulation is based on the Timoshenko beam theory [9]. The expressions for the matrix equation of motion using the Lagrange's formulation for the rotors as well as the disks are [3]:

Finite Rotor Element Equations

$$([M_T^e] + [M_R^e])\{\ddot{q}^e\} - \omega[G^e]\{\dot{q}^e\} + [K_B^e]\{q^e\} = \{Q^e\} \quad (A.1)$$

Rigid Disk Equation

$$([M_T^d] + [M_R^d])\{\ddot{q}^d\} - \omega[G^d]\{\dot{q}^d\} = \{Q^d\}, \quad (A.2)$$

Bearing Equation

The dynamic equation of motion of the bearings, in the fixed frame coordinates as shown in Fig. 3, can be written as

$$[C^b]\{\dot{q}^b\} + [K^b]\{q^b\} = \{Q^b\} \quad (A.3)$$

in fixed frame coordinates, where

$$\{q^b\} = \begin{bmatrix} V \\ W \end{bmatrix}, \quad (A.4)$$

$$[K^b] = \begin{bmatrix} K_{VV}^b & K_{VW}^b \\ K_{WV}^b & K_{WW}^b \end{bmatrix}, \quad (A.5)$$

$$[C^b] = \begin{bmatrix} C_{VV}^b & C_{VW}^b \\ C_{WV}^b & C_{WW}^b \end{bmatrix}. \quad (A.6)$$

In Eqn. (A.3), $\{Q^b\}$ represents the external force vector applied on the bearings. The elements of the stiffness and the damping coefficient matrix are considered to be nonlinear. These matrices contain cross-coupling terms representing a nonisotropic bearing with the principle coupled axes oriented at (45°, -45°) to the normal z-axis.

NOMENCLATURE

[]	matrix
'	differentiation with respect to position
.	differentiation with respect of time
$\mathbb{E}$	fixed reference frame (XYZ)
T	rotating reference frame (xyz)
(B, Γ)	small angle rotations about (Y, Z)
θ	trial weight addition angle

ϕ_j j-th complex eigenvector of the original system

ϕ_j^* j-th complex ei

η_j j-th modal displacement

$\{\sigma\}$ generalized force vector

$[\mu]$ generalized mass matrix

$[\kappa]$ generalized stiffness matrix

$[\Psi]$ matrix of translation displacement functions; $\psi_i(s)$, i=1,2,3,4

$[\Phi]$ matrix of rotation displacement function:

$\psi_i^1(s)$, i=1,2,3,4,

ω speed of rotation of shaft

η_d, ζ_d location of disk mass centre relative to T

$\eta(s)$ $\zeta(s)$ distributed location of element cross section mass centre relative to T

α complex influence coefficient

μ element mass per unit length

ℓ element length

$\{q\}$ displacement vector relative to E[1]

$\{q_c\}\{q_s\}$ unbalance response associated with cos Ωt, sin Ωt[1]

s axial position along an element

t time

$[A]$ matrix of complex influence coefficient

$[\bar{A}]$ conjugate of the complex influence coefficient matrix

$[C]$ system damping matrix

$[D]$ dynamical matrix

E_j forward component of the j-th modal force

$\bar{E}_j$ backward component of the j-th modal vector

$\{F\}$ overall exciting force vector

$[G]$ system gyroscopic matrix

$[I]$ identify matrix

$\bar{I}_D$, $\bar{I}_p$ elemental diametral and polar inertia per unit length

$[K]$ system stiffness matrix

$[M]$ system mass matrix

$\bar{P}$ potential energy[1]

$\{Q_c\}$,$\{Q_s\}$ unbalance force associated with cos Ωrt, s

R_1, R_2 major and minor diameters of the elliptical response orbital

S_1 Sommerfeld number

T trial weight

$\bar{T}$ kinetic energy[1]

$[T]$ reduction transformation matrix

$\{U\}$ a complex vector defining the correction weights

$\bar{U}$ a complex conjugate of the elements of vector u.

(V, W) translations in (Y,Z)

$\{X\}$ overall displacement vector

M_d, I_D, I_p disk mass, diametral inertia, and polar iertia

$[M^d]$, $[G^d]$ disk mass, gyroscopic, matrices[1]

$[M^e]$,$[G^e]$,$[K^e]$ elemental mass, gyroscopic, stiffness matrices[1].

$[C^b]$, $[K^b]$ bearing damping and stiffness matrices

C_{VV}^b, C_{VW}^b, C_{WV}^b, C_{WW}^b elements of $[C^b]$

K_{VV}^b, K_{VW}^b, K_{WV}^b, K_{WW}^b elements of $[K^b]$

TABLE 1 ROTOR DETAILS

Shaft Diameter	0.05 m
Total Length of Shaft	0.76 m
Modulus of Elasticity of Shaft	2.07×10^{11} Pa.
Shaft Density	7.68×10^3 kg/m^3
Disk Weight	20.45 kg.
Type of Bearing	Plain Cylindrical
Bearing L/D Ratio	1
Viscosity of Oil	69×10^{-6} N sec/m^2
Disk Eccentricity	6.35×10^{-6}m (In-plane 45°)

[1] Where appropriate the superscripts d, e, b, s refer to disk, element, and bearing respectively, and subscripts T, R, B refer to translational, rotational, and bending respectively.

TABLE 2 COMPARISION OF THE DAMPED NATURAL FREQUENCIES OF ORIGINAL AND THE REDUCED SYSTEMS

Frequency No.	Original System CPM	Retained Degree of Freedom											
		12 CPM	Percent Deviation %	13 CPM	Percent Deviation %	14 CPM	Percent Deviation %	15 CPM	Percent Deviation %	16 CPM	Percent Deviation %	25 CPM	Percent Deviation %
1	1260.417	1288.009	2.5	1282.845	0.4	1282.845	1.2	1260.417	2.1	1256.153	0.03	1256.114	0.0
2	3532.476	3935.456	21.4	3934.310	11.3	3934.310	21.5	3532.476	10.2	3236.352	0.0	3236.323	0.0
3	4976.434	5142.606	3.6	5008.300	2.6	5008.300	0.3	4576.434	3.2	4965.775	0.0	4965.902	0.0
4	94802.36	94901.76	0.3	94900.05	0.0	94900.05	0.3	94802.36	0.1	94780.93	0.2	94564.60	0.0
5	122354.28	135613.95	11.4	135592.75	0.1	135592.75	3.9	122354.28	9.6	122342.5	0.5	121819.65	0.1

TABLE 3 COMPARISON OF THE MAXIMUM RESPONSE AMPLITUDES BETWEEN THE FULL AND REDUCED SYSTEMS

Rotor Speed RPM	Measuring Plane No.	Maximum Rotor Response		
		Full System m	16 Degrees System m	Percent Deviation %
The First Critical (1253.63)	1	7.178×10^{-5}	7.170×10^{-5}	0.48
	2	2.979×10^{-4}	2.964×10^{-4}	0.56
	3	6.184×10^{-4}	6.774×10^{-4}	0.63
	4	7.769×10^{-4}	7.724×10^{-4}	0.63
	5	6.814×10^{-4}	6.774×10^{-4}	0.63
	6	2.979×10^{-4}	2.964×10^{-4}	0.56
	7	7.178×10^{-5}	7.170×10^{-5}	0.48
The Second Critical (4882.36)	1	2.380×10^{-6}	2.370×10^{-6}	0.40
	2	3.655×10^{-5}	3.644×10^{-5}	0.29
	3	6.172×10^{-5}	6.169×10^{-5}	0.05
	4	7.137×10^{-5}	7.089×10^{-5}	0.71
	5	6.172×10^{-5}	6.169×10^{-5}	0.05
	6	3.655×10^{-5}	3.644×10^{-3}	0.29
	7	2.380×10^{-6}	2.370×10^{-6}	0.40
The Third Critical (8357.83)	1	1.554×10^{-6}	1.586×10^{-6}	0.52
	2	3.490×10^{-5}	3.469×10^{-5}	0.61
	3	5.928×10^{-5}	5.877×10^{-5}	0.87
	4	6.847×10^{-5}	6.776×10^{-5}	1.05
	5	5.928×10^{-5}	5.877×10^{-5}	0.87
	6	3.490×10^{-5}	3.469×10^{-5}	0.61
	7	1.594×10^{-6}	1.586×10^{-6}	0.52

TABLE 4 COMPARISON OF UNBALANCE RESPONSE FOR CASES WITH AND WITHOUT GYROSCOPIC EFFECTS

Rotor Speed RPM.	Measuring Plane No.	Maximum Response Amplitude		Percent Deviation %
		With Gyroscopic Effect m	Without Gyroscopic Effect m	
The First Critical (1253.63)	1	7.170×10^{-5}	7.176×10^{-5}	0.09
	2	2.964×10^{-4}	2.966×10^{-4}	0.06
	3	6.774×10^{-4}	6.783×10^{-4}	0.13
	4	7.724×10^{-4}	7.730×10^{-4}	0.08
	5	6.774×10^{-4}	6.783×10^{-4}	0.13
	6	2.964×10^{-4}	2.966×10^{-4}	0.06
	7	7.170×10^{-5}	7.176×10^{-5}	0.09
The Second Critical (4882.36)	1	2.370×10^{-6}	2.374×10^{-6}	0.17
	2	3.644×10^{-5}	3.619×10^{-5}	-0.68
	3	6.169×10^{-5}	6.138×10^{-5}	-0.50
	4	7.089×10^{-5}	7.063×10^{-5}	-0.37
	5	6.169×10^{-5}	6.138×10^{-5}	-0.50
	6	3.644×10^{-5}	3.619×10^{-5}	-0.68
	7	2.370×10^{-6}	2.374×10^{-6}	-0.17
The Third Critical (8357.83)	1	1.586×10^{-6}	1.590×10^{-6}	0.25
	2	3.469×10^{-5}	3.454×10^{-5}	-0.43
	3	5.877×10^{-5}	5.872×10^{-5}	-0.08
	4	6.776×10^{-5}	6.774×10^{-5}	-0.03
	5	5.887×10^{-5}	5.872×10^{-5}	-0.08
	6	3.469×10^{-5}	3.454×10^{-5}	-0.43
	7	1.586×10^{-6}	1.590×10^{-6}	0.25

TABLE 5 BALANCE IMPROVEMENTS WHEN BALANCING BELOW AND AT CRITICAL SPEEDS

Rotor Speed R.P.M. (1)	Measuring Plane No. (2)	Before Balancing m (3)	After 1st Balance Run (760 RPM.) m (4)	% Reduction Due to 1st Balance Run (5)	After 2nd Balance Run (1190 RPM.) m (6)	% Reduction Due to 2nd Balance Run (7)	Critical Speed Balance (1253.60 RPM.) m (8)	% Reduction (9)
760.00	1	6.014×10^{-6}	6.89×10^{-8}	98.8	6.883×10^{-8}	0.4	-	-
	2	1.947×10^{-5}	8.965×10^{-8}	99.5	8.257×10^{-8}	5.7	-	-
	3	3.075×10^{-5}	1.102×10^{-7}	99.6	1.092×10^{-7}	0.8	-	-
	4	3.479×10^{-5}	1.906×10^{-7}	99.4	1.831×10^{-7}	3.8	-	-
	5	3.075×10^{-5}	1.102×10^{-7}	99.6	1.092×10^{-7}	0.8	-	-
	6	1.947×10^{-5}	8.965×10^{-8}	99.5	8.257×10^{-8}	5.7	-	-
	7	6.014×10^{-6}	6.891×10^{-8}	98.8	6.883×10^{-8}	0.4	-	-
1190.00	1	5.671×10^{-5}	1.851×10^{-7}	99.6	1.010×10^{-7}	45.4	-	-
	2	2.938×10^{-4}	1.147×10^{-6}	99.5	3.190×10^{-7}	72.2	-	-
	3	4.803×10^{-4}	1.853×10^{-6}	99.3	4.208×10^{-7}	77.2	-	-
	4	5.463×10^{-4}	1.620×10^{-6}	99.7	8.026×10^{-7}	50.4	-	-
	5	4.803×10^{-4}	1.853×10^{-6}	99.3	4.208×10^{-7}	77.2	-	-
	6	2.938×10^{-4}	1.147×10^{-6}	99.5	3.190×10^{-7}	72.2	-	-
	7	5.671×10^{-5}	1.851×10^{-7}	99.6	1.010×10^{-7}	45.4	-	-
1253.60	1	7.170×10^{-5}	3.672×10^{-7}	99.4	1.774×10^{-7}	51.7	1.708×10^{-7}	99.7
	2	2.964×10^{-4}	1.682×10^{-6}	99.4	1.006×10^{-6}	40.1	1.003×10^{-6}	99.6
	3	6.774×10^{-4}	2.839×10^{-6}	99.5	1.753×10^{-6}	38.2	1.750×10^{-6}	99.7
	4	7.724×10^{-4}	3.373×10^{-6}	99.5	1.330×10^{-6}	60.5	1.328×10^{-6}	99.8
	5	6.774×10^{-4}	2.839×10^{-6}	99.5	1.753×10^{-6}	38.2	1.750×10^{-6}	99.7
	6	2.964×10^{-4}	1.682×10^{-6}	99.4	1.006×10^{-6}	40.1	1.003×10^{-6}	99.6
	7	7.170×10^{-5}	3.672×10^{-7}	99.4	1.774×10^{-7}	51.7	1.708×10^{-7}	99.7

TABLE 6 BALANCE IMPROVEMENTS WHEN BALANCING AT CRITICAL SPEEDS

Rotor Speed RPM. (1)	Measuring Plane No. (2)	Before Balancing m (3)	After 1st Balance Run m (4)	% Reduction Due to 1st Balance Run (5)	After 2nd Balance Run m (6)	% Reduction Due to 1st & 2nd Balance Run (7)	After 3rd Balance m (8)	% Reduction Due to 1st & 3rd Balance Run (9)
First Critical (1253.63)	1	7.170×10^{-5}	1.780×10^{-7}	99.7	1.216×10^{-7}	31.5	1.497×10^{-7}	15.9
	2	2.964×10^{-4}	1.007×10^{-6}	99.6	1.021×10^{-6}	-1.5	4.137×10^{-7}	58.9
	3	6.774×10^{-4}	1.790×10^{-6}	99.7	1.772×10^{-6}	1.0	6.985×10^{-7}	60.6
	4	7.724×10^{-4}	1.328×10^{-6}	99.8	1.656×10^{-6}	-24.4	1.453×10^{-6}	12.2
	5	6.774×10^{-4}	1.790×10^{-6}	99.7	1.772×10^{-6}	1.0	6.985×10^{-7}	60.6
	6	2.964×10^{-4}	1.007×10^{-6}	99.6	1.021×10^{-6}	-1.5	4.137×10^{-7}	58.9
	7	7.170×10^{-5}	1.780×10^{-7}	99.7	1.216×10^{-7}	31.7	1.497×10^{-7}	15.9
Second Critical (4882.36)	1	2.370×10^{-6}	1.381×10^{-6}	41.7	1.520×10^{-6}	-10.0	1.382×10^{-6}	0.0
	2	3.644×10^{-5}	1.123×10^{-6}	96.9	2.128×10^{-6}	-89.3	1.123×10^{-6}	0.0
	3	6.169×10^{-5}	1.603×10^{-7}	99.7	1.247×10^{-6}	-67.7	1.602×10^{-7}	0.1
	4	7.089×10^{-5}	1.289×10^{-5}	81.8	1.152×10^{-6}	91.0	1.288×10^{-5}	0.1
	5	6.169×10^{-5}	1.603×10^{-7}	99.7	1.247×10^{-6}	-67.7	1.602×10^{-7}	0.1
	6	3.644×10^{-5}	1.123×10^{-6}	96.9	2.128×10^{-6}	-89.3	1.123×10^{-6}	0.0
	7	2.370×10^{-6}	1.381×10^{-6}	41.7	1.520×10^{-6}	-10.0	1.382×10^{-6}	0.0
Third Critical (8357.83)	1	1.586×10^{-6}	2.758×10^{-6}	-82.6	1.234×10^{-6}	44.7	4.074×10^{-6}	-47.6
	2	3.469×10^{-5}	4.231×10^{-6}	87.8	3.243×10^{-5}	-666.5	1.594×10^{-5}	-273.0
	3	5.877×10^{-5}	7.061×10^{-8}	99.9	3.664×10^{-5}	—	2.664×10^{-6}	62.2
	4	6.776×10^{-5}	3.764×10^{-5}	44.4	6.733×10^{-5}	(78.0)	3.835×10^{-6}	89.81
	5	5.887×10^{-5}	7.061×10^{-8}	99.9	5.644×10^{-5}	—	2.664×10^{-6}	61.2
	6	3.469×10^{-5}	4.231×10^{-6}	87.8	3.243×10^{-5}	-666.5	1.594×10^{-5}	-273.0
	7	1.586×10^{-6}	2.758×10^{-6}	-82.6	1.234×10^{-6}	44.7	4.074×10^{-6}	-47.6

TABLE 7 CORRESPONDING BALANCE WEIGHTS MAGNITUDE AND ANGLES WHEN BALANCE ROTOR AT THE FIRST THREE CRITICAL SPEEDS

Balance Plane No.	Calculated Correction Weights					
	1253.63 RPM		4882.36 RPM		8357.83 RPM	
	Weight g	Angle Deg.	Weight g	Angle Deg.	Weight g	Angle Deg.
1	7.13	-36.5	30.2	-39.6	6.1	-37.5
2	51.5	-46.2	46.3	-48.9	2.3	-43.1
3	7.13	-36.5	30.2	-39.6	6.1	-37.5

TABLE 8 EFFECT OF VARYING THE TWO OUTER BALANCING PLANES ON THE BALANCED RESPONSE FOR THE FIRST CRITICAL SPEED

Measuring Plane No.	Distance Along Rotor m	Maximum Response Amplitude - m						
		Unbalanced Response	$a_1 = 0.025$	$a_1 = 0.063$	$a_1 = 0.127$	$a_1 = 0.190$	$a_1 = 0.228$	$a_1 = 0.292$
1	0.0	7.170×10^{-5}	1.394×10^{-6}	1.157×10^{-6}	1.774×10^{-7}	1.736×10^{-9}	1.637×10^{-9}	1.752×10^{-9}
2	0.127	2.964×10^{-4}	9.131×10^{-6}	9.184×10^{-6}	1.006×10^{-6}	9.839×10^{-9}	9.512×10^{-9}	9.888×10^{-9}
3	0.254	6.774×10^{-4}	1.561×10^{-6}	1.547×10^{-5}	1.753×10^{-6}	1.614×10^{-8}	1.564×10^{-8}	1.625×10^{-8}
4	0.381	7.724×10^{-4}	1.889×10^{-5}	1.700×10^{-5}	1.3301×10^{-6}	1.843×10^{-8}	1.785×10^{-8}	1.849×10^{-8}
5	0.508	6.774×10^{-4}	1.561×10^{-5}	1.547×10^{-5}	1.753×10^{-6}	1.614×10^{-8}	1.564×10^{-8}	1.625×10^{-8}
6	0.635	2.964×10^{-4}	9.131×10^{-6}	9.184×10^{-6}	1.006×10^{-6}	9.839×10^{-9}	9.512×10^{-9}	9.888×10^{-9}
7	0.762	7.170×10^{-5}	1.394×10^{-6}	1.157×10^{-6}	1.774×10^{-7}	1.736×10^{-9}	1.637×10^{-9}	1.752×10^{-9}

TABLE 9 CORRESPONDING BALANCE WEIGHT MAGNITUDES AND ANGLES DUE TO THE EFFECT OF VARYING THE LOCATION OF THE TWO OUTER BALANCING PLANES

Balancing Plane No.	Calculated Correction Weights											
	a_1 = 0.025		a_1 = 0.063		a_1 = 0.127		a_1 = 0.190		a_1 = 0.228		a_1 = 0.292	
	Weight g	Angle Deg.	Weight g	Angle Deg.	Weight g	Angle Deg.	Weight g	Angle Deg.	Weight g	Angle Deg.	Weight g	Angle Deg.
1	0.54	48.4	13.0	36.2	13.23	37.5	19.35	-44	38.0	-45.0	38.75	44.9
2	66.74	44.3	45.8	50.6	53.8	46.8	0.04	-86	0.001	-37.0	.001	-37.0
3	0.54	48.4	13.0	36.2	13.23	37.5	19.35	-44	38.0	-45.0	38.75	44.9

TABLE 10 EFFECT OF VARYING THE MIDDLE BALANCING PLANE ON THE BALANCED RESPONSE FOR THE FIRST CRITICAL SPEED

Measuring Plane No.	Distance Along Rotor m	Maximum Response Amplitude - m			
		Unbalanced Response	a_1 = 0.127 a_2 = 0.381	a_1 = 0.127 a_2 = 0.444	a_1 = 0.127 a_2 = 0.469
1	0.0	7.170×10^{-5}	1.708×10^{-7}	5.735×10^{-6}	8.023×10^{-6}
2	0.127	2.964×10^{-4}	1.003×10^{-6}	7.665×10^{-6}	1.043×10^{-6}
3	0.254	6.774×10^{-4}	1.750×10^{-6}	1.506×10^{-6}	2.228×10^{-6}
4	0.381	7.724×10^{-4}	1.328×10^{-6}	8.486×10^{-6}	1.101×10^{-6}
5	0.508	6.774×10^{-4}	1.750×10^{-6}	7.848×10^{-6}	1.0127×10^{-6}
6	0.635	2.964×10^{-4}	1.003×10^{-6}	6.538×10^{-6}	8.600×10^{-6}
7	0.762	7.170×10^{-5}	1.708×10^{-7}	5.59×10^{-6}	7.658×10^{-6}

TABLE 11 CORRESPONDING BALANCE WEIGHT MAGNITUDES AND ANGLES DUE TO THE EFFECT OF VARYING THE LOCATION OF THE MIDDLE BALANCING PLANE

Balance Plane No.	Calculated Correction Weight					
	a_1 = 0.127 a_2 = 0.381		a_1 = 0.127 a_2 = 0.444		a_1 = 0.127 a_2 = 0.469	
	Weight	Angle Deg.	Weight	Angle Deg.	Weight	Angle Deg.
1	13.23	-37.5	21.23	-31.86	24.99	-30.76
2	53.8	-46.8	80.11	-46.3	62.0	-46.41
3	13.23	-37.5	21.23	-34.84	24.99	-17.31

TABLE 12 BALANCED RESPONSE AMPLITUDE WITH DIFFERENT NUMBER OF BALANCING PLANES

Measuring Plane No.	Distance Along Rotor	Maximum Response Amplitude - m					
		Unbalanced Response	3	4	5	6	7
1	0.0	7.170×10^{-5}	1.736×10^{-9}	1.639×10^{-8}	1.637×10^{-9}	2.103×10^{-8}	2.102×10^{-9}
2	0.127	2.964×10^{-4}	9.839×10^{-9}	9.484×10^{-8}	5.476×10^{-9}	1.282×10^{-7}	1.389×10^{-8}
3	0.254	6.774×10^{-4}	1.614×10^{-8}	1.557×10^{-7}	1.556×10^{-8}	2.118×10^{-7}	2.111×10^{-8}
4	0.381	7.724×10^{-4}	1.843×10^{-8}	1.786×10^{-7}	1.785×10^{-8}	2.395×10^{-7}	2.395×10^{-8}
5	0.508	6.774×10^{-4}	1.614×10^{-8}	1.557×10^{-7}	1.556×10^{-8}	2.112×10^{-7}	2.111×10^{-8}
6	0.635	2.564×10^{-2}	9.837×10^{-9}	9.484×10^{-8}	9.476×10^{-9}	1.282×10^{-7}	1.389×10^{-8}
7	0.762	7.170×10^{-5}	1.736×10^{-9}	1.637×10^{-8}	1.637×10^{-9}	2.103×10^{-8}	2.102×10^{-9}

Table 13 CORRESPONDING BALANCE WEIGHT MAGNITUDES AND ANGLES DUE TO THE NUMBER OF BALANCING PLANES

Balancing Plane No.	Calculated Correction Weights									
	Number of Balancing Planes									
	3		4		5		6		7	
	Weight g	Angle Deg.	Weight g	Angle Deg.	Weight g	Angle Deg.	Weight g	Angle Deg.	Weight g	Angle Deg.
1	19.35	-44.0	19.35	-46.2	19.35	-37.2	0.002	-75.3	0.002	-73.6
2	00.4	-86.0	19.35	-43.4	19.35	-38.4	19.35	-39.6	19.35	-38.4
3	19.35	-44.0	19.35	-43.4	0.009	-43	19.35	-45.0	19.35	-43.2
4	--	--	19.35	-46.2	19.35	-38.4	19.35	-45.0	0.006	-16.0
5	--	--	--	--	19.35	-37.2	19.35	-39.6	19.35	-43.2
6	--	--	--	--	--	--	0.02	-75.3	19.35	-38.4
7	--	--	--	--	--	--	--	--	0.002	-73.6

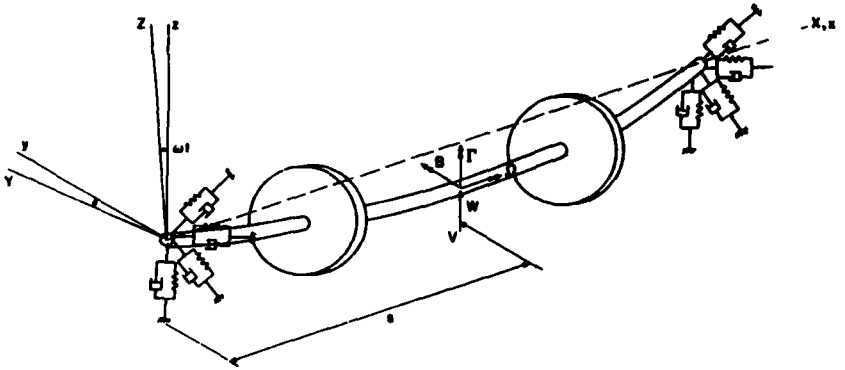

Fig.1 System Configuration and Coordinates.

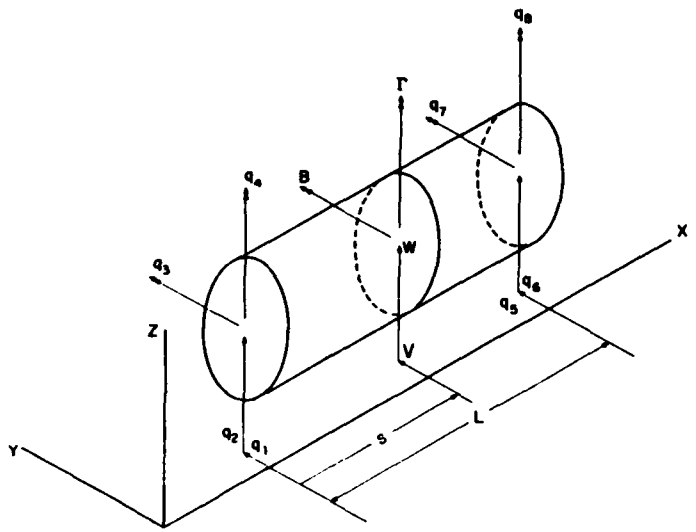

Fig 2 Typical finite rotor element and coordinates

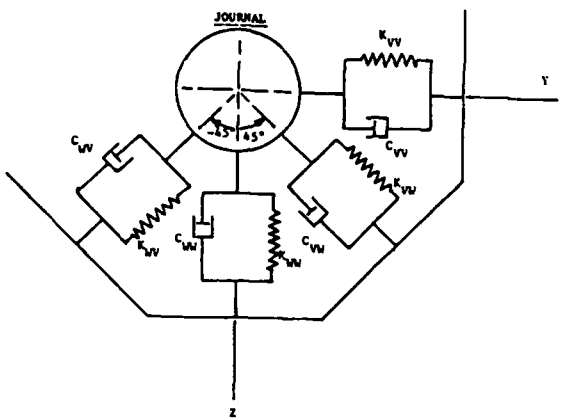

FIG. 3 JOURNAL BEARING STIFFNESS AND DAMPING COEFFICIENTS

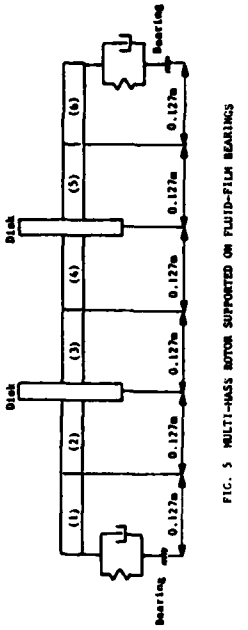

FIG. 5 MULTI-MASS ROTOR SUPPORTED ON FLUID-FILM BEARINGS

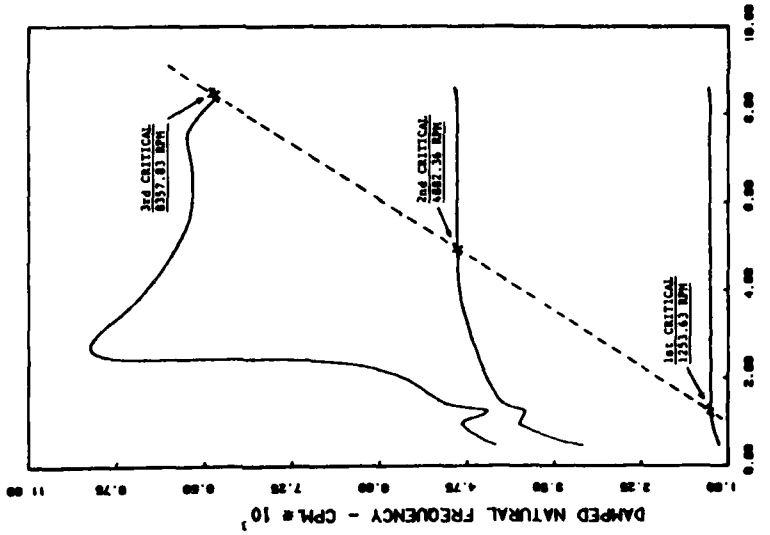

FIG. 6 DAMPED CRITICAL SPEED MAP FOR ROTOR SYSTEM

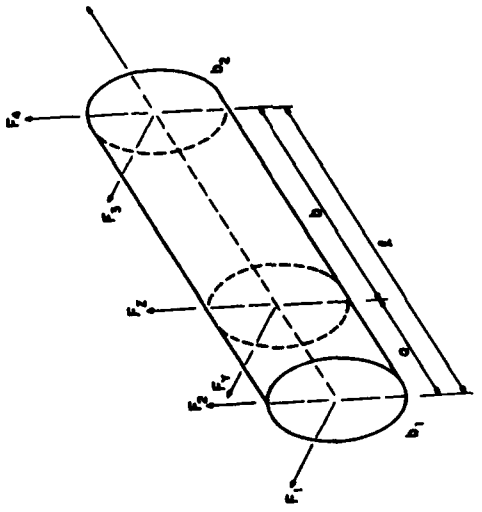

Fig. 4 Variable balance plane.

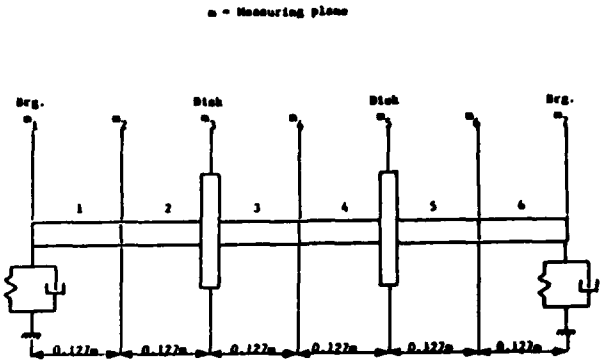

FIG. 7 ROTOR MEASURING PLANE LOCATIONS

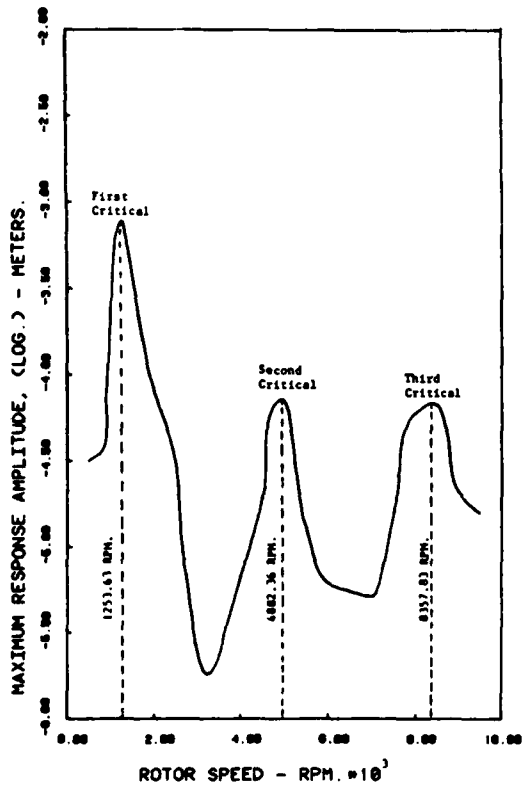

FIG. 8 UNBALANCE ROTOR RESPONSE AT THE MIDDLE OF THE ROTOR

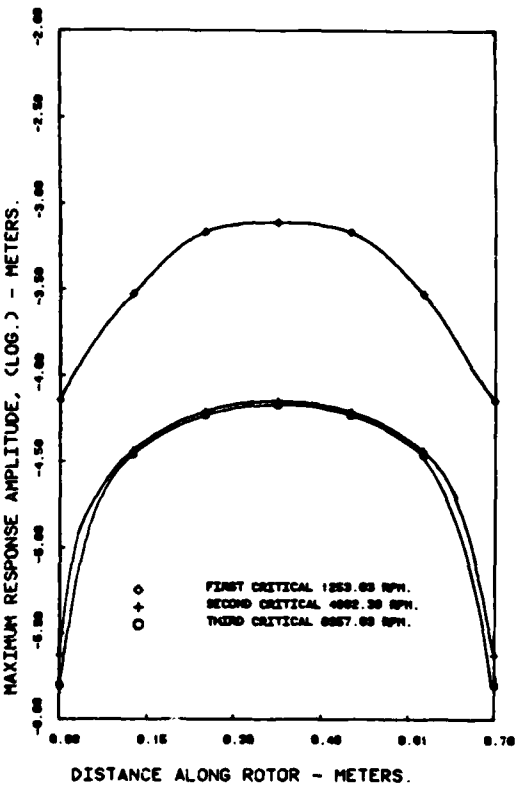

FIG. 9 UNBALANCE RESPONSE AT THE FIRST THREE CRITICAL SPEEDS

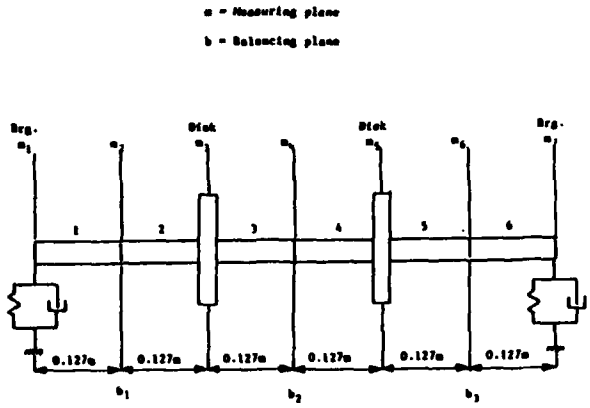

FIG. 10 SCHEMATIC OF THE ROTOR BEARING SYSTEM (SHAFT -0.05 x 0.76m)
(3-plane balance)

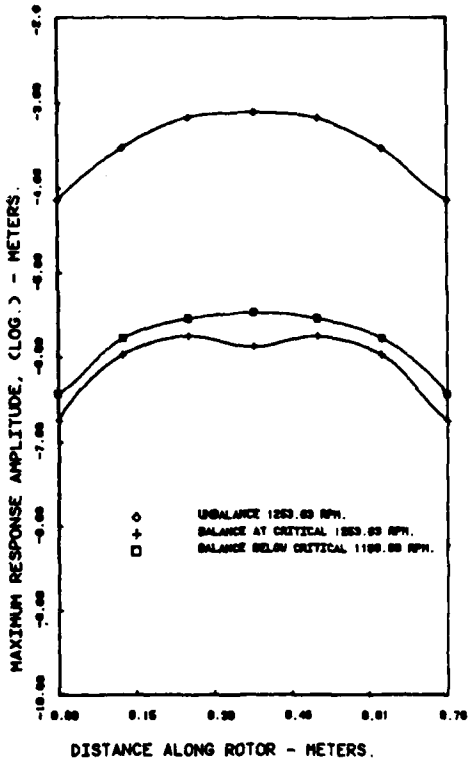

FIG. 11 BALANCE IMPROVEMENTS WHEN BALANCING AT AND BELOW CRITICAL SPEEDS

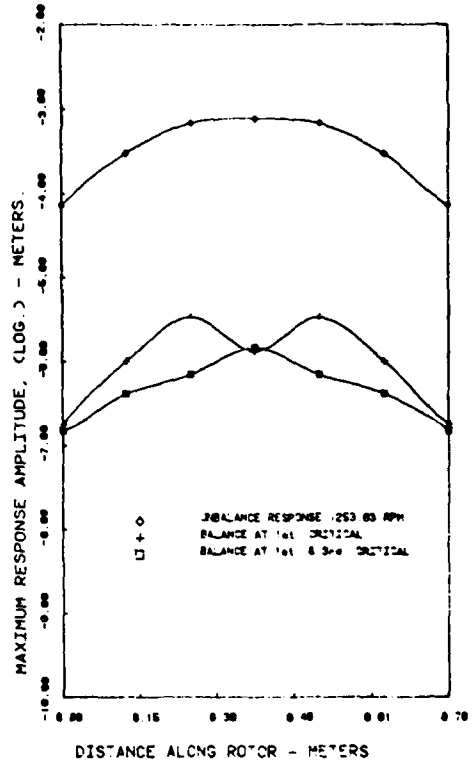

FIG. 12 DAMPED ROTOR RESPONSE AT FIRST CRITICAL SPEED

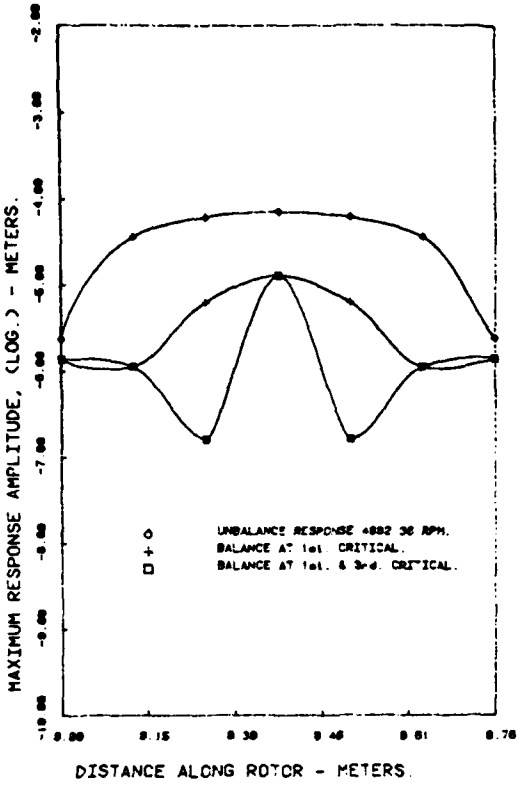

FIG. 13 DAMPED ROTOR RESPONSE AT SECOND CRITICAL SPEED

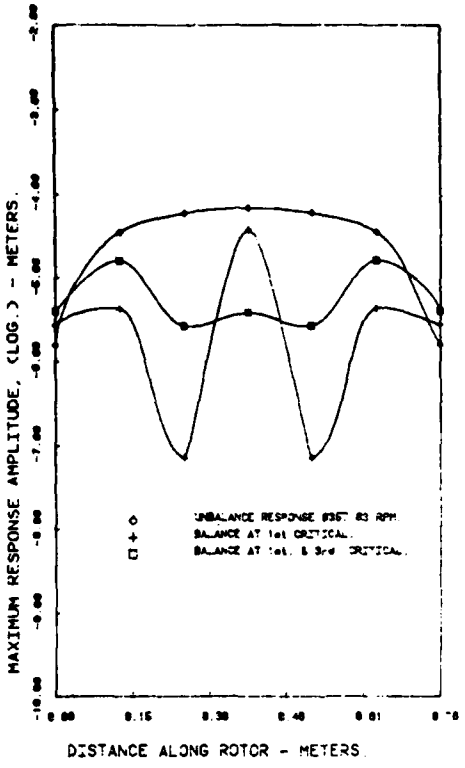

FIG. 14 DAMPED ROTOR RESPONSE AT THIRD CRITICAL SPEED

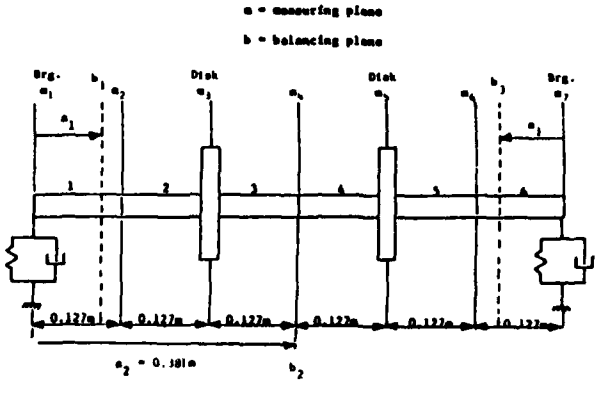

FIG. 15 SCHEMATIC OF A ROTOR BEARING SYSTEM RELATIVE BALANCE PLANE LOCATIONS

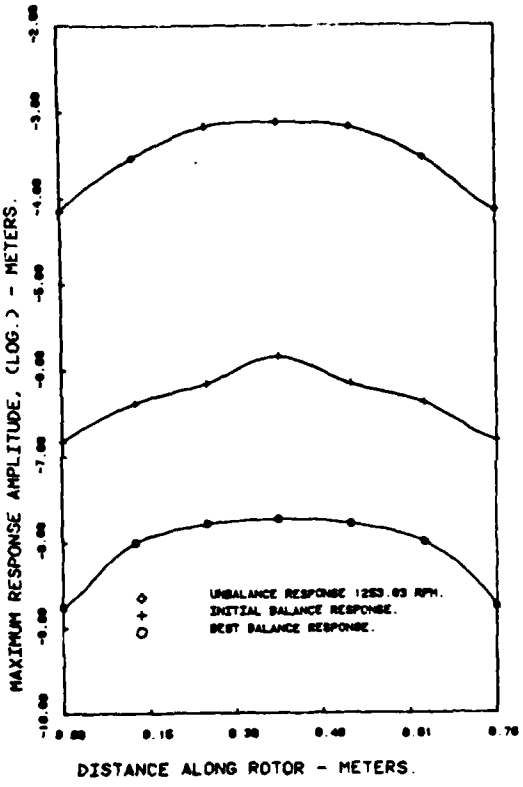

FIG. 16 BALANCE IMPROVEMENTS WHEN BALANCING AT FIRST CRITICAL BY VARYING THE TWO OUTER PLANES

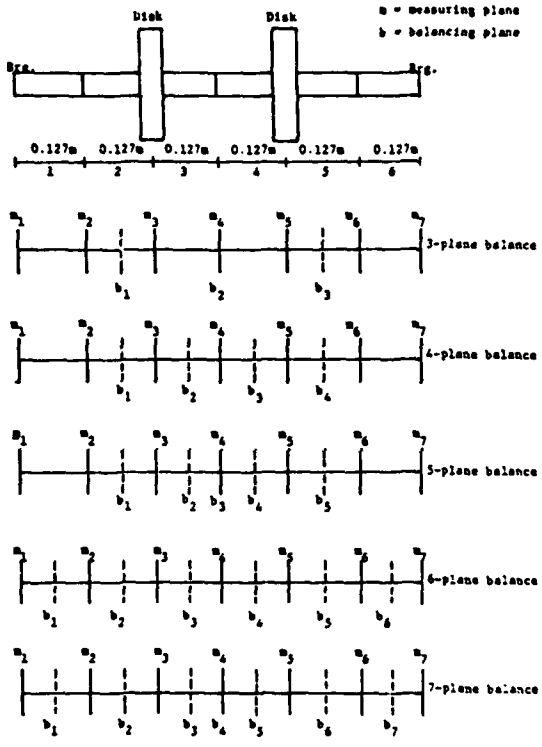

FIG. 17 SCHEMATIC OF THE BALANCING AND MEASURING PLANE ROTOR LOCATIONS

DISCUSSION

Mr. Leon (Liberty Technology Center, Inc.): In your studies, did you alter the unbalanced distribution of the rotors and repeat your study?

Mr. Sharan: No. I did not do that for that type of distribution.

STRUCTURAL DAMAGE DETECTION BY THE SYSTEM IDENTIFICATION TECHNIQUE

J. C. S. Yang, T. Tsai, V. Pavlin, J. Chen, W. H. Tsai
University of Maryland
College Park, Maryland

Over an extended period of time, exposure to severe loading very often results in fracture or crack damage of structures which can ultimately lead to fatigue failure. The research described in this paper, concerns the development of techniques with the potential to detect and track progressive fracture by observing changes in the identified system parameters: mass, stiffness and damping matrix elements. The method, called the system identification technique, has two steps: a process of retrieving the eigenvalues and eigenvectors during a dynamic response phase and the determination of mass, stiffness and damping matrices from these values. The proposed technique was verified on cantilever beam continuous structure systems through finite element simulation and experimental studies. Results from both studies have indicated the feasibility of damage detection by identifying the structural system matrices. For a cantilever beam system, the location of crack type damage seems to be best identified by the flexibility matrix which is the inverse of the stiffness matrix.

1. INTRODUCTION

Many ships and offshore structures have a predicted design life which is generally based on conservative design criteria to compensate for uncertainties in the load environment and associated damage effects. Severe loading over an extended period of time, may lead to fatigue failures of exposed structures. Initiation and propagation of cracks change the structural response of the system which manifests in a change in the dynamic equations of motion. Therefore, the System Identification Technique, from which the dynamic equations of motion may be deduced from experimental data, offers the potential of being able to detect cracks, flaws and other features by observing changes of structural parameters such as mass, stiffness and damping elements of matrices.

The identification and modeling of multi-degree of freedom dynamic systems through the use of experimental approaches, is a problem of considerable importance in the area of system dynamics, automatic controls and structural analysis. Indication of the wide range of applicability of this subject is shown in the literature related to system parameters identification efforts (Refs. 1-11).

Purely mathematical model representation of the real problem may prove to be a very powerful tool for the analysis and design of complex structural systems. The mathematical model representation could, of course, be devised from a theoretical understanding of the system and its components, or from a finite element model in the case of purely structural systems. These techniques are inferior compared to one which is based on an actual experimental response approach. Furthermore, when the system becomes more complex and sophisticated, it becomes more difficult to understand its mechanisms, and, therefore, to develop an appropriate theoretical model, which will give a good prediction of its dynamical response.

For these reasons, the objective of this research is to develop a new and more accurate dynamic system identification technique for determination of dynamic equations of motion, from dynamic response data, of a system with high modal density. This project seeks to demonstrate that it is feasible to detect damage in structures due to existing cracks or flaws by observing the changes of structural parameters as elements of mass [M], stiffness [K] and damping [C] matrices, and also to observe changes in the power spectral density and resonant frequencies.

The ultimate objective of the subsequent

research is to correlate the cracks, flaw sizes and their location with the obtained changes in system parameters.

2. MATHEMATICAL MODEL OF THE SYSTEM IDENTIFICATION TECHNIQUE

Let us begin by considering a structural system which can generally be represented by an N degree-of-freedom linear system. The dynamics of the system are governed by its equation of motion:

$$[M]\,[\ddot{X}] + [C]\,[\dot{X}] + [K]\,[X] = [f] \qquad (1)$$

where $[X]$, $[\dot{X}]$, $[\ddot{X}]$ are the displacement, velocity, and acceleration column vectors of degree N, respectively. Force $[f]$ is also an N-column vector. The $[M]$, $[K]$, and $[C]$ are N x N mass, stiffness, and damping matrices, respectively.

The system identification technique involves the identification of $[M]$, $[K]$, and $[C]$ matrices of the system, from the known responses $[X]$, $[\dot{X}]$, $[\ddot{X}]$ and the known forcing function $[f]$.

Adding to equation (1) a trivial differential equation:

$$[M]\,[\dot{X}] - [M]\,[\dot{X}] = 0 \qquad (2)$$

a set of equations which describe the motion of the same structural system are obtained:

$$\left[\begin{array}{c|c}[0] & [M] \\ \hline [M] & [C]\end{array}\right]\left[\begin{array}{c}\ddot{X} \\ \hline \dot{X}\end{array}\right] + \left[\begin{array}{c|c}[M] & [0] \\ \hline [0] & [K]\end{array}\right]\left[\begin{array}{c}\dot{X} \\ \hline X\end{array}\right] = \left[\begin{array}{c}0 \\ \hline f\end{array}\right] \qquad (3)$$

or in the condensed form:

$$[D]\,[\dot{q}] + [E]\,[q] = [Q]$$

where the matrices are defined as:

$$[D] = \left[\begin{array}{c|c}[0] & [M] \\ \hline [M] & [C]\end{array}\right]$$

$$[E] = \left[\begin{array}{c|c}[M] & [0] \\ \hline [0] & [K]\end{array}\right] \qquad (4)$$

$$[\dot{q}] = \left[\begin{array}{c}\ddot{X} \\ \hline \dot{X}\end{array}\right],\ [q] = \left[\begin{array}{c}\dot{X} \\ \hline X\end{array}\right],\ [Q] = \left[\begin{array}{c}0 \\ \hline f\end{array}\right]$$

After performing the Laplace transformation, we obtain:

$$[B\,(s)]\,[q\,(s)] = [Q\,(s)] \qquad (5)$$

where

$$[B\,(s)] = \left[[D]s + [E]\right]$$

is the system matrix. It can be proved that $[D]$ and $[E]$, which contain the system's $[M]$, $[C]$, $[K]$ matrices, can be represented by the eigenvalues P_k, and eigenvectors $[Y_k]$, produced from the system matrix and determined by the homogeneous equation (Ref. 12):

$$[B\,(P_k)]\,[Y_k] = 0 \qquad (6)$$

When $[M]$, $[K]$, and $[C]$ are symmetric, the following expressions can be proved:

$$\begin{aligned}[D] &= [Y]^{-1T}[I]\,[Y]^{-1} \\ [E] &= [Y]^{-1T}[-P]\,[Y]^{-1}\end{aligned} \qquad (7)$$

where

$$Y = [y_1, y_2, y_3, \text{---}, y_N]$$

is an eigenvector matrix while the eigenvalues matrix is:

$$\left[\begin{array}{c|c|c}p_1 & 0 & 0 \\ \hline 0 & p_2 & 0 \\ \hline 0 & 0 & p_n\end{array}\right]$$

It can be shown that the system's transfer function could be represented as a function of eigenvalues and eigenvectors, that is:

$$[H(s)] = [Y][s-P]^{-1}[Y]^T = \sum_{k=1}^{N}\left[\frac{y_k y_k^T}{s-p_k} + \frac{y_k^* y_k^{*T}}{s-p_k^*}\right] \qquad (8)$$

or

$$[H(s)] = \sum_{k=1}^{2n}\frac{[a_k]}{s-p_k} \qquad (9)$$

where

P_k = kth root of $\{\det\,(B(s)) = 0\}$

$[a_k]$= residue matrix for the kth root

In general, the ij-th element of the residue matrix $[a_k]$ is written as:

$$a_{ij}(k) = y_{ik}y_{jk} \qquad (10)$$

which provides the connection between residues and eigenvectors.

The transfer function H(s) is experimentally measurable. Using various curve-fitting procedures (Refs. 13-16), the eigenvalue and eigenvectors can be retrieved from the transfer function as indicated by Equations (9) and (10).

The proposed technique has been verified on a two-degree of freedom system simulated by analog computer circuits (Ref. 17). The results indicated that the system identification could accurately determine the mass, stiffness and damping matrices of a lumped spring-mass-dashpot system whose degree of freedom is low. The work described below includes the continuing verification of the stated technique on continuous structural systems. The physical system considered was a cantilever beam. The verification was conducted in two ways: NASTRAN finite element simulation and experimental measurement.

3. NUMERICAL APPROACH IN DETECTION OF DAMAGE OF A CANTILEVER BEAM

In the measurement of real structure response signals, error often exists. Such error can greatly affect the accuracy of the identified system matrices, especially when the degree of freedom of the structural system is high. At the initial stage of development of the system identification technique, it is desirable to generate structural signals as close to theoretical values as possible to be used as verification of the technique. Numerical approach was adopted in which a cantilever beam was modeled with the NASTRAN computer program to generate the numerical vibration signals.

The mesh configuration of the finite element model of the beam is shown in Fig. 1. The dimension of the beam is 1" wide, 12" long, and 1/8" thick. The model is composed of 200 CQUAD4 bending elements of MSC/NASTRAN version of the finite element method. The material of the beam is mild steel whose properties are:

Young's Modulus $E = 3.0 \times 10^{7}$ lb/in^2

Poisson Ratio $\nu = 0.33$

Mass Density $\rho = 7.557 \times 10^{-4}$ slug/in^3

Six stations were chosen from which the frequency response functions were taken. These are labeled stations 1 through 6, located along the beam center line and separated 2 inches apart (Fig. 1). Dynamic forces were applied at station 2. Transfer functions at the six stations, which are defined as the ratio of the Fourier Transform of the dynamic responses at the six stations to that of the input force at station 2, were obtained using NASTRAN modal analysis method. Dampings were introduced into the system by adding artificial modal damping coefficient to each mode. The attained transfer functions containing no noise except the numerical inaccuracies were used as input data for theoretical verification of the identification technique.

The frequencies, dampings and the amplitudes of vibration at the six stations were obtained using a frequency domain curve fitting routine. This constituted the first phase of the signal processing which retrieved eigenvalues and eigenvectors from the system's dynamic responses. The second phase of the signal processing is to construct the [M], [C], [K] matrices from the eigenvalues and eigenvectors.

To demonstrate the capability of damage detection of the proposed technique, two grid points on each side of the beam, located 3 inches away from the clamped edge, were released by splitting each grid point into two (Fig. 2b). The splitting of the two grid points induced first stage damage to the structure. Again the computer programs were run to obtain the frequencies, dampings and the [M], [C], [K] matrices for the damaged structure.

Two more stages of damage were introduced and the same system identification procedure was carried out for all the damage cases. In the second damage stage, two grid points on the second rows from each side of the beam, located 3 inches from the clamped edge, were released (Fig. 2c). In the third damage stage, two additional grid points on the third rows were released (Fig. 2d).

The severeness of the damage induced by splitting the grid points can be demonstrated by the resulting frequency changes which, as seen from Table 1, are very small. The mass matrices obtained for the four damage cases are all close to diagonal with off-diagonal elements one or two order of magnitude smaller than the diagonal elements. The diagonal elements of the mass matrices are listed in Table 2, which show very small changes ($\leq$ 1%) for the damages produced by splitting the grid points. Because of the complex nature of the damping mechanism, the obtained damping matrices will not be correlated to their physical implications. For the obtained stiffness matrices, it was found that their inverses, the flexibility matrices, can provide better physical correlation for a cantilever beam system. The flexibility matrices are near diagonal, whose diagonal elements are listed in Table 3 for the four damage cases. It is found from these values that for response stationsbefore the damage location the flexibility does not change significantly, while for response stations after the damage locationthe flexibilities change progressively according to the severeness of damage and the distances from the damage location. This trend is illustrated by the graphical depiction of Fig. 3.

To investigate the correlation between the location of damage and the changes in the elements of the flexibility matrix, theoretical derivation can be conducted to obtain the analytical expression of the flexibility matrix. The expressions of the diagonal elements of the flexibility matrix of a cantilever beam are listed in the Appendix for the six response stations. As can be seen from the Appendix, the elements of the flexibility matrix are algebraic sums of terms inversely proportional to the local stiffness, $E_i I_i$. The progressive changes in the matrix elements due to the change in local stiffness at a particular station are clearly displayed in the analytical expressions.

TABLE 1

Natural Frequencies in Hz for the NASTRAN Simulated Responses of the Cantilever Beam with Four Damage Cases

Modes	No Damage	1st Stage Damage	2nd Stage Damage	3rd Stage Damage
1	24.991	24.970	24.828	24.499
2	157.67	157.66	157.62	157.53
3	443.82	443.53	441.70	437.55
4	873.60	872.83	868.36	858.68
5	1446.93	1446.46	1444.18	1439.11
6	2136.62	2135.90	2132.73	2125.30

TABLE 2

Diagonal Elements of the Mass Matrices (10^{-3} slugs)

Stations	No Damage	1st Stage Damage	2nd Stage Damage	3rd Stage Damage
1	0.1314	0.1313	0.1318	0.1312
2	0.1979	0.1987	0.1995	0.1989
3	0.2038	0.2028	0.2040	0.2041
4	0.2008	0.2004	0.2008	0.2010
5	0.2011	0.2017	0.2021	0.2035
6	0.1923	0.1927	0.1931	0.1943

TABLE 3

Diagonal Elements of the Flexibility Matrices (10^{-3} in/lb)

Stations	No Damage	1st Stage Damage	2nd Stage Damage	3rd Stage Damage
1	0.5033	0.5016	0.5031	0.5021
2	3.9860	3.9756	3.9976	4.0220
3	14.343	14.391	14.430	14.901
4	31.540	31.940	31.803	33.063
5	62.948	62.425	62.389	64.624
6	101.66	101.81	102.40	105.34

4. EXPERIMENTS WITH A CANTILEVER BEAM

In addition to the numerical verification of the system identification technique described in section 2 as applied to a continuous structural system, an experimental verification was also conducted. A cantilever beam having dimensions 19-1/2 inches long, 1 inch wide, and 1/4 inch thick was used in the experiment. The beam was made of aluminum, with Young's modulus 1.03×10^7 lb/in^2, Poisson's ratio $\nu \doteq 0.33$ and mass density $\rho = 2.485 \times 10^{-4}$ slug/in^3. Six accelerometers were attached to the beam at six stations (Fig. 4). A hammer was set up to excite the aluminum cantilever beam with transient or random impact at station 5, as shown in Fig. 5a. The transfer functions from the impact station to any accelerometer station were obtained by feeding the output acceleration signal and input forcing function into a spectrum analyzer: the Nicolet 660B dual channel FFT analyzer supported by a Data General MP/200 computer (see Fig. 5b). In the analyzer, the input and output signals were digitized and the Fast Fourier Transform of the signal was performed. The instantaneous transfer functions were obtained by dividing the two spectra. The final transfer function was ob-

tained by averaging a series of instantaneous transfer functions.

The obtained transfer functions were processed further, according to the mathematical procedure suggested by the proposed structure identification technique. The final results are represented in the form of structural matrices [M], [C], and [K]. It should be emphasized that the phase 1 (transfer function) was experimentally accomplished, in contrast to the finite element analysis described previously. As such, this is a totally experimental approach which will be an effective and useful technical approach for damage detection.

The saw cut on the cantilever beam, introduced between stations 2 and 3, represents the damages of the structure in the experiment (Fig. 4). The frequencies and damping values of the lowest vibration modes were obtained from the transfer functions for no cut case and the cut case (Table 4). Significant changes due to cut exist in the experimentally determined frequencies. Table 5 and 6 list the diagonal elements of the mass and flexibility matrices for the no cut and cut cases. It is also found that the damage introduced by the saw cut results with significant changes in the flexibility elements.

TABLE 4

Experimental Values of Frequencies and Damping Ratios of the Aluminum Cantilever Beam

Modes	NO CUT		CUT CASE	
	Natural Freq. (Hz)	Damp. Ratio (%)	Natural Freq. (Hz)	Damp. Ratio (%)
1	19.53	0.360	19.00	0.247
2	122.05	0.241	115.85	0.183
3	339.26	0.125	332.36	0.0788
4	661.73	0.0946	646.91	0.0805
5	1085.22	0.120	1037.46	0.0979
6	1594.59	0.0974	1591.36	0.0973

TABLE 5

Diagonal Elements of the Mass Matrices (10^{-6} slugs)

Stations	No Cut	Cut
1	2.9460	2.8029
2	6.7463	6.0645
3	6.9833	7.8842
4	7.0791	8.3550
5	7.2694	7.9536
6	6.4664	6.5813

TABLE 6

Diagonal Elements of the Flexibility Matrices (in/lb)

Stations	No Cut	Cut
1	0.3257	0.2526
2	1.8184	1.4985
3	7.5954	7.8514
4	18.594	21.003
5	33.817	51.553
6	66.075	87.246

Theoretical study, as illustrated by the results of NASTRAN simulation, indicates that the diagonal elements of the flexibility matrix [F] should deviate in an orderly fashion with respect to the location of the damage. Comparing the flexibility matrices of the cases cut and no cut (Fig. 6), this orderly deviation does exist in the diagonal elements and allows one to identify the location of the cut.

5. CONCLUSIONS AND DISCUSSIONS

The feasibility of using the system identification technique for a continuous structural system, such as a cantilever beam, has been demonstrated. Both the numerical simulation and experimental verification indicate that the technique is capable of identifying structural damages. Furthermore, for a cantilever beam, the location of the damage can be identified by observing the changes in the diagonal elements of the flexibility matrix.

However, to obtain useful results for more practical purposes, a number of improvements to the technique will be necessary. In the experiment conducted, the cut made to the cantilever beam was considered a very severe structural damage, thus resulting in significant changes of the system's matrices and made the system identification possible. For real applications damages of a precatastrophy type are usually very small. If the error during the signal processing is large enough to suppress the deviations in [M], [C], [K] matrices due to damages, then it is impossible to detect structural damages by observing changes in the identified [M], [C], [K] matrices. Therefore, the requirement of high accuracy signal processing is essential for practical purposes.

For the present system identification technique, the accuracy can be controlled in three steps: (1) the signal acquisition in vibration measurements; (2) retrieval of the system's eigenvalues and eigenvectors; and (3) conversion of eigenvalues and eigenvectors to the [M], [C], and [K] matrices. The first step requires careful calibration of the measurement transducers. The second step involves the accuracy of the analog to digital signal conversion and numerical accuracy in the proper eigenvalue retrieval algorithm. The third step is purely numerical and consists only of a series of matrix operations.

In our present research, an aluminum cantilever beam of sufficient length system has been used. This retained the system in lower vibration frequencies so that the lowest six modes were well within the accelerometer response characteristics. Attention has also been given to the structural symmetry so that unwanted vibrations, such as torsional modes, were eliminated. Efforts were directed to improve the measurement accuracy.

New mathematical approaches to convert the eigenvalues and eigenvectors to the [M], [C], and [K] matrices can be pursued to provide better accuracy. For example, one can use only matrices of dimension N x N for an N-degree of freedom system in the computation algorithms. As compared to the system matrices of dimension 2N x 2N, used in the present research, such approach contains four times less the number of unknown variables. It is expected that accuracy will be improved by the reduction of matrix dimensions in the numerical array operations.

For a continuous structural system, the number of degrees of freedom is infinity. If it is to be modeled with an N degree-of-freedom [M], [C], and [K] matrices, then the conditions under which the system identification procedure is proper should also be verified for practical application.

APPENDIX: Diagonal Elements of the Flexibility Matrix of a Cantilever Beam

$$f_{11} = 2G_1L_1^2$$

$$f_{22} = 2G_1(L_{12}^2 + L_{12}L_2 + L_2^2) + 2G_2L_2^2$$

$$f_{33} = 2G_1(L_{13}^2 + L_{13}L_{23} + L_{23}^2) + 2G_2(L_{23}^2 + L_3L_{23} + L_3^2) + 2G_3L_3^2$$

$$f_{44} = 2G_1(L_{14}^2 + L_{14}L_{24} + L_{24}^2) + 2G_2(L_{24}^2 + L_{24}L_{34} + L_{34}^2) + 2G_3(L_{34}^2 + L_{34}L_4 + L_4^2) + 2G_4L_4^2$$

$$f_{55} = 2G_1(L_{15}^2 + L_{15}L_{25} + L_{25}^2) + 2G_2(L_{25}^2 + L_{25}L_{35} + L_{35}^2) + 2G_3(L_{35}^2 + L_{35}L_{45} + L_{45}^2) + 2G_4(L_{45}^2 + L_{45}L_5 + L_5^2) + 2G_5L_5^2$$

$$f_{66} = 2G_1(L_{16}^2 + L_{16}L_{26} + L_{26}^2) + 2G_2(L_{26}^2 + L_{26}L_{36} + L_{36}^2) + 2G_3(L_{36}^2 + L_{36}L_{46} + L_{46}^2) + 2G_4(L_{46}^2 + L_{46}L_{56} + L_{56}^2) + 2G_5(L_{56}^2 + L_{56}L_6 + L_6^2) + 2G_6L_6^2$$

$$G_i = \frac{L_i}{6E_iI_i} \qquad L_{ij} = L_i + \ldots + L_j$$

where L_i is the distance between response stations

I_i the moment of inertia of the beam cross section

E_i the local Young's Modulus

6. REFERENCES

1. Bekey, G.A., "System Identification, an Introduction and a Survey," Simulation, Oct. 1970, pp. 151-166.

2. Hart, G.C., and Yao, J.T.P., "System Identification in Structural Dynamics, Dynamic Response of Structures: Instrumentation Testing, Methods and System Identification, ASCE/EMD Technical Conference, UCLA, Match 1976.

3. M. Richardson, R. Potter, "Identification of the Modal Properties of an Elastic Structure from Measured Transfer Function Data," 20th I.S.A., Albuquerque, N.M., May 1974.

4. R. Potter, M. Richardson, "Mass, Stiffness and Damping Matrices from Measured Modal Parameters," I.S.A. Conference and Exhibit, N.Y., N.Y., October 1974.

5. R. Potter, "A General Theory of Modal Analysis for Linear Systems," Hewlett-Packard Co., 1975.

6. W.G. Flannelly, J.H. McGarrey, A. Berman, "A Theory of Identification of the Parameters in the Equations of Motion of a Structure Through Dynamic Testing," U. of Technology, Loughborough, England, March 1970.

7. A.L. Klosterman, "On the Experimental Determination and Use of Modal Representations of Dynamic Characteristics, Ph.D. Thesis, U. of Cincinnati, 1971.

8. S.R. Ibrahim, E.C. Milulcik, "A Method for the Direct Identification of Vibration Parameters from the Free Response," Shock and Vibration Bulletin, Bulletin 47, Part 4, Sept. 1977.

9. Cole, H.A., "On-Line Failure Detection and Damping Measurement of Aerospace Structures by the Random Decrement Signatures," NASA CR-2205, 1973.

10. Yang, J.C.S., Caldell, D.W., "Measurement of Damping and the Detection of Damages in Structures by the Random Decrement Technique," 46th Shock and Vibration Bulletin, 1976, pp. 129-136.

11. Yang, J.C.S., Aggour, M.S., Dagalakis, M., Miller, F., "Damping of an Offshore Platform Model by the Random Decrement Method," Proceedings of the Second ASCE/EMD Specialty Conference, Atlanta, Ga., pp. 819-832, 1981.

12. M.A. Lishaa, "Development of a System Identification Technique for Structural Systems," M.S. Thesis, University of Maryland, 1982.

13. E.C. Levy, "Complex-Curve Fitting," IRE Trans. on Automatic Control, Vol. AC-4, pp. 37-44, May 1959.

14. C.K. Sanathanan and J. Koerner, "Transfer Function Synthesis as a Ratio of Two Complex Polynomials," IEE Trans. on Automatic Control. Vol. AC-8, pp. 56-58, January 1963.

15. P.J. Lawrence and G.J. Rogers, "Sequential Transfer-function Synthesis from Measured Data," Proc. IEE, Vol. 126, No. 1, pp. 104-106, January 1979.

16. M.T. Jong and K.S. Shanmugam, "Determination of a Transfer Function from Amplitude Frequency Response Data," Int. J. Control, Vol. 25, No. 6, pp. 941-948, 1977.

17. J.C.S. Yang, T. Tsai, W. Tsai, R.Z. Chen, "Detection and Identification of Structural Damage from Dynamic Response Measurement," submitted to 4th International Offshore Mechanics and Arctic Engr. Symposium, 1985.

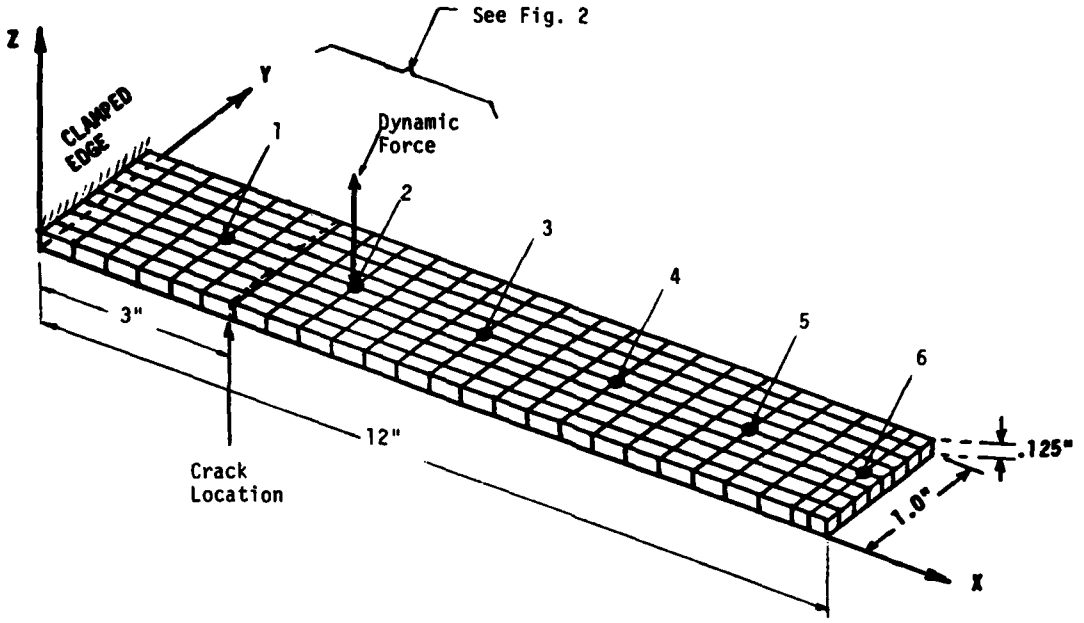

Fig. 1 Mesh Configuration, Location of Forcing, Crack and Stations of NASTRAN Simulated Steel Cantilever Beam

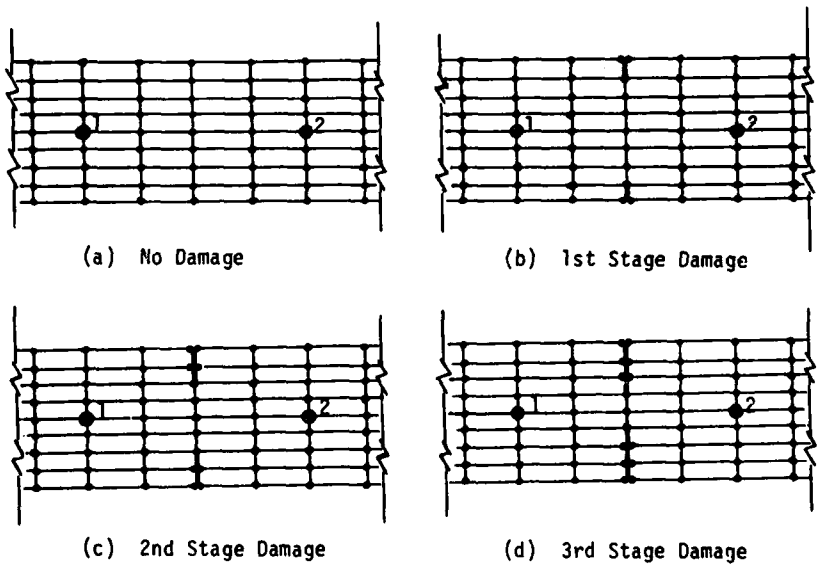

Fig. 2 NASTRAN Grid Points Arrangements for Simulated Damages

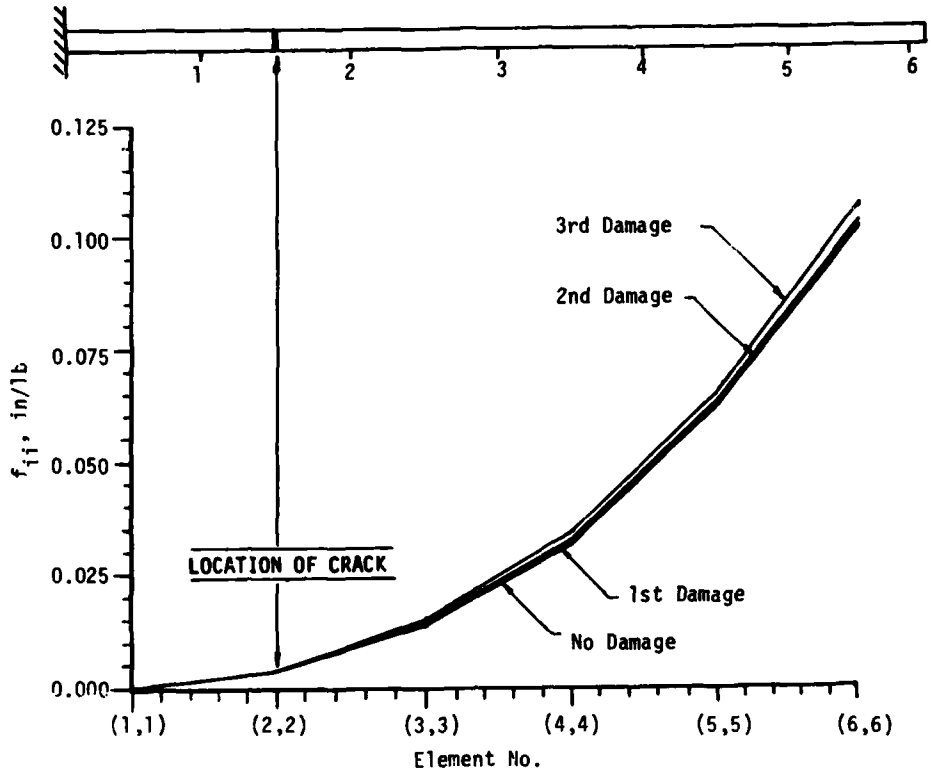

Fig. 3 Diagonal Elements of the Flexibility Matrix of the NASTRAN Simulated Steel Cantilever Beam

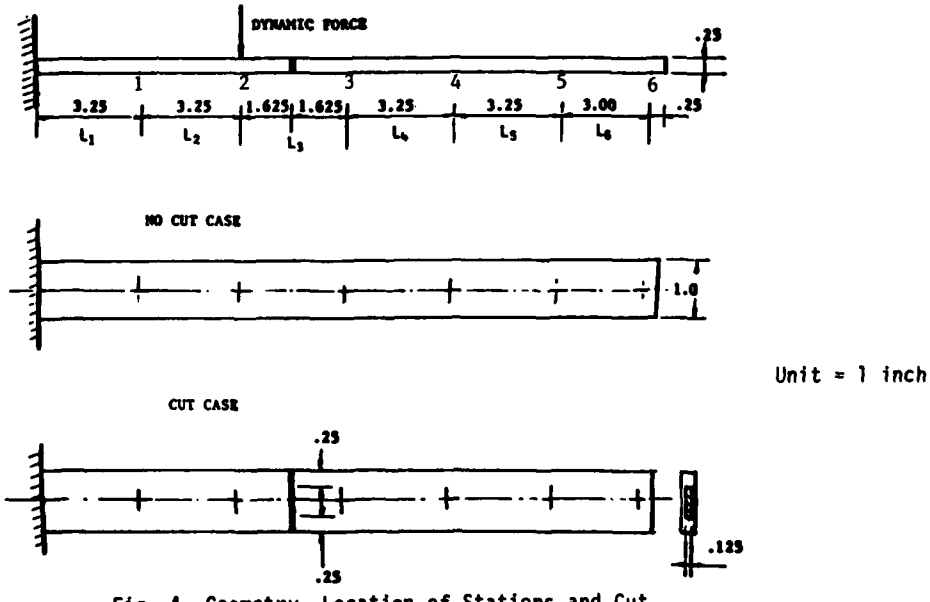

Fig. 4 Geometry, Location of Stations and Cut of the Aluminum Cantilever Beam

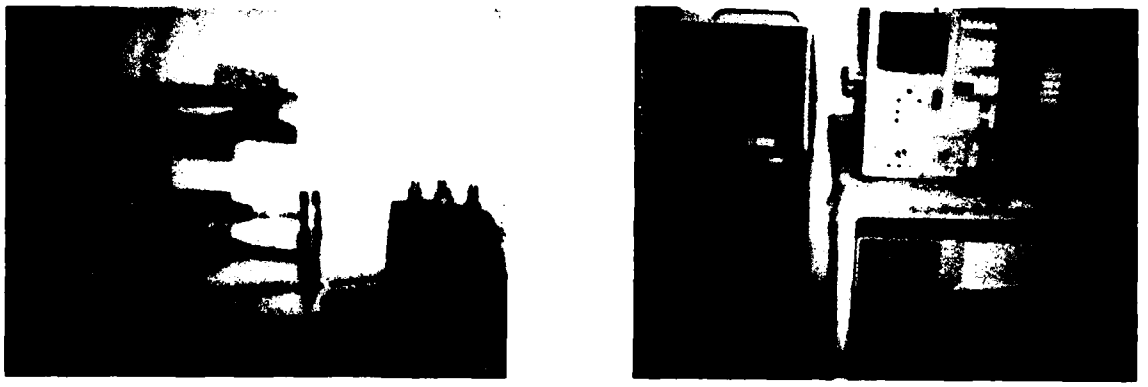

a. Set-up of cantilever beam with mechanism for application of excitation force

b. NICOLET 660B, dual channel FFT analyzer, supported by Data General MP/200 computer

Fig. 5 Set-Up of Cantilever Beam Experiment

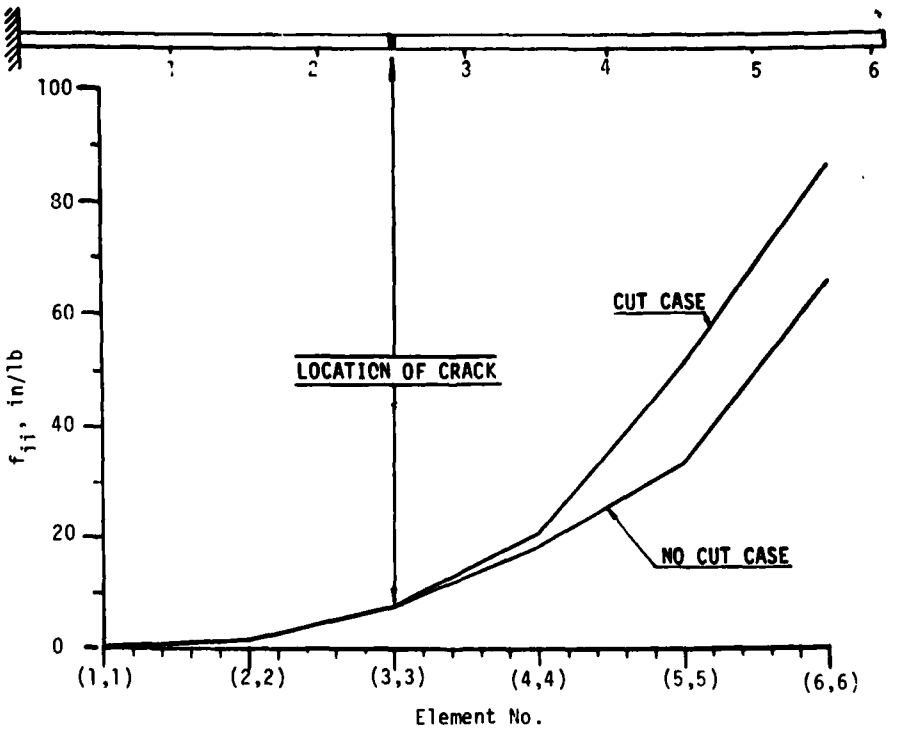

Fig. 6 Diagonal Elements of the Flexibility Matrix of the Aluminum Cantilever Beam

TIME DOMAIN MODAL ANALYSIS OF A SLOTTED CYLINDRICAL SHELL

W. Q. Feng[1], F. Q. Zhang[2], and T. C. Huang
Department of Engineering Mechanics
University of Wisconsin-Madison
Madison, Wisconsin 53706 USA

The modal parameters will change if a structure changes from being perfect to being defective. This paper investigates a cylindrical shell with a longitudinal slot by the time domain method. The 11 sets of mode vectors, all of them nearly real modes, are investigated and the modal shapes are plotted. When the slotted shell is compared with the original perfect shell, it is found that several new mode vectors are created for the slotted shell, and the characteristics of the kept modes, the mode shapes of the perfect shell which remain for the slotted shell, will change also.

INTRODUCTION

For many engineering problems, engineers must know what kind of physical phenomena change when a structure changes. One such problem occurs when a structure cracks; two aspects of this problem are when the structure changes from being perfect to being defective and when the crack propagates. In order to study these problems, it is necessary to have fundamental knowledge of the changes of the dynamic properties of a structure.

Reference [1] investigated the change in the modal parameters of a perfect cylindrical when it becomes a shell with a slot which is lengthened incrementally. The modal parameters were determined for each length of the slot, both experimentally and analytically. The conclusion of Reference [1] is that the presence of the slot will not only reduce the magnitude of the damped natural frequencies of the shell, but will also increase the number of the natural frequencies.

In this paper, the time domain method of analysis was used to investigate the same problem. In addition, the mode vectors are studied in detail.

EXPERIMENTAL MODAL ANALYSIS

The test object is an aluminum cylindrical shell having a mean diameter of 264.3mm, a length of 263.0mm and a thickness of 4.3mm, with a longitudinal edge slot 1mm wide and 152.4mm long. The upper end of the shell is free and the lower end of the shell is assumed to be simply-supported, but the shell itself is more constrained due to the actual fixture, which is a circular plate inside the lower end of the shell. The shell model is shown in Fig. 1. The experimental set-up for the time domain analysis is shown schematically in Fig. 2.

Points 1 to 25 were used as response measurement points and an appropriately chosen point R was used as the reference point (Fig. 1). When an impluse acted upon the surface of the shell, the free vibration response signals were taken and digitized through our Nicolet Digital Scope, Model 260A. The cutoff frequency was 1600 Hz and the sampling interval was 0.0001 second. The effect of noise and error in measurement was reduced by averaging 10 sets of the system matrix using a total record length corresponding to 400 samples or 0.04 second. The oversized mathematical model with 50 degrees of freedom is used in the system matrix.

The time response signals are recorded and digitized by a dual channel digital scope. There is a total of 26 measurement stations including the reference station R (Fig. 1). A total of 25 sets of response signals at two stations, one of which is the reference station R, was recorded, digitized and computed separately. There was a maximum of only 2% difference between each damped natural frequency, computed by our program for the time domain modal analysis, and the mean value of the 25 damped natural frequencies. The whole set of tests was repeated several times to test the consistency of modal vectors. The modal vectors obtained from these sets of tests show nearly identical results.

There is only a 15 Hz difference between the first mode of damped natural frequency of 155.1 Hz, and the second mode of 171.8 Hz. In this situation, where the modes are closely spaced, it is easy to identify the closely spaced damped natural frequencies in one computer run, but difficult to obtain their stable and nearly real modal vectors. We developed the skill of producing each close

---

1 On leave from Wuhan Institute of Water Transportation and Engineering, Wuhan, China

2 On leave from Chinese University of Science and Technology, Hefei, Anhui, China

mode separately and obtain very stable and nearly real modes for each of these two closely spaced modes.

It is very difficult for the modes having damped natural frequencies of 513.8 Hz, 1280 Hz, and 1519.6 Hz to be excited producing the modal nodes at the edges of the slot. The problem was solved by choosing the appropriate excitation position by trial and error and developing our skill for exciting either symmetical or anti-symmetrical modes.

RESULTS AND DISCUSSION

The time domain modal analysis was done by our program for the time domain modal analysis. A total of 11 modes was obtained. The results of the 25 points for the damped natural frequencies, damping factors and modal vectors are shown in Table 1. The mode shapes and phase angles for all 11 modes are plotted in Fig. 3.

Table 1 and Fig. 3 show that the phase angles are in general within ten degrees of either zero or 180 degrees. We therefore conclude that almost all 11 modes are nearly real ones. If we draw a line through the middle point of the slot and the center of the circle, the mode number 2, 4, 5, 7, 10 and 11 are nearly symmetrical to the line. In Fig. 4, A* is defined as the anti-symmetrical point of A, if A* is obtained through the following two steps: (1) by obtaining the symmetrical point A_1 of point A to the line ab, (2) by obtaining the symmetrical point A* of point A_1 to the circular arc. The mode number 1, 3, 6, 8 and 9 shown in Fig. 3 is very good anti-symmetrical, according to the above definition.

A perfect cylindrical shell has mode shapes, as shown in Fig. 5a, b, c and d for the cases of $m = 0$ and $n = 2, 3, 4$ and 5, respectively, where m is the number of modal nodes along the longitudinal direction and n is the circumferential half wave number [3]. The mode shapes have 2, 3, 2 and 5 aymmetrical axes for $n = 2, 3, 4$ and 5, respectively. The shell with a longitudinal slot not only exhibits the mode shapes which the perfect shell has, but creates one, two or more new mode shapes. There are two effects on the retained modes, the perfect shell modes that are retained by the slotted shell. First of all, these retained modes have only one symmetrical axis, which goes through the center of the circle and the middle of the slot. Secondly, the local modes in the slot region have an even number of modal nodes along the edges of the slot. All the new modes are anti-symmetrical as defined above. Their local modes along the edges of the slot have an odd number of nodes. The comparison of the number of nodes on the perfect and on the slotted shell is shown in Table 2.

In order to determine the mode shape between points 5 and 6, as well as points 9 and 10, we measured several extra points on each circular arc ab and cd, and determined the mode shape for 513.8 Hz as shown in Fig. 6a. We guessed that the mode shape is degenerated from the shape shown in Fig. 6b because of the large deflection at the points 7 and 8 caused by the existence of the long slot.

CONCLUSION

According to the results presented above, it may be concluded that the time domain method is a very powerful tool in modal analysis. The two effects of the slot on the cylindrical shell, in addition to its well known effect on the damped natural frequencies are that the characteristics of the retained modes change and that the new anti-symmetrical modes are created.

REFERENCES

1. Tang, Z. Q. and Huang, T. C., "Modal Analysis of a Cylindrical Shell with a Longitudinal Crack," Modal Testing and Modal Refinement, AMD-Vol. 59, ASME, 1983, pp. 77-84.

2. Ibrahim, S. R. and Mikalcik, E. C., "A Method for the Direct Identification of Vibration Parameters from Time Response," Shock and Vibration Bulletin, No. 47, September 1977, pp. 183-198.

3. Leissa, Arthur W., Vibration of Shells, NASA, SP-288, 1973.

Table 1 Results of Time Domain Analysis for the Shell with a Slot
(Frequency in Hz, Phase Angle in Degree)

Mode No.	1	2	3	4	5	6
Damped Natural Frequency	155.1	171.8	344.3	438.4	513.8	642.0
Damping Factor	0.006732	0.008288	0.003399	0.000562	0.02158	0.000386
Response Point	Mode Amplitude and Phase Angle					
	Ampl./Phase	Ampl./Phase	Ampl./Phase	Ampl./Phase	Ampl./Phase	Ampl./Phase
1	0.017/193.0	1.000/ 0.0	0.150/189.3	2.509/ 0.4	1.207/184.4	0.123/182.9
2	1.539/180.2	0.415/ 30.0	5.190/ 5.1	0.579/181.4	0.430/ 5.2	2.056/ 1.5
3	1.362/189.9	0.882/205.0	0.074/208.1	2.697/181.2	1.515/ 2.6	2.676/181.1
4	0.223/181.3	1.028/184.7	3.717/185.4	0.657/180.5	1.574/ 0.2	2.644/181.2
5	0.770/ 8.1	1.243/196.1	5.027/184.6	1.931/ 0.7	0.415/ 20.0	0.122/ 2.3
6	2.052/ 0.9	0.201/249.3	1.907/ 0.7	2.390/ 0.9	3.685/ 3.2	2.065/ 1.6
7	2.504/ 7.1	0.545/ 15.2	15.773/ 2.4	2.891/182.5	11.782/ 1.5	4.960/182.4
8	2.457/182.5	1.302/ 7.9	17.010/180.4	3.409/180.6	12.383/ 2.1	5.139/ 2.3
9	2.406/195.6	0.581/ 59.0	1.782/182.2	2.396/ 1.2	3.933/ 0.9	2.094/181.0
10	0.603/186.1	0.923/181.0	4.694/ 4.5	1.794/ 0.9	0.606/ 7.8	0.020/183.3
11	0.573/ 5.9	1.064/182.2	3.488/ 3.2	0.757/180.3	1.318/ 6.7	2.721/ 0.5
12	1.717/ 2.2	0.827/190.5	0.071/ 58.9	2.645/180.9	1.866/ 6.5	2.585/ 1.4
13	1.491/ 2.7	0.317/ 44.8	5.363/186.2	0.475/180.3	0.657/ 14.9	2.729/180.1
14	1.486/ 0.4	0.637/ 25.5	10.426/ 1.4	2.883/181.3	7.051/ 1.0	3.839/180.0
15	1.798/182.3	2.006/ 16.0	10.713/181.0	2.653/181.3	6.773/ 1.4	3.912/ 0.8
16	0.795/ 1.7	0.565/ 10.9	5.364/ 0.4	2.416/184.2	1.332/ 4.6	2.069/182.6
17	0.959/180.6	1.191/ 9.1	5.454/180.8	2.574/183.1	1.196/ 6.2	2.100/ 2.9
18	0.089/181.5	0.508/ 0.1	0.140/211.3	1.692/180.8	3.200/181.8	0.042/ 65.6
19	0.045/244.9	0.253/ 4.6	0.027/ 87.0	0.884/181.0	1.563/184.3	0.018/ 83.4
20	0.081/189.6	0.645/ 0.7	0.049/257.6	1.845/ 0.1	0.661/194.7	0.010/198.8
21	0.045/238.1	0.193/ 1.4	0.025/ 89.5	0.590/ 0.2	0.408/226.9	0.003/ 2.8
22	0.250/192.9	0.647/181.0	2.223/185.8	0.433/180.8	0.553/ 0.8	1.556/180.9
23	0.030/ 63.5	0.168/187.1	0.718/189.0	0.140/181.1	0.138/ 35.6	0.492/181.1
24	0.310/ 15.2	0.829/183.6	2.155/ 5.7	0.415/180.4	0.734/ 1.7	1.531/ 1.0
25	0.086/ 16.1	0.289/186.6	0.681/ 6.4	0.127/181.5	0.178/ 33.9	0.478/ 1.4

Table 1 (Cont.) Results of Time Domain Analysis for the Shell with a Slot (Frequency in Hz, Phase Angle in Degree)

Mode No.	7	8	9	10	11
Damped Natural Frequency	842.1	1075.8	1282.1	1366.2	1519.6
Damping Factor	0.000253	0.000624	0.006663	0.000439	0.003608
Response Point	Mode Amplitude and Phase Angle				
	Ampl./Phase	Ampl./Phase	Ampl./Phase	Ampl./Phase	Ampl./Phase
1	1.970/181.8	0.100/ 1.4	0.079/210.1	2.393/ 2.0	0.461/ 2.4
2	1.737/ 2.0	0.915/181.7	0.514/ 3.9	2.855/181.5	0.522/181.8
3	0.183/182.5	1.533/ 2.1	2.056/183.5	2.790/ 1.7	0.167/ 5.1
4	2.329/182.1	0.884/182.7	1.399/ 3.0	1.038/ 1.1	2.602/ 0.0
5	1.481/181.9	1.907/182.4	3.024/ 4.1	2.778/181.6	0.078/ 63.5
6	2.204/ 2.1	1.657/ 2.1	3.337/190.7	2.433/ 1.9	* / *
7	2.491/183.3	4.151/187.7	18.887/187.7	4.921/187.7	8.578/ 9.5
8	2.675/181.7	4.313/ 5.0	20.499/ 7.9	5.789/183.6	8.725/ 7.4
9	2.173/ 1.8	1.631/182.0	3.485/ 3.6	2.279/ 1.8	3.707/180.2
10	1.544/181.7	1.884/ 2.5	2.706/187.4	2.605/182.6	0.082/ 52.6
11	2.220/181.0	0.780/ 1.6	1.349/185.7	1.128/ 1.6	2.029/ 8.6
12	0.205/182.4	1.484/182.5	1.907/ 3.4	3.038/ 2.2	0.238/ 4.9
13	1.715/ 0.9	1.069/ 1.2	0.760/180.1	3.044/181.3	0.412/185.9
14	2.415/182.9	2.116/185.5	3.429/ 6.8	3.171/187.5	2.737/185.3
15	2.381/183.1	2.089/ 5.6	3.360/188.6	3.273/188.2	2.911/183.9
16	1.979/182.4	0.349/182.5	13.973/ 6.5	4.481/190.8	* / *
17	1.952/183.4	0.358/ 2.1	13.342/187.2	4.116/188.7	* / *
18	0.751/182.0	0.001/ 74.2	0.074/132.5	0.716/187.4	2.443/184.5
19	0.353/187.0	0.011/202.6	0.030/186.0	0.211/181.8	0.678/182.2
20	1.379/181.7	0.010/ 10.8	0.043/208.4	1.575/ 1.5	0.796/181.4
21	0.439/181.5	0.002/220.0	0.027/264.1	0.473/ 2.2	0.779/185.9
22	1.340/181.7	0.456/183.0	0.777/ 2.3	0.570/ 1.2	1.204/180.0
23	0.429/181.8	0.143/184.8	0.122/ 0.8	0.196/ 2.6	1.085/181.3
24	1.306/181.8	0.448/ 2.8	0.731/180.0	0.556/ 0.7	1.290/182.2
25	0.419/182.0	0.144/ 3.6	0.135/194.5	0.189/ 2.7	1.122/190.9

* Indicates missing data.

Table 2 Comparison of the Number of Modal Node of the Perfect and Slotted Shells (Damped Natural Frequency in Hz)

	Perfect Shell		Slotted Shell					
m and n	Damped Natural Frequency	No. of Modal Node	Damped Natural Frequency	No. of Modal Node	Damped Natural Frequency	No. of Modal Node	Damped Natural Frequency	No. of Modal Node
m=0, n=2	190.0	4	155.1	3+1	171.8	4+0	-	-
m=0, n=3	510.0	6	344.3	5+1	438.4	6+0	515.8	6+2
m=0, n=4	945.0	8	642.0	7+1	842.1	8+0	1282.1	7+3
m=0, n=5	-	10	1075.8	9+1	1366.2	10+0	-	-
m=1, n=4	-	-	1519.6	8+2	-	-	-	-

Notes for Table 2:

1. m indicates the number of modal node along the logitudinal wave and n the circumferential half wave number.

2. The results of frequency for perfect shell are quaoted from Reference 1.

3. In the columns of number of modal node for the slotted shell, the first number indicates the number of modal node along the upper circumference and the second one, the number of modal node along the two edges of the slot.

4. The number of modal node for the case m=0, n=3 and damped natural frequency 513.8 Hz will be discussed in the section of "Results and Discussion".

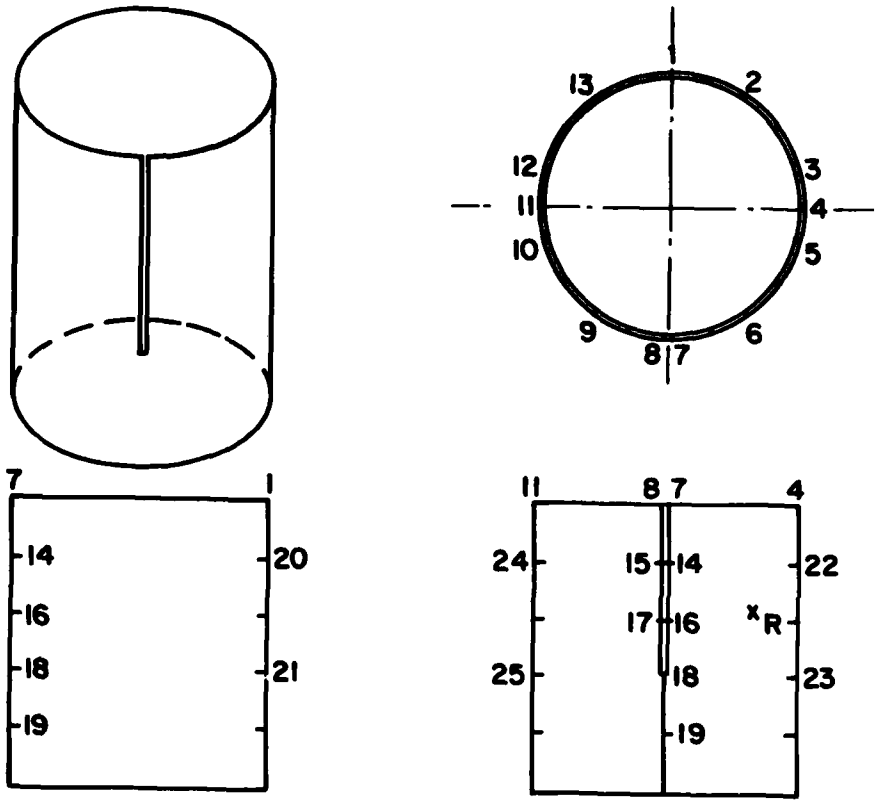

Fig. 1 Shell Model and 26 Measurement Stations

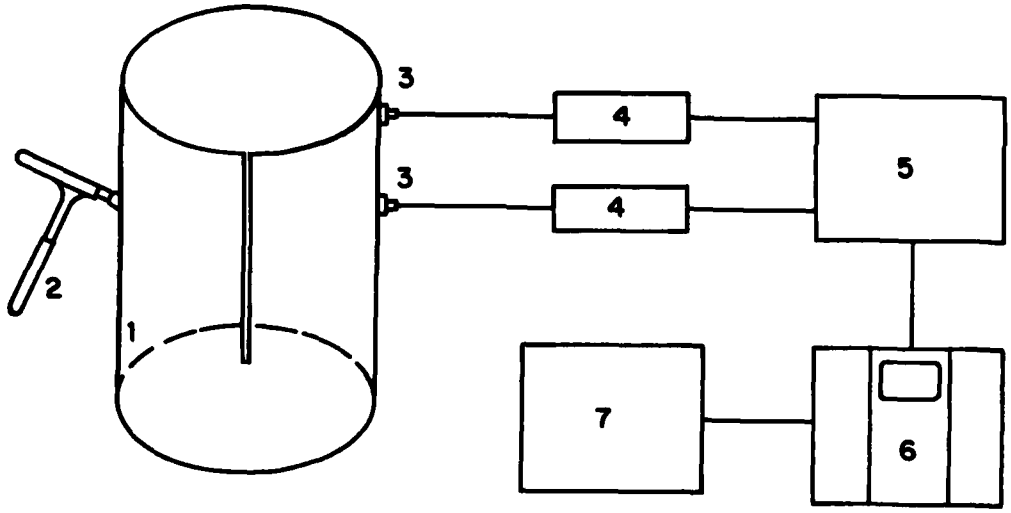

1. Shell
2. Hammer
3. Accelerometers
4. Charge Amplifier
5. Dual-channel Filter
6. Digital Scope - Nicolet Model 206
7. Computer

Fig. 2 Schematic Diagram for the Frequency Domain Experimental Setup

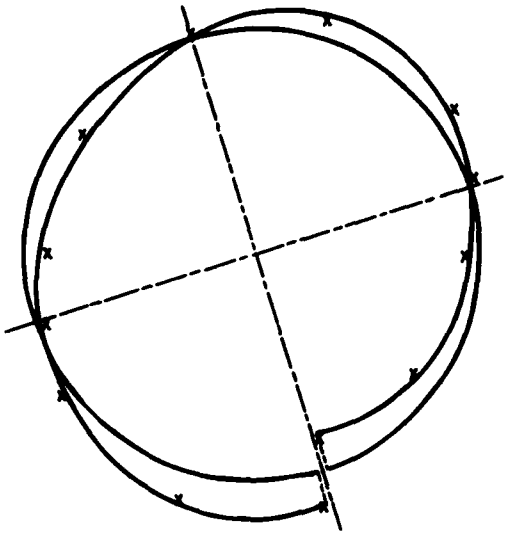

(a) Mode Shape - Top View

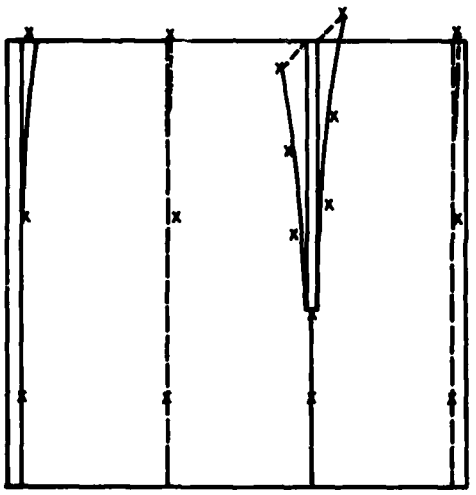

(b) Mode Shape - Side View

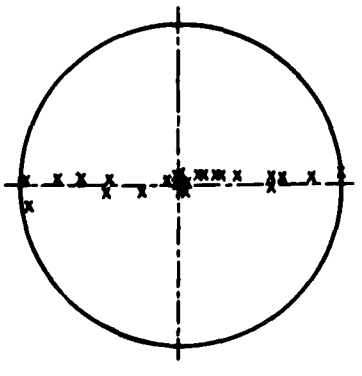

(c) Phase Angles

Fig. 3.1 Mode 1, f_d = 155.1Hz

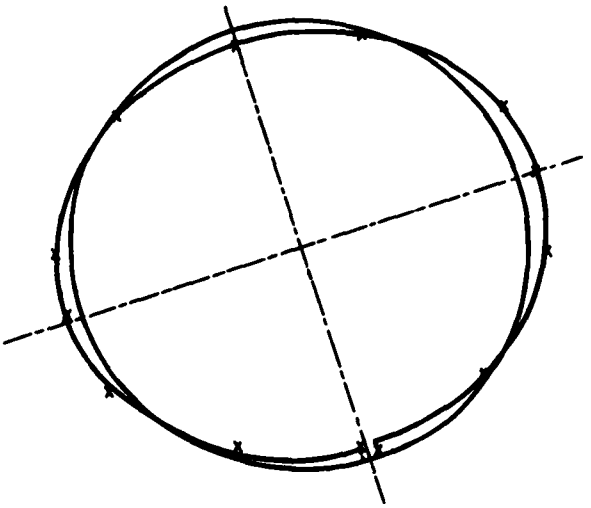

(a) Mode Shape - Top View

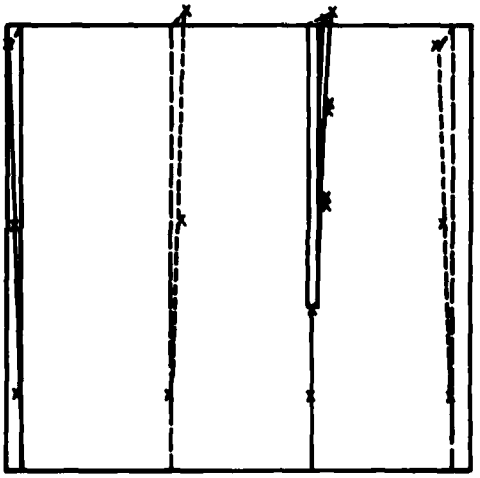

(b) Mode Shape - Side View

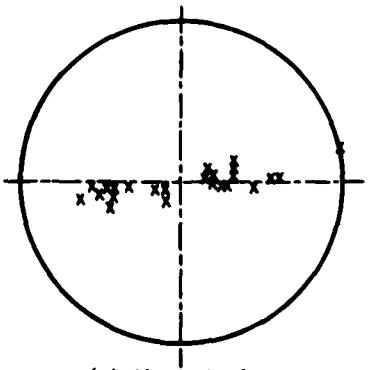

(c) Phase Angles

Fig. 3.2 Mode 2, f_d = 171.8Hz

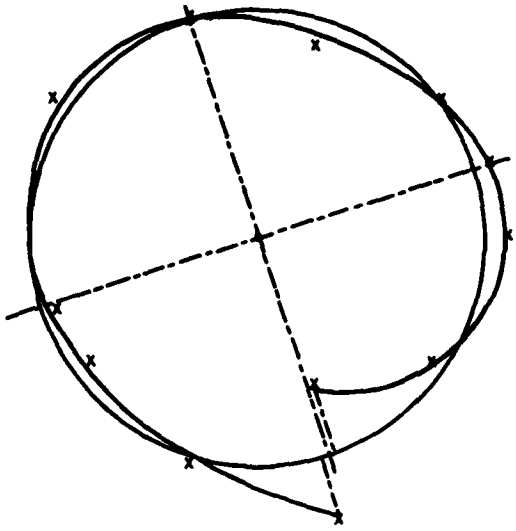

(a) Mode Shape - Top View

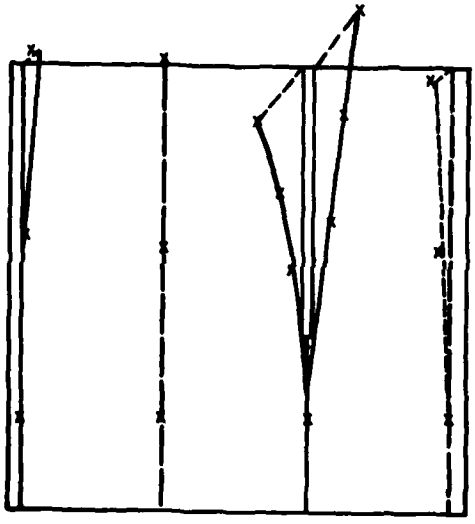

(b) Mode Shape - Side View

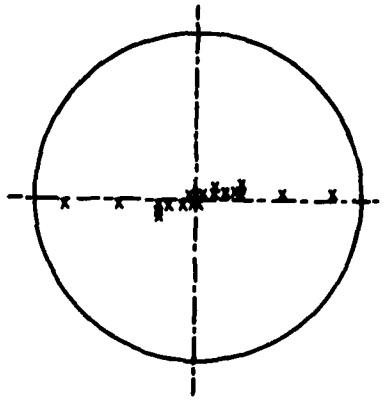

(c) Phase Angles

Fig. 3.3 Mode 3, f_d = 344.3Hz

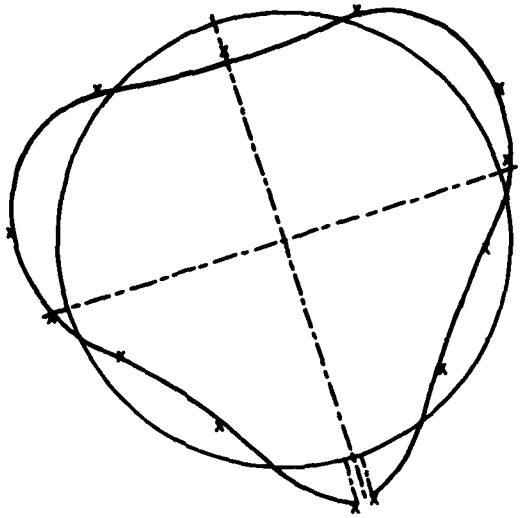

(a) Mode Shape - Top View

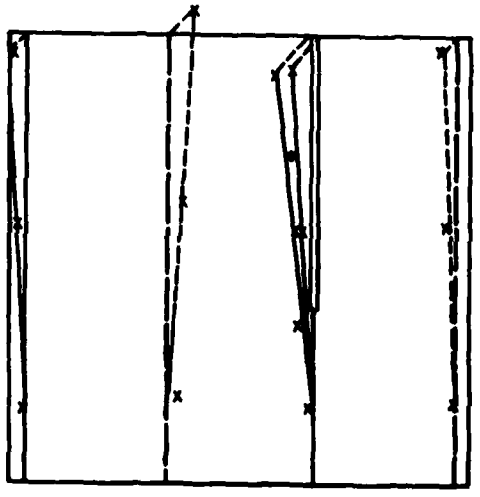

(b) Mode Shape - Side View

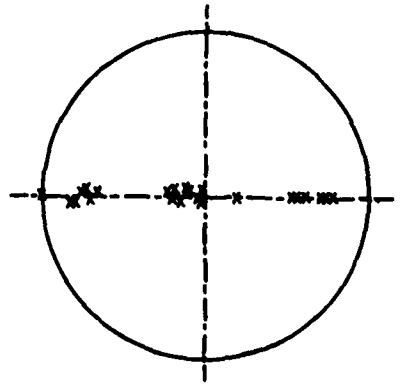

(c) Phase Angles

Fig. 3.4 Mode 4, f_d = 438.4Hz

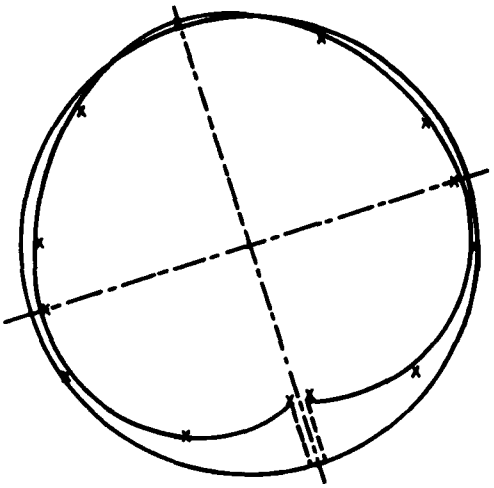

(a) Mode Shape - Top View

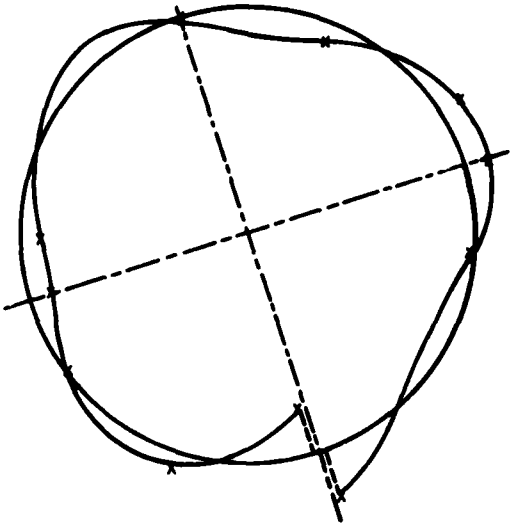

(a) Mode Shape - Top View

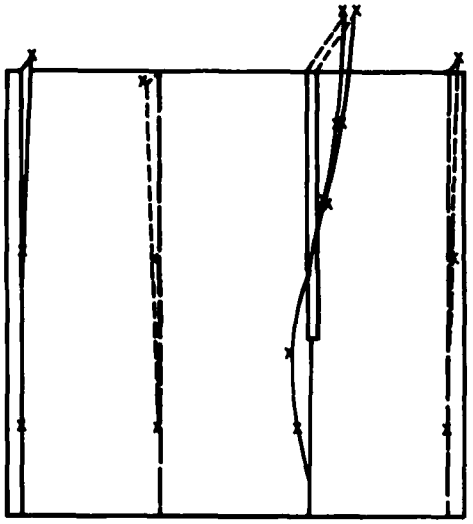

(b) Mode Shape - Side View

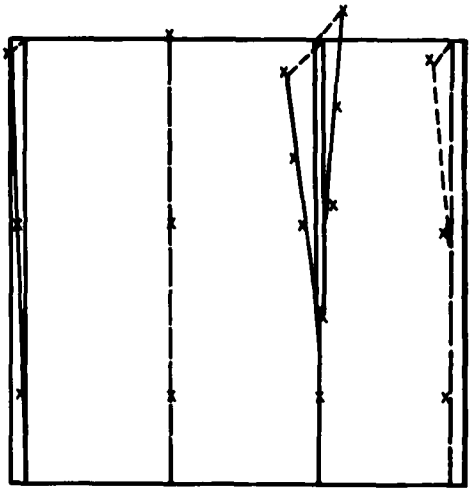

(b) Mode Shape - Side View

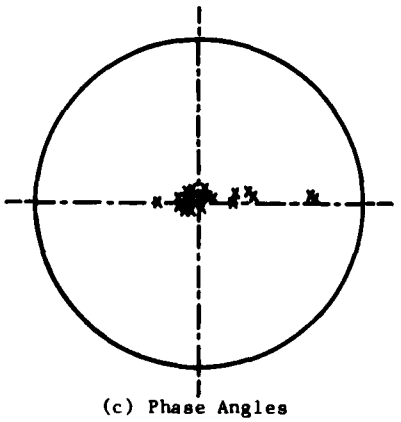

(c) Phase Angles

Fig. 3.5 Mode 5, f_d = 513.8Hz

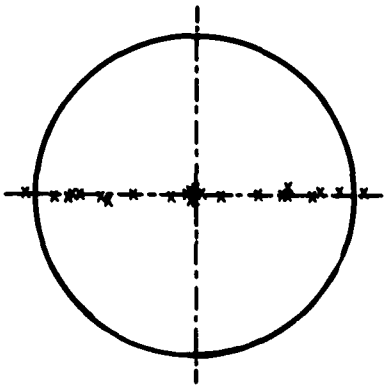

(c) Phase Angles

Fig. 3.6 Mode 6, f_d = 642.0Hz

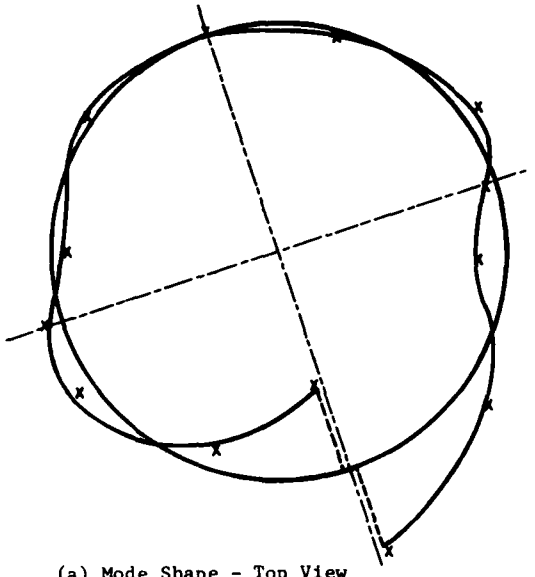

(a) Mode Shape - Top View

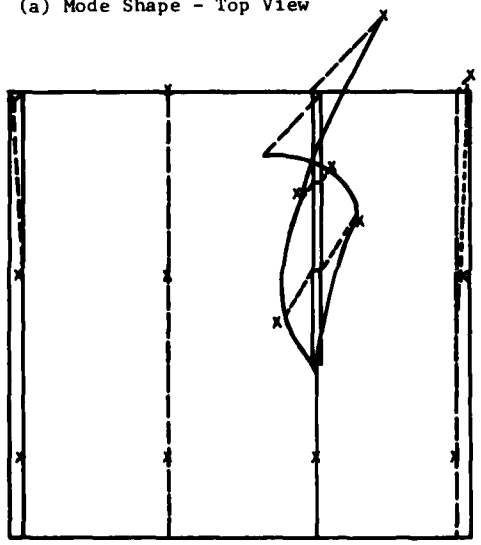

(b) Mode Shape - Side View

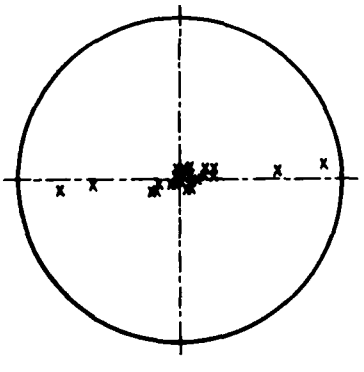

(c) Phase Angles

Fig. 3.7 Mode 7, f_d = 842.1Hz

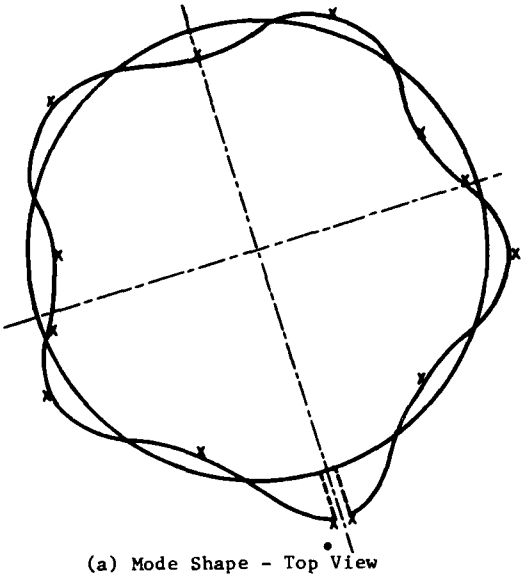

(a) Mode Shape - Top View

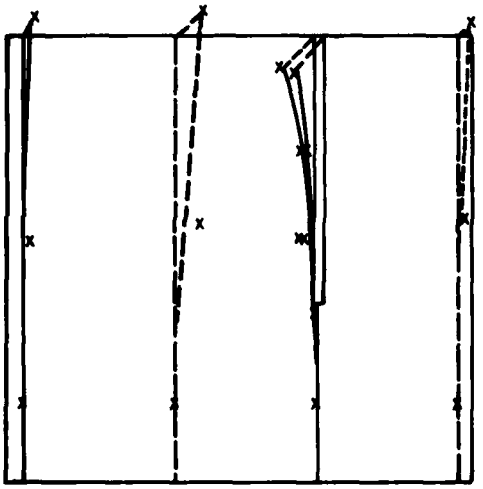

(b) Mode Shape - Side View

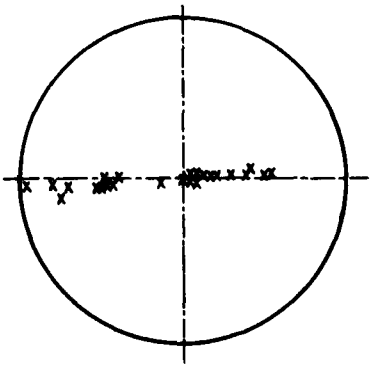

(c) Phase Angles

Fig. 3.8 Mode 8, f_d = 1075.8Hz

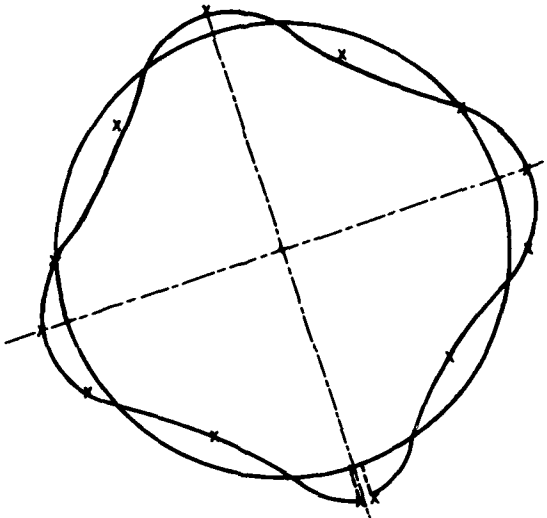

(a) Mode Shape - Top View

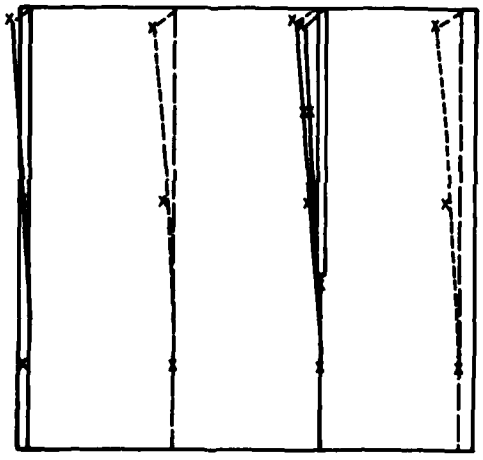

(b) Mode Shape - Side View

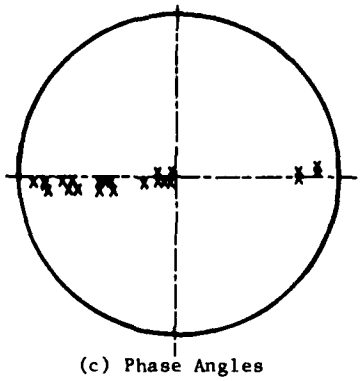

(c) Phase Angles

Fig. 3.9 Mode 9, f_d = 1281Hz

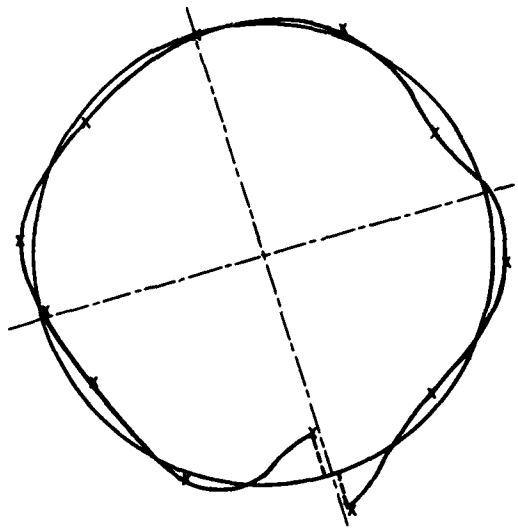

(a) Mode Shape - Top View

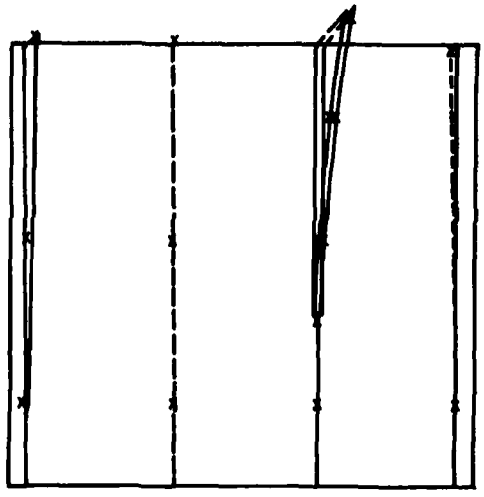

(b) Mode Shape - Side View

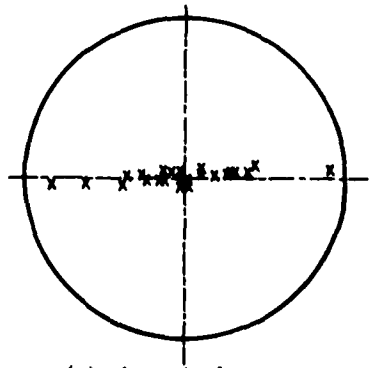

(c) Phase Angles

Fig. 3.10 Mode 10, f_d = 1366.2 Hz

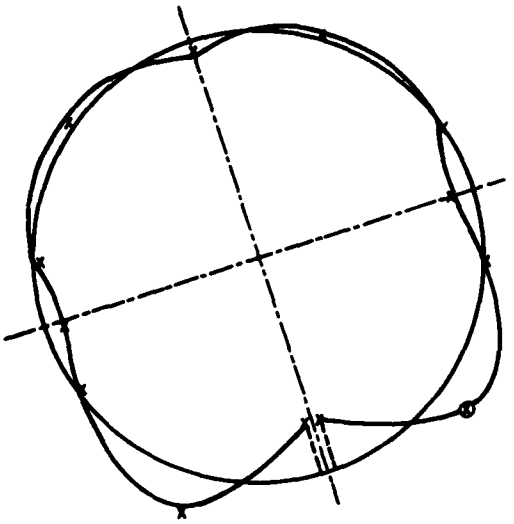

(a) Mode Shape - Top View

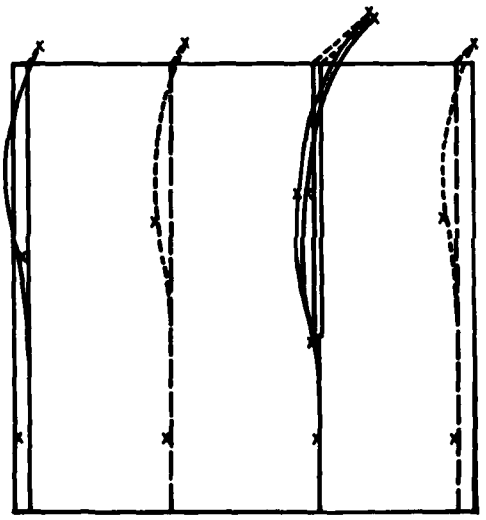

(b) Mode Shape - Side View

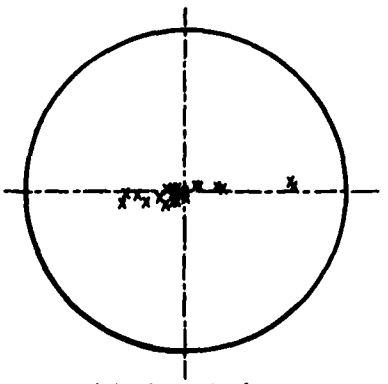

(c) Phase Angles

Fig. 3.11 Mode 11, f_d = 1519.6Hz

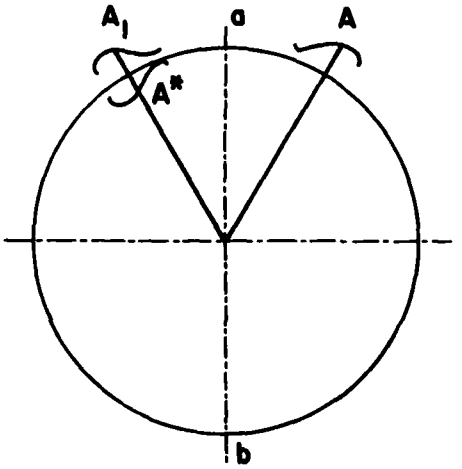

Fig. 4 Definition of Anti-Symmetry

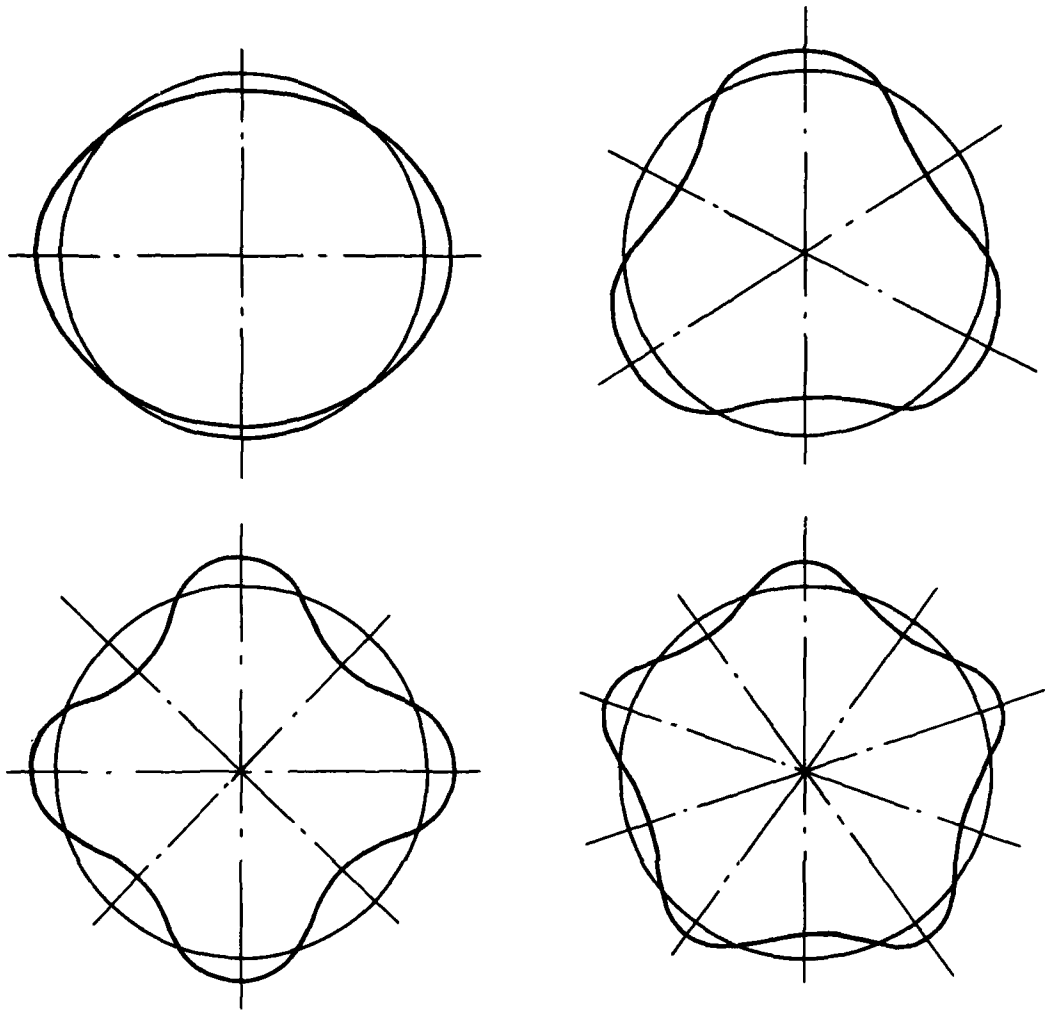

Fig. 5 Mode Shapes for a Perfect Shell

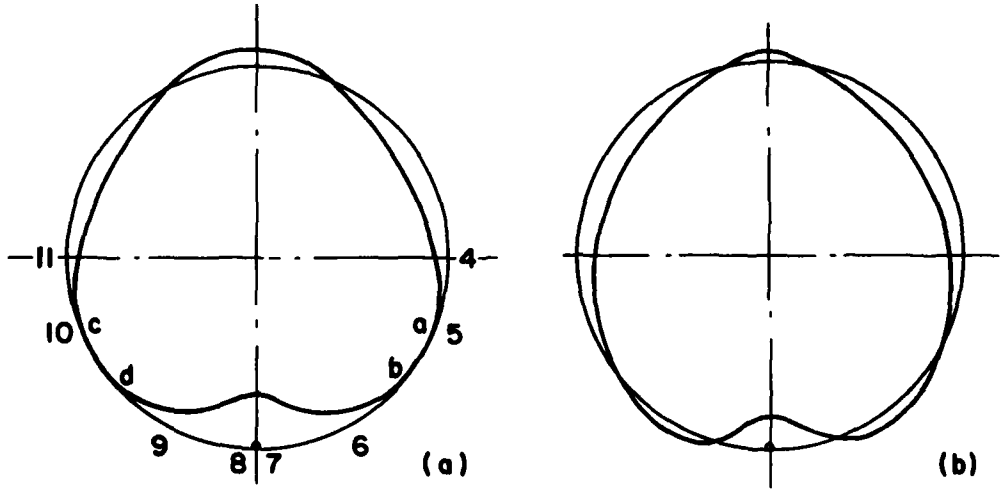

Fig. 6 A Detailed Study of Mode Shapes for 513.8Hz

APPLICATION OF THE ITD ALGORITHM TO LANDSAT TRANSIENT RESPONSES

R. R. KAUFFMAN
GENERAL ELECTRIC COMPANY, SPACE SYSTEMS DIVISION
PHILADELPHIA, PENNSYLVANIA

Frequency, damping, and three degree-of-freedom mode shapes were estimated from data transmitted from the orbitting Landsat-4 and Landsat-5 earth observation spacecraft. The data was comprised of three channels of time history data corresponding to orthogonal rotations of the spacecraft. The data was processes using the Ibrihim Time Domain Technique. It was found that multiple modes could be characterized per channel of data. Damping estimates are on the order of 0.2% for low frequency (< 3 Hz) modes and on the order of 0.5% for high frequency modes.

INTRODUCTION

The purpose of this paper is to present results from the application of the Ibrahim Time Domain (ITD) algorithm to estimate the dynamic characteristics of orbital spacecraft. The spacecraft considered are the Landsat-4 and Landsat-5 earth resources satellites. This study was undertaken to validate analytical predictions of the spacecrafts' response to Thematic Mapper (TM) and Multi-Spectral Scanner (MSS) periodic excitation, and to determine spacecraft modal damping values.

The orbital configuration of these spacecraft is shown in Fig. 1. The two primary sensors are the TM and the MSS. Both instruments incorporate scanning mirrors which alternately impact rubber bumpers at either end of their travel. The TM is much larger than the MSS and provides much higher resolution. The high resolution of the Landsat TM makes it susceptible to self-induced vibration, or jitter, and requires the ground correction of the images. The TM provides an order of magnitude improvement in resolution over the MSS.

Because initial analyses indicated that the jitter resulting from the mirror impacts would cause unacceptable distortion of the TM images an Angular Displacement Sensor (ADS) was attached to the TM base. Payload Correction Data (PCD) which is comprised of Gyro data (< 2.0 Hz) and ADS data (2.0 Hz through 125.0 Hz) is transmitted from orbit. This data corresponds to three orthogonal angular displacements of the TM. This allows the measured motion of the TM to be transmitted to the ground for correction of the jitter induced distortion. The magnitude of jitter must remain below set limits for the sensors to obtain accurate images.

The periodic excitation from the scanning mirrors is caused by force pulses in alternate directions

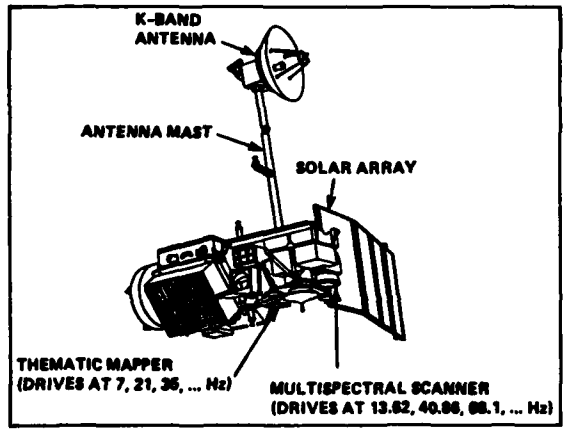

Fig. 1 - Landsat-4 vehicle

as the mirror impacts resilient stops at either end of its travel. The Fourier components of the resulting pulse train are rich in the odd harmonics of the scanning frequency (7.053 Hz for the TM and 13.656 Hz for the MSS). The spacecraft dynamic response to the scanning forces is dependent on the structural dynamic characteristics as the Attitude Control System (ACS) does not operate at 7 Hz and above. Since analytic predictions of jitter are highly dependent on the modal characteristics of the structure, it is vital that these characteristics be accurately determined. To define the spacecraft dynamics, a modal math model of the spacecraft was synthesized from existing finite element models of the spacecrafts main body and appendages. The resulting spacecraft model shows large amplifications of the excitation forces at the numerous structural resonances which begin with a solar array resonance at 0.4 Hz. The model has 70 modes below 50 Hz. Very large jitter responses occur with the scanning frequency or one of its odd harmonics coincide with a structural resonant frequency. Although pre-flight modal tests were used to partially validate

the dynamic model, a range of values were used in the pre-flight analysis. A modal damping variation from 0.05 to 1.0 percent was used because it could not be reliably measured on the ground. Therefore, the objective of this study was to analyze the PCD to determine the modal frequencies and damping coefficients and compare these with analytic values. Also of interest is how consistent the modal frequencies are between spacecraft.

The Landsat data is relatively unique. The data covers a much broader frequency range than is normally available from orbital vehicles. Orbital data is normally limited to frequencies below that of the structural modes and is used for control system evaluation. The Landsat data covers a frequency range of more than two orders of magnitude above the fundamental structural frequency of 0.4 Hz. In the past modal parameters have rarely been measured in orbit and with limited results. Ref. [6] documents an example where orbital measurements on the OSO-8 were transmitted to earth. From this data, the damping of one mode was successfully determined.

A relatively new Ibrahim Time Domain (ITD) analysis technique was selected to process the PCD. This technique can use either random vibration or free decay data to estimate the resonant frequencies, modal damping coefficients, and mode shapes. It requires no knowledge of the applied force. It is extremely powerful in that many modes can be obtained from the analysis of a limited number of channels of data. The coding of the method was obtained from the NASA Langely Research Center and was a revision to the original Ibrahim code made by R. Pappa.

This study uses the ITD method to evaluate the modal analysis and is comprised of three main activities: investigation of the ITD algorithm's characteristics using a simple Five Degree-of-Freedom (DOF) system, application of the algorithm to a finite element model of Landsat-4, and application of the algorithm to data transmitted from the orbiting spacecraft.

In the first part of the study, a simple five DOF system is used to investigate the characteristics of the ITD algorithm. This algorithm characterizes a structure using time history data. The data may be of two forms: free decay or random vibration. In this study, only free decay data is considered. The algorithm's sensitivity to noise in the data and to several user input parameters is investigated. Also considered is the ability to characterize multiple modes from a single channel of data. This ability is required for the following parts of the study.

Next, a finite element model of the Landsat-4 spacecraft is used to simulate orbital conditions. A forcing function representing an MSS shutdown event was applied to the model and the time history responses developed are input to ITD. This model gives an indication of how well the algorithm will work under ideal conditions (very low noise levels, linear system, actual free decay data, etc.). This sets an upper bound on the performance expected in the final portion of the study.

The final portion of the study involves Landsat-4 and Landsat-5 time history data measured in orbit. The modal parameters generated from the data are compared with both the original analytic model and with modal parameters generated via ITD from analytic time history data.

THEORY

The ITD method uses free decay transient responses or random excitation responses to identify the natural frequencies, complex mode shapes, and critical damping ratios of a structure. In this study, only free decay transient responses are considered. The ITD method reduces these transient decays into their complex exponential forms.

Invoking the assumption that any structure may be represented by an equivalent finite lumped mass system results in:

$$(\lambda^2 [M] + \lambda [C] + [K]) \{ P \} = 0, \quad (1)$$

The goal of modal vibration testing is to determine values of λ (eigenvalues) and P (mode shapes) that satisfy the above equation. It should be noted that for underdamped modes, λ and P occur as complex conjugate pairs and the following relationshps are valid.

$$\lambda = a + ib, \quad (2)$$

$$W_d = b, \quad (3)$$

$$W_n = \sqrt{a^2 + b^2}, \quad (4)$$

$$\rho = a/\sqrt{a^2 + b^2}, \text{ and} \quad (5)$$

$$W_d = \sqrt{1 - \rho^2}\, W_n \quad (6)$$

where W_d and W_n are the damped and undamped natural frequencies and ρ is the damping ratio.

The free response of a linear multi-degree-of-freedom system at station i and time t_j may be given as:

$$X_i(t_j) = X_{ij} = \sum_{K=1}^{2m} P_{ik} e^{\lambda_k t} \quad (7)$$

where m is the number of modes that are excited. Eq. (7) can be written in matrix form as:

$$[X] = [P][\Lambda]. \tag{8}$$

Similar equations can be written at times Δt_1 and Δt_2 later. It can be shown that manipulation of these equations results in

$$([\hat{\phi}][\phi]^{-1} - \bar{\lambda}[I])\,\psi = 0 \tag{9}$$

where

$$[\phi] = \begin{bmatrix} X \\ X_{\Delta t_1} \end{bmatrix}$$

$$[\phi] = \begin{bmatrix} X_{\Delta t_1} \\ X_{\Delta t_2} \end{bmatrix}, \text{ and}$$

$$\psi = \begin{bmatrix} P \\ P_{\Delta t_1} \end{bmatrix}$$

Eq. (9) is an eigenvalue problem which enables the computation of a system's modes, frequencies, and damping using only measured free decay data at various locations. The following expressions relate the eigenvalues of Eq. (9) ($\bar{\lambda}$) to those of Eq. (1) (λ):

$$\bar{\lambda} = \beta + i\gamma \tag{10}$$

$$\lambda = a + ib \tag{11}$$

$$a = \frac{1}{2\Delta t} \ln(\gamma^2 + \beta^2) \tag{12}$$

$$b = \frac{1}{\Delta t} \tan^{-1}(\gamma/\beta) \tag{13}$$

The eigenvectors (modes) of Eq. (1) (P) are simply the first n elements of the eigenvectors of Eq. (9).

The mode shapes are compared via the modal dot product. The cosine of the angle between modes $\{P_j\}$ and $\{P_k\}$ may be defined as:

$$\cos(\theta) = \frac{\sum_{i=1}^{n} P_{ij} \cdot P_{ik}}{\left[\sum_{i=1}^{n} (P_{ij})^2\right]^{1/2} \left[\sum_{i=1}^{n} (P_{ik})^2\right]^{1/2}} \tag{14}$$

where n is the number of degrees of freedom in the modes being compared. The value of the dot product can range from -1.0 to 1.0. The sign of the dot product merely indicates the phase relationship of the two modes (positive for in phase, negative for out of phase). The magnitude of the dot product indicates the level of agreement between the shape of the two modes. A magnitude of one indicates perfect agreement while a value of zero indicates no agreement. A dot product value of 0.85 indicates good agreement.

When using the ITD algorithm, there are several guidelines for parameter selection that should be followed. They are:

$$N1 \leq \frac{SF}{2(f_\pi)} \tag{15}$$

$$NDELTA < N1, \tag{16}$$

$$N2 \cong 2*NDELTA, \tag{17}$$

$$\frac{NCOL}{SF} > \frac{3}{f_{min}}, \text{ and} \tag{18}$$

$$N1 \neq N2. \tag{19}$$

The variables in expressions (15) through (19) are defined as follows:

N1	-	Number of time steps shifted from ϕ to $\hat{\phi}$,
N2	-	Number of time steps shifted within halves (for creation of "transformed stations") of response matrices
NDELTA	-	Number of time steps shifted between upper and lower halves of response matrices
NCOL	-	Number of time steps used
SF	-	Sample frequency
f_π	-	Maximum expected frequency content, and
f_{min}	-	Minimum expected frequency content.

For more information on the ITD method, see Ref. [1] through [5].

FIVE DEGREE-OF-FREEDOM MODEL

A five degree-of-freedom (DOF) model was developed to evaluate the ITD method and to determine ITD input parameter sensitivity. The lumped mass model that was used is shown in Fig. 2. The undamped natural frequencies of this system can be determined by an exact analytical method.

The analytically determined modal parameters

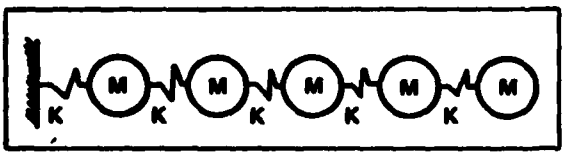

Fig. 2 - Sample five DOF model

were compared to ITD results for a wide variety of ITD input parameters. Overall, the ITD algorithm showed good results. Fig. 3 shows the effect of white noise in the data on ITD damping results. The calculated frequency was virtually uneffected by noise. Fig. 4 plots NDOF against damping ratio for a signal distortion of 0.568%. As can be seen, the ITD solution shows good agreement with the analytic data. The reduced number of measurement stations had very little effect on the calculated frequencies.

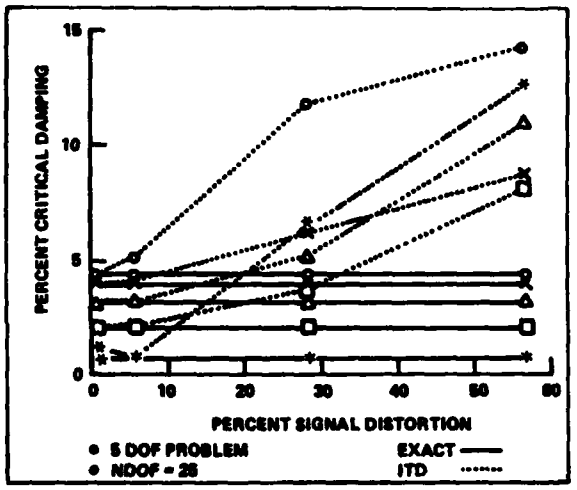

Fig. 3 - Effects of white noise

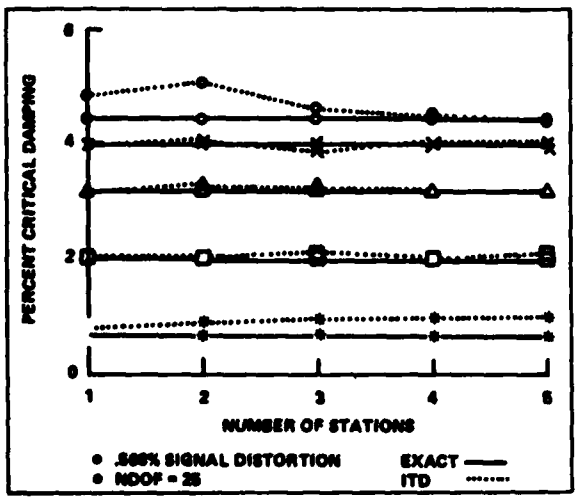

Fig. 4 - Effects of reduced measuring stations

ANALYTICAL ORBITAL MODEL ANALYSIS

A finite element model of the Landsat-4 spacecraft in its orbital configuration was developed. This model was synthesized from various substructure models verified by preflight test data and combined by a stiffness coupling routine. The total orbital model is comprised of 257 nodes and 819 dynamic DOF's.

There are two main sources of excitation that are considered in this analysis. These are the TM and the MSS. These systems are illustrated in Fig. 1. The TM and MSS excite the structure through the motion of large scanning mirrors. These mirrors impact resilient stops as they scan back and forth. In this analysis, it is assumed that when a sensor is shutdown, its scanning mirror's motion stops instantaneously. Actually, the mirror will continue to scan at a decreasing rate for several cycles while energy is lost in various mechanical processes.

Transient response time histories were generated for eight DOF's in the model via the DYNAMO transient response routine MERTA. In all cases, an infinitesimal amount of white noise (SNR = 10^6) was added to the time history data. The DOF's chosen were the TM cg θ X, θ Y, and θ Z, and the MSS cg θ X, the solar array drive θ Y, and the K-band antenna gimbal drive θ X, θ Y, and θ Z directions. The three DOF's for the TM correspond to the measurement stations on the satellite while forcing functions may be applied at the remaining DOF's. After the transient responses are run, Fast Fourier Transforms (FFT) of them are generated. While the FFT is not part of the ITD algorithm, it compliments the ITD results by giving the relative magnitude of the modal responses. It should be noted that for the sampling frequency and sample size used in this analysis, the FFT frequency resolution is limited to one Hz. Also, for all FFT's plotted, the 0. Hz frequency component is set to zero. Due to the relatively large magnitude of the rigid body motion, dynamic responses tend to get swamped.

The ITD algorithm was applied to simulated MSS data. This data corresponds in format to PCD. The MSS excites the structure through the motion of a scanning mirror. Data is measured upon shutdown of the MSS to achieve free decay data. A parametric study varying NDOF was performed. Fig. 5 presents this study. Each curve on the plot represents the frequency of a particular mode for various values of NDOF. The frequencies converge on the correct results as NDOF increase. As can be seen in Table 1, for the case with NDOF = 60, the analytical and ITD frequencies agree quite well. Additionally, the damping values show fairly good agreement for most of the modes. It should be noted that damping values coverge more slowly than frequency values.

TABLE 1
Comparison of Analytical and ITD Modal Parameters
NDOF = 60 Case***MSS θ - X Exitation

ANALYTIC MODE NUMBER	ANALYTIC FREQ. (Hz)	ANALYTIC DAMPING (% C/C)	ITD FREQ. (Hz)	% Δ	ITD DAMPING (% C/C_0)	% Δ	MODE SHAPE DOT PRODUCTS
11	1.615	1.0	1.336	-17.28	19.016	1801.60	-.983
12	2.145	1.0	2.166	.98	1.313	31.30	-.940
24	14.078	1.0	14.102	.18	.980	-2.00	-.918
27	16.771	1.0	16.758	-.08	.724	-27.60	1.000
30	20.066	1.0	20.081	.07	1.103	10.30	1.000
39	28.881	1.0	28.892	.04	1.104	10.40	.998
41	32.893	1.0	32.869	-.07	.981	-1.90	-.998
45	35.112	1.0	35.053	-.17	.941	-5.90	.998
49	38.196	1.0	37.959	-.59	2.238	123.80	.828
50	38.238	1.0	38.214	-.06	.779	-22.10	.998
58	42.144	1.0	41.964	-.43	1.177	-17.70	-.924
67	48.578	1.0	48.583	.01	1.161	16.10	-1.000
92	65.967	1.0	65.949	-.03	.852	-14.80	-.997
108	78.513	1.0	78.407	-.14	1.163	16.30	1.000

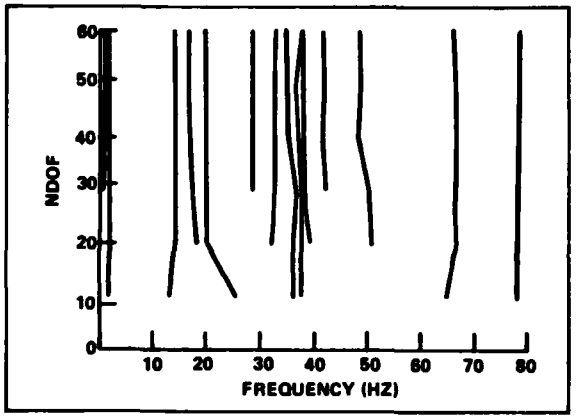

Fig. 5 - NDOF vs. frequency FEM data

Several points can be made about this analysis of the orbital model. First, it should be noted that one of the guidelines mentioned in this Section was not met. Rearranging Eq. (18) yields:

$$F_{min} > \frac{3\ SF}{NCOL} \qquad (20)$$

Since both SF and NCOL are equal to 500, expression (20) implies that any results for modes with a frequency less than 3 Hz will be questionable. Looking at Table 1 shows that damping values calculated for modes in this low frequency range are generally inaccurate. However, all other modal parameters show good agreement with the actual values. In order to decrease the value of f_{min}, it would be necessary to decrease the sampling frequency or increase the amount of data used. Both of these actions have bad effects. Decreasing the sampling frequency can lead to the loss of high frequency data and aliasing. Increasing the amount of data used increases both the run time and computer memory required. This can lead to greatly increased computer costs. A possible solution to this problem is the use of digital filters to allow analysis of narrower bandwidths of data.

It should be possible to determine which modes will be excited by a particular forcing function by looking at the mode shape. Thus, a Theta-X forcing function should excite Solar Array bending modes, Boom Y-bending modes and Gimbal Drive Assembly bending modes. A Theta-Y forcing function should excite Solar Array torsion modes, Boom X-bending modes, and Aximuth Drive modes. A Theta-Z forcing function should excite Elevation Drive and Solar Array edgewise modes. Finally, various local modes are not likely to be excited. It was found that there is good correlation between expected and actual results. The method does have difficulty picking up higher order appendage modes. This is not surprising considering the extremely limited instrumentation being simulated. These higher order modes are not likely to be well coupled with the center body. Also, the fundamental solar array modes were not excited. These modes have frequencies lower than the 3 Hz minimum frequency allowed for in expression (20). Therefore, it is not surprising that these fundamental modes are not recovered.

Twelve modes were extracted from the simulation data. The frequencies of these modes fell between 14. and 79. Hz. The calculated (via ITD) frequencies and mode shapes agree very well with the original analytical modal parameters. The calculated damping values showed good agreement with the original values. These results verified the viability of using the ITD algorithm to analyze data in the format transmitted from orbit.

ORBITAL DATA ANALYSIS

The data used in this analysis can be divided into two major subdivisions: Gyro data (< 2 Hz) and Payload Control Data (PCD) (0-125 Hz). While the Gyro filter starts to roll off at 2 Hz, it is possible to measure responses to a somewhat higher frequency. Also, the wide bandwidth of the PCD precluded its use for determining modal characteristics below 3 Hz. Thus, both types of data must be analyzed to investigate the entire frequency range from 0 through 125 Hz.

Both the PCD and Gyro data correspond to Theta-X, Theta-Y, and Theta-Z angular displacements of the TM. The Gyro data has a sampling rate of 15.635 samples/second and thirty seconds of data are required for the ITD analysis. The PCD has a sampling rate of 500 samples/second and one second of data is required for the ITD analysis.

Three flight events are considered. These are a Landsat-4 MSS shutdown, a Landsat-5 MSS shutdown and a Landsat-5 TM shutdown. In each of the events, the appropriate instrument is shutdown. The PCD recorded after the shutdown is theoretically a free decay. In practice, the actual data is somewhat contaminated by solar array drive, Ku-band antenna drive, and attitude control system activity. The extent of this contamination can not be accurately gauged. It should also be noted that when the Landsat-4 data was measured, the TM had shut down shortly before the MSS and may have influenced the results.

This data presents several challenges to the ITD algorithm. First, with only three rotational channels of data, the instrumentation is very limited. The data includes the effects of noise and structural nonlinearities. Also, as was mentioned in the preceeding paragraph, several onboard systems created an undetermined amount of contamination in the data. This contamination will cause the data not to be a true free decay, which is the form assumed by the ITD algorithm.

In spite of these difficulties, the method worked quite well. For each flight event investigated, approximately twenty modes have been characterized. The frequencies measured show good agreement with analytical predictions, with 75% to 80% of the measured frequencies falling within 10% of the predicted frequencies. There is also good agreement with FFT results. The calculated modal parameters are shown in Table 2.

TABLE 2
Results of ITD Analyses of Orbital Data

Analytic Modal		Landsat-4 MSS Shutdown				Landsat-5 MSS Shutdown				Landsat-5 TM Shutdown			
Mode #	Freq (Hz)	Freq (Hz)	Δ Freq (%)	Damp (%C/CC)	Dot Product	Freq (Hz)	Δ Freq (%)	Damp (%C/CC)	Dot Product	Freq (Hz)	Δ Freq (%)	Damp (%CC/CC)	Dot Product
7	0.428	0.394	- 7.9	0.418	-0.763	0.392	- 8.4	0.215	-0.931	0.381	-11.0	1.307	0.968
8	0.762	0.858	12.7	1.007	0.974	0.796	3.7	-0.102	0.999	0.789	3.5	-0.918	-0.100
9	1.209	1.174	- 2.9	0.525	-0.721					1.409	16.5	3.196	-0.722
10	1.321					1.180	-10.7	0.618	0.952				
11	1.615					1.769	9.5	0.237	0.578	1.555	- 3.7	0.550	-0.940
12	2.145	2.794	30.3	-0.004	0.948	2.754	28.4	-0.030	-0.999	2.381	11.0	0.493	-1.000
16	4.152	4.150	- 0.1	0.303	-0.888	4.618	11.0	-0.675	0.935	5.410	30.3	-8.018	0.941
17	6.470									6.161	- 4.8	3.446	-1.00
18	6.915	5.394	-22.0	10.008	0.852								
22	12.636	11.299	-10.6	9.941	-0.731								
24	14.076					13.044	- 7.3	2.66	-0.918				
27	16.771	15.104	- 9.9	2.336	-0.912					17.126	2.1	1.822	-0.464
28	18.163	17.463	- 3.9	5.156	0.951	16.814	- 7.4	1.81	0.734	18.199	- 5.3	0.726	0.976
29	19.402					19.656	1.3	-0.329	0.886				
30	20.066	20.922	4.3	1.680	0.990	21.419	6.7	0.827	-0.982				
33	23.506									21.121	-10.1	2.857	-0.955
35	25.017	23.617	- 5.6	2.603	0.894								
38	28.665	27.136	- 5.3	5.263	0.941					28.096	- 2.0	1.400	-0.691
41	32.893									31.245	- 5.0	1.497	0.992
49	39.236					37.021	- 5.2	1.00	0.991				
51	39.811	39.086	- 1.9	1.423	0.986								
52	39.906									37.955	- 2.4	-8.312	0.967
54	39.549									39.489	- 0.2	-0.696	0.116
56	40.399	39.396	- 2.5	1.104	0.718	41.141	1.9	1.92	0.842				
57	41.887					42.464	1.4	1.02	0.999				
60	42.656	42.761	0.2	2.795	-0.889					40.897	- 4.1	0.539	0.699
67	46.587	46.347	- 4.6	1.266	-0.957	46.601	- 4.1	1.39	-0.996	48.475	- 0.2	-1.401	0.990
71	49.568									50.571	0.01	0.348	-0.937
73	51.010					52.390	2.7	0.909	0.917				
76	54.736									52.857	- 3.4	1.838	0.900
83	58.906					59.204	0.5	1.48	0.963				
85	60.269	60.126	- 0.4	1.678	0.963					59.268	- 1.8	-0.896	-0.972
92	65.967	63.627	- 3.6	1.218	-0.465	64.769	- 1.8	0.478	-0.939				
93	66.209									64.901	- 2.0	1.682	-0.515
94	67.140	67.142	0.004	3.537	-0.941								
99	70.538	68.497	- 3.3	0.965	0.773	68.088		1.58	-0.928				
106	76.993					68.741	-12.0	6.662	0.996				

One point of interest is that the fundamental flexible mode (analytic mode 7), a solar array flapping mode, is consistently found to be about 10% lower in frequency that expected. This is likely to be due to various effects that were present during ground based testing. Several effects that were present during testing may have caused this frequency shift.

The solar array was hung on a bungee suspension system to simulate zero-g conditions. However, suspension effects were included analytically and do not appear to account for the shift.

Virtual air mass is significant and was included as a cylinder of air about the solar array chord. Tip effects could reduce the virtual air mass which would explain the higher orbital model frequency.

Also, as the ground test was performed at much higher amplitudes than are seen in orbit, clamps were used to preload the hinge joints to prevent gapping during the test. Therefore, structural nonlinearities could be present which could explain the frequency shift. This data is a confirmation of the importance of such effects in the testing of large space structures.

One of the primary goals of this analysis is to determine the structural damping in orbit. The damping values are critical in determining the magnitude of jitter displayed by the spacecraft, with lower damping leading to high jitter. As a worst case analysis, prelaunch jitter predictions assumed a damping value of 0.05% for all modes.

The smallest reasonable (i.e., non-negative) damping value extracted from the orbital data was found to be 0.215%. Additionally, as a general trend, low frequency modes (below 3 Hz) tended to have damping on the order of 0.5% while higher frequency modes tended to have damping on the order of 1 %. Thus it would appear that the prelaunch damping estimate was conservative by about an order of magnitude. This conclusion should be viewed with some caution as damping is the modal parameter least accurately characterized by the ITD algorithm. Additionally, the ITD generated damping values tend to be biased high. Allowing for this, a conservative estimate for orbital damping values is on the order of 0.2% for low frequency modes and 0.5% for high frequency modes. Thus, the prelaunch worst case analysis was adequate.

It should also be noted here that there is some evidence that the damping increases as response levels increase. In comparing Landsat-5 MSS and TM shutdown, both modes 7 and 11 show significantly higher damping levels for the TM case. These modes are the first and second solar array flapping modes. The only other mode for which a reasonable damping value was found for both events is mode 28. The MSS case damping is roughly twice that of the TM. However the MSS data shows a relatively poor mode shape match so the damping comparisons are questionable.

Also of interest is that the Landsat-4 MSS shutdown damping values are generally higher than the corresponding Landsat-5 values. This may be due to the fact that in the Landsat-4 data the TM had shutdown shortly before the MSS shutdown event. The effect of the TM may not have had time to die out. This would lead to higher response levels which may explain higher damping values.

Another major concern of this study was determining how consistent the resonant frequencies were between the two spacecraft. It was found that 90% of the modes occurring in the two MSS shutdown events were within 10% in frequency. Conversely, if Landsat-5 TM data is compared with either MSS case, only about 55% of the excited frequencies are within 10%. Thus it appears that the resonant frequencies are more dependent on forcing function than spacecraft and the two spacecraft are modally very similar.

The use of gyro data to determine low frequency data was very successful. Only one mode below 3 Hz was not excited in at least one of the events. That mode, number 13, is expected to occur at 2.869 Hz and is a Ku-band antenna elevation drive mode. Thus it is both well above the roll-off frequency of the filter used on the data and is a mode shape unlikely to be excited by the scanning mirrors' motion. Thus all the modes expected from the low frequency data were characterized.

There was one anomalous result from the gyro data. A response of approximately 0.2 Hz was found. While this response may be due to some onboard activity, no definite relation was found to any major satellite system. A more likely explanation is that this response represents a subharmonic of the fundamental solar array bending mode at approimately 0.39 Hz. The 0.2 Hz mode is similar in shape to the 0.39 Hz mode. Such responses sometimes occur in non-linear structures, though generally at much lower amplitudes than the primary response. The solar array may be considered nonlinear due to non-linear effects in its hinges. The ITD algorithm is more likely to pick up such harmonics in narrow bandwidth data including few modes, such as the gyro data.

CONCLUDING REMARKS

It was found that analytic predictions and measured data showed good correlation. As orbital data measurement was far from a controlled experiment

and instrumentation was very limited, this points out the power of the ITD algorithm. With further development, the ITD algorithm could become a very powerful tool for modal analyses.

The use of narrow bandwidth gyro data to determine low frequency modes was particularly successful. This points out the potential for using digital filtering of data to investigate narrow bandwidths of data instead of the entire frequency range at once. This should lead to improved results. Also of importance for future work is the development of software which more accurately predicts damping values. Current programs are biased toward predicting high damping values. Several developments currently underway in the industry should correct this problem.

REFERENCES

1. Ibrahim, S.R., "User's Manual for the Ibrahim Time Domain (ITD) Modal Vibration Identification Program," MASA Langley Research Center Contract NAS1-15281, May 1979.

2. Ibrahim, S.R. and Pappa, R.S., "Large Modal Survey Testing Using the Ibrahim Time Domain (ITD) Identification Technique," AIAA Paper No. 81-0528-CP, April 1981.

3. Kauffman, R.R., "Application of the Ibrahim Time Domain Algorithm to Spacecraft Transient Responses," 25th SDM Conference, May 1984.

4. Pappa, R.S. and Ibrahim, S.R., "A Parametric Study of the Ibrahim Time Domain Modal Identification Algorithm," The Shock and Vibration Bulletin, Part 3, pp 43 to 72, May 1981.

5. Pappa, R.S., "Some Statistical Performance Characteristics of the ITD Identification Algorithm," AIAA Paper No. 82-0768, May 1982.

6. Slafer, L.I., "In-Orbit Evaluation of the Control System/Structural Mode Interactions of the OSO-8 Spacecraft," Hughes Aircraft Company Report.

DISCUSSION

Voice: Did they actually try to correct any of the images?

Mr. Kauffman: They have to. That is standard procedure for the Thermatic Mapper because they cannot tell without correction exactly where it is pointed.

Voice: In what way would your analysis help them in that?

Mr. Kauffman: The major thing we did was to confirm that our pre-test analysis had been adequate, and also that it had been conservative. We assumed damping as low as .05% in our analysis. The jitter of the spacecraft is very sensitive to the damping. In this case we determined the damping was higher than the damping we assumed and that the analysis was adequate. They had already been able to determine that they were getting adequate correction from the image processing.

Mr. Huang (University of Wisconsin): In your conclusion did you mention that the Ibrahim Time Domain has a noise problem?

Mr. Kauffman: What we are saying is, at least from our analysis of the small model, if you start running up to 20%, 30% or 40% signal distortion, 30% noise or very high noise levels, it breaks down. In general you don't see that in our kind of application. So, it was not a problem for us.

Mr. Huang: Although we do not use Ibrahim's program, we developed our own program, we checked the simulation with a procedure similar to Ibrahim's, and it is very good. The noise is eliminated by expanding the system matrix.

Mr. Kauffman: What noise level did you go to?

Mr. Huang: We tried several levels.

Mr. Kauffman: Did you go as high as 10%?

Mr. Huang: We went higher than 10%. We tried our own, so we just wondered. We thought Ibrahim's method should be very good, too, because we were more or less influenced by his method.

THE IDENTIFICATION MATRIX AND CONVERGENCE OF PARAMETERS IN "OFF-LINE" SYSTEM IDENTIFICATION

Ken Tomita and Darrell A. Frohrib
Mechanical Engineering Department, University of Minnesota
111 Church Street S.E., Minneapolis, Minnesota 55455

The identification matrix characterizes the mathematical properties of a system's model in conjunction with an identification algorithm; uniqueness of obtained system parameters is guaranteed. The identification matrix is the second partial derivative of an error criterion with respect to system parameters. The matrix can be reformulated as part of the identification algorithm based on the least square identification concept. The identification matrix also relates least square identification to output distinction identifiability. Numerical examples of these roles of the identification matrix are presented.

NOMENCLATURE

A(p)	system matrix (function of parameters (p))
B(p)	excitation matrix
C(p)	measurement matrix
H	Hamiltonian
H_{rr}	second order partial derivative of Hamiltonian with respect to a vector (r)
I	unit matrix
J	integrated square error or performance index
N	N-th iteration stage
O_{xx}	observability Gramian (observability matrix) or second order partial derivative of the performance index (J) with respect to a state vector (x) at the zero slope point
O_{pp}	identifiability matrix or second order partial derivative of the performance index (J) with respect to parameters (p) at the zero slope point
Q	weighting matrix in the performance index (J) (positive definite symmetric)
T	transition matrix
T_{xx}	partitioned transition matrix
a	known coefficient in an example system
e	error
h	first order partial derivative of Hamiltonian
k	known coefficient in an example system
p	parameter vector
r	augmented state vector
s	known output from an actual system
t	time
t_o	initial time
t_1	final time
u	input vector
v	Lagrange multiplier or co-state vector for parameters (p) in an adjoint system
w	Lagrange multiplier or co-state vector for the state, x, in an adjoint system
x	state vector of a mathematical model
x_0	initial condition for x
y	output vector of a mathematical model
z	augmented perturbed error state vector
z_x	partitioned vector of z
superscript T	transpose
superscript *	true value
∂	partial derivative

INTRODUCTION

This paper discusses identifiability and convergence characteristics associated with a deterministic "off-line" identification method. Deterministic "off-line" identification refers to systems which are governed by a first order, linear, time invariant vector differential equation without stochastic noise. The "off-line" problem refers to treatment of data previously acquired in system test. System parameters are formulated as unknown but constant; coefficients of the system's vector differential equation are a function of system parameters. It is assumed that the system can be monitored during a time interval prior to identification; the identification problem becomes that of seeking "best fit" parameters from stored test data.

While identifiability generally establishes uniqueness of identified parameters, there are two different identifiability definitions associated with this formulation (4); one is

least square identifiability (2), and another is output-distinction identifiability (3,4). In least square identifiability, conceptually depicted in Figure 1, an optimization concept is involved to minimize square error between measured data from the actual system and the output of the corresponding system model. If the error has a local minimum for a set of identified parameters, the system is termed "locally identifiable" in a least square sense. Whereas least square identifiability involves test data, output-distinction identifiability, depicted in Figure 2, involves comparison of outputs of mathematical models for various model parameter settings.

In the work reported here (1), the identification algorithm based on the least-square identifiability concept (5,6,7) is expressed in a new form, which is convenient for engineering use in both characterizing system models from test data and validating the models themselves.

BACKGROUND

The identification algorithm derived from least square identifiability can be obtained by using the minimum principle (optimal control minimization technique) and the quasilinearization technique (5,6,7). This iterative algorithm contains a linear algebraic equation which determines uniqueness of the identified parameters. In this development (1), the matrix of the linear algebraic equation relates model initial conditions, model parameters, and adjoint system model response error. The matrix can be separated into two parts: a transition matrix and the so-called observability Gramian (8,10). Observability Gramian contains an observability matrix and an identifiability matrix. Earlier work in identification algorithms (5,6,7) has studied the parameter characterization (p) of linear time-invariant systems:

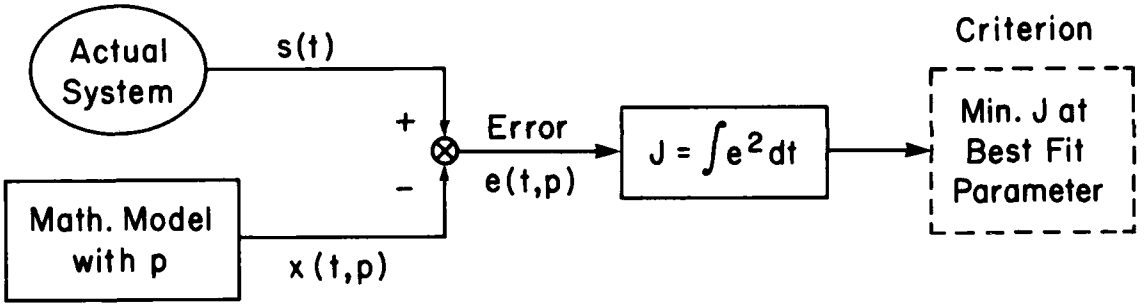

Figure 1: Least Square Identifiability

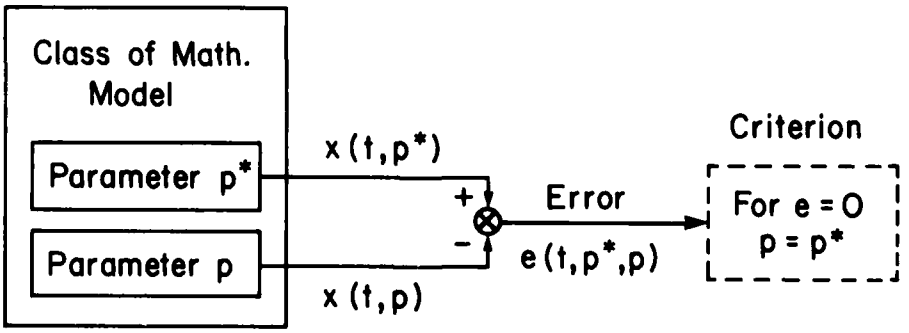

Figure 2: Output Distinction Identifiability

$$\dot{x}(t) = A(p)\,x(t) + B(p)\,u(t)$$

$$x(t_o) = x_o$$

$$y(t) = C(p)\,x(t) \qquad (1)$$

$$\dot{p}(t) = 0$$

$$p(t_o) = p$$

The error difference in the time responses of an actual system and its model equations (1) is called the performance index, J, and is expressed:

$$J = 1/2 \int_{t_o}^{t_1} (s(t) - x(t))^T Q\,(s(t) - x(t))\,dt \qquad (2)$$

In a least square sense, optimum parameters are those that produce a local minimum for J. According to the minimum principle (8,9), the necessary conditions for the extremum provide the following equations:

$$\dot{x} = \partial H/\partial w = A(p)x + B(p)u$$

$$(= Hw) \qquad (3\text{-}1)$$

$$\dot{p} = \partial H/\partial v = 0$$

$$(= Hv) \qquad (3\text{-}2)$$

$$\dot{w} = -\partial H/\partial x = -A^T(p) + C^T(p)\,Q(s - y) \qquad (= -Hx) \qquad (3\text{-}3)$$

$$\dot{v} = -\partial H/\partial p$$

$$(= -Hp) \qquad (3\text{-}4)$$

$$= \partial (x^T C^T(p) Q(s - y))/\partial p - \partial (x^T A^T(p) w)/\partial p - \partial (u^T B^T(p) w)/\partial p$$

$$H = 1/2\,(s - x)^T Q(s - x) + w^T (A(p)x + B(p)u) + v^T(0)$$

In Equations 3-1 through 3-4, vectors w and v become state vectors of an adjoint system for the model. Initial and final conditions on w and v are zero, whereas the model's initial and final conditions are unknown due to system test limitations.

Because of the two-point boundary condition regarding w and v and nonlinearity of the system, it is impossible to obtain solutions by straightforward integration. One way to solve this problem is quasilinearization where solution vectors at the N+1-th iteration stage are linearized around the N-th solution curves (7,8). These equations become time-varying linear with regard to the N-th iteration so that their solution curves can be expressed in terms of a transition matrix. By using this transition matrix, the final conditions can be related to the initial conditions: that is, the model's initial states and system's parameters. Hence, our two-point boundary problem is transformed into a conventional initial value problem. Moreover, linearization errors at each iteration are evaluated by means of simple integration, and these errors are passed to the next iteration stage.

As Equations 3-1 through 3-4 are linearized with respect to the vectors x, p, w, and v, and first order variations on these vectors are analyzed, it can be shown (7) that the transition matrix, $T(t,t_0)$ and the error vector, z(t), are governed by the following equations:

$$\dot{T}(t,t_0) = H_{rr}(t)\;T(t,t_0) \qquad (4)$$

$$\dot{z}(t) = H_{rr}(t)\;z(t) + h(t) - H_{rr}(t)\;r(t) \qquad (5)$$

where

$$T = \begin{bmatrix} T_{wx} & T_{wp} & 0 & 0 \\ 0 & I & 0 & 0 \\ T_{xx} & T_{xp} & T_{xw} & 0 \\ T_{px} & T_{pp} & T_{pw} & I \end{bmatrix}$$

$$H_{rr} = \begin{bmatrix} A(p) & H_{wp} & 0 & 0 \\ 0 & 0 & 0 & 0 \\ -C^T Q C & -H_{xp} & -A^T(p) & 0 \\ -H_{px} & -H_{pp} & -H_{pw} & 0 \end{bmatrix}$$

$$r = \begin{bmatrix} x \\ p \\ w \\ v \end{bmatrix} \quad h = \begin{bmatrix} H_w \\ 0 \\ -H_x \\ -H_p \end{bmatrix} \quad z = \begin{bmatrix} z_x \\ z_p \\ z_w \\ z_v \end{bmatrix}$$

All initial conditions are zero except $T(t_0,t_0)$, which is the identity matrix.

From the relation between the final conditions and the initial conditions, the linear algebraic equations are obtained, which iteratively provide the model's initial states, x_0, and the system parameters, p:

$$\begin{bmatrix} T_{xx}(t_1,t_0) & T_{xp}(t_1,t_0) \\ T_{px}(t_1,t_0) & T_{pp}(t_1,t_0) \end{bmatrix}^N \begin{bmatrix} x_0 \\ p \end{bmatrix}^{N+1}$$

$$= - \begin{bmatrix} z_w(t_1) \\ z_v(t_1) \end{bmatrix}^N \qquad (6)$$

The partitioned transition matrices and error vectors appearing in the above equation are computed based upon x_0 and p at the N-th iteration as indicated by the superscript N; improved x_0 and P for the N+1-th iteration are produced by solving Equation 6.

Based on zero derivatives of the performance index as depicted in Figure 3, the identifier (identification algorithm), Equations 4, 5, and 6, seeks the best-fit parameter by iteratively adjusting the system parameter. However, the zero derivatives may occur at a maximum value, at a saddle point value, or a minimum value. As a result, the identifier may not necessarily provide the best fit parameter, as shown in a numerical experiment later.

From the standpoint of uniqueness of the identified parameters, the algebraic equation, Equation 6, plays a crucial role: when the non-zero vectors z_w and z_v are given the necessary and sufficient conditions for existence and uniqueness of the identified parameters is non-singularity of the square matrix of Equation 6.

NEW FORM OF IDENTIFIABILITY

Based upon Equation 4, an analytical expression for the square matrix of Equation 6 indicates that it can be separated into two parts: the transition matrix and the Gramian (1):

$$\begin{bmatrix} T_{xx} & T_{xp} \\ T_{px} & T_{pp} \end{bmatrix}^N = - \underbrace{\begin{bmatrix} T_{xw} & 0 \\ T_{pw} & I \end{bmatrix}^N}_{\text{Transition}} \underbrace{\begin{bmatrix} O_{xx} & O_{xp} \\ O_{px} & O_{pp} \end{bmatrix}^N}_{\text{Gramian}} \qquad (7)$$

Matrix $O_{xx}(t_1,t_0)$ is an indication of the mathematical adequacy of a measurement system used in test (8,10). This observability Gramian is the second order partial derivative of the performance index with respect to the state initial condition x_0, (1):

$$O_{xx}(t_0,t_1) = \partial(\partial J/\partial x_0)/\partial x_0^T$$

$$\text{at } \partial J/\partial x_0 = 0$$

Matrix $O_{pp}(t_0, t_1)$, can be regarded as the identifiability matrix, which provides mathematical information about the uniqueness of the identified parameter p, and also verifies a local minimum (1):

$$O_{pp}(t_0,t_1) = \partial(\partial J/\partial p)/\partial p^T > 0$$

$$\text{at } \partial J/\partial p = 0$$

This demonstrates that the response error of a model in relationship to the actual system is minimized.

To illustrate the role of matrix O_{pp}, the following first order system is presented:

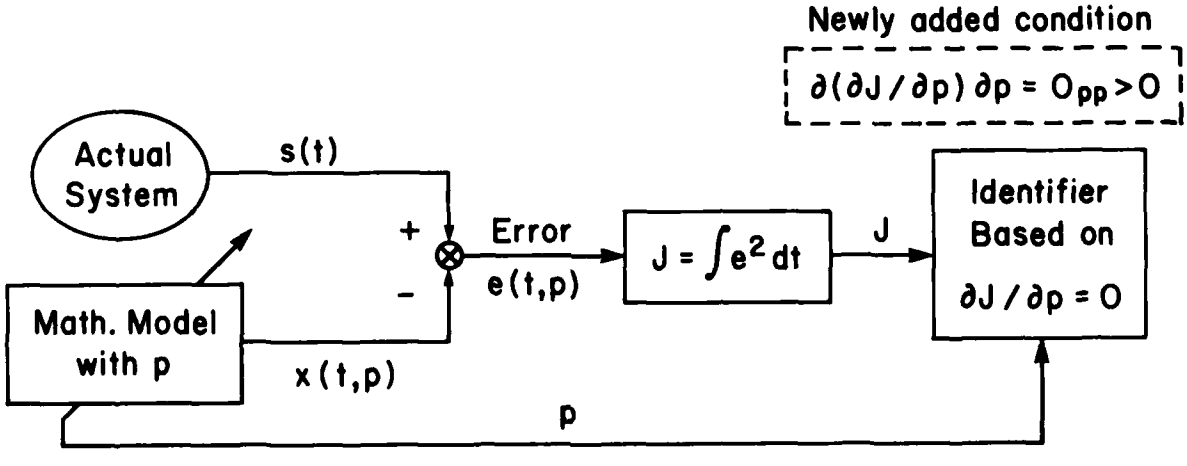

Figure 3: Standard Identification Algorithm

$$\dot{s}(t) = -k\,p^*\,(p^* - a)\,s(t)$$

and

$$\dot{x}(t) = -k\,p\,(p - a)\,x(t)$$

$$s(0) = s_0^*.$$

In this example, k and a are known coefficients: $k = -0.5$ and $a = 3$. If, for example, the true values of p^* and s_0^* are unity respectively, minima of performance index J would occur at $p = 1.0$ but also at 2.0 when $x_0 = 1.0$ (Figure 5). It is possible that the identification algorithm (Equations 4 - 6) would provide a solution ($p = 1.5$ and $x_0 = 1.058$). There, the performance index is also a local maximum in terms of p, and a local minimum with respect to x_0 (a saddle point).

At all of the above points, the first derivatives, $\partial J/\partial p$, are zero; O_{pp} is positive (indicating a minimum) at ($p = 1.0$, $x_0 = 1.0$) and ($p = 2.0$, $x_0 = 1.0$). At the saddle point, ($p = 1.5$, $x_0 = 1.058$), which is not a minimum, O_{pp} assumes a negative value, which indicates that this point represents a minimum with respect to x_0, but a maximum with respect to p.

The standard identification algorithm of (Equation 4-6) provides three points which are potential solutions; the value of separating out the identification matrix, O_{pp} is that the correct solutions of this potential set of three points can be clarified (Figure 3). This is true because O_{pp} provides curvature information identifying true minima (Figure 5). Computational results are shown in Tables 1 through 3.

Whereas the identification matrix, O_{pp}, is employed as a verification tool for validity of obtained solutions during identification processes, there is another way of using O_{pp}; that is, verification of a mathematical model's identifiability. This can be done with a slight modification in Figure 1, such as replacement of s(t) by the same mathematical model with different parameters.

Output distinction identifiability, conceptually depicted in Figure 2, can be interpreted in terms of least square identifiability, Figure 1, as $J = 0$ because $x(t,p^*) = x(t,p)$ when $p = p^*$. Uniqueness of $p = p^*$ can also be interpreted as $\partial J/\partial p = 0$ and its positive curvature indicator, $\partial(\partial J/\partial p)/\partial p$, since a value of J at $p = p^*$ need be a minimum. As illustrated in Figure 4, comparison of outputs of a model's various parameters can be made. By utilizing the identification algorithm derived from the least-square identifiability concept, verificiation of a mathematical model's identifiability can be performed numerically. For this purpose, a mathematical assumption is necessary; that is, that the iterative algorithm, Equations 4, 5, and 6, gives converged solutions, and subsequently that w(t) and v(t) are zero (precise arguments are presented in (1)).

For illustrative purposes, identifiability of the previous mathematical model at the point ($p = 1.5$, $x_0 = 1.0$) is examined. Evaluation of O_{pp} at ($p = 1.5$, $x_0 = 1.0$) gives $O_{pp} = 0$; contour levels of O_{pp}, that of the performance index, J, and $\partial J/\partial p$ are shown in Figures 6, 7, and 8, respectively. As seen in the figures, $J = 0$ and $\partial J/\partial p = 0$ at ($p = 1.5$, $x_0 = 1.0$).

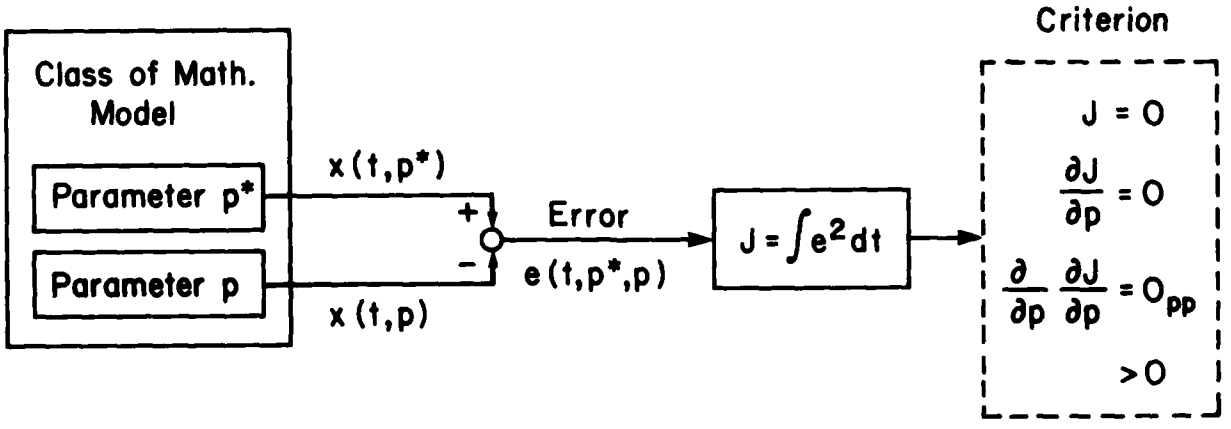

Figure 4: Combined Identifiability

However, because of $O_{pp} = 0$, one of the identifiability requirements is violated. This indicates that if the parameter of the actual system happens to take $p^* = 1.5$, by implementing the mathematical model into the standard identification algorithm a nontrival solution during identification processes cannot be obtained. A suggested alternative way is to modify either the mathematical model or the identification algorithm employing a second variation effect, or both, if the actual parameters occurs at $p^* = 1.5$.

This new identifiability matrix is a substantial asset in characterizing systems in relation to test and modeling strategies. Its complete development is available in (1).

ACKNOWLEDGEMENTS

This project was partially supported by the University of Minnesota Computer Center.

REFERENCES

1. Tomita, K., Ph.D. Dissertation, Department of Mechanical Engineering, University of Minnesota, to appear.
2. Bellman, R. and K. J. Aström, "On Structural Identifiability," Mathematical Biosciences, Vol. 7, pp. 329-339, 1970.
3. Grewal, M. S. and K. Glover, "Identifiability of Linear and Nonlinear Dynamical Systems," IEEE Transactions on Automatic Control, Vol. AC-21, pp. 833-837, December, 1976.
4. Vajda, S., "Further Comments on DiStefana and Cobelli's Paper," IEEE Transactions on Automatic Control, Vol. AC-27, pp. 1136, October 1982.
5. Kumar, K. S. P. and R. Sridhar, "On the Identification of Control Systems by the Quasi-Linearization Method," IEEE Transactions on Automatic Control, Vol. AC-9, pp. 151-154, 1964.
6. Bellman, Rr., H. Kagiwada, and R. Kalaba, "Quasilinearization System Identification and Prediction," International Journal of Engineering Sciences, Vol. 3, pp. 327-334, 1965.
7. Sage, A. P. and J. L. Melsa, System Identification, Academic Press, 1971.
8. Lee, E. B. and L. Markuks, Foundations of Optimal Control Theory, John Wiley and Sons, Inc., 1967.
9. Sage, A. P. and C. C. White, Optimum Systems Control, second edition, Prentice Hall, 1977.
10. Brockett, R. W., Finite Dimensional Linear Systems, John Wiley and Sons, Inc., 1970.

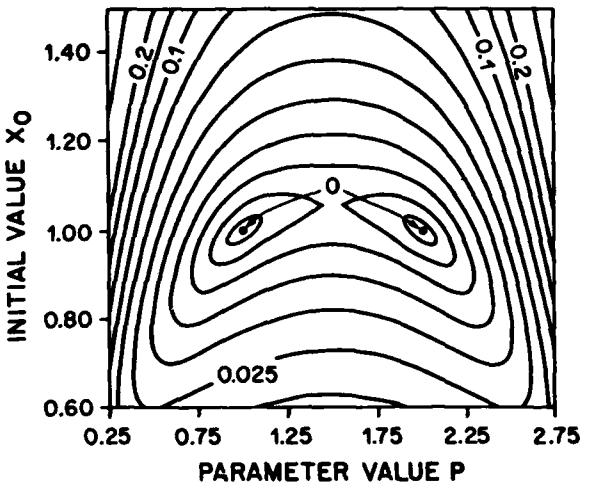

Figure 5: Error Level Contours

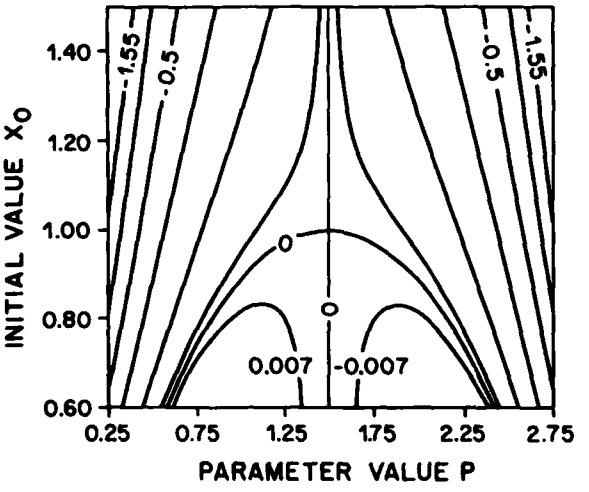

Figure 7: Contours of Error Derivatives

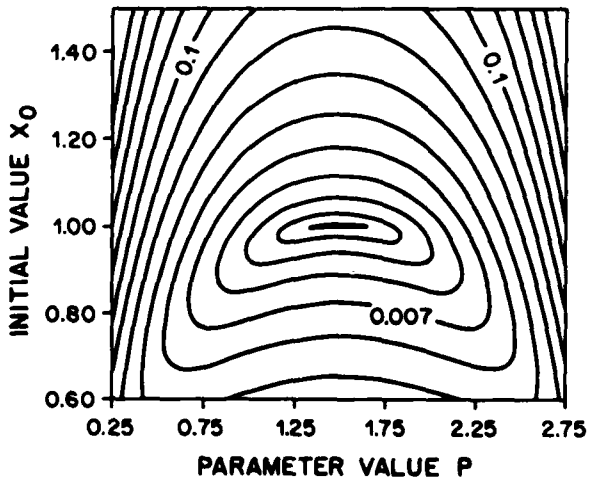

Figure 6: Error Level Contours

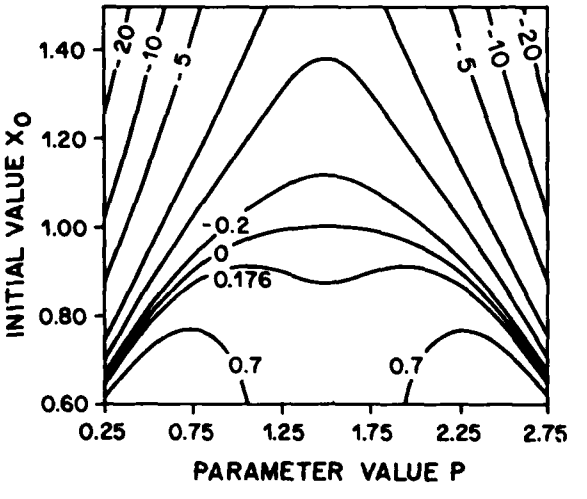

Figure 8: 0_{pp} Level Contours

Table 1

ITRTN	PARAMETER	INITIAL C.	ERROR	DJ/DPI	DJ/DXOI
0	.80000E+00	.6535[illegible]E+00	.23702E-01	.3295[illegible]E-01	-.16059E+00
1	.96737E+00	.10974E+01	.26674E-02	-.1719[illegible]E-01	.53824E-01
2	.93043E+00	.98839E+00	.80012E-04	-.3277[illegible]E-02	.28576E-02
3	.10281E+01	.10086E+01	.12100E-04	.5570[illegible]E-03	.92521E-03
4	.98731E+00	.99740E+00	.26342E-05	-.4[illegible]C1E-03	.30910E-03
5	.10002E+01	.10001E+01	.11490E-08	.17[illegible]94E-05	.20019E-04
6	.10000E+01	.10000E+01	.17579E-13	-.3[illegible]E-07	.14340E-07

	CXX	CXP	CPX	CPP
0	.567[illegible]E+00	-.54584E+00	-.54584E+00	.12503E+01
1	.50837E+00	-.51653E-01	-.51653E-01	-.37380E+00
2	.51727E+00	-.14547E+00	-.14547E+00	.67906E-01
3	.49312E+00	-.11320E+00	-.11320E+00	.44864E-01
4	.50[illegible]E+00	-.12[illegible]4E+00	-.12894E+00	.64557E-01
5	.49[illegible]E+00	-.12451E+00	-.12451E+00	.61410E-01
6	.49963E+00	-.12462E+00	-.12462E+00	.61641E-01

Table 2

ITRTN	PARAMETER	INITIAL C.	ERROR	DJ/DPI	DJ/DXOI
0	.13064E+01	.12571E+01	.10284E-01	-.76643E-02	.93429E-01
1	.12837E+01	.10512E+01	.57690E-03	.22040E-02	.13299E-02
2	.14733E+01	.10064E+01	.86100E-03	.30110E-03	.34974E-02
3	.14863E+01	.10587E+01	.85061E-03	.17617E-03	.12864E-01
4	.15000E+01	.10588E+01	.85182E-03	.44779E-06	.18389E-01
5	.15000E+01	.10587E+01	.85182E-03	.24162E-08	.11799E-04
6	.15000E+01	.10587E+01	.85182E-03	.84051E-16	.34706E-14

	CXX	CXP	CPX	CPP
0	.45191E+00	.16006E-01	.16606E-01	-.48890E+00
1	.45381E+00	-.43515E-01	-.43515E-01	-.81282E-02
2	.44453E+00	-.49677E-02	-.49677E-02	-.26107E-01
3	.44443E+00	-.26970E-02	-.26970E-02	-.12872E-01
4	.44439E+00	-.68505E-05	-.68505E-05	-.12933E-01
5	.44439E+00	-.36953E-07	-.36953E-07	-.12863E-01
6	.44439E+00	-.12854E-14	-.12854E-14	-.12863E-01

Table 3

ITRTN	PARAMETER	INITIAL C.	ERROR	DJ/DPI	DJ/DX01
0	.11000E+01	.[illegible]2[illegible]79E+00	.92[illegible]7E-02	.16[illegible]0E-01	-.93357E-01
1	.11594E+01	.10[illegible]70E+01	.[illegible]1522E-03	.13[illegible]9E-02	.71195E-02
2	.12537E+01	.10[illegible]30E+01	.4512[illegible]E-03	.25[illegible]4E-02	.98260E-04
3	.19908E+01	.11309E+01	.43[illegible]8E-02	.1794[illegible]E-01	.06902E-01
4	.20223E+01	.10006E+01	.18051E-04	.1608[illegible]4E-02	.32765E-02
5	.19[illegible]0E+01	.10[illegible]8[illegible]E+01	.15342E-04	-.[illegible]058[illegible]7E-03	.19511E-03
6	.20067E+01	.[illegible]90[illegible]8[illegible]E+00	.76761E-06	.27453E-03	.25001E-03
7	.19[illegible]8E+01	.10001E+01	.58529E-09	-.46469E-05	.48563E-05
8	.20000E+01	.10000E+01	.16[illegible]9E-14	.11[illegible]6E-07	.71155E-06
9	.20000E+01	.10000E+01	.50[illegible]2E-27	.40[illegible]3E-13	.13210E-13

	DYX	DYP	DPX	DPP
0	.47[illegible]3E+00	-.20506E+00	-.20506E+00	.48217E+00
1	.46[illegible]4E+00	-.67059E-01	-.67059E-01	-.23110E-01
2	.45[illegible]4E+00	-.55[illegible]4E-01	-.55044E-01	.33951E-02
3	.49757E+00	.23822E-01	.23822E-01	-.46773E+00
4	.50[illegible]5E+00	.12603E+00	.12603E+00	.46511E-01
5	.49[illegible]1E+00	.11255E+00	.11255E+00	.48166E-01
6	.50[illegible]5E+00	.12[illegible]7E+00	.12077E+00	.62545E-01
7	.49978E+00	.12454E+00	.12454E+00	.61530E-01
8	.49983E+00	.12462E+00	.12462E+00	.61640E-01
9	.49983E+00	.12462E+00	.12462E+00	.61640E-01

MODEL EVALUATION OF SPINAL INJURY LIKELIHOOD FOR VARIOUS EJECTION SYSTEM PARAMETER VARIATIONS

Eberhardt Privitzer
Air Force Aerospace Medical Research Laboratory
Wright-Patterson Air Force Base, Ohio

The Air Force Aerospace Medical Research Laboratory's (AFAMRL) Head-Spine Model (HSM), a discrete element model of the human head-spine structure, is described. This model was developed to provide a mathematical means for the investigation of three-dimensional head-spine structure dynamic response and injury likelihood in impact environments and to serve as a design tool for the evaluation of crewmember-ejection system impact interactions. Results are presented from a study which involved the use of the HSM to evaluate the effects of variations in certain ejection system parameters on head-spine structure ejection response and injury likelihood.

INTRODUCTION

Human impact acceleration tolerance considerations used in current ejection system design practices are limited primarily to system acceleration components paralleling the spinal axis (i.e., $+G_z$ components). The Dynamic Response Index (DRI) Model [1, 2], which is based on a single degree of freedom, mass-spring-dashpot representation of the head, upper torso and lower spine, is the design guide currently used to evaluate ejection system catapult accelerations for military aircraft. It has been extensively correlated with ejection injury data and thus provides a useful criterion for evaluating the lower spine injury probabilities which might be associated with proposed ejection system acceleration profiles. The one-dimensional nature of the DRI and similar models [3, 4], however, limits their applicability to events in which the nonaxial components of the spinal response are negligible.

Increased performance capabilities and operational requirements of recently developed and proposed military aircraft have necessitated considerable expansion of the safe ejection envelope. The accomplishment of this requires the development of a much more comprehensive, three-dimensional, functional description of human ejection tolerance which can address not only ejection system performance parameters (acceleration profile) but additional system parameters governed by, e.g., restraint system configuration, cockpit/seat geometry and mission requirements also.

The Air Force Aerospace Medical Research Laboratory (AFAMRL) is currently developing six-degree-of-freedom acceleration tolerance criteria which bound seat translational and rotational acceleration levels [5]. These criteria, which are based on data from ejection and impact test experience, are required for the digital flight controller which will "fly" the next generation ejection seat. This system is being developed by the Aerospace Medical Division's Crew Escape Technology (CREST) Office also located at AFAMRL [6, 7]. These six-degree-of-freedom acceleration tolerance criteria, although much needed, still do not directly address other system variables affecting human acceleration tolerance such as restraint system configuration, cockpit/seat geometry and head/helmet encumbering devices or protective clothing which may be associated with mission requirements. Some of these variables, particularly restraint system configurations, have been investigated experimentally using human volunteers. These experimental studies, however, are restricted to noninjurious acceleration exposures and affect ejection system designs as, primarily, retrofit concepts (e.g., [8]).

The three-dimensional description of human acceleration tolerance referred to above, is not attainable through any single avenue of approach. Such a description, because of the complexity and severity of ejection-system-crewmember interactions, must be implemented analytically and yet must evolve through extensive experimental and ejection experience considerations. This paper discusses the use of a three-dimensional mathematical model of the human head-spine structure to provide a description of the effects of variations in

several ejection system parameters on head-spine ejection-induced dynamic response and spinal injury likelihood. This study, which was requested by the CREST Office, was specifically concerned with the effects of varying the head-pad location relative to the plane of the seatback and the catapult acceleration vector angle and magnitude. A general description will first be provided for the AFAMRL Head-Spine Model (HSM) followed by the specific approach and results for this study.

DESCRIPTION OF THE MATHEMATICAL MODEL

The HSM is a three-dimensional mathematical model describing the mechanical behavior, in terms of system kinematics and internal loads, of the human head-spine-torso structure. Its fully three-dimensional formulation is just one of the features which signigicantly distinguishes it from earlier such models. The HSM consists of two distinct components: a computer program, SAM (Structural Analysis of Man), which is actually a general purpose program for the dynamic analysis of three-dimensional structures; and a data base containing inertial, material, geometric and connectivity data describing the head-spine-torso structure as well as other data items, descriptive of the specific problem and output to be generated, required by SAM. The HSM has been described previously in [9-13], hence, only a brief description will be given here.

In the head-spine-torso structure, the spinal elements, consisting of the seven cervical (C1-C7), twelve thoracic (T1-T12) and five lumbar (L1-L5) vertebrae plus associated intervertebral discs and, to a lesser degree, articular processes, constitute the primary structural member for transmission of vertical loads. At AFAMRL, we are particularly concerned with dynamic compressive and bending loads experienced by the spine during the ejection event. A secondary loading path provides for the transmission of viscera-abdominal wall system pressures through the diaphragm to the rib-cage-lung system and then to the spine through the costo-vertebral and costo-transverse joints [9, 12 and 14].

The development of the HSM required the formulation of descriptions of local and global spinal geometries, head and torso inertial distributions, the material behavior of the primary spinal connective tissues and a measure of spinal injury.

Geometry

Describing the local spinal geometries amounts to the defining of the geometries of the individual vertebrae. This is accomplished by specifying the global, X_k, $k = 1,2,3$, coordinates (a right-handed Cartesian system fixed in space) of a number of points, called secondary nodes, which serve as the "attachment points" of deformable elements and correspond to the centroids of the attachments of the connective tissues - the intervertebral discs, articular facets and the spinal ligaments. Each vertebra is contained in a rigid body representing the inertial characteristics of a segment or a portion of a segment of the torso. A segment of the torso, corresponding to a specific vertebral level, is defined as the material bounded by parallel planes, perpendicular to the vertical (Z or X_3) axis and passing through the centers of the inferior and superior intervertebral discs, and by the torso wall.

The initial overall static spinal configuration is a function of the position of the body (i.e., standing, sitting, etc.), the geometry and material properties of external interaction surfaces (e.g., an ejection seat back and seat pan) and a number of physiological variables. Fig. 1 shows frontal (X_2X_3 or YZ) and sagittal (X_1X_3 or XZ) plane views of the HSM. Depicted are only those components of the model whose local geometries do not change. None of the deformable elements representing the various spinal connective tissues are shown. The overall spinal geometry approximates that of a 50th percentile representative of the male Air Force flying population seated upright in a generic ejection seat (i.e., with the seatback parallel to the Z axis).

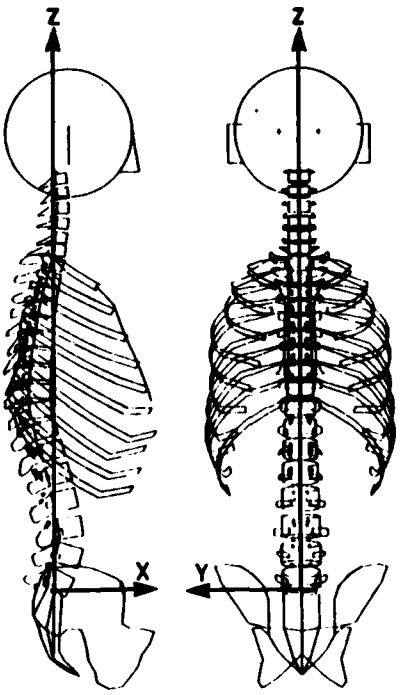

Fig. 1 - AFAMRL Head-Spine Model (HSM) sagittal (X_1X_3 or XZ) and frontal (X_2X_3 or YZ) plane views

Inertial Distribution

The inertial description of the torso consists of the specification, for each torso segment, of the global coordinates of the center of mass (called a primary node in the model); a "body" coordinate system, $\bar{X}_k$, a right-handed Cartesian system fixed on the body and with unit vectors $\vec{b}_k$, k = 1,2,3, coincident with the principal axes of inertia; the translational mass and the three principal moments of inertia, $\vec{I}_k$. The inertial properties of the torso segments were based directly on the work of Liu and Wickstrom [15]. The global components of the $\vec{b}_k$ (direction cosines between the $\bar{X}_k$ and X_k axes) arranged in the matrix

$$[\lambda]_I = [\vec{b}_1, \vec{b}_2, \vec{b}_3]_I = \begin{bmatrix} b_{11} & b_{21} & b_{31} \\ b_{12} & b_{22} & b_{32} \\ b_{13} & b_{23} & b_{33} \end{bmatrix}_I \qquad (1)$$

define the transformations,

$$\{A\} = [\lambda]_I\{\bar{A}\} \text{ and } \{\bar{A}\} = [\lambda]_I^T\{A\} \qquad (2)$$

for any vector, $\vec{A}$, with body and global components $\bar{A}_k$ and A_k, respectively. Since the X_k are fixed in space and the $(\bar{X}_k)_I$ are fixed on rigid body, I, the updated components of the $(\vec{b}_k)_I$ or, equivalently, $[\lambda]_I$, define the orientation of body I with respect to the global axes [9].

The inertial descriptions of the head plus helmet and encumbrances, the pelvis and any other rigid bodies are defined similarly. Note that the term "rigid bodies" is used only to indicate that their inertial properties remain constant relative to their body coordinate systems, and that distances between a segment's primary node and secondary nodes (sometimes called rigid links) remain constant.

Deformable Elements

The torso segments interact through deformable elements (springs, beams, pressure-volume and special-purpose elements described in detail in [9 and 12]) which represent the various connective tissues: the intervertebral discs, spinal ligaments and articular facets; the primary musculature of the cervical spine; the elastic properties of the viscera-abdominal wall system; the costo-vertebral, costo-transverse and costo-sternal joints and the intercondral cartilage and intercostal tissues of the rib cage [see also 14 and 17].

A local, or element, coordinate system, $\hat{X}_k$, a right-handed Cartesian system with unit vectors $\vec{e}_k$, k = 1,2,3, described as a rigid-convected or corotational coordinate system by Belytschko and Hsieh [16], is defined for each element. In the case of a three-dimensional beam element with nodes I and J, for example, the element coordinate system, $\vec{e}_k$, is as follows: the origin is at node I; $\vec{e}_1$ is directed from I to J; the direction of $\vec{e}_2$ is determined from the average of the node I and J rotations about $\hat{x}_1$; $\vec{e}_3$ is obtained from the vector product of $\vec{e}_1$ and $\vec{e}_2$. The global components of the $\vec{e}_k$ (direction cosines between the $\hat{x}_k$ and X_k axes) arranged in the matrix

$$[\mu]_E = [\vec{e}_1, \vec{e}_2, \vec{e}_3]_E = \begin{bmatrix} e_{11} & e_{21} & e_{31} \\ e_{12} & e_{22} & e_{32} \\ e_{13} & e_{23} & e_{33} \end{bmatrix}_E \qquad (3)$$

define the transformations

$$\{A\} = [\mu]_E\{\hat{A}\} \text{ and } \{\hat{A}\} = [\mu]_E^T\{A\} \qquad (4)$$

for any vector $\vec{A}$ with element and global components $\hat{A}_k$ and A_k respectively.

Transformations from element to body coordinate systems and vice versa are given by

$$\{\bar{A}\} = [\lambda]_I^T[\mu]_E\{\hat{A}\} \text{ and } \{\hat{A}\} = [\mu]_E^T\,[\lambda]_I\{\bar{A}\} \qquad (5)$$

respectively. In this example, the mass center of rigid body I would be a primary node associated with element E.

All element deformation quantities, $\{\hat{d}\}$, are defined with respect to the element coordinate systems thus eliminating all rigid body motion contributions. Element nodal force computations are based on small strain theory and, for the beam element, require that local nodal rotations be sufficiently small such that their decomposition into vectorial components remains valid [9]. Note, however, that overall displacements and rotations of the deformable elements can be arbitrarily large. Element nodal force (and moment) components are normally computed from equilibrium equations of the form

$$\hat{f}_i = k_{ij}\,\hat{d}_j + c_{ij}\,\dot{\hat{d}}_j \,. \qquad (6)$$

Material nonlinearities are generally introduced by defining the stiffness coeficients, k_{ij}, to be quadratic functions of deformation of the form

$$k_{ij} = k_1 + k_2\,\delta^2, \qquad (7)$$

where k_1 and k_2 are linear and cubic stiffness coefficients respectively and δ is a deformation quantity. The damping coefficients are defined as either

$$c_{ij} = 2\xi\sqrt{Mk_{ij}}\,, \qquad (8)$$

where ξ = specified fraction of critical damping,
$M = (m_I + m_J)/2$

and m_I and m_J are nodal translational or rotational masses; or

$$c_{ij} = \alpha k_{ij} , \qquad (9)$$

where α = stiffness proportional damping parameter, $= 2\xi/\beta$

and β = specified system natural circular frequency to be damped by an amount defined by ξ.

The most recent version of SAM also includes an exponential force-deformation relationship and a three-parameter viscoelastic stress-strain law which are used to represent the material behavior of the ligaments and muscle elements, respectively, in a recently developed, highly detailed three-dimensional model of the head-cervical spine structure (HCSM) [17, 18]. The experimental and analytical bases for the selection of the material properties for the HSM deformable elements are described in [9, 12, 19, 20 and 21].

External Environment

The mechanical environment external to the HSM can be defined in terms of elastic planes, spring elements, special-purpose restraint system-torso interaction algorithms and the specification of forces on and/or accelerations of model primary nodes.

An ejection seat is defined by a system of elastic planes. Interactions between the HSM and a plane are defined by relationships similar to those expressed in Eqs. (6) through (9), with $\hat{d}_j$ and δ in (6) and (7) both representing the relative normal displacement of a rigid body with respect to the plane and $\dot{\hat{d}}_j$ in (6) representing the relative normal velocity. A force is applied to the primary node only if

$$\hat{d}_j < 0 \text{ and } \dot{\hat{d}}_j \leq 0,$$

i.e., the rigid body has penetrated the plane and is either moving into or is stationary relative to the plane. The motion of a plane is defined by specifying its acceleration profile (which is internally integrated twice to provide displacements) and the direction cosines between the plane's acceleration vector and the global axes.

A restraint system between the ejection seat and the HSM is approximated in either of two ways. The first, which is used most often, consists of using spring elements between the elastic planes and appropriate primary nodes in the HSM. Rather than being directly attached to and moving with a plane, the motion of the attachment point of a restraint system spring element is prescribed such that the resultant force (nonzero only in tension) is always normal to the plane. This approach to restraint system modeling has been used with reasonable success in a number of applications (see, e.g., [22]) including the effort described in this paper.

The second approach involves the specification of a restraint system force time history; the conversion of this into contact forces acting on rigid bodies approximating the geometry and inertial characteristics of the shoulders; and the transmission of these contact forces into resultant forces and moments acting at the T1, T2 and T3 torso segment primary nodes through beam elements approximating the deformation characteristics between the shoulders and the remainder of the upper torso [11]. This approach, which accounts for loss of contact but neglects friction between the restraint system components and the torso, has been applied to the study of head-spine system response to crewmember retraction [23, 24].

Numerical Integration of Equations of Motion

SAM uses an explicit numerical integration scheme to solve for HSM kinematics. The approach requires no matrix inversions since all element nodal loads are computed at the element level, i.e., with respect to the element coordinate systems, $\hat{x}_k$. After the element by element computations have determined the element nodal loads, these are transformed and assembled into an internal nodal force array, F^{int} (defined in the X_k coordinates) and an internal nodal moment array, $\bar{M}^{int}$ (the components of which are defined in the various $\bar{X}_k$ coordinate systems).

Global translational accelerations at time step j+1 are then obtained by the direct solution of Newton's Second Law for each translational degree of freedom, i.e.,

$$\ddot{u}_{iI}^{j+1} = (F_{iI}^{ext} - F_{iI}^{int})/m_I \qquad (10)$$

where i corresponds to the X_i degree of freedom for primary node I, m_I is the translational mass associated with node I, and

F_{iI}^{ext} = global components of the prescribed external force array.

The angular accelerations are obtained from the Euler equations of motion written in the body coordinates. Since these are coincident with the principal axes of inertia, all products of inertia are zero and the angular accelerations at time step j+1 are given by

$$\begin{aligned}
\bar{\alpha}_x^{j+1} &= [\bar{M}_x^{ext} - \bar{M}_x^{int} - (\bar{I}_z - \bar{I}_y)\,\bar{\omega}_y\bar{\omega}_z]/\bar{I}_x \\
\bar{\alpha}_y^{j+1} &= [\bar{M}_y^{ext} - \bar{M}_y^{int} - (\bar{I}_x - \bar{I}_z)\,\bar{\omega}_x\bar{\omega}_z]/\bar{I}_y \qquad (11) \\
\bar{\alpha}_z^{j+1} &= [\bar{M}_z^{ext} - \bar{M}_z^{int} - (\bar{I}_y - \bar{I}_x)\,\bar{\omega}_x\bar{\omega}_y]/\bar{I}_z
\end{aligned}$$

where an additional subscript, say J, identifying the primary node has been omitted for convenience:

X, Y and Z refer to body coordinates $\bar{X}_k$ for body (primary node) J; $\bar{\omega}_x$, $\bar{\omega}_y$ and $\bar{\omega}_z$ are the angular velocities in $\bar{X}_k$ components computed during time step j; $\bar{I}_x$, $\bar{I}_y$ and $\bar{I}_z$ are the principal moments of inertia with respect to the $\bar{X}_k$ system; and

$\bar{M}_k^{ext}$ and $\bar{M}_k^{int}$ = external and internal

moments about the origin of the $\bar{X}_k$ system for body J.

Once the accelerations have been determined, the velocities (translational and angular) are updated using an equation based on a central-difference expression for the acceleration at the midpoint of the integration interval, i.e.,

$$\dot{u}_{iI}^{j+1} = \dot{u}_{iI}^{j} + \frac{\Delta t}{2}\left(\ddot{u}_{iI}^{j+1} + \ddot{u}_{iI}^{j}\right)$$

and (12)

$$\bar{\omega}_{iI}^{j+1} = \bar{\omega}_{iI}^{j} + \frac{\Delta t}{2}\left(\bar{\alpha}_{iI}^{j+1} + \bar{\alpha}_{iI}^{j}\right)$$

where Δt = integration time step.

Displacements are updated using a three-term (i.e. up to and including the second derivative) Taylor's Series expansion on the previous time step displacements, i.e.,

$$u_{iI}^{j+1} = u_{iI}^{j} + \Delta t\, \dot{u}_{iI}^{j} + \frac{\Delta t^2}{2}\ddot{u}_{iI}^{j} \cdot \qquad (13)$$

Updating the orientation of, for example, rigid body I requires that the global components (i.e., direction cosines) of its unit vectors, $\vec{b}_k$, be updated. The formulation for this process begins with a three-term Taylor's Series expansion on the $\vec{b}_k^{\,j}$ similar to Eq. (13) and proceeds with the substitutions of vector products, involving angular accelerations and velocities and the $\vec{b}_k^{\,j}$, for the time derivatives of the unit vectors. This formulation is discussed in detail by Belytschko et al. in [9].

Unlike an implicit numerical integration scheme which has, essentially, unrestricted numerical stability (albeit at the potentially large expense of matrix inversion and iteration requirements), an explicit scheme such as outlined above requires the selection of an integration step which will insure a stable solution [25]. The stability limit, Δt_s, or maximum allowable integration time step, for SAM is determined by selecting the element in the model having the highest natural frequency and equating the solution propagation speed, V_s, and the wave speed, c, for this element. This results in

$$\Delta t_s = \frac{2}{\beta}, \qquad (14)$$

where $\beta = 2\pi/T$ is the natural circular frequency for free vibration of the element and T the natural period. Hence,

$$\Delta t_s = \frac{T}{\pi} \cdot \qquad (15)$$

In practice, the actual integration time step used is less than Δt_s.

Spinal Injury Prediction

The HSM has a spinal injury prediction capability called SIF (Spinal Injury Function) which addresses the predominant spinal injury mode associated with aircrewmember ejection; vertebral body compressive fracture resulting from combined axial compression and bending loads. The SIF provides an indication of the likelihood of vertebral body compressive yielding associated with axial compression and bending (anterior-posterior (AP) or lateral (L)) loads computed at each vertebral level of the thoracolumbar (TL) spine during a simulation. It is computed from

$$SIF_v = \left\{ \left|\frac{P}{P_y}\right| + \max\left[\left|\frac{M_{AP}}{M_{AP}^*}\right|_y , \left|\frac{M_L}{M_L^*}\right|_y \right] \right\}_v^{max} \qquad (16)$$

where V = vertebral level; P, M_{AP} and M_L = computed instantaneous equilibrium values of the compressive load and the local AP and lateral bending moments, respectively; and P_y, $M_{AP_y}^*$ and $M_{L_y}^*$ are the corresponding yield values.

The P_y are based on axial compression load-deformation data (to failure) obtained by [26] (as reported by [27]) and [28]. No corresponding data for AP and L bending were found. $M_{AP_y}^*$ and $M_{L_y}^*$ were, therefore, generated by treating each vertebral body as an elliptical cylinder with midheight major and minor radii, a and b and the assumption of a homogeneous distribution of material with mechanical properties intermediate to those of the vertebral body core (trabecular bone) and shell (cortical bone). The effective yield stress for this material is then given by

$$\sigma_y^* = \frac{P_y}{A} \qquad (17)$$

where A = midheight cross-sectional area = πab. Using the flexure formula from strength of materials, the bending moment which produces a stress σ_y^*, in the extreme fibers at the midheight of such an elliptical vertebral body can be related to P_y by

$$M_{AP_y}^* = \frac{I_{AP}}{bA} P_y \text{ and } M_{L_y}^* = \frac{I_L}{aA} P_y \qquad (18)$$

for AP and lateral bending, respectively. In equation (18) I_{AP} and I_L are the second moments of A about the major, 2a, and minor, 2b, diameters, respectively, Since

$$I_{AP} = \frac{b^2}{4}A \text{ and } I_L = \frac{a^2}{4}A, \qquad (19)$$

Eqs (18) take on the rather simple form,

$$M^*_{AP_y} = \frac{b}{4} P_y \quad \text{and} \quad M^*_{L_y} = \frac{a}{4} P_y \qquad (20)$$

where a and b are based on [28, 29].

The SIF, as given by Eq. (16), represents a ratio of computed quantities to specified yield quantities. A value of SIF=1 at any vertebral level, V, is therefore taken to correspond to a 50% likelihood of compressive yielding due to combined axial compression and bending at that level. The likelihoods or probabilities associated with values of SIF $\neq$ 1 are obviously dependent upon the chosen distribution function. For example, Payne [27] reports probability distribution functions, for vertebral compressive failing loads normalized to L5, based on both Normal and Gamma probability densities. Applying his Normal distribution function to the SIF we find, for example, that SIF values of 0.9 and 1.1 would correspond to 16% and 84% probabilities, respectively, while 10% and 90% probabilities would correspond to SIF values of 0.87 and 1.13 respectively. We have, however, not yet established the validity of applying a probability distribution function for vertebral failing loads based on axial compression experiments to the SIF which addresses vertebral body yielding due to combined axial compression and bending loads. Hence, although it is stated above that the SIF provides an indication of the likelihood of yielding, the only SIF value to which we currently actually assign a probability (i.e., 50%) is SIF=1.

Several different versions of varying complexity (i.e., number of degrees of freedom), of the HSM exist. These range from the SSM (Simplified Spine Model), having 48 degrees of freedom, to the CSM (Complex Spine Model), with 252 degrees of freedom. These differences in degrees of freedom translate into significant differences in computer time for similar simulations. A CSM simulation requires almost two orders of magnitude times the computer time of a similar SSM simulation. The level of detail (i.e., number and locations of response variables) desired determines which version of the HSM is used for a particular application. The system component(s) (usually the TL spine) whose response is of primary concern is modeled in detail, while the remaining components are approximated with only the degree of discretization necessary such that their contributions to the overall response of the model and their effects on the response of the primary component are reasonable (as determined by earlier studies comparing responses of different versions of the HSM [11, 12]).

HSM validation is an ongoing program at AFAMRL and involves comparisons of model predictions with data obtained from experimental programs and from reconstructions of operational ejections [11, 12, 30 and 31]. Validation of the HSM dynamic response and spinal injury prediction capability (i.e., SIF and the associated yield criteria) is scheduled to be completed by the end of calendar year 1986.

APPROACH

The Aerospace Medical Division's CREST Program Office requested that the HSM be used to evaluate the effects, on head-spine structure ejection-induced dynamic response and injury likelihood, of variations in the following ejection system parameters: head-pad location relative to the plane of the seatback, Δ, and catapult acceleration vector angle, α, and magnitude, a(t). The ranges for the variations of these parameters were also specified. Values requested for Δ were -2.54, 0 and +2.54 cm, where negative, zero and positive Δ indicate the front (+X) surface of the head-pad is aft, even and forwards, respectively, of the front surface of the seatback (for the remainder of this paper, X, Y and Z are used to identify the global axes with X, Y, and Z positive forwards, to the left, and up, respectively). Values specified for α were -10°, -5°, 0, +5° and +10° where α is measured from the Z axis (in the XZ plane) and negative, zero and positive values of α indicate that the X component of the catapult acceleration vector is negative, zero or positive, respectively. Two acceleration levels, which will be referred to as $a_1(t)$ and $a_2(t)$, were considered. Both were parabolic approximations to the first 150 msec of an ACES II catapult acceleration time history, i.e.

$$\vec{a}_i(t) = A_i \sqrt{\frac{t}{.15}} (\sin\alpha \vec{i} + \cos\alpha \vec{j}), \quad 0 \leq t \leq .15 \text{sec} \qquad (21)$$

where A_i, the 150 msec (and peak) magnitude of $\vec{a}_i(t)$ were specified to be 12 and 18 G (11,768 and 17,652 cm/sec^2) for $a_1(t)$ and $a_2(t)$ respectively. In the remainder of this paper, the vector symbol ($\rightarrow$) is omitted when $a_1(t)$ or $a_2(t)$ refer to acceleration level or magnitude.

For the HSM simulations, the $\vec{a}_i(t)$ were prescribed directly at the pelvis primary node and on a single elastic plane representing the seatback. Hence the pelvis and seatback moved together. A restraint system was defined using three spring elements between the seatback plane and the primary nodes of the T1, T2 and T3 torso segments. The motions of the seatback "attachment points" of these spring elements were constrained such that their Z displacements were identical (to within a time step) to those of their corresponding torso segment primary nodes, thus assuring that the tensile forces developed in the springs were always normal to the seatback.

Of primary interest in this study were the effects of the aforementioned parameter variations on TL spine injury likelihood as determined by the SIF. The version of the HSM used

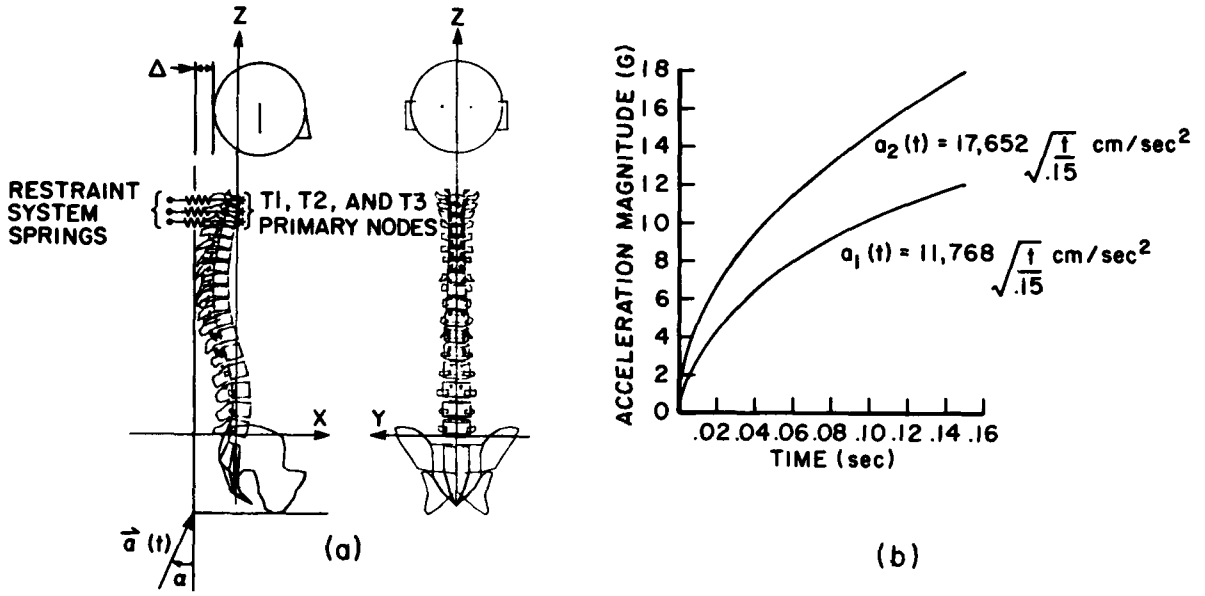

Fig. 2 - (a) HSM version used in this study and definition of parameters
(b) Parabolic approximations to ACES II catapult acceleration time history

in this study was, therefore, one in which the TL spine is modeled in detail while simplified approximations are used for the remaining subsystems. Fig. 2 depicts the sagittal (XZ) and frontal (YZ) plane views of this model and again defines the ejection system parameters which were evaluated. This HSM contains a fully discretized representation of the TL spine, i.e., each vertebral level and the interconnecting intervertebral discs, spinal ligaments and articular facets are included. The head/helmet and pelvis are modeled as rigid bodies, the cervical spine as a single three-dimensional beam element and the secondary loading and stiffening effects of the viscera-abdominal wall-diaphragm-rib-cage system are accounted for with a column of nonlinear beam elements which approximately parallels the primary column. These nonlinear beam elements, whose only nonzero stiffnesses are cubic stiffness coefficients for local AP and lateral bending deformations, interconnect the primary nodes directly and provide resistance to large relative rotations only.

RESULTS AND DISCUSSION

Each of Figs. 3a, b and c shows the effects of variations in α ($-10° \leq \alpha \leq +10°$); with Δ = constant (-2.54, 0 and +2.54 cm for Figs. 3a, b and c respectively) and for the 12 G acceleration profile ($a_1(t)$), on TL spine injury likelihood as determined by the HSM SIF (Eq. 16). Results for α = -5° and +5° were not included since these turned out to be intermediate to those which were plotted. The SIF are plotted as functions of TL spine vertebral level (T1 through L5).

It can be seen, in all three figures, that increasingly negative values of α (corresponding to increasing -X components of $a_1(t)$) have the primary effect of increasing SIF in the mid-to-upper thoracic spine with the magnitude of this increase and the number of affected vertebral levels also becoming larger with increasingly positive values of Δ. Also noteworthy is that in going from α = +10° to α = -10°, the maximum value of SIF shifts from the mid-lumbar spine to the mid-thoracic spine (obviously true for Δ = 0 and +2.54 cm; not quite the case for Δ = -2.54 cm but the trend is there).

Mechanical insight into the reasons for these changes in SIF can be gained by plotting the axial (P/P_y) and bending (M/M_y) contributions to SIF versus vertebral level. This has been done in Fig. 4 for the SIFs of Fig. 3b, i.e., for Δ = 0. It is immediately apparent that the increase in upper thoracic SIF is primarily attributable to increased bending, specifically, flexion (forward bending) in the upper thoracic spine. It is also apparent that the bending response in the lower thoracic and lumbar spine is not significantly affected (with the exception of T12) and that the SIF changes in these regions, though for the most part small, are directly attributable to the axial response. In fact, the SIF and its axial contributions are seen to decrease in these regions.

Fig. 5 depicts HSM sagittal (XZ) plane configurations at 25, 75, 100, 125 and 150 msec for

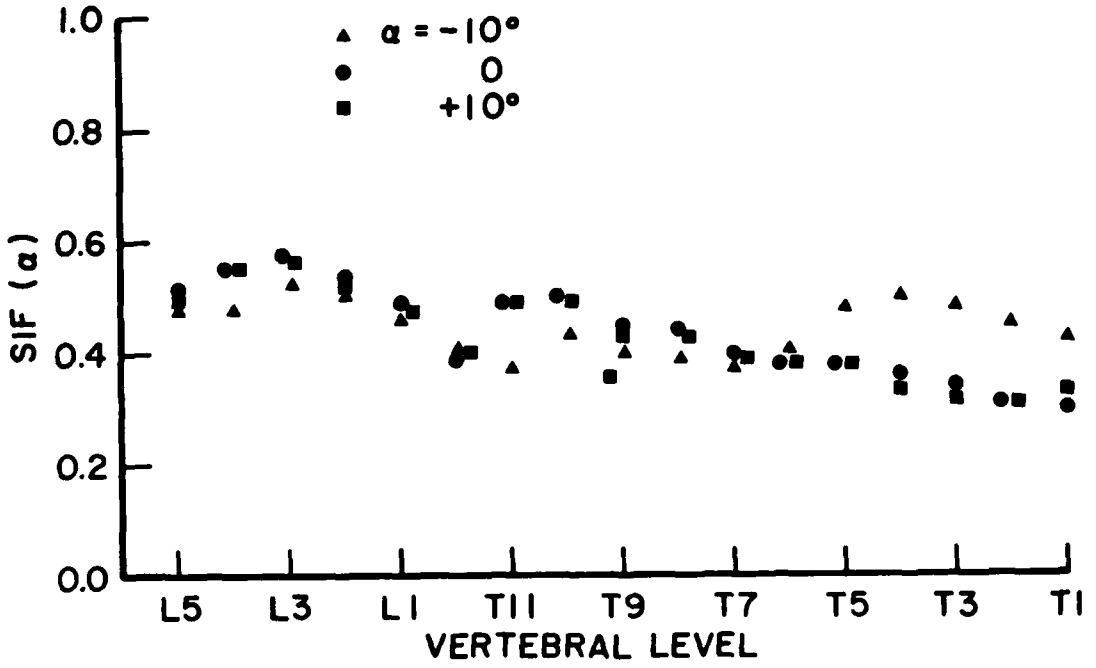

(a)

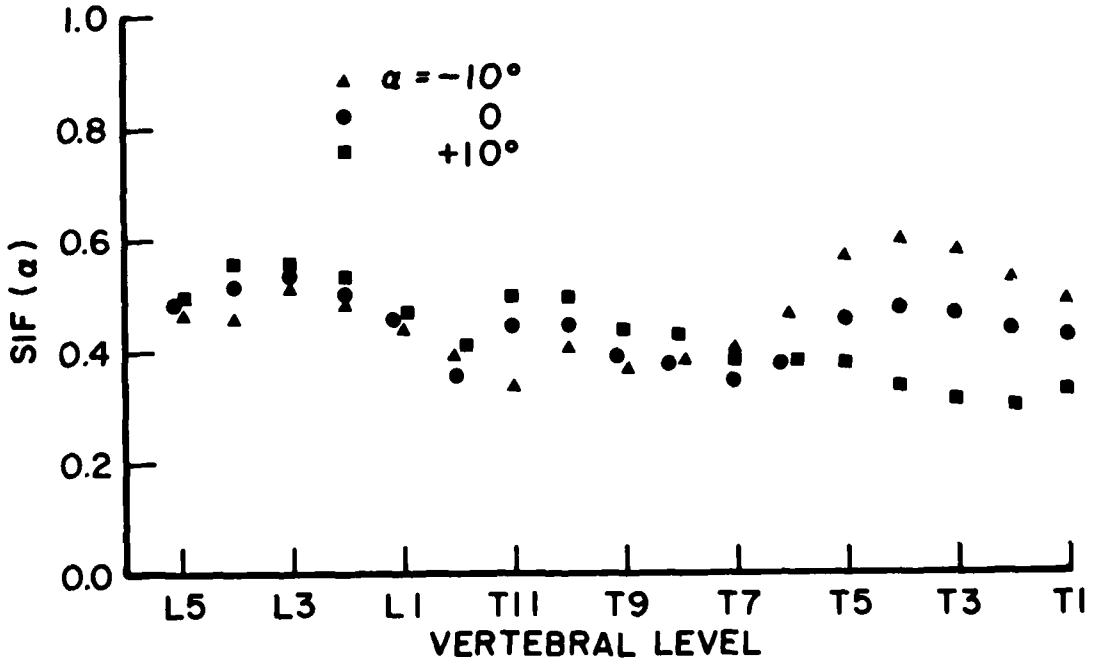

(b)

Fig. 3 - (a) SIF variations with α, $-10° \leq \alpha \leq +10°$ for $\Delta = -2.54$ cm and $a_1(t)$ (12 G profile); (b) $\Delta = 0$ cm;

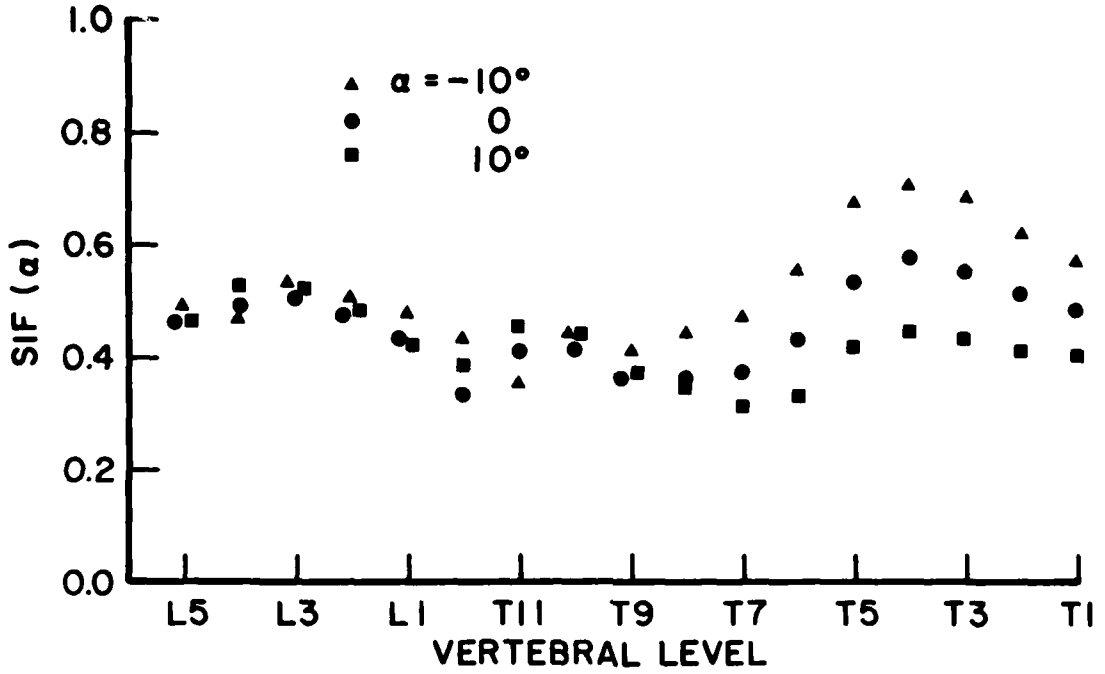

Fig. 3 - (c) SIF variations with α, $-10° \leq \alpha \leq +10°$ for Δ = +2.54 cm and $a_1(t)$ (12 G profile)

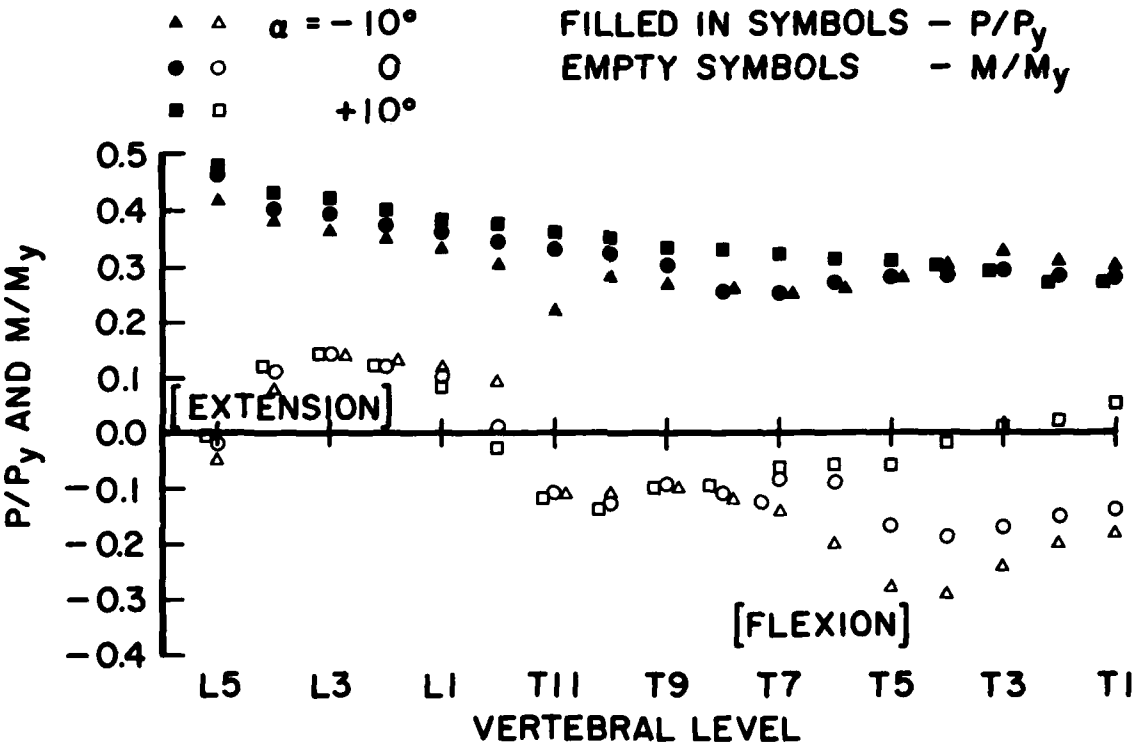

Fig. 4 - P/P_y and M/M_y (AP bending) from the SIFs of Fig. 3b

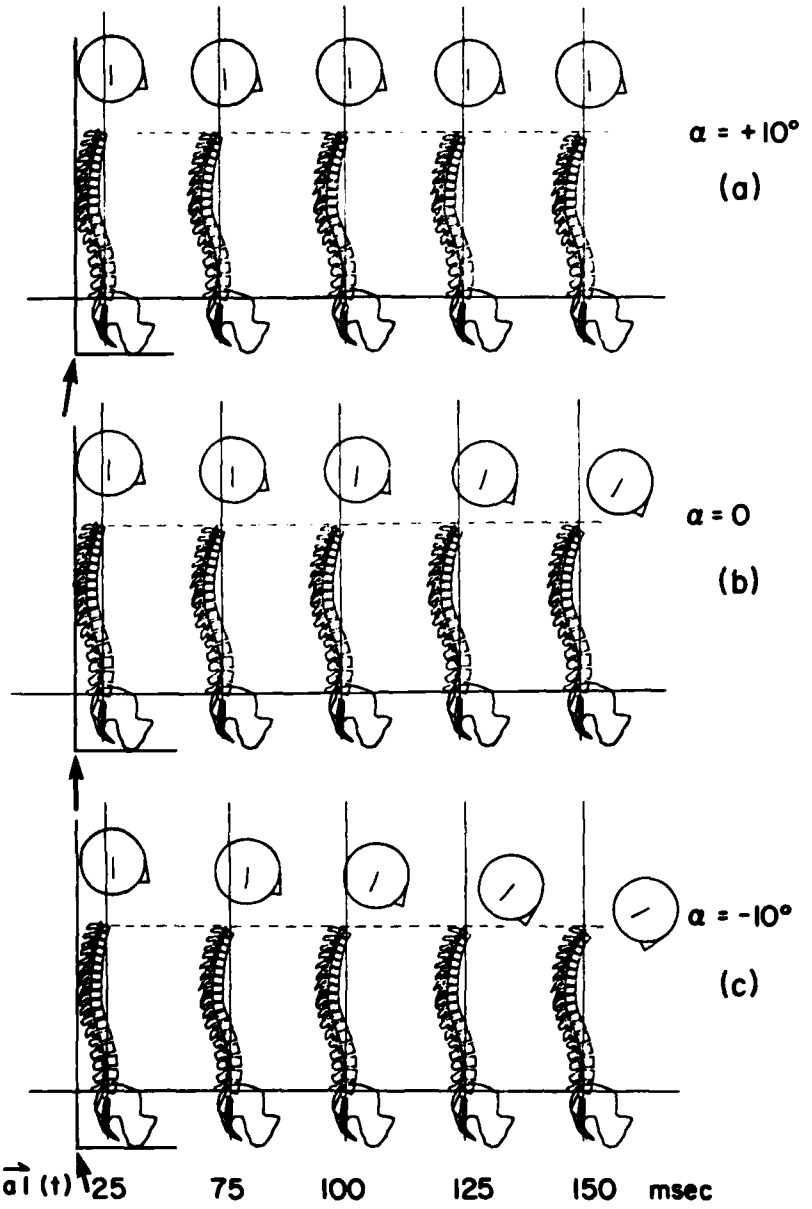

Fig. 5 - HSM sagittal (XZ) plane configurations for (a) $\alpha = +10°$, (b) $\alpha = 0$, (c) $\alpha = -10°$ with $\Delta = 0$ and $a_1(t)$

(a) $\alpha = +10°$, (b) $\alpha = 0$ and (c) $\alpha = -10°$ (with $\Delta = 0$ and $a_1(t)$), i.e., the three cases corresponding to the SIF and P/P_y and M/M_y plots in Figs. 3b and 4, respectively. It is readily apparent from these configurations, that as α decreases, or becomes increasingly more negative, the tendency for $a_1(t)$ to induce a positive rotation of the head and upper torso about Y (positive rotation of the head and upper torso flexion is somewhat limited by the restraint system but the forward translation and rotation of the head is limited only by the the cervical spine and its associated muscles and ligaments). The increase in the magnitude of this head motion with increasingly negative α is the primary source of the increased forward bending of the mid-to-upper thoracic spine while at the same time resulting in a decrease in the inertial axial compressive loading of the lumbar and lower thoracic spine (obviously the corresponding decrease in the +Z component of $a_1(t)$ also contributes to the decrease in the axial compression of the lower spine).

Each of Figs. 6a, b and c shows the effects of variations in Δ ($-2.54 \leq \Delta \leq +2.54$ cm); with α = constant (-10°, 0 and +10° for Figs. 6a, b and c respectively) and for the 12 G acceleration profile, on the HSM SIF. In all three figures, it can be seen that increasingly larger values of Δ with α constant produce similar variations in SIF as increasingly negative values of α, i.e., increases in mid-to-upper thoracic region SIF and a change in the location of the maximum of SIF from the mid lumbar to the mid-to-upper thoracic spine. Fig. 7 shows plots of the axial (P/P_y) and bending M/M_y) contributions for the SIFs of Fig. 6b. Again it is apparent that the SIF increases in the mid-to-upper thoracic spine are directly attributable to increased bending in this region.

Fig. 8 depicts HSM sagittal (XZ) plane configurations at 25, 75, 100, 125 and 150 msec for (a) Δ = -2.54 cm, (b) Δ = 0 and (c) Δ = +2.54 cm (with α = 0 and $a_1(t)$), i.e. the three cases corresponding to the SIF and P/P_y and M/M_y plots in Figs. 6b and 7, respectively. It is apparent that as Δ increases, the tendency for $a_1(t)$ to induce a positive Y rotation of the head and upper torso increases. Comparisons of Figs. 6b, 7 and 8 with Figs. 3b, 4 and 5, respectively, clearly show that increasing Δ (from -2.54 cm to +2.54 cm with α = 0) and decreasing α (from +10° to -10° with Δ = 0) produce quite similar changes in both head-spine structure kinematics and TL spine injury likelihood. This is not particularly surprising since decreasing Δ and increasing α both have the effect of decreasing the +Y angular acceleration of the overall center of mass (CM) (or, equivalently, increasing the magnitude of the -Y angular acceleration of the CM) while, conversely, increasing Δ and decreasing α both have the effect of increasing the +Y angular acceleration of the CM (or equivalently decreasing the magnitude of the -Y angular acceleration of the CM).

Fig. 9 compares the SIF for the 12 G ($a_1(t)$) and 18 G ($a_2(t)$) acceleration profiles for the case α = 0 (i.e., $\vec{a}_1(t)$ and $\vec{a}_2(t)$ are both straight up) and Δ = 0 (i.e., head-pad even with seatback). There is a fairly uniform increase, having an average value of 36%, in SIF for T1 through L5. Fig. 10 compares the HSM configurations from these two simulations. Kinematics for the two cases are qualitatively quite similar, with the 18 G profile obviously resulting in somewhat larger deformations.

Fig. 11 shows the SIF for three different combinations of α and Δ (and the 18 G profile in all three cases). The most severe case shown is obviously α = -5° and Δ = +2.54 cm, which turned out to be the most severe combination of these parameters considered in the study (the combination, α = -10°, Δ = +2.54 cm and $a_2(t)$ was not considered). For this case the SIF was greater than 1.0 (corresponding to 50% likelihood of vertebral body compressive yielding) for three vertebral levels, T3, T4 and T5, with the maximum occurring at T4.

It is also of interest to compare the SIF for α = -10°, Δ = +2.54 cm and $a_1(t)$ in Fig. 6a to that for α = 0, Δ = 0 and $a_2(t)$ in Fig. 9. Even though the first curve is based on an acceleration level 33-1/3% less than that of the second, the mid-to-upper thoracic spine (T5-T1) SIF is slightly higher for the first. The difference would be even more significant if the SIF for α = -10°, Δ = +2.54 cm and $a_1(t)$ were compared to any for $\alpha > 0$ and/or $\Delta < 0$ and $a_2(t)$. It is apparent then that certain combinations of α and Δ (primarily $\alpha < 0$ and $\Delta > 0$) may have at least as significant an effect on human ejection acceleration tolerance, as indicated by the SIF, as small variations about a system's design acceleration profile.

CONCLUSION

The Air Force Aerospace Medical Research Laboratory's Head-Spine Model (HSM) and its structural analysis software, SAM, have been described along with the application of the HSM to a problem in ejection system design. This problem was the qualitative evaluation of the effects of variations in Δ (head-pad location relative to the plane of the seat-back), α (catapult acceleration vector angle) and a(t) (catapult acceleration vector magnitude) on ejection-induced TL spine injury likelihood. Ranges for the parameter variations were specified and are representative of these parameters in existing ejection systems.

Results from the HSM ejection simulations were presented in the form of SIF plots versus TL spine vertebral levels and model sagittal (XZ) plane configurations. These results demonstrated that variations in α from +10° to -10° (with Δ constant) and Δ from -2.54 to +2.54 cm (with α constant) had similar effects on the SIF. Both sets of parameter variations (in the directions indicated) resulted in increases in mid-to-upper thoracic spine SIF and a change in location of the maximum value of the SIF from the mid-lumbar to the mid-thoracic spine. It was also demonstrated that the increases in mid-to-upper thoracic spine SIF were directly attributable to increased forward bending in this region and that the axial compression contributions to the SIF were considerably less affected. These observations hold for both acceleration levels.

Using the HSM, we have shown that ejection system geometric parameters, such as α and Δ, may have as significant effect on human ejection acceleration tolerance as the acceleration profile itself. None of the one-dimensional types of head-spine structure models (such as the DRI) which preceded the HSM, could have provided the type of quantitative (nor qualitative) results upon which this statement is based. The results presented here lead to the conclusion that limitations must be placed on α (for $\alpha < 0$) and Δ (for $\Delta > 0$) to insure minimum TL spine injury likelihood during the catapult acceleration phase of the ejection

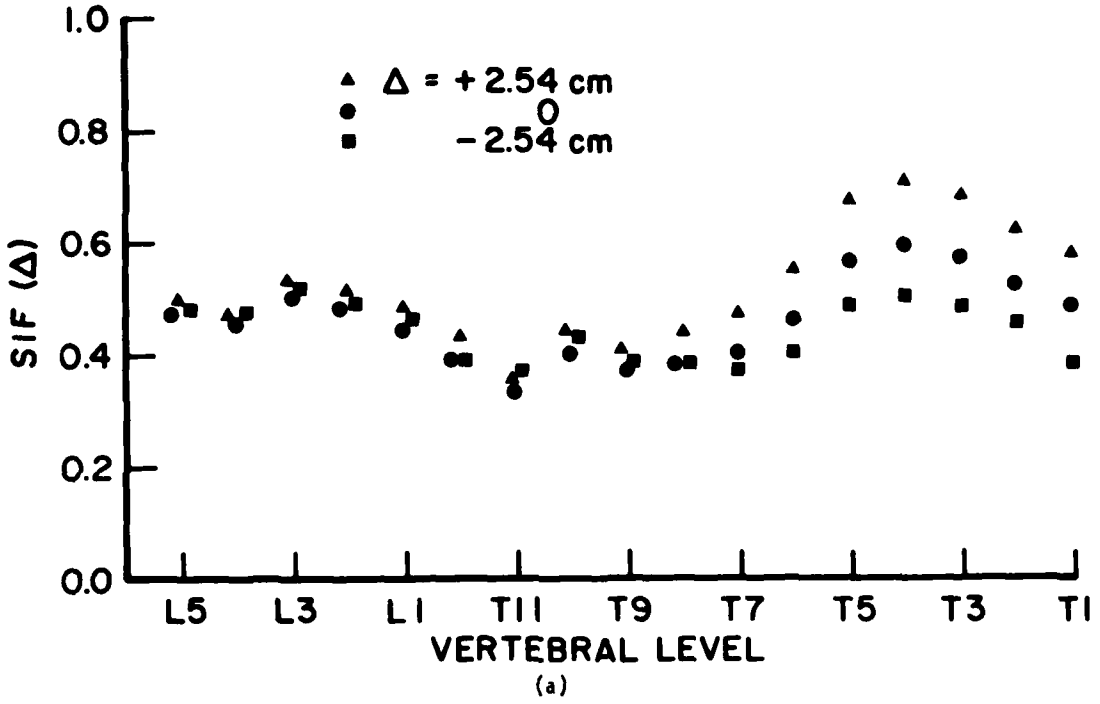

(a)

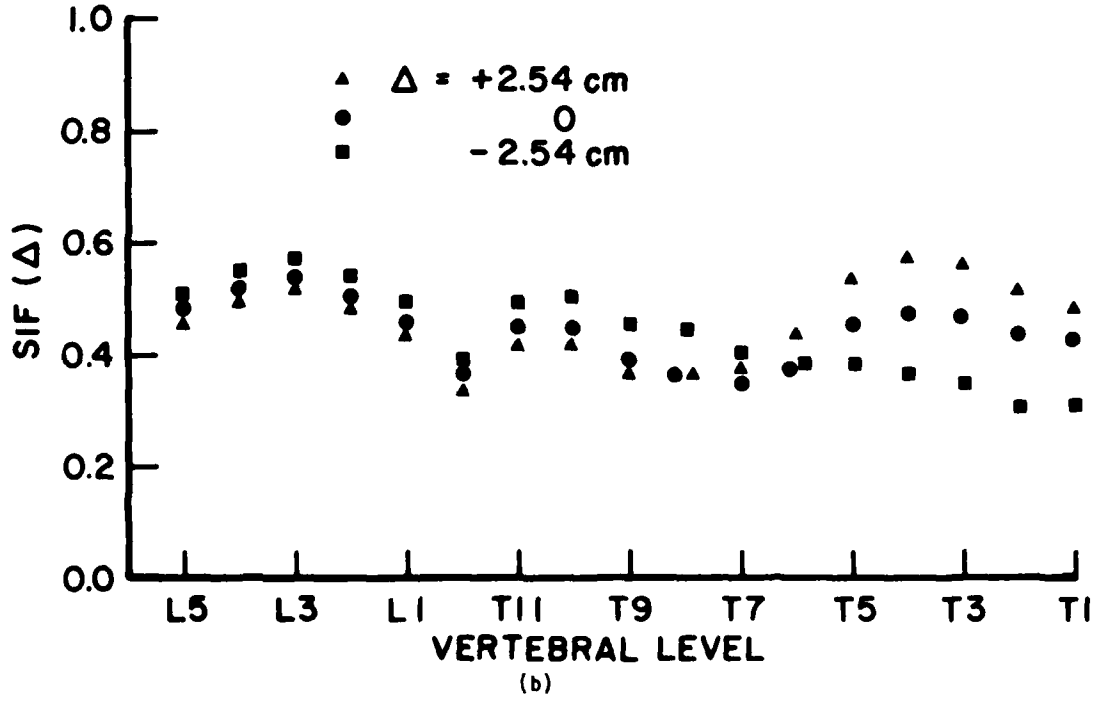

(b)

Fig. 6 - (a) SIF variations with Δ, -2.54 cm ≤ Δ ≤ +2.54 cm, for α = -10° and $a_1(t)$ (12 G profile) (b) α = 0°;

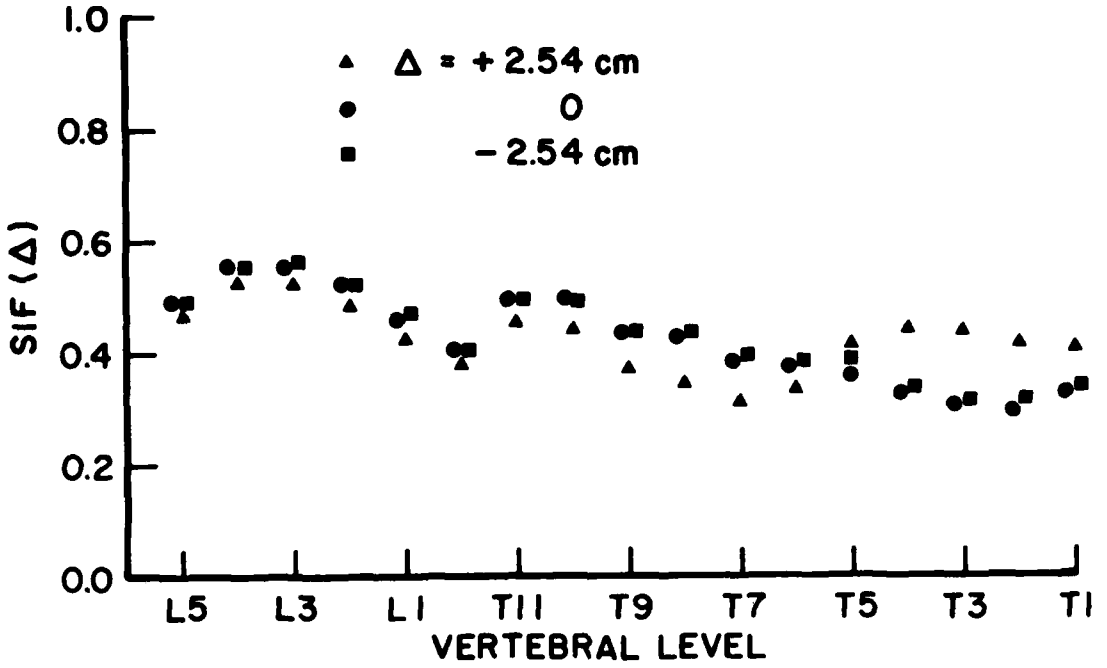

Fig. 6 - (c) SIF variations with Δ, -2.54 cm ≤ Δ ≤ +2.54 cm, for α = +10° and $a_1(t)$ (12 G profile)

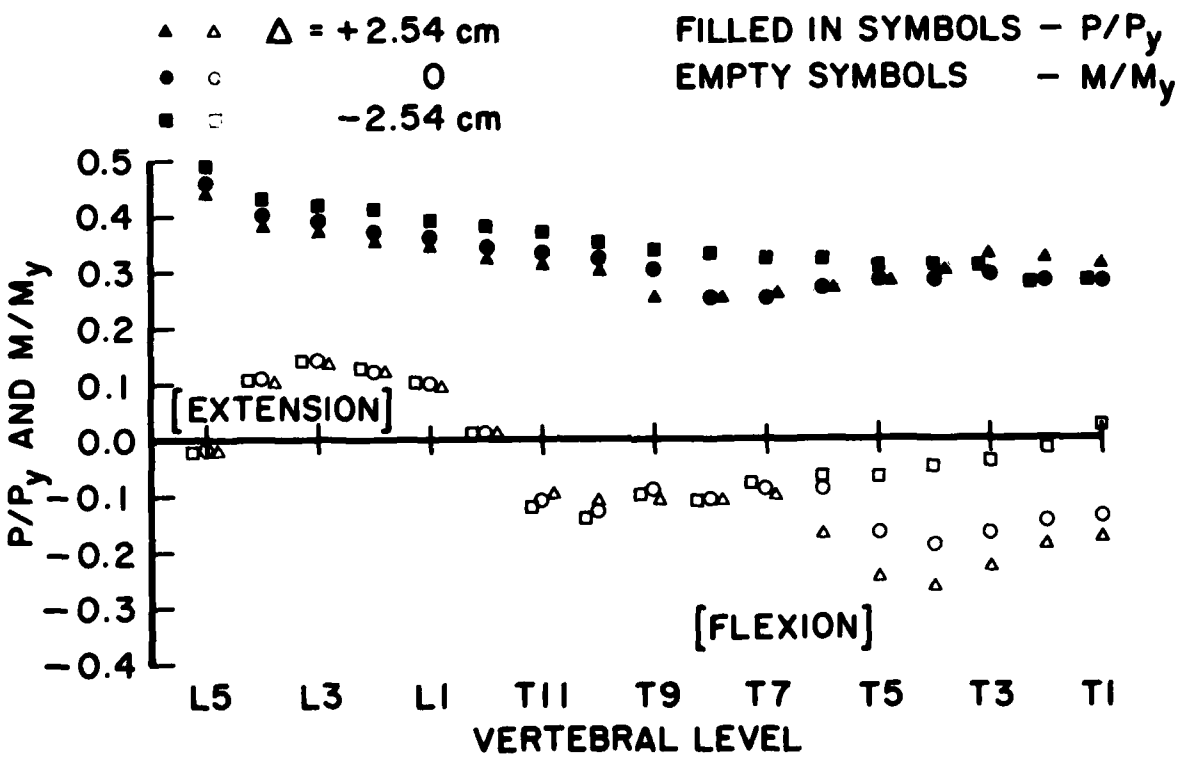

Fig. 7 - P/P_y and M/M_y (AP bending) from the SIFs of Fig. 6b

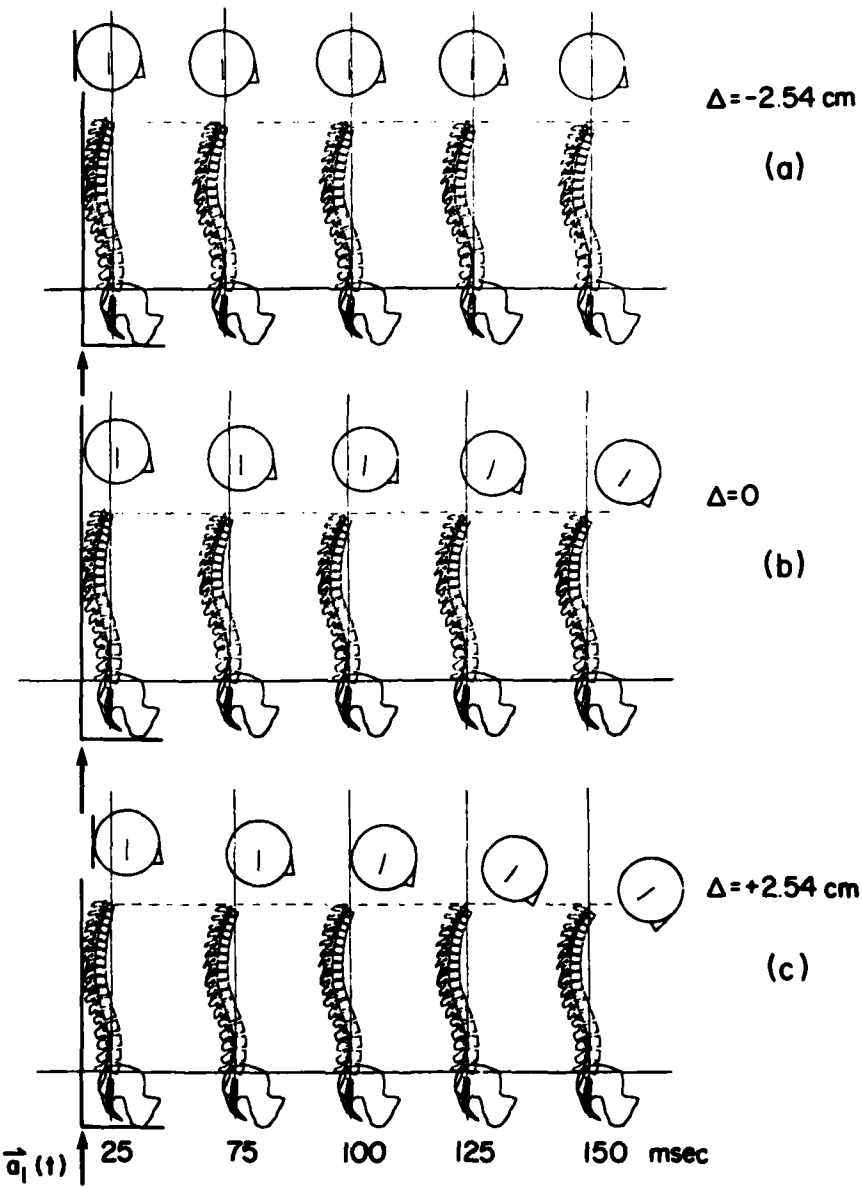

Fig. 8 - HSM sagittal (XZ) plane configurations at 25, 75, 100, 125 and 150 msec for (a) Δ = -2.54, (b) Δ = 0, (c) Δ = +2.54 cm, with α = 0 and $a_1(t)$

sequence. In a follow-on effort, we plan to determine the optimum combinations of α, Δ and acceleration level that will minimize TL spine injury likelihood for both a generic (such as used in the study presented herein) and specific ejection systems.

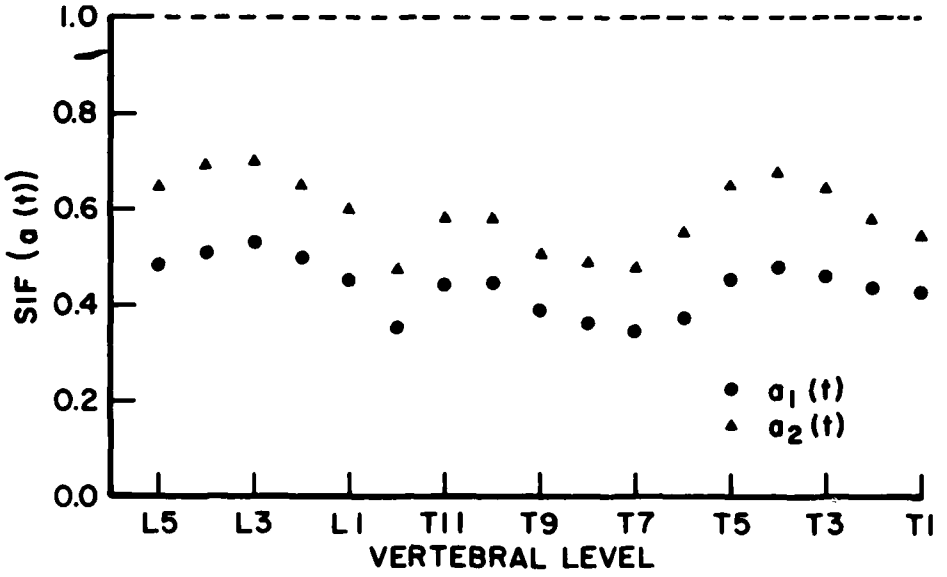

Fig. 9 - SIF for the 12 G ($a_1(t)$) and 18 G ($a_2(t)$) acceleration profiles; $\alpha = 0°$, $\Delta = 0$ cm

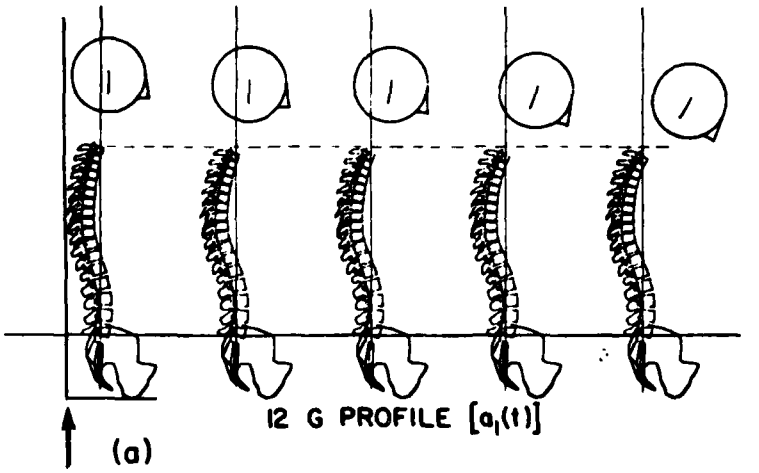

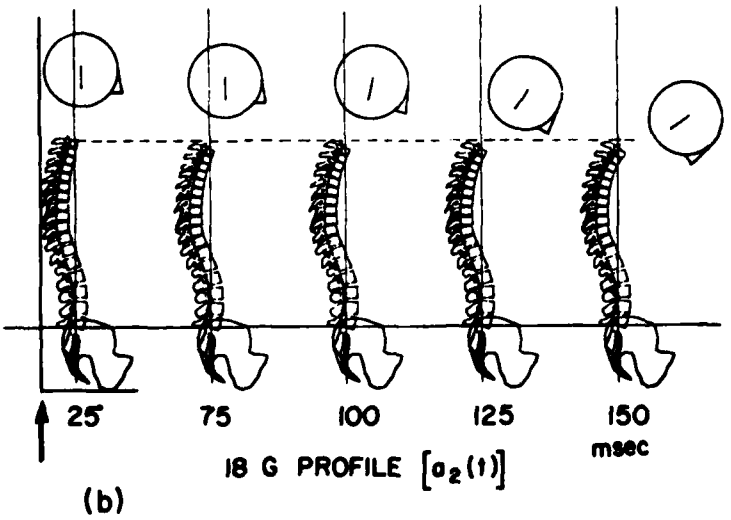

Fig. 10 - HSM configurations at 25, 75, 100, 125 and 150 msec for (a) $a_1(t)$ and (b) $a_2(t)$; $\alpha = 0°$, $\Delta = 0$ cm

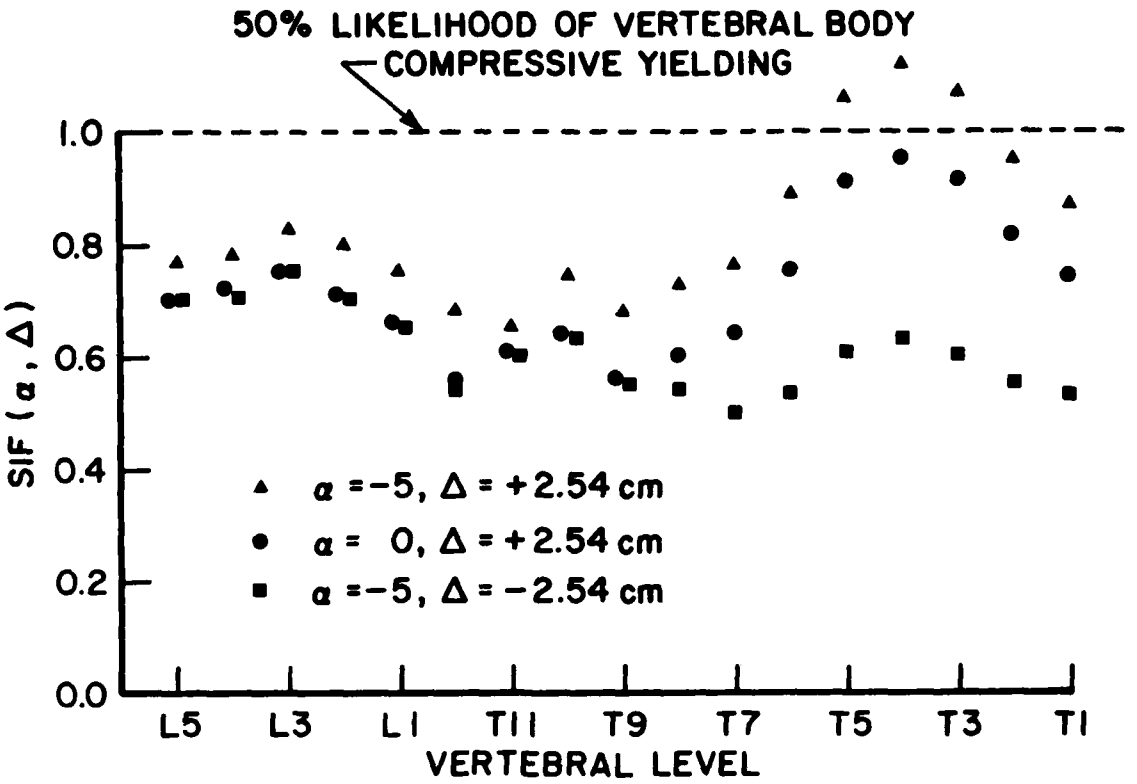

Fig. 11 - SIF (α,Δ): $\alpha = -5°$, $\Delta = +2.54$ cm; $\alpha = 0$, $\Delta = +2.54$ cm; $\alpha = -5°$, $\Delta = -2.54$ cm; and $a_2(t)$ (18 G profile)

REFERENCES

1. Brinkley, J.W. and Shaffer, J.T., "Dynamic Simulation Techniques for the Design of Escape Systems: Current Applications and Future Air Force Requirements," Proc. Symposium on Biodynamic Models and Appl., AMRL-TR-71-29, pp. 71-104, Dec. 1971

2. "Seat System, Upward Ejection, Aircraft, General Specification for," MIL-S-9479B (USAF), Mar. 1971

3. Latham, F., "A Study in Body Ballistics: Seat Ejection," Proc. Royal Society, 147, Series B, 121, 1957

4. Payne, P.R. and Band, E.G.U., "A Four Degree of Freedom Lumped Parameter Model of the Seated Human Body," Wyle Laboratories, Payne Division, Working Paper No. 59101-6, 1969

5. Brinkley, J.W., "A Six-Degree-of-Freedom Acceleration Exposure-Limit System for an Ejection Seat Advanced Development Program," unpublished AFAMRL working paper, 1984

6. Roberts, E.O. and Dobbek, R.J., "Escape by Continuous Control - CREST," SAFE Journal, Vol. 14, No. 1, pp. 22-26, Oct. 1983

7. Higgins, A.M. and Roberts, E.O., "CREST - Crew Escape Technologies for the 1990's," Proc. JANNAF Propulsion Conf., Feb. 1984

8. Hearon, B.F., Brinkley, J.W., Hudson, D.M. and Saylor, W.J., "Effects of a Negative G Strap on Restraint Dynamics and Human Impact Response," AFAMRL-TR-83-083, Dec. 1983

9. Belytschko, T., Schwer, L. and Schultz, A., "A Model for Analytic Investigation of Three Dimensional Spine-Head Dynamics," AMRL-TR-76-10, Apr. 1976

10. Belytschko, T., Schwer, L. and Klein, M.J., "Large Displacement, Transient Analysis of Space Frames," Intl. J. of Num. Methods in Engr., 11, pp. 65-84, 1977

11. Belytschko, T. and Privitzer, E., "Refinement and Validation of a Three-Dimensional Head-Spine Model," AMRL-TR-78-7, Aug. 1978

12. Privitzer, E., "Refinement and Validation of a Mathematicl Model of the Human Torso," Ph.D. Dissertation, University of Illinois in Chicago, unpublished, 1979

13. Privitzer, E. and Belytschko, T., "Impedance of a Three-Dimensional Head-Spine Model," Int'l J. Mathematical Modeling, Vol. 1, No. 2, pp. 189-209, 1980

14. Andriacchi, T., Schultz, A., Belytschko, T. and Galante, J., "A Model for Studies of Mechanical Interactions Between the Human Spine and Rib Cage," J. of Biomechanics, 7, pp. 497-507, 1974

15. Liu, Y.K. and Wickstrom, J.K., "Estimation of the Inertial Property Distribution of the Human Torso from Segmented Cadaveric Data," Perspectives in Biomedical Engr., 1973

16. Belytschko, T. and Hsieh, B.J., "Nonlinear Transient Finite Element Analysis with Convected Coordinates," Int'l. J. of Num. Methods in Engr., 7, pp. 255-271, 1972

17. Williams, J. and Belytschko, T., "A Dynamic Model of the Cervical Spine and Head," AFAMRL-TR-81-5, Nov. 1981

18. Williams, J. and Belytschko, T., "A Three-Dimensional Model of the Human Cervical Spine for Impact Simulation," J. Biomedical Engr., Vol. 105, pp. 321-331, Nov. 1983

19. Schultz, A., Belytschko, T. and Andriacchi, T., "Analog Studies of Forces in the Human Spine: Mechanical Properties and Motion Segment Behavior," J. Biomechanics, Vol. 6, pp. 373-383, 1973

20. Schultz, A., Benson, D. and Hirsch, C., "Force-Deformation Properties of Human Ribs," J. Biomechanics, Vol. 7, pp. 303-309, 1974

21. Schultz, A., Benson, D. and Hirsch, C., "Force-Deformation Properties of Human Costo-Sternal and Costo-Vertebral Articulations," J. Biomechanics, Vol. 7, pp. 311-318, 1974

22. Privitzer, E. and Ryerson, J., "Model Investigations of the Effects of Variations in Restraint System Loads on Occupant Response during Ejection," Proc. 53rd Scientific Meeting of the Aerospace Medical Association, May 1982

23. Privitzer, E., "Model Simulations of Pilot Retraction," Proc. 52nd. Scientific Meeting of the Aerospace Medical Assn., May 1981

24. Privitzer, E., "Model Investigations of Head-Spine Dynamics during Occupant Retraction/Ejection," presented at ORSA-TIMS Joint National Mtg., Oct. 1981

25. Smith, G.D., "Numerical Solution of Partial Differential Equations," Oxford University Press, 1965

26. Geertz, A., "Limits and Special Problems in the Use of Seat Catapults," AAF Aero Medical Center ATI No. 56946, translated Aug. 1946

27. Payne, P.R., "Some Aspects of Biodynamic Modeling for Aircraft Escape Systems," Proc. Symposium on Biodynamic Models and Appl., AMRL-TR-71-29, pp. 233-335, Dec. 1971

28. Kazarian, L. and Graves, G.A., "Compressive Strength Characteristics of the Human Vertebral Centrum," Spine, Vol. 2, No. 1, Mar. 1977

29. Lanier, R., "The Presacral Vertebrae of American White and Negro Males," Amer. J. Physical Anthro. XXV, pp. 341-420, 1939

30. Privitzer, E., Hosey, R. and Ryerson, J., "Validation of a Biodynamic Injury Prediction Model of the Head-Spine System," Proc. AGARD Aerospace Medical Panel Specialists Mtg., Paper No. 30, Koeln, W. Germany, Apr. 1982

31. Carroll, C.D. and Privitzer, E., "Analysis of Vertebral Injuries Sustained during G_z Impact," Abstract in J. Aviation, Space and Environmental Medicine, Vol. 55, No. 5, May 1984

DISCUSSION

Mr. Robbins (University of Michigan): I noticed in both the movies you presented, and in some of the earlier slides, the pelvis orientation was shown fixed, and there was an S curvature particularly evident in the lumbar spine. What data base did you use to determine there should be that much S curvature in a spine which represents a seated posture?

Mr. Privitzer: The pelvis is fixed because we are driving the pelvis directly.

Mr. Robbins: I am talking about the orientation of the pelvis, not that it was fixed.

Mr. Privitzer: I am not sure of the official name of the data base, but it is supposedly based on some x-ray data of seated pilots that were gathered in the early 1970's. I am not sure what they were seated in, though; it might have been in a seat with a lumbar pad. But, that is just one particular configuration; we can modify that configuration according to whatever situation we are dealing with.

Mr. Robbins: Have you modified the pelvic orientation to take the S out of the bottom in any of your simulations?

Mr. Privitzer: No. I have not. I have let it rotate. But, most of the time, we do not know enough about whatever is going on beneath the pelvis to let the pelvis respond. So, I usually put my input right at the pelvis.

Mr.Robbins: I guess my main concern was the spinal curvature. I would think that would be an important variable; whether you have an S or more of a straight column. It seems like it would have a lot of effect on the inner vertebral discs and in the injury function.

Mr. Privitzer: Yes. If we are addressing a specific ejection system, then ideally we would want to model the spinal curvature as it would be on the mean in that system. The only question is how we will get that data because you would have to x-ray people to get it, and you are not supposed to do that.

Mr. Robbins: Is the crest seat design fixed so you will have to use this function?

Mr. Privitzer: No.

Mr. Helfrich (Pacific Missile Test Center): You showed the two curves from the A1 and the A2 in the spinal injury function curve, and they were fairly constant. Do you think that is a linear function? If you went up to another g level would you expect the same thing, or do you think that would end up being nonlinear?

Mr. Privitzer: It will not be linear. The beam elements I used in this study are linear; I did not use a cubic stiffness in that. Some of the springs have had cubic stiffness terms, but most elements are linear. But, from the geometry, it is a large deformation problem. It is a small strain problem, but it is also a large displacement problem. So, you will have some nonlinear effects from that. I have done that problem, and it is a nonlinear type of behavior.

Mr. Helfrich: Which portions tend to get worse?

Mr. Privitzer: It gets worse in the upper thorastic spine first because of the bending; we also have more problems up there because of the difficulty in modeling the restraint system.

TIME DOMAIN MATHEMATICAL MODELING OF ELASTIC INSTABILITIES AND LARGE ELASTIC-PLASTIC DEFLECTIONS

Robert P. Brooks

Franklin Research Center
Philadelphia, Pennsylvania

Mathematical modeling and computational techniques, based on an explicit time integration scheme, are presented for the calculation of elastic instabilities and large elastic-plastic deflections of beam elements. The equations are formulated to facilitate their introduction into time-domain computer programs.

The simple models presented, demonstrate the phenomena of Euler, angle and lateral buckling, as well as plastic-buckling with strain-rate effects. This methodology can be implemented to analyze complex structures, consisting of members that may exhibit failure instability when subjected to large, short-duration loads.

LIST OF SYMBOLS

A - Area
A_S - Shear area
D - Length between adjacent mass centers of corresponding points on adjacent masses
E - Modulus of elasticity
G - Shear modulus
I - Inertia (area or mass)
J - Polar moment of inertia
K - Spring constant
k - Torsional rigidity
L - Length (axial direction)
M - Moment
m - Mass
P - Axial load
T - Torsion
t - Time
V - Shear force
X - Coordinate axis or motion
Y - Coordinate axis or motion
Z - Coordinate axis or motion
α - Rotation about the X-axis
β - Rotation about the Y-axis
γ - Rotation about the Z-axis

Subscripts

c - Compression/tension spring
m - Mass
S - Shear spring
α - Direction
β - Direction
γ - Direction

All other symbols are described in the text as they appear.

INTRODUCTION

The purpose of this paper is to present dynamic mathematical models of beam elements that respond correctly to buckling loads and exhibit large plastic deformations. The models are in the form of readily programmable logic, which the analyst can include in his or her own software. These models are aimed at predicting catastrophic failure in the time domain instead of detailed stress distribution.

Five mathematical modeling schemes are presented in this paper. The first three models are for (1) Euler buckling, (2) buckling of angles and (3) lateral buckling. When using these models, the analyst must know the failure mechanism. The fourth is a general model embodying all three buckling modes. The last model is an extension of the fourth one with added logic to approximate yielding and strain rate effects.

The primary use for these models is to analyze compression members subjected to large, short duration loads such as in shock loading. Analysis using these models demonstrates that the structural elements can withstand short duration loads which have a peak greater than static critical buckling load. In such cases costly and time consuming redesign can be avoided.

Another helpful application of these models is in the analysis of the failure of submarine hulls subjected to underwater explosions. One proposed theory of failure is that the web of the ring stiffener may "cripple" (buckle) when the submarine is

subjected to an underwater explosion. This failure mode is within the capability of these models.

BASIC BEAM MODEL

The modeling schemes presented in this paper are all variations of the beam model described in [1]. For that reason a brief review of that model is in order.

Timoshenko's theory of beam bending supplies the following basic equations:

$$M + EI\frac{\partial \gamma}{\partial L} = 0 \qquad (1A)$$

$$V - A_S G\left(\frac{\partial Y}{\partial L} - \theta\right) = 0 \qquad (1B)$$

$$\frac{\partial M}{\partial L} - V + \rho I\frac{\partial^2 \gamma}{\partial t^2} = 0 \qquad (1C)$$

$$\frac{\partial V}{\partial L} - \rho A\frac{\partial^2 Y}{\partial t^2} = 0 \qquad (1D)$$

The first two equations relate loading to movement. Equation (1A) expresses the relationship between internal bending moment (M) and relative cross-sectional rotation ($\partial\gamma/\partial L$). Equation (1B) stipulates the relationship between the vertical shear force on a beam cross-section (V), and the shear angle ($\partial y/\partial L - \gamma$).

The latter two equations relate accelerations to the loading. Equation (1C) defines the effect of rotary inertia ($\rho I\partial^2\gamma/\partial t^2$) developed by considering rotational motion of beam elements during vibration. Equation (1D) considers translation motion of the beam elements.

The axial and torsional loading of a rod gives the following equations:

$$F - AE\frac{\partial X}{\partial L} = 0 \qquad (1E)$$

$$T + kG\frac{\partial \alpha}{\partial L} = 0 \qquad (1F)$$

$$\frac{\partial F}{\partial L} - \rho A\frac{\partial^2 X}{\partial t^2} = 0 \qquad (1G)$$

$$\frac{\partial T}{\partial L} - \rho J\frac{\partial^2 \alpha}{\partial t^2} = 0 \qquad (1H)$$

Equation (1E) relates the axial force (F) to the relative axial motion ($\partial X/\partial L$). Torsion (T) is a function of rotation about the axis of the rod ($\partial\alpha/\partial L$) as shown in Equation (1F).

The last two equations relate loading and acceleration. Equation (1G) give the axial motion ($\partial^2 X/\partial t^2$) based on axial load. Equation (1H) describes how the rotational acceleration relates to the torsional loading.

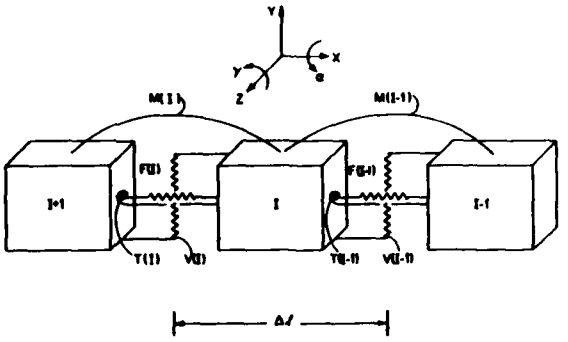

Fig.1 - Basic beam model

From consideration of Figure (1), the finite different form of the equation set is

$$M_i = \frac{EI}{\Delta L}(\Delta Y_i - \Delta Y_{i+1}) \qquad (2A)$$

$$V_i = \frac{A_S G}{\Delta L}\left(\Delta Y_{i+1} - \Delta Y_i + \Delta L\left(\Delta\gamma_{i+1} + \Delta\gamma_i\right)/2\right) \qquad (2B)$$

$$\ddot{\theta}_i = \left(-\Delta L(V_{i-1} + V_i)/2 + M_{i-1} - M_i\right)\Big/\Delta L\,\rho I \qquad (2C)$$

$$\ddot{Y}_i = (V_i - V_{i-1})/\rho A\Delta L \qquad (2D)$$

$$F_i = \frac{AE}{\Delta L}\left(\Delta X_{i+1} - \Delta X_i\right) \qquad (2E)$$

$$T_i = \frac{KG}{\Delta L}\left(\Delta\alpha_i - \Delta\alpha_{i+1}\right) \qquad (2F)$$

$$\ddot{X}_i = (F_i - F_{i-1})/\rho A\Delta L \qquad (2G)$$

$$\ddot{\alpha}_i = (T_{i-1} - T_i)/\rho J\Delta L \qquad (2H)$$

Equations (2A), (2B), (2E) and (2F) now form the static set, and equations (2C), (2D), (2G) and (2H) the dynamic set. The integration scheme which is aplied to each mass in the model, in readily programmable form is:

time = t + Δt

Dynamic equation loop:

- ACC_I = (forces or moments)/(mass or inertia)
- $VEL_i = VEL_i + ACC_i\,(\Delta t)$
- $DISP_i = DISP_i + VEL_i\,(\Delta t)$

Static equation loop:

- $LOAD_i = K(DISP_i - DISP_{i-1})$

The dynamic and static program loops are typical of the sets for each degree-of-freedom considered in a model. If all six degrees-of-freedom are included, then three translational and three rotational accelerations are calculated and integrated (as above) to obtain displacements. For six degrees-of-freedom, the static set contains six equations, corresponding to six loads: three moments and three forces. At the conclusion of the static equation loop all the calculations for the time increment are completed. Time is then updated and the process repeated, until the desired simulation time, or other criteria is reached.

EULER BUCKLING

Description

Column or Euler buckling is probably the simplest and best known form of elastic instability. This type of failure occurs when the compressive loads on a column are great enough that external moment (M_e), see Figure 2,

$$M_e = P\ (\delta - Y)$$

cannot be compensated for by the internal moment

$$M_i = EI \frac{\partial^2 Y}{\partial X^2}$$

The problem was originally solved for static loads by Leonhard Euler in 1744, hence the common name of the phenomena.

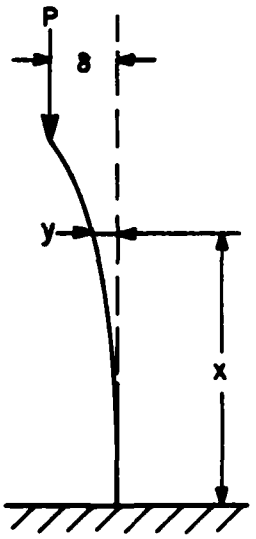

Fig.2 - Column buckling

Model

The dynamic model, Figure 3, which has been developed for buckling response to compressive loads is derived from the beam model in the previous section. In this model the tension/compression spring need not be parallel to the X-axis. Thus, if the internal compressive forces are great enough, the shear and moment springs may not be able to balance the Y component and buckling would result.

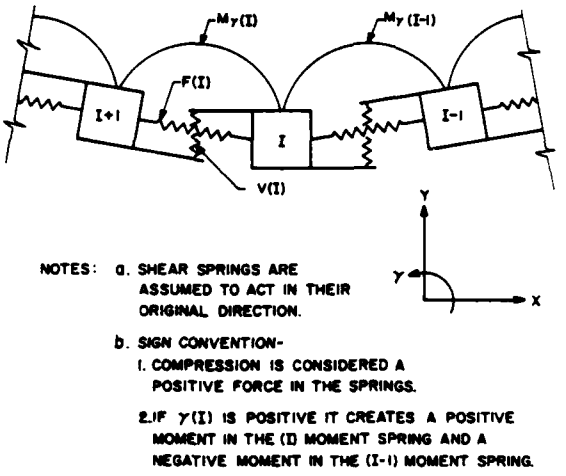

Fig.3 - Beam model for column buckling

The equations and logic for the model of Figure 3 are as follows:

The load equations, which are calculated each time increment for every set of springs in the model are:

$$\Delta X = X_i - X_{i+1} + \Delta L$$

$$\Delta Y = Y_i - Y_{i+1}$$

$$D = \sqrt{(\Delta X)^2 + (\Delta Y)^2}$$

$$F_i = K_C\ (\Delta L - D)$$

$$FX_i = F_i\ \Delta X / \Delta L$$

$$FY_i = F_i\ \Delta Y / \Delta L$$

$$V_i = K_S(Y_{i+1} - Y_i + (\Delta L/2)(\gamma_i + \gamma_{i+1}))$$

$$F\gamma_i = K_\gamma\ (\gamma_i - \gamma_{i+1})$$

where, ΔL = original mass spacing,

$K_C = AE/\Delta L$,

$$K_s = A_s G/\Delta L,$$

$$K_f = IE/\Delta L,$$

and, coordinate positions are measured from the original unstressed positions.

The corresponding acceleration equations are:

$$\ddot{X}_i = (FX_i - FX_{i+1})/m$$

$$\ddot{Y}_i = (V_i - V_{i+1} + FY_i - FY_{i+1})/m$$

$$\ddot{\Gamma}_i = (F\Gamma_{i+1} - F\Gamma_i - (\Delta L/2)(FS_i + FS_{i+1}))/I_m$$

The accelerations are numerically integrated twice to obtain the necessary displacements.

Verification

To verify the derived model, a free-free beam subjected to a constant compressive load was chosen as a test problem. The beam is 198.12 cm (78 in) in length with 5.08 cm (2 in) by 5.08 cm (2 in) cross section. Since this mathematical beam was perfect, it was necessary to perturbate one of the masses to start the dynamic simulation.

Figure 4 shows the maximum displacement of the oscillation of the center mass in the Y-direction as a function of compressive load. Figure 5 depicts the frequency exhibited by the model versus compressive force compared with the exact solution. The model shows very good agreement with theory, [2]. The simulation with p = 315,790 n (70,000 LB) was stopped at time = 0.0834 seconds. At that time the rate of center deflection was still increasing.

This type of model should be used if column buckling is suspected as a possibility, because it does not force buckling. The model will buckle only if the load is above critical and is of sufficient duration.

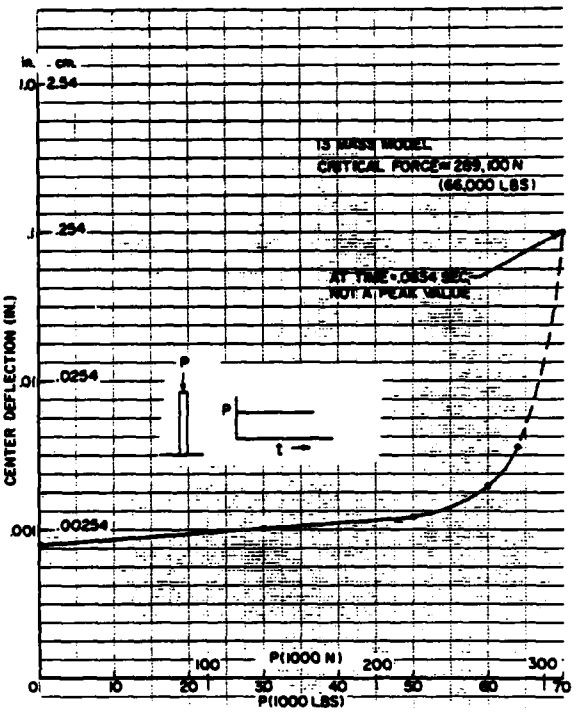

Fig.4 - Peak dynamic displacement of the center mass as a function of compressive load

BUCKLING OF ANGLES

Description

If an angle section is compressed as shown in Figure 6, it may fail in two different ways:

1. if the width (W) is relatively small, it will buckle as a column;
2. if W is large, the flanges will buckle.

The flange buckling mode is similar to the buckling of a plate hinged on three sides.

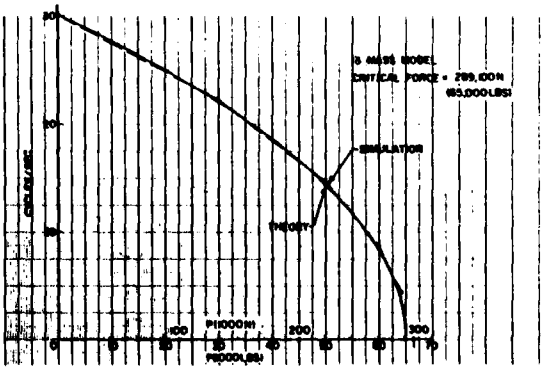

Fig.5 - Beam frequency as a function of compressive load

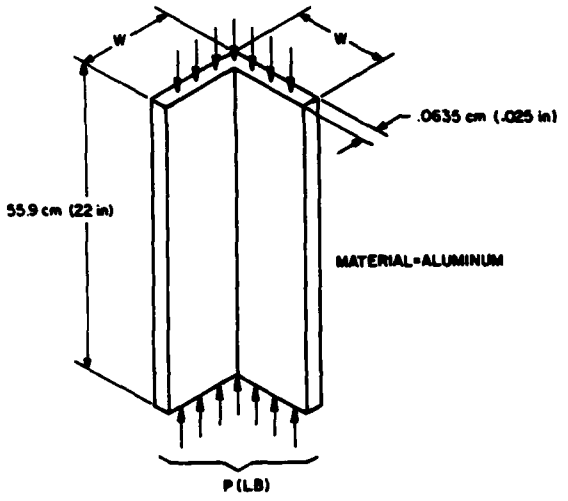

Fig.6 - Compression of angle section

Model

Though angle buckling has two failure modes and one of them is plate buckling, the problem is solved here by employing two beam models coupled along their length.

Figure 7 depicts a portion of the model. Each beam in the model appears similar to the previous buckling model (a tension/compression spring that may not remain axial, a torsion spring, two shear springs, and two moment springs between the mass faces). However, there is one important difference which allows for the torsional component of the axial stress. This phenomenon is shown and derived in Figure 8. When the equation on Figure 8 is added to the model, the flange buckling mode is included.

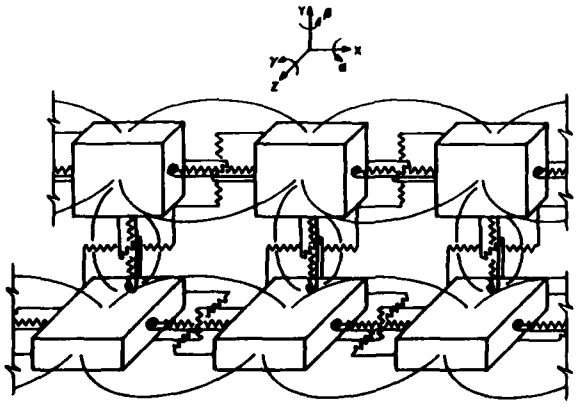

Fig.7 - Local buckling model

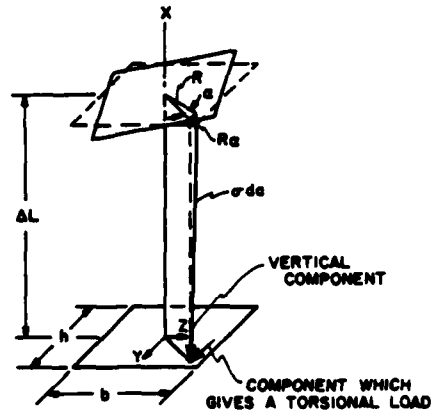

TORSION

$$T = \int_0^{\alpha} R\left[(\sigma dA)\left(\frac{R\alpha}{\Delta L}\right)\right] \qquad R = \sqrt{Y^2 + Z^2}$$

$$dA = dy\,dz$$

$$T = 4\int_0^{\frac{b}{2}}\int_0^{\frac{h}{2}} \frac{\sigma\alpha}{\Delta L}\left[Y^2 + Z^2\right] dy\,dz$$

$$T = (\sigma bh)\frac{\alpha}{12\Delta L}(b^2+h^2) = \frac{F\alpha}{12\Delta L}(b^2+h^2)$$

Fig.8 - Derivation of torsional component of axial stress

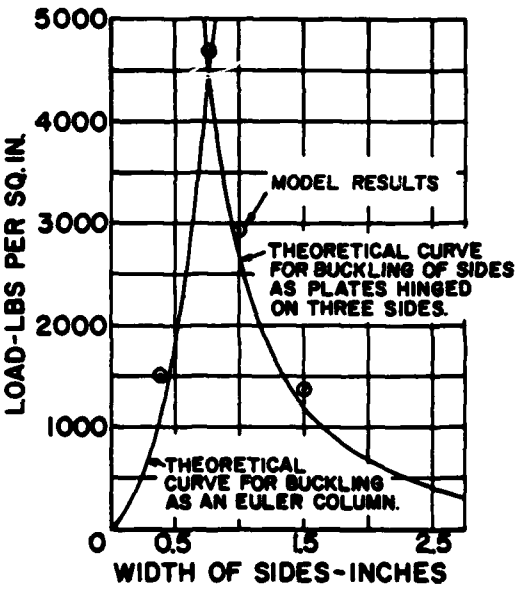

Fig.9 - Buckling of angle section

Verification

Timoshenko's work on elastic stability [2] includes a graph of the buckling strength

of an angle as a function of flange width. This graph is reproduced in Figure 9 and compared with the results of the dynamic angle buckling model. Since only static results were found, this model is not correlated in the frequency domain. The loading of this model is the same as in the previous section. That is, a constant compressive load is applied to the model and a small perturbation is applied to one of the masses. If the model oscillates there is no buckling and the load is increased for the next simulation. This is repeated until the model starts to collapse instead of oscillating. Again, the model results show very good correlation to theory and experimental results.

BEAM IN PURE BENDING

Description

Figure 10a depicts a narrow rectangular beam subjected to pure bending about Z-axis. As the bending moment increases the beam bends in the lateral direction and twists as illustrated in Figures 10b and 10c. When the external moment, M_0, becomes large, the torsional and lateral rigidities of the beam cannot compensate for small components of M_0 about X and Y axes resulting in buckling.

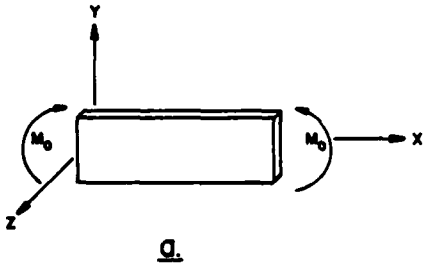

a.

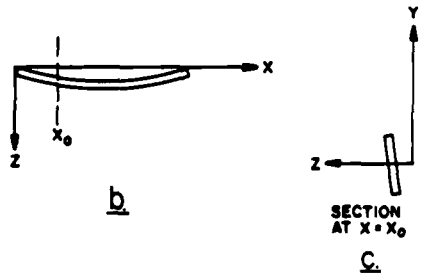

b.

c.

Fig.10 - Lateral deformation due to pure moment loading

Model

The springs which are necessary to allow the lateral buckling of the beam are shown in Figure 11a. Note that an axial spring is not included. For the previous problems it was necessary to calculate the components of the axial spring. For this problem it is necessary to calculate the components of the two moment springs and include them in the proper rotational acceleration equations. This scheme allows the applied load to excite the lateral bending and torsional motions of the model masses.

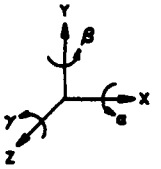

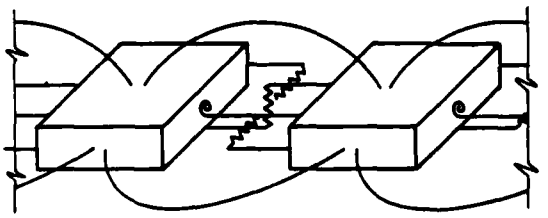

a.

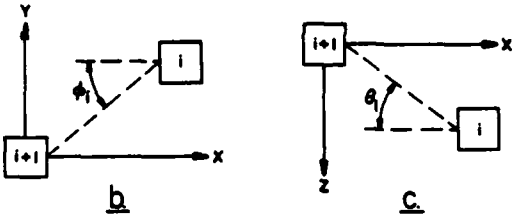

b.

c.

Fig.11 - Lateral buckling model

The following two equation sets are defined for the model. Figures 11b and 11c indicate the positive direction of the angle ϕ and θ used in the equation sets.

Load Equations

$$\phi_i = \text{TAN}^{-1}((Y_i - Y_{i+1})/\Delta L)$$

$$\theta_i = \text{TAN}^{-1}((Z_i - Z_{i+1})/\Delta L)$$

Shear force in the Y-direction

$$VY_i = K_S(Y_{i+1} - Y_i + (\Delta L/2)(\gamma_i + \gamma_{i+1}))$$

Shear force in the Z-direction

$$VZ_i = K_S\,(Z_{i+1} - Z_i - (\Delta L/2)(\beta_i + \beta_{i+1}))$$

$$\Delta\alpha_i = (\alpha_i + \alpha_{i+1})/2$$

Torsion

$$T\alpha_i = K_\alpha (\cos(\theta_i)\cos(\phi_i)(\alpha_i - \alpha_{i+1}) + \sin(\phi)(\beta_i - \beta_{i+1}) + \sin(\theta_i)(\gamma_i - \gamma_{i+1}))$$

Bending moment in β - direction

$$M\beta_i = K_\beta (\sin(\phi_i)\cos(\Delta\alpha_i)(\alpha_{i+1} - \alpha_i) + \cos(\Delta\alpha_i)\cos(\phi_i)(\beta_i - \beta_{i+1}) + \sin(\Delta\alpha_i)(\gamma_{i+1} - \gamma_i))$$

Bending moment in γ - direction

$$M\gamma_i = K\gamma (\cos(\Delta\alpha_i)\sin(\theta_i)(\alpha_{i+1} - \alpha_i) + \sin(\Delta\alpha_i)(\beta_{i+1} - \beta_i) + \cos(\Delta\alpha_i)\cos(\theta)(\gamma_i - \gamma_{i+1}))$$

Acceleration Equations

$$\ddot{Y}_i = (VY_i - VY_{i+1})/m$$

$$\ddot{Z}_i = (VZ_i - VZ_{i+1})/m$$

$$\ddot{\alpha}_i = (\cos(\phi_{i+1})\cos(\theta_{i+1})\, T\alpha_{i+1} - \cos(\phi_i)\cos(\theta_i)\, T\alpha_i - \cos(\Delta\alpha_{i+1})\sin(\phi_{i+1})\, M\beta_{i+1} + \cos(\Delta\alpha_i)\sin(\theta_i)M\beta_i - \sin(\theta_{i+1})\cos(\Delta\alpha_{i+1})M\gamma_{i+1} + \sin(\theta_i)\cos(\Delta\alpha_i)\, M\gamma_i)/I_\alpha$$

$$\ddot{\beta}_i = (\sin(\phi_{i+1})\, T\alpha_{i-1} - \sin(\phi_i)\, T\alpha_i + \cos(\phi_{i-1})\cos(\Delta\alpha_{i-1})\, M\beta_{i-1} - \cos(\phi_i)\cos(\Delta\alpha_i)\, M\beta_i - \sin(\Delta\alpha_{i-1})\, M\gamma_{i-1} + \sin(\Delta\alpha_i)\, M\gamma_i + (\Delta L/2)(VZ_i + VZ_{i-1}))/I_\beta$$

$$\ddot{\gamma}_i = (\sin(\theta_{i-1})T\alpha_{i-1} - \sin(\theta_i)\, T\alpha_i - \sin(\Delta\alpha_{i-1})M\beta_{i-1} + \sin(\Delta\alpha_i)\, M\beta_i + \cos(\theta_{i-1})\cos(\Delta\alpha_{i-1})M\gamma_{i-1} - \cos(\theta_i)\cos(\Delta\alpha_i)\, M\gamma_i - (\Delta L/2)(VY_i + VY_{i-1}))/I_\gamma$$

Verification

The ability of the model to predict static lateral buckling for the 198 cm (78 in) long beam with 5.08 cm (2 in) by 25.4 cm (10 in) cross-section is depicted in Figure 12. The ordinate of Figure 12 is the observed frequency of the model in the Z-direction. The abscissa is the ratio of the applied moment to the theoretical critical moment, [2]. Two different mass spacings are shown.

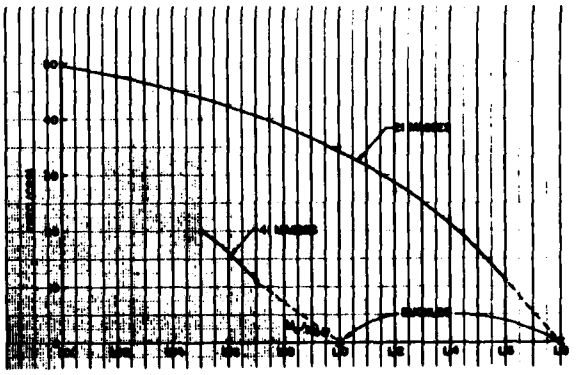

Fig.12 - Beam frequency as a function of the applied external moment M_0 with two different model definitions

As in the Euler buckling problem, this model shows an expected increase in period as the constant load, M_0 is increased. Also, the buckling load will approach the value predicted by theory as the mass spacing decreases. It should be noted that the points labeled as buckling points are not necessarily the lowest buckling values, but merely loads at which each model exhibited buckling.

GENERAL BUCKLING MODEL

Description

In order to solve some of the problems in elastic instability, modifications are made to the standard 3-D beam model; the calculation of the 3-D orientation of the tension/compression spring for Euler buckling, the calculation of the torsional component of axial stress due to twist for local buckling (angle section), and the calculation of the 3-D orientation of moment springs for lateral buckling (rectangular section).

If all of these effects were incorporated into one model, the resulting computer program could become quite cumbersome. Certainly another type of more general spring-mass model should be developed. Such a model should not require the analyst to know the actual buckling mechanism which might occur in the structural system problem before the program is run. Also, the possibility of including yielding effects should be kept in mind.

Model

All of the buckling problems considered so far involve axial stress; whether directly, as in Euler and local buckling, or indirectly as in the lateral buckling problem (pure moment loading may be considered a combination of tension and compression). In order to account for all three modes of buckling in one model it was necessary to replace the two

bending springs and the one tension/ compression spring with a group of tension/compression springs, each with possible components in all three directions. This spring group approximates the stress distribution over the cross-section of the beam.

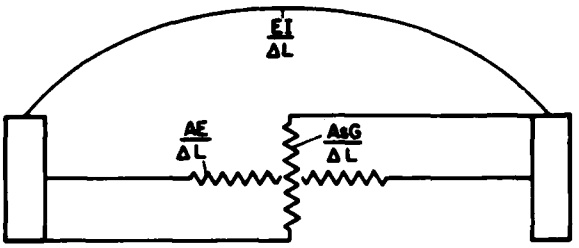

ELASTIC/STABLE

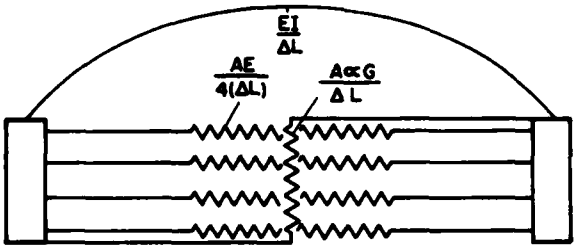

ELASTIC/UNSTABLE

Fig.13 - General buckling model (2-D)

Figure 13 illustrates a 2-D beam model with the old arrangement for stable elastic problems and the new arrangement. Shear forces and their contribution to bending are still calculated as given before in the discussion of the basic beam model.

Assuming that the tension/compression springs are evenly spaced, the first modeling decision is the number of springs. Table 1 shows the ratio of effective area moment of inertia of the spring group to the actual area moment of inertia of the rectangular cross-section as a function of the number of springs. Since it is more efficient to use less springs, and a mathematical model is usually stiffer than the real structure, four springs are recommended (4 by 4 or 16 springs in a 3-D model).

All of the effects necessary to predict the buckling modes presented in this report are present in this new model and are obtained by;

1. following the motion at each end of every spring,

TABLE 1

PERCENTAGE OF AREA OF INERTIA AS A FUNCTION OF NUMBER OF SPRINGS ON RECTANGULAR SECTION FOR A 2-D BUCKLING STUDY

Number of Springs	Effective Inertia X 100 / Actual Inertia
1	0
2	75
3	88.9
4	93.75
5	96
6	97.22
7	97.96
8	98.44
9	98.765
10	99

2. calculating the new length and force of every spring, and

3. calculating the contribution of the springs for each of the six degrees of freedom of both masses to which the springs are attached.

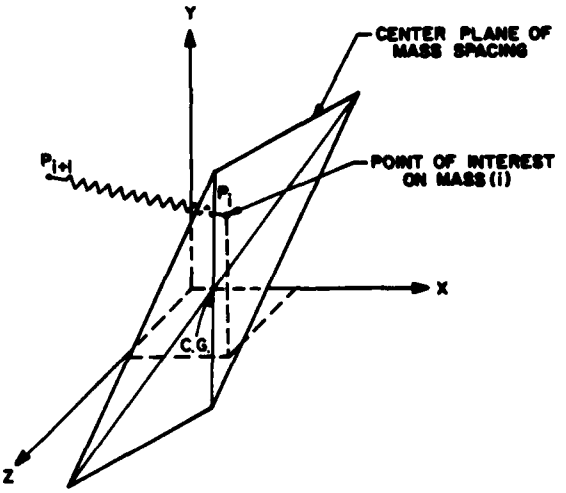

Fig.14 - Location of end point of a spring with respect to the C.G. of a mass

The following procedure describes how this is done for one point of interest as shown in Figure 14:

1. known from this time increment

$\dot{\alpha}_i$ $\dot{\beta}_i$ $\dot{\gamma}_i$ (rotational velocites of mass of interest)

X_i, Y_i, Z_i (location of mass with respect to original position)

known from last time increment X^*_{pi}, Y^*_{pi}, Z^*_{pi} (location of point of interest with respect to c.g. of mass)

calculate new position of point with respect to c.g. of mass assuming small incremental rotations

$$X_{pi} = X^*_{pi} + (\dot{\beta}_i)(\Delta t)(Z^*_{pi}) - (\dot{\gamma}_i)(\Delta t)(Y^*_{pi})$$

$$Y_{pi} = Y^*_{pi} + (\dot{\gamma}_i)(\Delta t)(X^*_{pi}) - (\dot{\alpha}_i)(\Delta t)(Z^*_{pi})$$

$$Z_{pi} = Z^*_{pi} + (\dot{\alpha}_i)(\Delta t)(Y^*_{pi}) - (\dot{\beta}_i)(\Delta t)(X^*_{pi})$$

calculate the position of this point with respect to the original position

$$\Delta X_{pi} = X_i + X_{pi}$$

$$\Delta Y_{pi} = Y_i + Y_{pi}$$

$$\Delta Z_{pi} = Z_i + Z_{pi}$$

Since the end points of the springs connected to a mass are assumed to lie in a plane (straight line if 2-D model), it is not necessary to follow every end point. Because three points define a plane, only two end points plus the mass C.G. locations are sufficient to define the locations of the other end points on the plane.

2. calculate the new length and force in the spring

$$X_L = \Delta X_{pi} + \Delta X_{i+1} + \Delta L$$

$$Y_L = \Delta Y_{pi} + \Delta Y_{i+1}$$

$$Z_L = \Delta Z_{pi} + \Delta Z_{i+1}$$

$$D = \sqrt{X_L^2 + Y_L^2 + Z_L^2}$$

Force

$$F = K(\Delta L - D)$$

3. calculate the load in all six directions for each mass

load in X-direction, mass (i) = $F_x = F(X_L/D)$

load in Y-direction, mass (i) = $F_y = F(Y_L/D)$

load in Z-direction, mass (i) = $F_z = F(Z_L/D)$

load in X-direction, mass (i+1) = $-F_x$

load in Y-direction, mass (i+1) = $-F_y$

load in Z-direction, mass (i+1) = $-F_z$

load in α-direction, mass (i) = $(F_z)(Y_{pi}) - (F_y)(Z_{pi})$

load in β-direction, mass (i) = $(F_x)(Z_{pi}) - (F_z)(X_{pi})$

load in γ-direction, mass (i) = $(F_y)(X_{pi}) - (F_x)(Y_{pi})$

load in α - dir., mass (i+1) = $-(F_z)(Y_{pi+1}) + (F_y)(Z_{pi+1})$

load in β - dir., mass (i+1) = $-(F_x)(Z_{pi+1}) + (F_z)(X_{pi+1})$

load in γ - dir., mass (i+1) = $-(F_y)(X_{pi+1}) + (F_x)(Y_{pi+1})$

When compared to the models of the previous sections, this logic is relatively simple to use. With this model, rectangular sections may be joined (as was done for the angle section) to form more complicated shapes, such as "I" beams where the entire cross-section does not remain plane under lateral or torsional buckling loads.

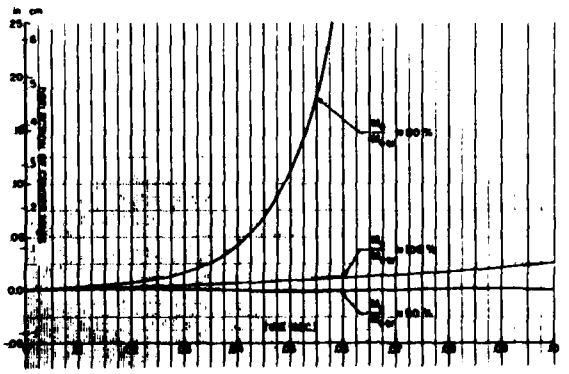

Fig.15 - Center mass motion of a beam loaded with a constant external moment, M_o, and given an initial small pertubation at the center

Verification

Two problems are utilized to examine the new model. The first problem is the lateral buckling of a narrow rectangular cross-section subjected to pure moment. The second problem is the column buckling of an "I" beam.

The results of the first problem are shown in Figure 15. The beam has the same dimensions as in the previous section and is simulated by 13 masses. The figure shows the deflection time histories of the center of the beam for three different values of the constant externally applied moment, M_0. As before, the center of the beam is given a small perturbation to get it moving. It is obvious that buckling will occur between 90% and 110% of critical loading. It appears that a loading of 100% critical is very close to the value necessary to buckle the model. The predicted critical moment is more accurate than that calculated in the previous lateral buckling problem because the effective area moment of inertia was lower than the real inertia, as indicated in Table 1.

The second problem is solved using three rectangular beam models connected to form an "I" beam with seven masses per beam. The connections between masses on different beams is the same type (with different spring constants) as between masses on the same beam. The model demonstrated buckling at 104% of critical load and did not buckle at 93%.

These two problems demonstrate that the new model and logic is proper.

PLASTICITY MODEL

Description

As mentioned in the last section, a general buckling model should be developed with forethought to elastic-plastic phenomena. Since the general model does allow for an approximation of the axial stress distribution, it is possible to monitor each spring on a mass surface so that a different point and slope on the stress-strain curves can be defined for each spring. These curves are dynamic in that they can change during a simulation due to permanent set. Logic of this type allows for elastic and plastic regions on the same cross section at the same time.

The problem considered in this section is based on an experiment performed at Brown University (test #S12, [3]) in which a mild steel frame, subjected to a concentrated explosive pressure pulse of short duration, exhibits viscoplastic behavior during large deflection. The impulse from the explosion is calculated in [3]. This impulse is used to obtain the initial velocity of the loaded area of the frame for the simulation presented in this section.

Model

In the General Buckling Model section, a logic was described that followed the end points of each spring, calculated new lengths and force, and found the contribution to the acceleration equations for each spring for each time increment. In the plasticity model, everything remains the same except for the force equation,

$$F = K(\Delta L - D).$$

Where K will be replaced by a nonlinear relationship if the force has exceeded the elastic region.

In this model, yielding (nonlinearity) will only occur in the individual tension/compression springs. This is accounted for by prescribing data such as is shown in Figure 16 as the initial form of the stress-strain curves used to calculate force. This data is based on information given in Ref. [3] and is used in the sample problem for this section. Permanent set is also accounted for, thus the stress-strain curves will be changing throughout the simulation.

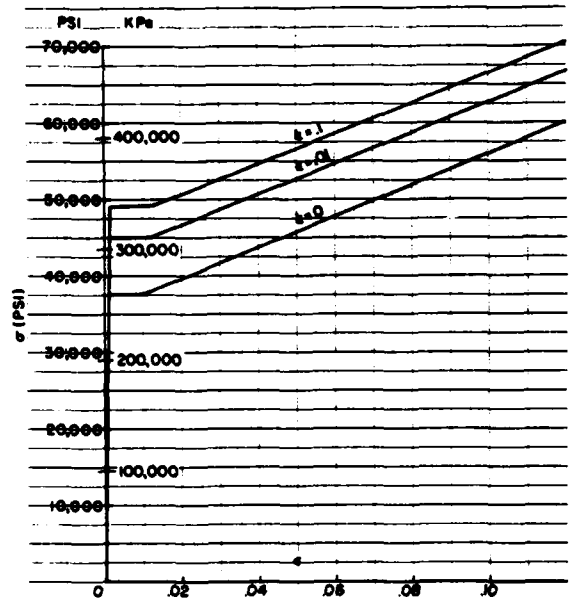

Fig.16 - Stress-strain-strain rate for plasticity model

The known quantities, logic, and equations necessary to incorporate Figure 16 into the model are:

1. Known from the preceeding time increment

   D_0 (length of spring)

D_{us} (unstressed length of spring, $\Delta L \pm$ permanent set)

ΔD_e (amount a spring can deform and still remain elastic, this comes from the $\dot{\epsilon} = 0$ curve on Figure 16)

2. Known from the current time increment

   D (length of spring)

3. Then, calculate the absolute value of strain rate,

   $\dot{\epsilon} = (D_0 - D)/((\Delta L)(\Delta t))$;

   calculate the percentage increase in yield strain due to strain rate effects

   $Q = (\dot{\epsilon}/40)^{.2}$) (refer to [3]);

   calculate the amount the spring may deform and remain elastic based on strain rate effects,

   $\Delta D_{sr} = (1. + Q)\ \Delta D_e$;

   calculate the change in length of the spring from its unstressed length,

   $\Delta D = D_{us} - D$

   If, $|\Delta D| \leq D_{sr}$, then calculate force as $F = K\Delta D$ and the logic is complete for this spring.

   If, $|\Delta D| > \Delta D_{sr}$, then calculate the static yield stress $\sigma = E\Delta D_e/\Delta L$

   And, calculate strain $\epsilon = |D_{us} - D|/\Delta L$

   If, $\epsilon \leq .01$, set $E_Y = 0$. (E_Y = Stress/Strain).

   If, $\epsilon > .01$, set $E_Y = 18{,}333$.

   Calculate the change in stress above yield,

   $\Delta\sigma = E_Y\ (|\Delta D| - \Delta D_{sr})/\Delta L$;

   and, the stress with strain rate effects is,

   $\sigma_{sr} = (1 + Q)\ (\sigma + \Delta\sigma)$.

   The new unstrained length of the spring is,

   $D_{usn} = D_{us} - (|\Delta D| - \Delta D_{sr} - (\Delta\sigma\Delta L/E))\ \Delta D/|\Delta D|$
   Calculate the new ΔD_e,

   $\Delta D_{en} = (\sigma + \Delta\sigma)\ \Delta L/E$.

   And finally, the force for one spring is

   $F = A(\sigma_{sr})\ \Delta D/|\Delta D|$ (where, A is the portion of the cross-sectional area acted on by one spring).

   The logic is simplified when strain rate effects are excluded.

   Note that shear forces and summation of moments is still calculated as in the previous section (General Buckling Model)

Verification

Figure 17 shows a 20.32 cm (8 in) high by 30.48 cm (12 in) long frame which was subjected to an explosive charge on the center steel block.

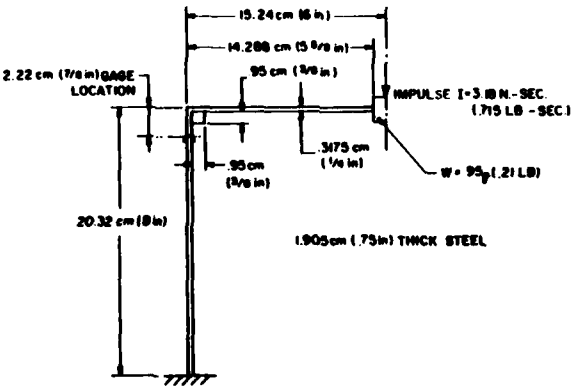

Fig.17 - Test setup for elestic-viscoplasitc problem

Only plane motion was considered in the model which necessitated four springs per face. Since symmetry was assumed, only half of the frame is modeled. The vertical leg was modeled with sixteen masses and the horizontal member by eleven masses.

The results of the simulation of this event are shown in Figures 18, 19 and 20. In Figure 18 the model strain histories at the top of the vertical columns are presented along with test results. The observed frequencies differs by about only 10% from test, the initial buildup does not match, and the final permanent set is within 83% of test. The model displacement history of the center steel block is given in Figure 19. The reader will notice that the frame is still oscillating at time = .043 sec (there is no damping included in the model). Probably the most important result is shown in Figure 20, which compares the final deflection of the frame model with the test result. The final deflection of the test is shown as a solid line and the model result, shown as a dashed line, is obtained by averaging the residual oscillation of the model.

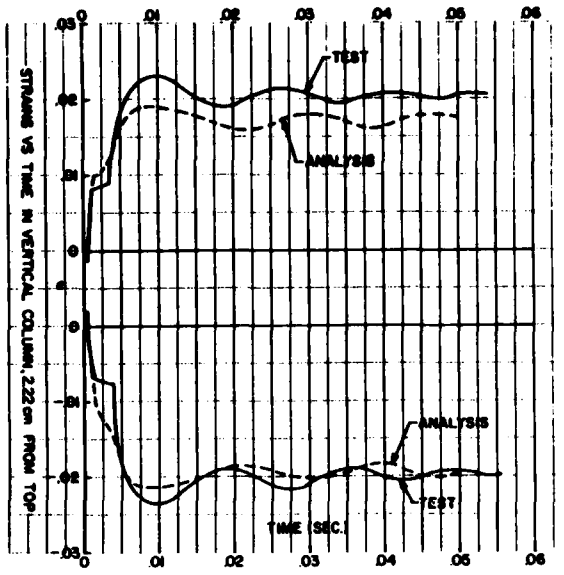

Fig.18 - Strain at gage location (top of column)

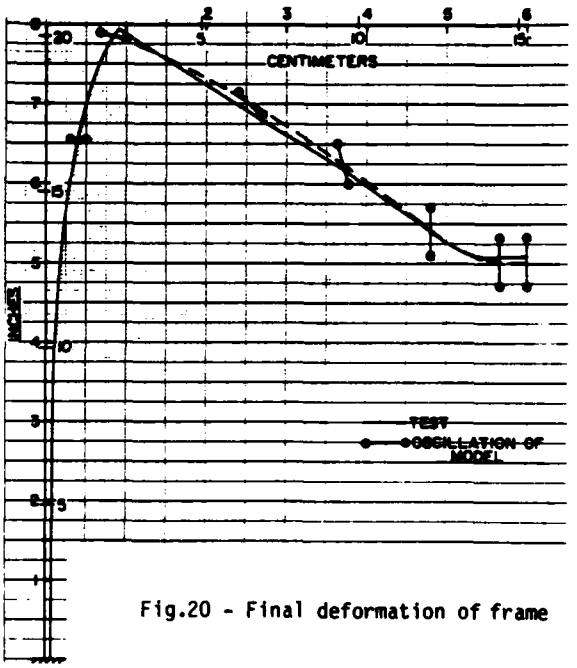

Fig.20 - Final deformation of frame

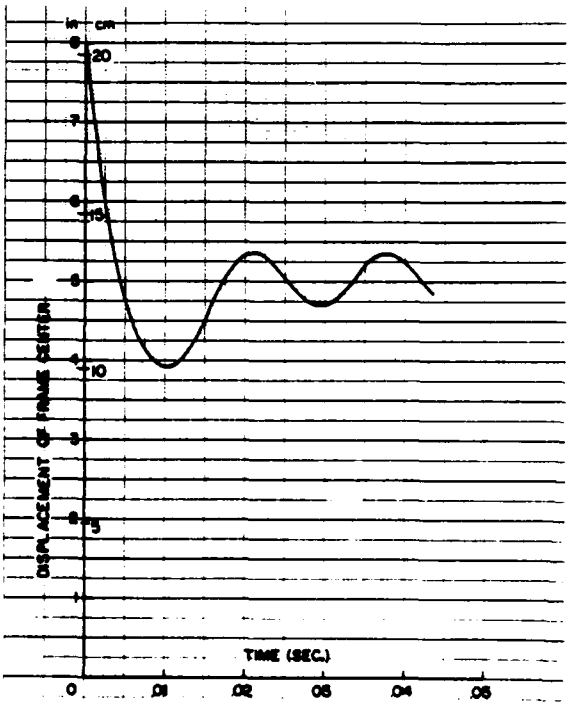

Fig.19 - Vertical frame motion (center)

CONCLUSION

The procedures developed herein for buckling of structures appears to have some validity with respect to static and dynamic buckling responses of compression members.

For computer efficiency, the first three models should be used if the mode of buckling is known. The general model should be used if the buckling mode is unknown.

The yielding model shows promise but only one comparison to test data has been attempted.

ACKNOWLEDGEMENT

The author wishes to express his appreciation to the M&T Co. of King of Prussia, PA, for their cooperation in preparation of this paper.

REFERENCES

1. Brooks, R.P. and McNaight, B.D., "Mathematical Model of a Typical Floating Shock Platform Subjected to Underwater Explosions,". The Shock and Vibration Bulletin, Part 2, Structural Analysis, Design Techniques, Bulletin 43, p. 143-163, June 1973

2. Timoshenko, S.P. and Gere, J.M., Theory of Elastic Stability, McGraw-Hill Second Edition, 1961

3. Bodner, S.R. and Symonds, P.S., "Experiments on Dynamic Plastic Loading of Frames,". Int. J. Solids Structures, Vol. 15, pp. 1-13, 5 June 1978

LOW ORDER DYNAMIC MODELS OF INDIAN REMOTE SENSING SATELLITE

M. Sambasiva Rao, B.G. Prakash and M.S.S. Prabhu
Structures Division, ISRO Satellite Centre,
Bangalore 560 017, India

Simple low order equivalent dynamic models of Indian Remote Sensing Satellite (IRS) are generated. The models consist of physical elements like springs, beams, etc., with lumped masses. Two decoupled models, one in longitudinal and the other in lateral direction, are generated representing the dynamic characteristics of the satellite adequately in the low frequency range of 0-100 Hzs. A building-block approach is followed in systematically constructing the models. First, conceptual models are generated based on the study of load paths, modes of vibration etc., from a detailed finite element analysis of IRS already made. The important spacecraft subsystem models are derived by simulating their base-fixed modes of interest using equivalent physical single degree of freedom systems by matching the frequencies and modal effective masses. This required a new approach in representing subsystems with multi-node interfaces for their equivalent masses and forces. Lastly the subsystem models are assembled and interface elements are tuned to match with the basic dynamic behaviour of IRS as observed from detailed finite element analysis. The dynamic models so constructed are used in the coupled dynamic analysis of the spacecraft and the launch vehicle and the design loads of spacecraft are refined. Also the models are used in carrying out many parametric studies to obtain changes in the dynamic behaviour of the spacecraft with design changes.

1. INTRODUCTION

A spacecraft is subjected to the most severe environment of its mission during the launch phase and it depends on the vehicle and spacecraft dynamics and their interaction. Since this interaction cannot be obtained before the spacecraft design is completed, an initial estimate of the design loads of the spacecraft is arrived at by performing a coupled dynamic analysis of the spacecraft with the vehicle assuming the spacecraft to be a rigid mass. Alternatively, previous experience with other similar spacecraft launched with the vehicle is also used in defining the initial dynamic environment for the spacecraft. However, a better load definition is obtained by carrying out a detailed coupled analysis of launch vehicle and spacecraft using the flexibility characteristics adequately [1]. The results of this coupled analysis then provide the refined loads useful for validating/improving the design of the spacecraft and its subsystems. Further, during the qualification tests, since the spacecraft is tested as a base-fixed system as against the flexible support provided by the vehicle in flight, the spacecraft loads would be generally higher than in actual flight. Realistic simulation of such base impedence in tests using a vibrator system is still in the infancy [2] and overtesting is generally controlled by 'notching' the input based on the results of detailed coupled analysis.

Dynamic models of spacecrafts developed for launch vehicle/spacecraft coupled analysis should possess some desirable characteristics which are the outcome of the functional needs of these models. Firstly, in the initial stages of a spacecraft project, not only design loads are approximate, but also there could be choices in the launch vehicle. The design of the spacecraft itself will not be available in all details. To work within these constraints, the dynamic model of the spacecraft should be as small as possible to be cost effective in conducting repeated analyses for accurate load definition with different environments. The small size also helps in carrying out parametric studies with respect to the spacecraft design. Secondly, it is desirable that the model be built up from simple physical rather than mathematical elements to simulate important subsystems. Mathematical elements are nothing but condensed

stifness and mass matrices which may correspond to physical and/or modal coordinates. The choice of physical elements mainly helps in identifying a major subsystem in the model, in computing loads on the subsystem straight away from coupled analysis and in directly linking changes in dynamic model to frequent changes in the design of the subsystem early in the project. Thirdly, the model should satisfactorily represent the flexibility characteristics of the spacecraft and the subsystems in the low-frequency spectrum of interest (generally 0-100 Hzs range). Fourthly, it is preferable to develop models separately in longitudinal (along vehicle axis) and lateral directions. This follows from the fact that most of the launch vehicles are axi - symmetric in nature and their models are generated decoupled in longitudinal and lateral directions.

The use of simple low order dynamic models for spacecraft structures is well recognised in literature and some procedures are available [3-7] for generating such models. Of all these procedures, the approach which uses modelling of important modes of a subsystem by equivalent single degree of freedom systems is the most attractive. These principles were applied at complete structural system level, in a previous paper [8], to derive an equivalent low order dynamic model of METEOSAT spacecraft. The spacecraft had a single (statically determinate) interface node with the APPLE spacecraft attached to it and the dynamic model was built using spring-mass systems and cantilever beams, carrying tip mass and inertia. The equivalent single d.o.f. system for a mode is obtained by matching the 'effective mass' (when a structure is subjected to base acceleration, the reaction forces/moments developed at the base can be expressed as a series summation where each term represents the contribution from a base restrained elastic mode of the structure which, in turn, is given as a product of base input acceleration, a transfer function and a characteristic mass associated with the mode called 'effective mass'. The modal effective mass is a square symmetric matrix corresponding to base d.o.f. and is independent of the type of normalisation performed on the mode) and natural frequency of the particular mode with the corresponding quantities of the model. As the sum of the effective masses of all modes of a structure is equal to its total mass it is necessary to represent in the model only such modes which have significant effective masses in relation to the rigid mass. The contribution of left out modes is represented by a so called rigid 'residual' mass. These effective mass principles are so far used in modelling structural systems having single node at the 'base' or interface with another system. Generally, spacecraft subsystems have multi-node interfaces with other subsystems and some important modifications are needed before effective mass concepts can be used to model such subsystems.

The present paper describes the generation of low order dynamic models of Indian Remote Sensing (IRS) Satellite. IRS is a first step in evolving an operational spacecraft to obtain timely, reliable and accurate information in the fields of agriculture, hydrology and geology for the natural resource management system. It is a sun-synchronous 3-axis stabilised system scheduled for launch in 1986. Two decoupled models of IRS representing the longitudinal and lateral behaviour of the spacecraft are developed as required by the launch vehicle authorities.

The development of equivalent dynamic models of IRS started with a conceptual model evolved on the basis of load paths, and location of major subsystems in the actual spacecraft. The results of static and free vibration analysis of a large detailed finite element model of the spacecraft [9] also provided an important data in arriving at the conceptual model. Each important subsystem is represented in the model by one or more of its base node(s)-fixed elastic modes, simulated by an equivalent simple single d.o.f. system like a spring-mass or a beam with a lumped mass. The selection of modes retained for representing a subsystem is based on their effective masses, obtained from a detailed analysis of the subsystem. The subsystem models thus generated are then connected in such a way that the complete model can represent the overall behaviour of IRS spacecraft as observed in the global modes of free vibration analysis of detailed finite element model. To account for the joint flexibility between subsystems, flexible springs are introduced at nodes corresponding to the interfaces. The stiffness of these springs are initially assumed based on the properties of actual elements joining the subsystems. Later they are tuned so that the results of the dynamic model match with the results of detailed finite element analysis. Except for the sizing of various physical elements used in the dynamic model, the entire configuration of the model is visualised at the conceptual model stage itself.

The IRS dynamic models thus developed are used in the coupled analysis of launch vehicle and spacecraft. The refined design loads are generated and used in validating the spacecraft design adequacy. Test specifications for the spacecraft and its subsystems are suitably modified. The simple dynamic models are also utilised in several parametric studies aimed at improving spacecraft design.

2. DETAILED FINITE ELEMENT ANALYSIS OF IRS STRUCTURE

2.1 Description of the structure

A brief description of IRS structure is given here for the purpose of an easy understanding of the modelling of the structure. Fig.1 shows a disassembled view of the spacecraft indicating the major structural elements and subsystems. The structure basically consists of ;

(a) a box like structure made up of four vertical decks V1, V2, V3 and V4 and two horizontal decks at the top and bottom. All the decks are of honeycomb construction and carry subsystem packages. They are connected to each other all along their common edges by a framework of angles.

(b) a main cylinder stiffned internally by 20 longitudinal stiffeners forming the major load transfer path. The top of the cylinder is attached to the top deck through a stiffening ring (angle) and the bottom is attached to the bottom deck. There is an intermediate ring (channel) which provides circumferential stiffening to the cylinder around the middle level.

(c) an interface ring (channel) with its top attached to the bottom of the cylinder. Its bottom interfaces with the launch vehicle at 4 points through lugs.

(d) an RCS deck (honeycomb) located midway in the cylinder and attached to the intermediate ring through 20 support brackets. This deck carries fuel tanks and other RCS elements for the control of the spacecraft.

(e) four main struts connecting the cylinder assembly with the bottom deck. They run between the intermediate ring and the bottom deck corners with pin-jointed ends. In addition to main struts there are 3 secondary struts on either side of the cylinder connecting the vertical decks V2 and V4.

The global axes system followed throughout the analysis work is shown in Fig.1.

2.2 Finite Element Analysis

A detailed dynamic analysis of the spacecraft structure is carried out by the application of finite element method using static condensation procedures available in the general purpose finite element software package ASKA. This work forms a part of detailed static and dynamic analysis of the satellite structure carried out by our entire group. Only relevant details needed for the purpose of this paper have been extracted from Ref.[9]. The IRS structure which is divided into 21 substructures is idealized by space frame and flat-shell elements. Structural elements such as stringers, stiffener rings, main and secondary struts, etc., are idealized by space frame elements which have the capability to account for eccentricity between a node and centroid of the beam. The cylinder and other honeycomb panels are idealized using flat-shell elements which incorporate the distance between face sheets of the honeycomb element, but the effect of the core material is not included. Local coordinate systems (different from global system) have been appropriately defined at many nodes of the structure. This, together with the condensation of relevant boundary degrees of freedom at substructure level, is used to define 'hinges' at relevant nodes in the required directions. Fig.2(a) shows the disassembled view of the finite element idealisation of the IRS structure showing various constituent substructures. The sketch does not show all the elements but shows only a selective view corresponding to dummy flange elements introduced for ease of understanding and clarity in plotting.

The detailed finite element model has a total of 2419 effective degrees of freedom out of which 1406 d.o.f. are condensed out at the substructure level and the remaining 1013 are carried to the main structure assembly. Whereas all the main structure equations are straight away used for static displacement and stress analysis, a further static condensation to the level of 485 d.o.f. (retained) is carried out for free vibration analysis. Mass and inertia properties of IRS spacecraft computed using this model are given in Table 1(a).

Results obtained for the first 35 system frequencies (upto 100 Hz) are given in Table 1(b) along with brief description of modes of vibration. Of these, the first three modes correspond to the global modes and are shown graphically in Fig.2(b,c,d). The remaining are mostly local subsystem modes. These results are carefully studied before deciding on which global and local modes should be represented in the low order dynamic models of IRS. Clearly the dynamic model must be able to represent the fundamental global longitudinal and lateral modes and also the important modes of major subsystems like top and bottom decks, vertical decks, RCS deck, etc., which fall within the frequency range of 0-100 Hzs. Though it is observed that there are several modes which come under this category all are not equally important. The question of finding out which of these modes are really important is sorted by performing a free vibration analysis of each major subsystem for its base-fixed modal effective masses and is discussed in a later section.

3. DEVELOPMENT OF DYNAMIC MODELS OF IRS

3.1 Conceptual Model

First an attempt is made here to evolve an equivalent low order dynamic model for IRS, conceptually. This forms an important step because as pointed out earlier, the complete framework of the model is frozen at this stage. It includes identifying major spacecraft subsystems to be represented in the model, simulation of these subsystems by simple equivalent single d.o.f. systems with the provision that they can be easily modified later to accommodate the subsystem design changes and assembling the models of the subsystems to represent the overall behaviour of the spacecraft. The physical nature of the spacecraft as per the structural design and the various equipment deck layouts and results of static and free

vibration analysis of detailed finite element model provide the necessary information to form the conceptual model. The next logical step is the estimation of the stiffness values of various physical elements and nodal masses to be used in the model. This is followed by tuning these values to match the behaviour of the dynamic model with that of the detailed finite element model. The entire procedure of obtaining simple low order models starting with a conceptual model is shown in the flow chart in Fig.3.

The mass distribution on IRS structure indicates that the vertical decks V2 and V4 are heavier than V1 and V3 and a sort of symmetry exists about the plane YZ (Fig.1). The symmetry can also be seen from the data given in Table 1. Therefore the plane YZ is chosen for representing the dynamic characteristics of the spacecraft in the small order model. The symmetry also helps in reducing a complex 3 dimensional structural system into a 2 dimensional system. Further, the design and detailed analysis of the spacecraft, allow generation of two separate decoupled models for representing longitudinal and lateral behaviour, further reducing the size of each model.

(i) Model for lateral vibration

When the structure vibrates in the YZ plane in the lateral direction (Y), it is reasonable to assume that the decks V1, V3, top and bottom decks act like rigid members. This follows from the fact that the equivalent in-plane stiffness of the honeycomb decks is much larger than the bending rigidity. Thus only V2 and V4 decks participate as elastic members in the vibration of box-like structure (see 2.1) and need to be modelled. The boundary condition for these decks correspond to a case in between all edges simply supported (SSSS) and all edges clamped (CCCC). Top, bottom, V1 and V3 decks being quite stiff in their own planes provide a simply supported condition along the edges of V2 and V4. The angle members running all along the edges of the box provide restraint against edge rotation whose magnitude depends upon the torsional rigidity of the angles. This is also supported from a review of detailed finite element analysis results [9]. However, to start with, this rigidity can be neglected and V2 and V4 modelled as SSSS decks mainly from the point of view of convenience. Finally by using flexible torsional springs (with one end grounded) at the edges, suitable edge conditions can be simulated. In addition it is assumed that secondary struts also provide a point support to the decks at the place of their attachment. Now V2 and V4 can be modelled by beam mass systems ABC and DEF respectively as shown in Fig.4, using the principles indicated in Appendix . Each beam mass system (ABC or DEF) consists of one or more parallel beams having a lumped mass or inertia. Each beam is an equivalent single d.o.f. representation of an important base-fixed elastic mode of the deck V2 or V4 and is obtained by matching the effective mass and natural frequency of the corresponding mode. The modes selected for simulation in the model are based on the frequency range of excitation, here 0-100 Hzs, and the relative value of modal effective mass as compared to the subsystem rigid-mass. After accounting for such 'dynamic masses' of the deck in this way, the residual or 'static mass' is lumped at the base or supports of the deck, such that the centre of gravity of the model remains same as that of the subsystem. The parallel beam arrangement for a subsystem has the advantage that any future modifications in that component can be easily accommodated in the model without affecting the other components.

The stiffened cylinder and the interface ring are mainly stiffness elements, their mass being quite low. From the first and second modes of vibration of IRS as seen from the results of detailed analysis, it can be concluded that the cylinder behaves more like a cantilever beam. The cylinder aspect ratio i.e., length to diameter, being small (of the order of 1) it is necessary to include both bending and transverse shear deformations in the beam model used for simulating the cylinder. Thus the cross sectional moment of inertia of the cylinder due to lumped areas of the various stringers on the periphery and also the shape factor, given as the ratio of average to maximum shear flow in the cylinder cross section when subjected to transverse shear force, are computed and incorporated in the beam model as the initial estimates. As both top and bottom decks are quite rigid in lateral (Y) direction, the beam model of the cylinder can be directly connected to the middle points of rigid beams representing the top and bottom decks as shown in Fig.4.

The main struts connect the cylinder and the bottom deck. As the bottom deck is assumed to be rigid in the lateral dynamic model, the flexibility of main struts need not be represented. On the other hand the secondary struts which connect the main cylinder with V2 and V4 are mainly stiffness elements and considerably affect the vibration of the decks. The struts are long, slender and pin-ended. These characteristics of the struts enable us to simulate them by equivalent linear springs in the dynamic model, as shown in Fig.4. The detailed analysis results also support this as no significant bending of the struts is observed.

The RCS deck is one of the heavy and major subsystems in IRS. The mass distribution on this deck is such that it has a large moment of inertia about the middle plane of the deck. Consequently, whether IRS is vibrating in lateral or longitudinal direction RCS deck undergoes out-of-plane vibration. Based on modal effective masses, suitable equivalent spring mass systems are constructed to model the RCS deck behaviour in spacecraft lateral vibration. The RCS subsystem

model is represented by IJ in Fig.4.

Fig.4 thus shows the conceptual dynamic model of IRS in lateral direction developed as explained above.

(ii) Model for longitudinal vibration:

When the spacecraft vibrates in the YZ plane in the longitudinal direction (Z), all the vertical decks V1, V2, V3 and V4 behave like rigid elements and only the top, bottom and RCS decks need simulation in the dynamic model as elastic members as far as the box-like structure is concerned. The vertical decks provide simply supported edge conditions for the top and bottom decks. The cylinder also provides a simply supported condition for top and bottom decks all along its interface. This is due to the fact that the vertical decks and the cylinder are relatively stiff in the longitudinal direction. As in the lateral model, equivalent parallel beam-mass systems are generated for top and bottom decks. These systems have 4 point supports as indicated by ABCD and EFGH in Fig.5 for top and bottom decks respectively. Again flexible torsional springs are provided at the support points to account for the rotational restraint generated by stiffening members like angles and channels running all along the interface edges of these decks.

From the first mode of vibration of the IRS structure as indicated by the detailed analysis it can be observed that it involves the vibration of only vertical deck assembly moving parallel to cylinder axis, the cylinder periphery providing support for both top and bottom decks. This behaviour cannot be represented by the dynamic model if we connect by linear elements the middle points of top and bottom decks as is done in the lateral model. An intermediate support corresponding to the actual periphery of the cylinder should be provided in the model for the top and bottom decks. To achieve this objective, the cylinder is modelled by equivalent linear springs and joined with the top and bottom decks as shown in Fig.5.

In the longitudinal vibration, the secondary struts do not play any role as they are connected to the vertical decks which are assumed to be rigid. The main struts, however, are simulated by equivalent linear springs joining the middle of the cylinder with ends of bottom deck. The RCS deck is again simulated by an equivalent spring mass system as in the lateral case and is identified by IJ in Fig.5.

The complete conceptual dynamic model of IRS derived using the above ideas is shown in Fig.5.

3.2 Simulation of subsystems

In order to determine the physical properties of various elements visualised in the conceptual model, the major subsystems are analy sed individually using detailed finite element idealisations similar to the ones employed in the detailed structural analysis of the spacecraft. General purpose structural analysis program ASKA is extensively used in these analyses and the details of the results are discussed here.

(i) The main cylinder: The stiffened cylinder is divided into two elements cutting it off at the level of RCS deck. The cross section of the cylinder is simplified as a thin shell with lumped areas corresponding to stringers on its periphery. The equivalent spring constant of each element representing the cylinder in the longitudinal direction is computed from the cross sectional area and length. Similarly the moment of inertia of the beam element used for simulating lateral vibration characteristics of the cylinder is obtained from the second moment of the lumped areas on the simplified cross section. The shape factor K_T is also calculated for the beam (.312) as the ratio of average and maximum shear flows in the cylinder when it is subjected to a transverse symmetric load. To check the adequacy of the beam model in the lateral direction, both the detailed finite element model and the equivalent model of the cylinder are subjected to unit tip load with their base clamped. The displacements obtained indicated good matching. The uniformly distributed mass of the cylinder is lumped at the 3 nodes in the model using a lumped mass approach.

(ii) The struts: The main struts (2 Nos. on either side of cylinder) and the secondary struts (3 Nos. on either side of the cylinder) are assumed to behave like uniform rods. Thus they have only axial stiffness based on their cross sectional area and length and are located in different directions. Their effective spring constants are computed taking into account their new length and number (one on each side of the cylinder) of springs representing them in the dynamic model. Only main struts are simulated in the longitudinal model and only secondary struts are simulated in the lateral model.

(iii) The RCS deck: The detailed finite element idealisation of RCS deck is used with its boundary simply supported in obtaining its free vibration frequencies and the effective masses of the corresponding modes. Because of the multinode interface of RCS deck the total reaction force transmitted to the base when the entire base is subjected to unit longitudinal acceleration is computed as effective mass of a mode in the longitudinal direction. Knowing this mass and the corresponding frequency in the longitudinal direction, the mode is simulated in the model by a spring-mass system where the mass equals the effective mass. A similar approach is followed in the lateral case also. The details of RCS deck analysis are shown in Table 2(a). It is found necessary to simulate only one mode each in the longitudinal as well as in the lateral models. The rest of the mass of the subsystem after subtracting the 'dynamic mass' is lumped at the base of the RCS model which corresponds

to middle point of the cylinder.

(iv) V2 deck: In the longitudinal model, V2 deck is simulated by linear springs of large stiffness to represent its rigidity. Its rigid mass including that of the solar panels, is lumped at both the ends of the spring such that the centre of gravity is at the same level as that obtained in the detailed analysis of V2 deck. For obtaining the equivalent beam-mass models of the deck to represent its out of plane behaviour, modal effective masses of the deck are computed with respect to the 3 lateral support d.o.f. corresponding to top and bottom decks and secondary struts. Because of statically indeterminate nature of the beam in this case, effective forces corresponding to unit lateral base acceleration are matched between the modal model and the deck by a trial and error procedure in addition to matching the natural frequencies. The results of the free vibration of V2 deck are shown in Table 2(b). An example calculation for the equivalent beam-mass representation of the deck mode is given in the Appendix.

(v) V4 deck: The procedure adopted for obtaining equivalent models for this deck is similar to that of V2 deck and the results of free vibration of V4 deck are included in Table 2(c).

(vi) V1 and V3 decks: Their total mass is simulated in the models at the four corners corresponding to the edges of top and bottom decks, such that the CG is properly represented.

(vii) Top and bottom decks: In the lateral model these are represented as rigid beam members. In the longitudinal model the top deck is simulated by a beam supported at four points and carrying a mass; and the bottom deck by 2 identical beams supported at two points and carrying lumped masses. Again effective longitudinal base forces for unit base acceleration are considered for modelling these beams. The results of the free vibration analysis of top and bottom decks are shown in Tables 2(d) and 2(e) respectively.

(viii) Interface ring: The interface ring is treated as an extension of the stiffened cylinder and the same spring and beam characteristics as that of the cylinder are used in representing it in the dynamic models.

(ix) Interface joints: At all the nodes corresponding to subsystem interfaces, flexible torsional springs, with one end grounded, are introduced to realistically account for the joint flexibilities. To start with, these spring constants are set to high values.

The final longitudinal dynamic model of IRS constructed using the subsystem model data is shown in Fig.6. Similarly the lateral model is shown in Fig.7.

3.3 Tuning of the dynamic models

It may be recalled that most of the subsystem models are developed with the assumption that their interfaces with other subsystems are simply supported. This is mainly done because it is easy to simulate them by simply supported multi-span beam-mass systems. But, in the actual structure, at these interfaces, stiffening members like rings, channel or angle members exist which apply some constraint against the rotation and this must be taken into account in dynamic models also. For this purpose flexible torsional springs, with one end grounded, are included at various interface nodes in the dynamic models. Though the stiffness values of these springs can be estimated fairly well from the cross sectional geometry of the corresponding members in the spacecraft, such an exercise is not done and instead they are all initially assumed to be high. The reason for following this procedure is this: the various local modes of subsystems simulated in the model can be adjusted to match with the appropriate frequencies obtained in the detailed finite element analysis by suitably altering the stiffnesses of these torsional springs. This is true not only for local modes but for global modes too, which, however, may need tuning of some beam or linear spring elements also.

First we look at the tuning of frequencies of longitudinal model of IRS (Fig.6), which requires simulation of the overall longitudinal mode 3 (Table 1) of the spacecraft, the RCS deck mode 7 and top deck mode 15. The first mode is a global one and the latter two are local. It is also clear that adjusting slightly any of these frequencies does not seriously affect other ones. Thus tuning of each frequency can be done almost independently. The RCS mode is represented by a linear spring, element 6, in the low order model and its frequency can be manipulated through its spring constant. There are 8 torsional springs, elements 7-14, in the model which can be used for adjusting the other two frequencies. Considering that symmetry has to be maintained about Z-axis because of the nature of the model, the effective torsional spring stiffnesses at our disposal reduce to four. Further, it is easy to visualise that the global longitudinal mode frequency is sensitive to the spring stiffnesses of elements 11-14 and the top deck frequency to those of the remaining torsional springs, viz., elements 7-10. The size of the model being small (21 d.o.f.) the trial and error procedure which can be used for tuning the stiffnesses of these torsional springs to adjust the two frequencies of the model is not a difficult task. We now turn our attention to tuning the lateral model (Fig.7) frequencies of IRS. The global lateral mode 1 can be adjusted by altering the bending rigidity of the adaptor simulated by beam element 8 in the model. The first lateral mode of V4 deck i.e., mode 12 can be adjusted through torsional springs 6 and 7. Similarly the second lateral mode frequency of V2 deck can be manipulated through torsional springs 4 and 5. RCS deck frequency, (mode 13) can be corrected by altering the linear spring stiffness of element 3. Trial and error procedure can be easily employed

in tuning the lateral model element stiffnesses also as the size of the model again is quite small (21 d.o.f.).

Thus the trial and error procedure of adjusting the various stiffness constants is effected till a satisfactory tuning of important global and local mode frequencies of the dynamic models with those of detailed analysis of the structure is achieved. However, it is ensured that the final values of torsional spring constants are within the range of actual torsional stiffnesses of interface members and are not mathematical adjustments.

3.4 Dynamic Models of IRS

Complete details on stiffness parameters of various elements, nodal mass distribution, mass and inertia properties and natural frequencies corresponding to the tuned longitudinal dynamic model of IRS (Fig.6) are given in Table 3. Similar details on lateral dynamic model (Fig. 7) are presented in Table 4. A good matching of results obtained using the detailed finite element model and low order models developed in this paper can be seen by comparing Table 1 with Tables 3 and 4. For ready reference this exercise is shown in Table 5.

The dynamic models of IRS generated here mainly took into account the constraints imposed by the vehicle authorities. Consequently, two decoupled models, one for longitudinal behaviour and the other for lateral behaviour are developed. Thus a complex structure with mass distribution in 3 dimensions is reduced to a simple model in 2 dimensions. This has been possible due to the symmetry in the structure and its mass distribution in IRS. A plane with heavier mass is therefore considered for modelling. But in the process, the dynamic behaviour in the other perpendicular plane (corresponding to V1, V3 deck vibration) of IRS and also its torsional vibration characteristics could not be simulated in the model. But it is easy to see that all these aspects can be incorporated in the model if 3 dimensional low order dynamic model is generated again using the same principles of this paper. This work is currently in progress.

It is appropriate here to mention some of the limitations of the procedures mentioned in this paper in deriving equivalent low order dynamic models of structures. Simulation of modes of structures with single base node by equivalent single d.o.f. systems is straight forward but it is not so when the base has multiple nodes (or statically indeterminate). In the present paper a trial and error procedure is successfully employed in obtaining equivalent models for some systems with more than one base node. Though it is found that in such cases it is possible to generate simple single d.o.f. systems, some more effort is needed to evolve a general procedure for systematically obtaining simple models for structural systems with statically indeterminate interfaces.

4. SOME PARAMETRIC STUDIES USING IRS DYNAMIC MODELS

The small order dynamic models of IRS derived in this paper are very useful for performing parametric studies to improve the design efficiency of IRS structure. Three such studies conducted are reported here. The first one is a study on the design adequacy of the structure to accommodate possible increase in the payload at a later stage. The second one relates to raising the overall longitudinal frequency of the spacecraft and the third one aims at improving the design of secondary struts which mainly influence the behaviour of vertical decks.

The IRS payload being a very heavy package (175 Kgs) situated at the top of the spacecraft (on the top deck) exercises considerable influence on the natural frequencies and stress levels of the overall spacecraft. The present position of the payload is such that most of its mass is located directly on the main cylinder. This has a large influence on the fundamental frequency of the spacecraft in the lateral direction but not much in the longitudinal direction where the top, bottom and vertical decks move parallel to the cylinder axis. If the payload position is altered such that its mass is uniformly distributed on the top deck, it will affect the fundamental longitudinal frequency significantly. The frequency constraints imposed by the vehicle on the spacecraft are 15 Hzs in lateral direction and 30 Hzs in longitudinal direction. With the present payload configuration, the spacecraft has a fundamental lateral frequency of 25.7 Hzs and a longitudinal frequency of 36.7 Hzs. Thus there is a good margin available with respect to lateral frequency constraint but is somewhat close in the longitudinal case. So it is desirable to maintain the longitudinal frequency atleast at the present level even if there is a change, in future, in payload mass and its distribution. With this in view, a study has been made, using the low order longitudinal dynamic model of IRS, to see how the spacecraft frequencies and stresses due to static acceleration loads change with payload mass changes. The height of the centre of gravity of the payload from its base is assumed to vary proportionally with its mass. Suitable design changes are proposed to improve the situation where needed. Details of the results of the study are presented in Table 6.

From the design of the IRS structure and the free vibration analysis results it is clear that the main struts play an important role in deciding the overall fundamental longitudinal frequency of the spacecraft. It is also reasonable to assume that changing the area of cross section of the main struts (thereby altering their stiffness) is the best way to control the fundamental longitudinal frequency of the spacecraft. Thus a study of the variation of this frequency with respect to the main strut area is conducted using the longitudinal low order dynamic model of IRS. The results of the study are shown graphically in Fig.8. The present design area

for the main struts is taken as the base value (100%). The study revealed that there is considerable scope to raise the longitudinal frequency of the spacecraft by changing the area of the main struts. The frequency is observed to vary almost linearly with respect to the strut area in 100% to 300% zone.

Finally a study is carried out, using the low order lateral dynamic model of IRS, to estimate the variation of the fundamental frequency of V4 deck with respect to the cross sectional area of the secondary struts (see Fig. 9). The present design value for strut cross sectional area is taken as base value (100%). From Fig.9 it can be seen that the area of the secondary struts can be reduced to about 60% of the present value without any appreciable change in the frequency of the V4 deck.

5. SUMMARY AND CONCLUSIONS

In this paper, equivalent dynamic models are generated for Indian Remote Sensing Satellite (IRS). They are of small size, decoupled in longitudinal and lateral directions, consist of physical elements and are built-up from important subsystem models. They represent the flexibility characteristics of the spacecraft in the low frequency range and also the rigid body properties like mass, centre of gravity, inertia, etc. The advantage of having small order dynamic models of structures using physical elements are emphasised here and a method for generating such models is illustrated through IRS. It may be noted that the method, however, is quite general, can be used in other structural systems too and not restricted to spacecraft application.

Subsystem models in this paper are derived by simulating the important base-fixed modes by equivalent single degree of freedom systems. This sort of simulation is easy for subsystems with single base node where the modal 'effective mass' and frequency can be matched. But in a spacecraft where most of the subsystems have multi-node bases a different approach is required for modal simulation. In such cases the 'effective forces' at the base for unit base acceleration are matched by trial and error procedure. This procedure requires further standardisation and is being attended to. These concepts are incorporated in the general purpose finite element structural analysis program ASKA (see Fig.10) and used extensively in IRS subsystem model generations.

The dynamic models of IRS are used in the coupled analysis of the spacecraft with the launch vehicle. This has resulted in refined load levels which are used in validating and improving the design of the spacecraft and also in its qualification tests. Being small and representing the spacecraft behaviour accurately in the low frequency zone, the dynamic models are found to be very convenient in parametric studies carried out to predict changes in the dynamic behaviour of spacecraft with design changes. Currently the models are constructed in 2 dimensions, mainly due to constraints from the vehicle side, but generalisation to 3 dimensions is straight forward.

ACKNOWLEDGEMENTS

The authors gratefully acknowledge the efforts of all members of Structural Analysis Section whose structural analysis of IRS has been used in this work. The authors thank Mr. A.V. Patki, Director, Mechanical Systems Group, for his encouragement and help during the course of this work. Thanks are also due to Dr. P.S. Nair, Head, Structures Division, and Prof. S. Durvasula, Aerospace Engineering Department, Indian Institute of Science, Bangalore for their useful suggestions.

REFERENCES

1. A. Girard, J.F. Imbert and M. Vendrenne, "Payload Dynamic Behaviour Study on the Ariane Launcher", Paper presented at International Astronautical Federation (IAF) XXVIIIth Congress, Prague, 25 Sept-1 Oct, 1977.

2. A. Girard and S. Michel, "Launch Vehicle Simulation For Uniaxial Vibration Testing of Satellites", ESA Journal, 1982, Vol.6, PP 439-448.

3. H.N. Abramson, Ed. "The Dynamic Behaviour of Liquids In Moving Containers", 1966, NASA-SP-106.

4. R.M. Bamford, B.K. Wada and W.H. Gayman, 1971, "Equivalent Spring Mass Systems for Normal Modes", Jet Propulsion Lab., Calif., TM: 33-380.

5. J.F. Imbert and A. Mamode, 1977, "The Effective Mass Concept in Base Excitation Dynamics and Its Application to Solar Array Dynamics", Proc. of NASTRAN Users' Conference, Munich, MacNeal Schwindler Corporation Ed.

6. F.H. Wolf and A.J. Molnar, 1978, "Reduced System Models Using Modal Oscillators For Subsystems (Rationally Normalised Modes), Shock and Vibration Bull., No. 48, Part 1, PP 111-118.

7. M. Sambasiva Rao, P.S. Nair and S. Durvasula, 1980, "Effective Mass And Its Application to Vibration Problems", ISRO Satellite Centre, Bangalore, India, Report No. 21-80-07-05-012.

8. M. Sambasiva Rao, P.S. Nair and S. Durvasula, "Equivalent Dynamic Models For Spacecraft And Its Subsystems", Paper Communicated for Publication in ESA Journal.

9. Structural Analysis Section, April 1983, "PDR Document on Structural Analysis of IRS", ISRO Satellite Centre, Bangalore, India, Report No.IRS-ISAC-21-83-04-05-019.

TABLE I

Free Vibration Analysis Results of IRS Using Detailed Finite Element Model

(a) Mass and Inertia Properties			
Structural Mass in Kgs			150.6
Total Spacecraft Mass in Kgs			876.4
Centre of gravity location in M	$\overline{X}$	=	0.0092
(From the base of spacecraft)	$\overline{Y}$	=	0.0129
	$\overline{Z}$	=	0.8570
Moments of Inertia about spacecraft base in Kg M^2	I_{xx}	=	1.03E+3
	I_{yy}	=	0.99E+3
	I_{zz}	=	0.41E+3
	I_{xy}	=	0.19E+2
	I_{yz}	=	-0.11E+2
	I_{zx}	=	-0.12E+2

(b) Natural Frequencies and Modes

Mode No.	Frequency in Hzs	Mode Description
1	25.6	Lateral (Y) Global Mode
2	26.6	Lateral (X) Global Mode
3	36.2	Longitudinal (Z) Global Mode
4	45.0	Local Solar Panel Mode
5	45.6	Local Solar Panel Mode
6	46.0	Local Solar Panel Mode
7	46.5	Lateral Mode of V1 and RCS Decks
8	47.0	Lateral Mode of V1 and V3
9	48.1	Lateral Mode of V1 and V3
10	49.6	Solar Panel Assembly Mode
11	49.6	Solar Panel Assembly Mode
12	54.3	V4 and Solar Panel Assembly Mode
13	57.6	Antisymmetric Bending Mode of RCS and Global Torsion
14	60.1	Solar Panel Assembly Mode
15	61.1	Combined Mode of Top Deck and Solar Panel Assembly
16	62.2	Solar Panel Assembly Mode
17	62.7	Solar Panel Assembly Mode
18	63.8	Solar Panel Assembly Mode
19	65.9	Solar Panel Assembly Mode
20	67.2	Solar Panel Assembly Mode
21	68.8	Solar Panel Assembly Mode
22	70.2	Combined Mode of Vertical Decks, RCS and Solar Panel Assembly
23	72.1	Combined Mode of Vertical Decks, RCS and Solar Panel Assembly
24	78.9	Combined Mode of Vertical Decks, RCS and Solar Panel Assembly
25	82.5	Combined Mode of RCS and V4
26	84.9	Solar Panel Assembly Mode
27	85.2	Solar Panel Assembly Mode
28	85.5	Combined Mode of Solar Panel Assembly and Vertical Decks V1 and V3
29	86.2	Combined Mode of Solar Panel Assembly and Vertical Decks V1 and V3

Table 1 (continued)

(b) Natural Frequencies and Modes

Mode No.	Frequency in Hzs	Mode Description
30	89.3	Combined Mode of Solar Panel Assembly and Vertical Decks V1,V3 and V4
31	89.3	Local RCS Deck Mode
32	93.9	Local Solar Panel Assembly Mode
33	94.3	Local Solar Panel Assembly Mode
34	96.9	Local Solar Panel Assembly Mode
35	97.4	Local Solar Panel Assembly Mode

TABLE 2

Free Vibration Analysis Results of IRS Subsystems
(using detailed finite element models with simply supported base conditions)

(a) RCS Deck (With Fixed Base) (Total Rigid Mass = 103.94 Kgs)

Mode No.	Frequency in Hzs	Total Effective Force (Mass) in Kgf and its Direction
1*	55.22	20.56 (Z)
2	63.24	0.0
3	73.46	91.81 (X)
4*	75.56	69.46 (Y)
5	87.25	8.34 (X)

(b) V2 Deck (Total Rigid Mass = 73.94 Kgs)

Mode No.	Frequency in Hzs	Effective Mass Matrix (Kgs)	Effective Force Vector(Kgf) (Y)	Total Effective Mass(Kgs) (Y)
1	51.25	$\begin{bmatrix} 0.843 & -0.116 & 1.743 \\ -0.116 & 0.016 & -0.239 \\ 1.743 & -0.239 & 3.602 \end{bmatrix}$	$\begin{bmatrix} 2.47 \\ -0.339 \\ 5.106 \end{bmatrix}$	7.24
2*	68.85	$\begin{bmatrix} 7.096 & -0.913 & 9.876 \\ -0.913 & 0.117 & -1.271 \\ 9.876 & -1.271 & 13.745 \end{bmatrix}$	$\begin{bmatrix} 16.059 \\ -2.067 \\ 22.35 \end{bmatrix}$	36.34

(c) V4 Deck (Total Rigid Mass = 88.46 Kgs)

Mode No.	Frequency in Hzs	Effective Mass Matrix (Kgs)	Effective Force Vector(Kgf) (Y)	Total Effective Mass(Kgs) (Y)
1*	46.70	$\begin{bmatrix} 6.437 & 0.468 & 12.016 \\ 0.468 & 0.034 & 0.874 \\ 12.016 & 0.874 & 22.43 \end{bmatrix}$	$\begin{bmatrix} 18.921 \\ 1.376 \\ 35.320 \end{bmatrix}$	55.62
2	74.94	$\begin{bmatrix} 4.089 & -2.914 & 1.822 \\ -2.914 & 2.076 & -1.298 \\ 1.822 & -1.298 & 0.812 \end{bmatrix}$	$\begin{bmatrix} 2.997 \\ -2.136 \\ 1.336 \end{bmatrix}$	2.20

Table 2 (continued)

(d) Top Deck (Total Rigid Mass = 278.9 Kgs)

Mode No.	Frequency in Hzs	Effective Mass Matrix (Kgs)	Effective Force Vector (Kgf) (Z)	Total Effective Mass (Kgs) (Z)
1*	61.92	$\begin{bmatrix} 0.027 & 0.039 & -0.866 & -0.884 \\ 0.039 & 0.056 & -1.243 & -1.268 \\ -0.866 & -1.243 & 27.470 & 28.020 \\ -0.884 & -1.268 & 28.020 & 28.590 \end{bmatrix}$	$\begin{bmatrix} -1.684 \\ -2.416 \\ 53.381 \\ 54.458 \end{bmatrix}$	103.74
2	94.76	$\begin{bmatrix} 1.057 & 0.719 & 0.569 & 0.993 \\ 0.719 & 0.490 & 0.387 & 0.676 \\ 0.569 & 0.387 & 0.306 & 0.535 \\ 0.993 & 0.676 & 0.535 & 0.934 \end{bmatrix}$	$\begin{bmatrix} 3.338 \\ 2.272 \\ 1.797 \\ 3.138 \end{bmatrix}$	10.55

(e) Bottom Deck (Total Rigid Mass = 72.5 Kgs)

Mode No.	Frequency in Hzs	Effective Mass Matrix (Kgs)	Effective Force Vector (Kgf) (Z)	Total Effective Mass (Kgs) (Z)
1*	62.33	$\begin{bmatrix} 1.136 & 0.749 & 1.450 & 2.838 \\ 0.749 & 0.494 & 0.956 & 1.871 \\ 1.450 & 0.956 & 1.851 & 3.623 \\ 2.838 & 1.871 & 3.623 & 7.089 \end{bmatrix}$	$\begin{bmatrix} 6.173 \\ 4.070 \\ 7.880 \\ 15.421 \end{bmatrix}$	33.54
2	91.35	$\begin{bmatrix} 0.031 & -0.111 & -0.239 & 0.125 \\ -0.111 & 0.399 & 0.858 & -0.450 \\ -0.239 & 0.858 & 1.845 & -0.969 \\ 0.125 & -0.450 & -0.967 & 0.506 \end{bmatrix}$	$\begin{bmatrix} -0.194 \\ 0.696 \\ 1.497 \\ -0.786 \end{bmatrix}$	1.21

* Modes corresponding to these subsystems are simulated in the dynamic models.

TABLE 3

Characteristics of IRS Low Order Dynamic Model (Longitudinal)

(a) Element Stiffnesses (Spring Constant K for Spring and Bending Rigidity EI for Beam Elements)

Element Number	Element Type	Element Stiffness	Element Number	Element Type	Element Stiffness
1	Linear Spring	7.6425E+8 N/M	11	Torsional Spring	1.0 E+6 NM
2	Linear Spring	5.7007E+8 N/M	12	Torsional Spring	1.0 E+6 NM
3	Linear Spring	6.2600E+8 N/M	13	Torsional Spring	2.0 E+4 NM
4	Linear Spring	1.4500E+7 N/M	14	Torsional Spring	2.0 E+4 NM
5	Linear Spring	1.4500E+7 N/M	15	Beam	3.5945E+3 N/M
6	Linear Spring	1.8000E+6 N/M	16	Beam	2.5264E+5 N/M
7	Torsional Spring	1.0000E+6 NM	17	Beam	2.5264E+5 N/M
8	Torsional Spring	1.0000E+6 NM	18	Beam	3.5945E+3 N/M
9	Torsional Spring	1.0000E+6 NM	19	Beam	1.0452E+3 N/M
10	Torsional Spring	1.0000E+6 NM	20	Beam	1.0452E+3 N/M
			21	Beam	1.0452E+3 N/M
			22	Beam	1.0452E+3 N/M

Table 3 (continued)

(b) Nodal Masses

Node No.	Mass in Kgs	Node No.	Mass in Kgs	Node No.	Mass in Kgs	Node No.	Mass in Kgs
1	5.7	5	104.0	9	111.25	13	58.85
2	12.9	6	61.45	10	62.45	14	21.0
3	98.44	7	111.25	11	58.85	15	17.0
4	12.0	8	61.45	12	62.45	16	17.0

(c) Mass and Inertia Properties

Total Spacecraft Mass in Kgs			876.02
Centre of Gravity Location in M (From the base of the spacecraft)	$\bar{Y}$	=	0.0
	$\bar{Z}$	=	0.8520
Moments of Inertia About Spacecraft Base in Kg M^2	I_{xx}	=	1.1E+3
	I_{yy}	=	0.9E+3
	I_{yz}	=	0.0

(d) Natural Frequencies and Modes

Mode No.	Frequency in Hzs	Mode Description
1	36.7	Symmetric (about Z) vibration mode of V2 and V4 in longitudinal direction. Top and bottom decks bend symmetrically about Z axis.
2	37.4	Same as mode 1, except this is unsymmetric about Z axis. This is a fictitious mode because of d.o.f. selected in the configuration (symmetric) of the model.
3	46.5	RCS longitudinal mode.
4	60.9	Symmetric mode about Z axis involving top deck and slight motion of V2 and V4 in longitudinal direction.

TABLE 4

Characteristics of IRS Low Order Dynamic Model (Lateral)

(a) Element Stiffnesses (Spring Constant K for Spring and Bending Rigidity EI for Beam Elements)

Element Number	Element Type	Element Stiffness	Element Number	Element Type	Element Stiffness
1	Linear Spring	2.2500E+7 N/M	9	Beam@	3.3854E+7 N/M
2	Linear Spring	2.2500E+7 N/M	10	Beam@	3.3854E+7 N/M
3	Linear Spring	9.4400E+6 N/M	11	Beam	4.0149E+4 N/M
4	Torsional Spring	1.0000E+5 NM	12	Beam	4.0149E+4 N/M
5	Torsional Spring	1.0000E+5 NM	13	Beam	4.6293E+3 N/M
6	Torsional Spring	3.0000E+5 NM	14	Beam	2.6610E+4 N/M
7	Torsional Spring	3.0000E+5 NM	15	Beam	2.6610E+4 N/M
8	Beam	6.8670E+6 N/M	16	Beam	2.6610E+1 N/M

@ For these beams shape factor K_T = 0.312

Table 4 (continued)

(b) Nodal Masses

Node No.	Mass in Kgs	Node No.	Mass in Kgs	Node No.	Mass in Kgs	Node No.	Mass in Kgs
1	5.7	5	81.3	9	80.46	13	69.5
2	54.2	6	36.34	10	55.62	14	12.0
3	50.94	7	0.5	11	0.5	15	69.2
4	144.6	8	74.85	12	74.85	16	65.28

(c) Mass and Inertia Properties

Total Spacecraft Mass in Kgs			876.0
Centre of Gravity Location in M (From the base of the spacecraft)	$\bar{Y}$	=	0.013
	$\bar{Z}$	=	0.852
Moments of Inertia about Spacecraft Base in Kg M^2	I_{xx}	=	1.1E+3
	I_{yy}	=	0.9E+3
	I_{yz}	=	0.1E+2

(d) Natural Frequencies and Modes

Mode No.	Frequency in Hzs	Mode Description
1	25.7	Overall lateral (Y) bending mode.
2	54.8	Lateral mode of V4.
3	57.8	Lateral mode of RCS deck.
4	72.0	Lateral mode of V2 (actually this is second mode of the deck which is simulated in the model because of its larger effective mass)

TABLE 5

Matching of Important Frequencies of IRS Between Detailed and Low Order Models

Mode No. (Detailed Model) Ref. Table 1	Frequency in Hzs			Remarks
	Detailed Model Ref. Table 1	Low Order Models		
		Longitudinal Ref. Table 3	Lateral Ref. Table 4	
(1)	(2)	(3)	(4)	(5)
1	25.6		25.7	Y Global Mode.
2				X Global mode. Not simulated.
3	36.2	36.7		Z Global mode.
4-6				Solar panel modes. Not simulated.
7	46.5	46.5		RCS mode Z.
8-9				V1 and V3 modes. Not simulated.
10-11				Solar panel modes. Not simulated.
12	54.3		54.8	V4 mode.
13	57.6		57.8	RCS mode Y.
14				Solar panel mode. Not simulated.
15	61.1	60.9		Top deck mode.

Table 5 (continued)

(1)	(2)	(3)	(4)	(5)
16-21				Solar panel modes. Not simulated.
22	70.2			First V2 mode. No significant effective mass. Not simulated.
23	72.1		72.0	Second V2 mode.
24-25				V2, V4 modes. No significant effective mass. Not simulated.
26-30				Solar panel, V1, V3 modes. Not simulated.
31				RCS mode. No significant effective mass. Not simulated.
32-35				Solar panel modes. Not simulated.

TABLE 6

Details of Results of Parametric Study for Change in IRS Payload Mass

	Details of study	Present payload	20% Increase in payload mass	40% Increase in payload Mass
A.	Stiffness Calculations			
1.	Mass of payload in Kgs	175.0	210.0	245.0
2.	Height of payload CG in M from spacecraft base	1.364	1.394	1.424
3.	Fundamental frequency in Hzs in lateral direction	25.7	24.5	23.3
4.	Fundamental frequency in Hzs in longitudinal direction			
	- Present payload distribution	36.7	36.2	35.7
	- Payload as uniformly distributed load on top deck plate	34.3	33.5	32.8
5.	Percentage increase in main strut area to raise longitudinal frequency to 36.7 Hzs	20%	30%	35%
6.	Increase in spacecraft mass due to main strut area increase (in Kgs)	0.3	0.5	0.6
7.	Percentage increase in top deck plate stiffness (core thickness) to raise longitudinal frequency to 36.7 Hzs	200%	200%	250%
8.	Increase in spacecraft mass due to top deck plate core thickness increase(in Kgs)	1.5	1.5	2.5
B.	Strength Calculations			
1.	Percentage increase in top deck plate stress for longitudinal acceleration (present stress 3 Kg/mm^2)	0.0	20%	40%
2.	Percentage increase in top deck plate stress for lateral acceleration (present stress 1.25 Kg/mm^2)	0.0	45%	95%
3.	Percentage increase in cylinder stress for longitudinal acceleration (present stress 4 Kg/mm^2)	0.0	4%	8%
4.	Percentage increase in cylinder stress for lateral acceleration (present stress 5 Kg/mm^2)	0.0	8%	15%

APPENDIX

GENERATION OF EQUIVALENT MODELS FOR MODES OF A SUBSYSTEM

1. General expression for 'effective mass' of a normal mode of a base-fixed system

Let r and l refer to the 'base' and interior d.o.f. of a structural system respectively. Here 'base' is used to represent the support of a system as well as its interface with another system. In partitioned matrix form the equations of equillibrium of the system when subjected to prescribed base motion is given by;

$$\begin{bmatrix} M_{rr} & M_{rl} \\ M_{lr} & M_{ll} \end{bmatrix} \cdot \begin{bmatrix} \ddot{X}_r \\ \ddot{X}_l \end{bmatrix} + \begin{bmatrix} C_{rr} & C_{rl} \\ C_{lr} & C_{ll} \end{bmatrix} \cdot \begin{bmatrix} \dot{X}_r \\ \dot{X}_l \end{bmatrix}$$

$$+ \begin{bmatrix} K_{rr} & K_{rl} \\ K_{lr} & K_{ll} \end{bmatrix} \begin{bmatrix} X_r \\ X_l \end{bmatrix} = \begin{bmatrix} F_c(t) \\ 0 \end{bmatrix} \quad ..(1)$$

where M, C, K are structural mass, damping and stiffness matrices respectively and X is the displacement vector. The response at any point in the structure can now be expressed as:

$$X = [\Phi_c \quad \Phi_E] \begin{Bmatrix} \delta \\ \eta \end{Bmatrix} \quad ..(2)$$

where Φ_c are constrained modes and Φ_E are elastic modes of the base-fixed system. Φ_c are obtained by solving $K\Phi_c = 0$ with a unity matrix corresponding to base d.o.f. δ is prescribed base displacement input and η are generalised modal coordinates. Assuming that the eigen vectors are orthogonal with respect to damping matrix in addition to stiffness and mass and substituting Eq. (2) in Eq. (1) and premultiplying throughout by $[\Phi_c \quad \Phi_E]^T$ Eq. (1) becomes;

$$f_c(t) = M_c \ddot{\delta} + L^T \ddot{\eta} \quad ..(3)$$

$$m\ddot{\eta} + c\dot{\eta} + k\eta = -L\ddot{\delta} \quad ..(4)$$

where f_c is the base reaction force, M_c is the mass matrix condensed with respect to base d.o.f. (Guyan's reduction) and L are modal participation factors given by $\Phi_E^T M \Phi_c$. m, c, k are diagonal matrices denoting generalised mass, modal damping ratio and stiffnesses of the base-fixed elastic modes of the system. Eq.(4) actually represents a system of decoupled linear equations each corresponding to a single d.o.f. system subjected to external loads. A typical i th equation is given by;

$$m_i\ddot{\eta}_i + c_i\dot{\eta}_i + k_i\eta_i = -L_i\ddot{\delta} \quad ..(5)$$

where L_i is i th row of L

Solving Eq.(5) for steady-state response conditions, assuming the excitation to be harmonic, we get;

$$\eta_i = \frac{L_i}{m_i} H_i \ddot{\delta} \quad ..(6)$$

where

$$H_i = \frac{(\omega/\omega_i)^2}{[1-(\omega/\omega_i)^2] + 2i\xi_i(\omega/\omega_i)} \quad ..(7)$$

In Eq.(7), ω is the excitation frequency, ω_i is the natural frequency of i th elastic mode of the base-fixed system, ξ_i is the modal damping ratio ($c_i/(2m_i\omega_i)$). Substituting Eqs.(6) and (7) in Eq.(3), the total base reaction force can be obtained as:

$$f_c(t) = [M_c + \sum_i M_i^e H_i]\ddot{\delta} \quad ..(8)$$

where M_i^e is called the 'effective mass' of i th base-fixed elastic mode of the system and is given by;

$$M_i^e = \frac{L_i^T L_i}{m_i} \quad ..(9)$$

For more information on this topic Reference [5] can be consulted. A procedure implemented in ASKA for computing modal effective masses is given in the form of a flow chart in Fig.10.

2. Generation of Equivalent Models for a Normal Mode

Equivalent single d.o.f. systems can be generated for a normal mode by matching its natural frequency and effective mass, in the case of systems with single base node. But for systems with multiple nodes at the base the 'effective force' of a mode obtained by multiplying the effective mass with unit base acceleration is conveniently matched by a trial and error method. Here this procedure is illustrated with respect to V2 deck of IRS.

Step 1: The V2 deck (see Fig.7) is first analysed for its out of plane free vibration characteristics, like natural frequencies, modes and modal effective masses by applying simply supported boundary conditions all along its edges and a point support at the middle where the secondary struts join. 3 nodes A,B,C lying on the middle line of the plate are chosen as base nodes to compute the effective masses. The 'V' coordinates at these points are thus taken into the 'r' set described above and all other remaining d.o.f. into the 'l' set. In order to simulate the simple support condition around the plate, a stiffener having large bending and axial stiffnesses with zero torsional stiffness is attached to its edges. The stiffener has negligible mass. Further at A and C the translational d.o.f U and W and rotational d.o.f. θ_z are suppressed. The resulting frequencies in 0-100 Hzs range and the modal effective masses are given in Table 2(b).

Step 2: Now the simply supported deck V2 is simulated in the model by a beam simply supported at 3 points A,B and C. The properties of this beam are adjusted to represent the second mode of the deck for which the effective mass and effective force vector are given in Table 2(b). The effective forces at the support of the beam are given by R_A = -2.066, R_B = 22.35 and R_C = 16.058, which when added up give a total effective force (or a total effective mass in Y direction) of 36.34 Kgf acting in a direction transverse to the beam. The location of this force is required to be estimated such that the reaction forces at the supports match with its effective force vector. For this purpose, it is assumed that bending rigidity of the beam in the span AB is (EI) and in the span BC it is k(EI). Using Clapyron's theorem of 3 moments, the constant k is found to be 8.673. The distance of the point T where the total effective force acts on the beam is computed approximately as 0.356 M from support C, the total length of the beam ABC being 1.068 m. The beam configuration thus arrived at produces reaction forces at the supports given by R_A = 2.07, R_B = 22.35 and R_C = 16.06 and matches satisfactorily with effective force vector.

Step 3: The final step involves estimating the bending rigidity of the beam in both the spans. At T the total effective mass of 36.34 Kgs is lumped and the value of (EI) is obtained so that the beam has a natural frequency equal to that of the mode it represents, i.e., 68.85 Hzs.

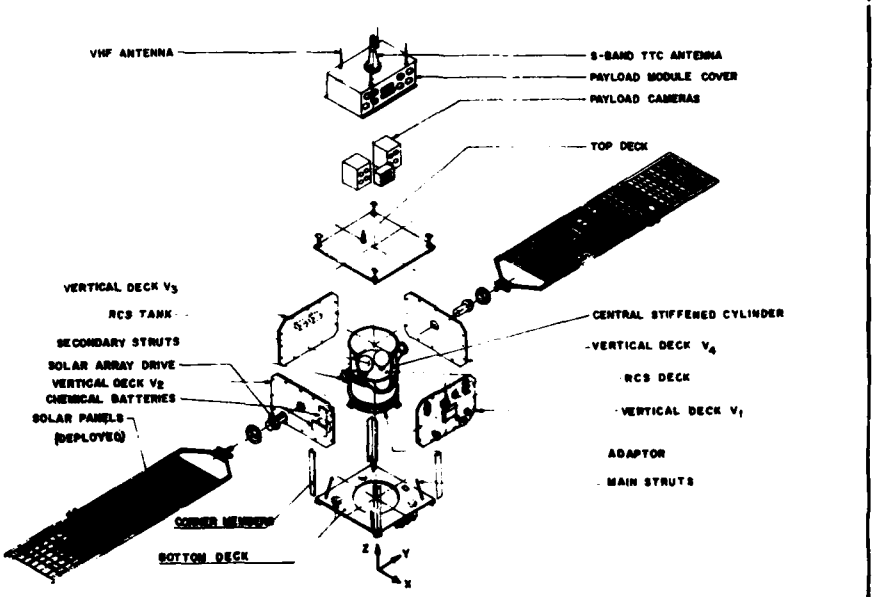

FIG.1.-EXPLODED VIEW OF IRS SPACECRAFT (ON ORBIT CONFIGURATION)

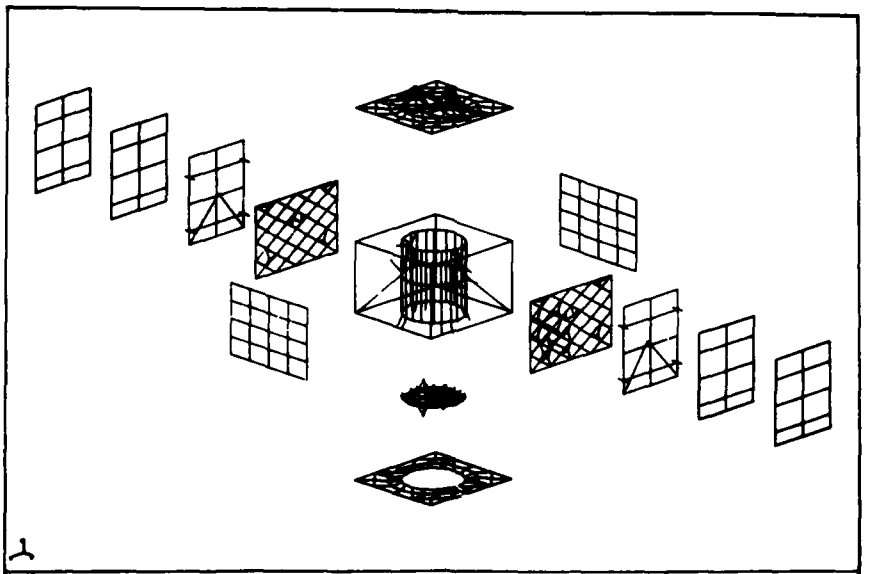

FIG.2a-DISASEMBLED VIEW IRS

ISAC STRUCTURES BANGALORE

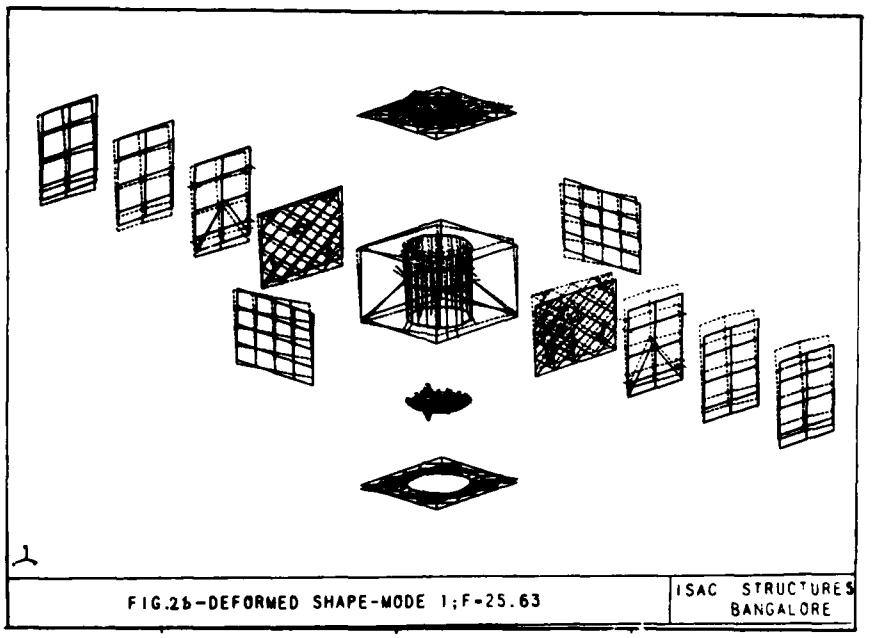

FIG.2b–DEFORMED SHAPE-MODE 1;F=25.63 | ISAC STRUCTURES BANGALORE

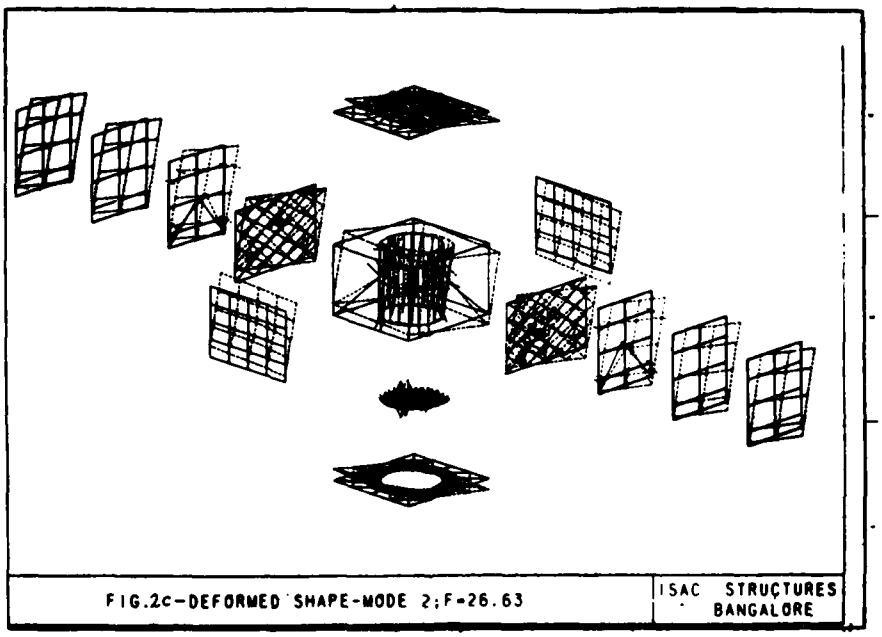

FIG.2c–DEFORMED SHAPE-MODE 2;F=26.63 | ISAC STRUCTURES BANGALORE

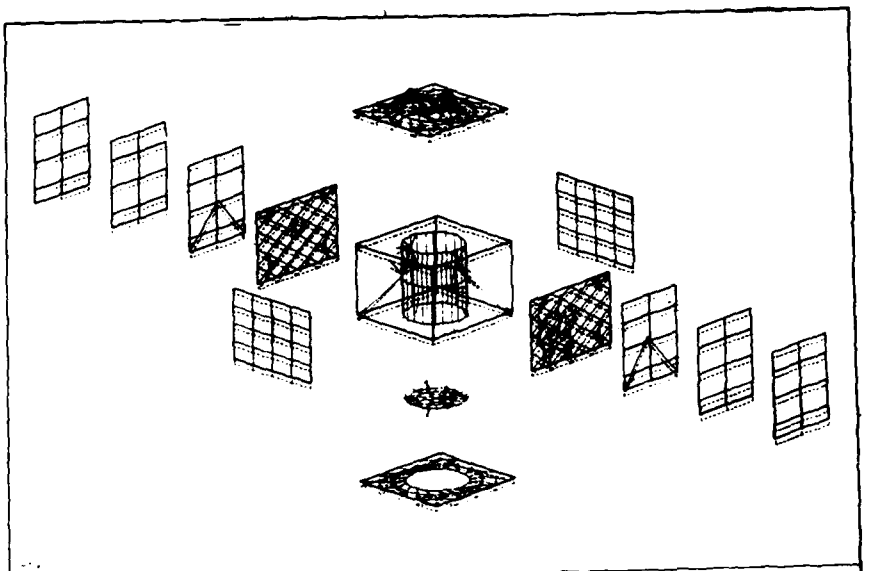

FIG.2d—DEFORMED SHAPE-MODE 3;F=36.20

ISAC STRUCTURES BANGALORE

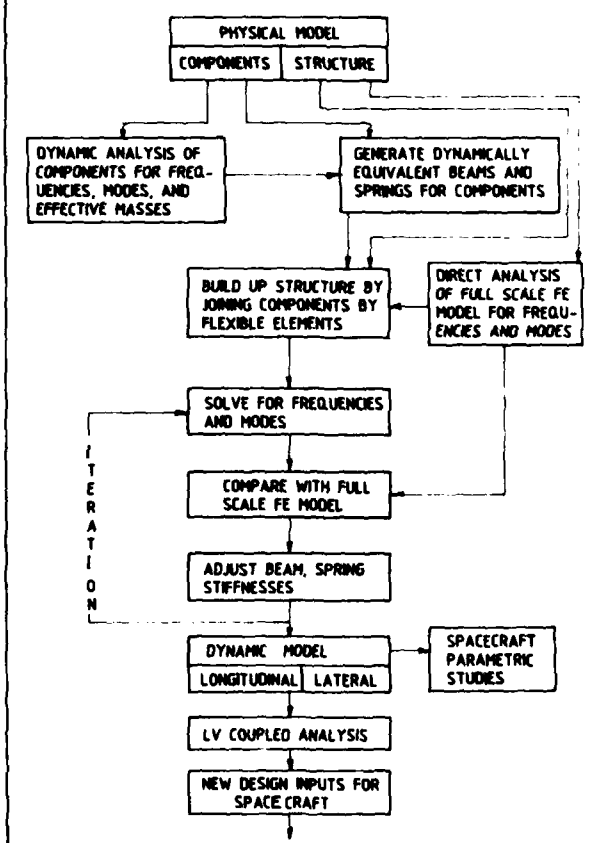

FIG. 3. GENERATION OF DYNAMIC MODEL FOR COUPLED ANALYSIS

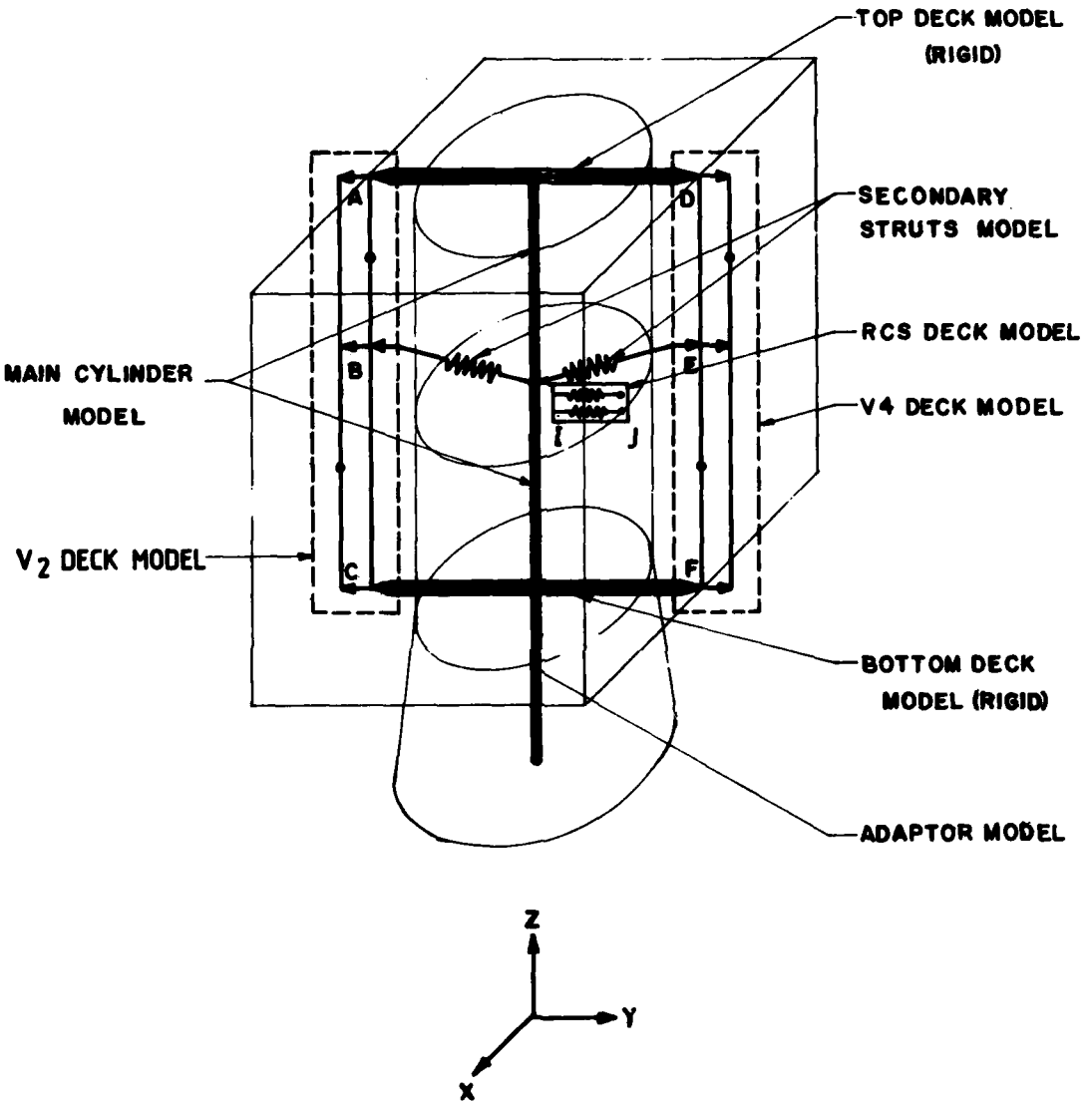

FIG. 4. IRS LATERAL CONCEPTUAL MODEL

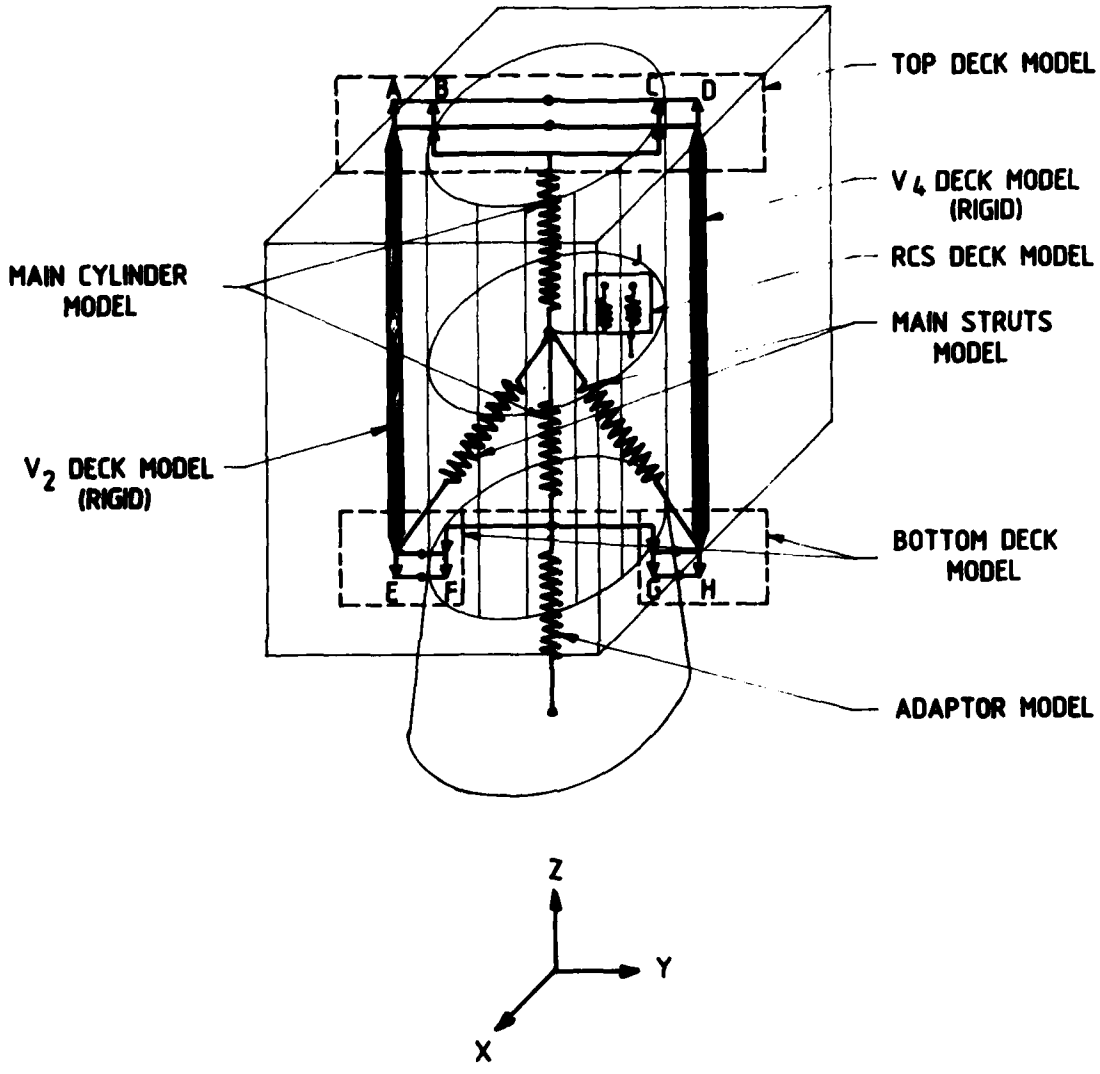

FIG. 5. IRS LONGITUDINAL CONCEPTUAL MODEL

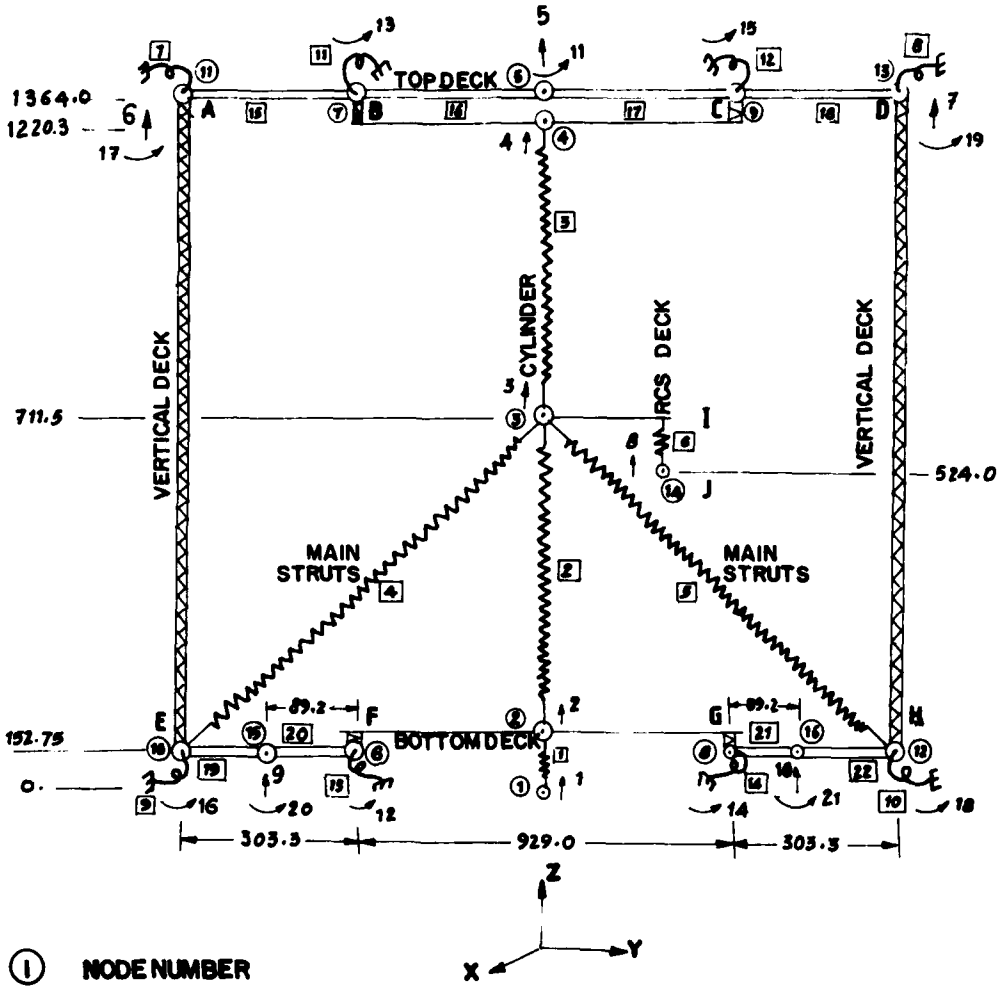

(I) NODE NUMBER

[I] ELEMENT NUMBER

→ I

↷ 10 D.O.F. NUMBER

⊙ NODE AND MASS POINT

—— SAME NODE

16 NODES

22 ELEMENTS

10 W- D.O.F. + 11 θx — D.O.F.
(TOTAL 21 D.O.F.)

-WW- LINEAR FLEXIBLE SPRING

TORSIONAL FLEXIBLE SPRING - ONE END GROUNDED

FLEXIBLE BEAM WITH NO AXIAL STIFFNESS

RIGID LINEAR SPRING

ALL DIMENSIONS ARE IN MM

FIG-6 IRS DYNAMIC MODEL LONGITUDINAL

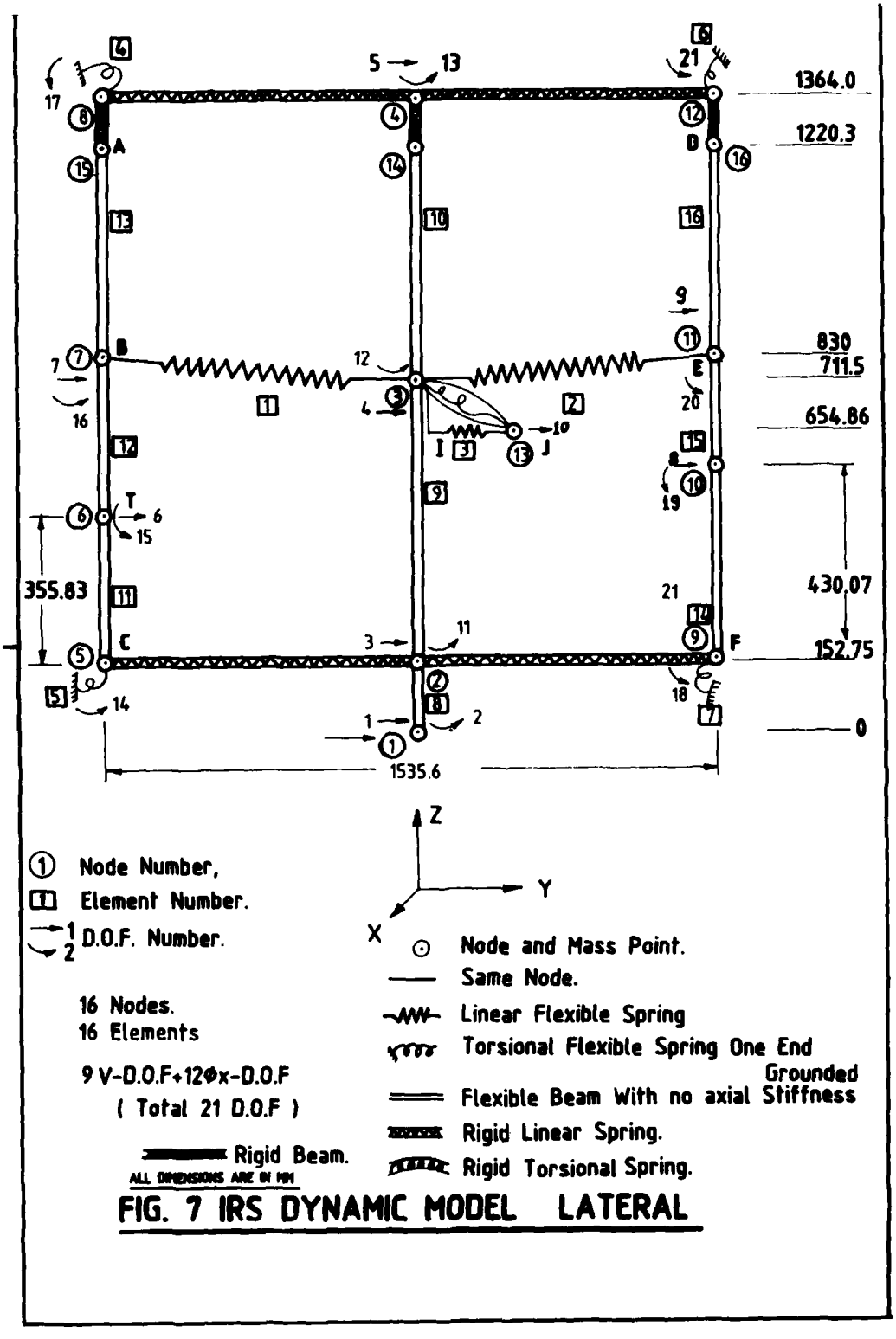

FIG. 7 IRS DYNAMIC MODEL LATERAL

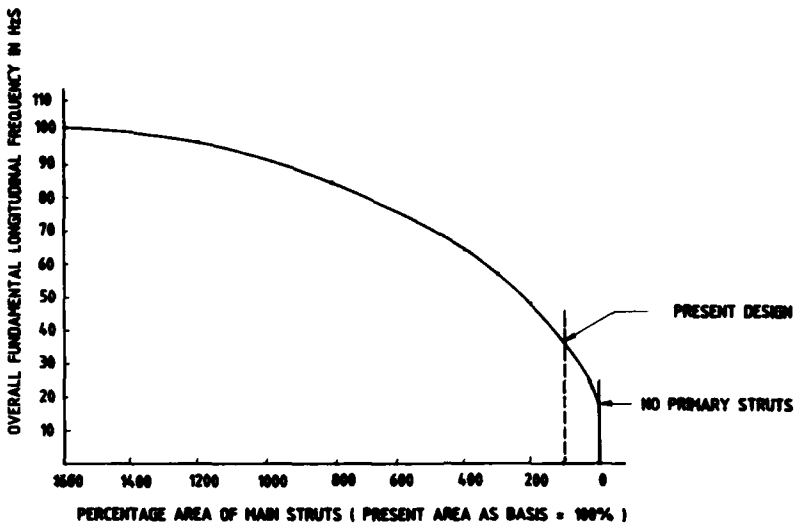

FIG. 8. VARIATION OF FUNDAMENTAL LONGITUDINAL FREQUENCY OF IRS WITH MAIN STRUT STIFFNESS

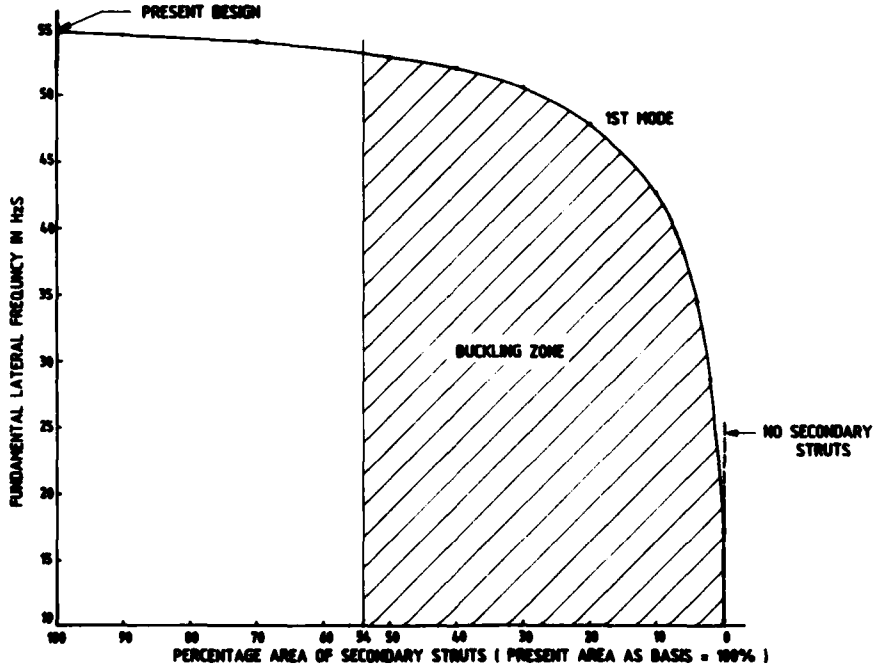

FIG. 9. VARIATION OF V_4 DECK FREQUENCY WITH SECONDARY STRUT STIFFNESS

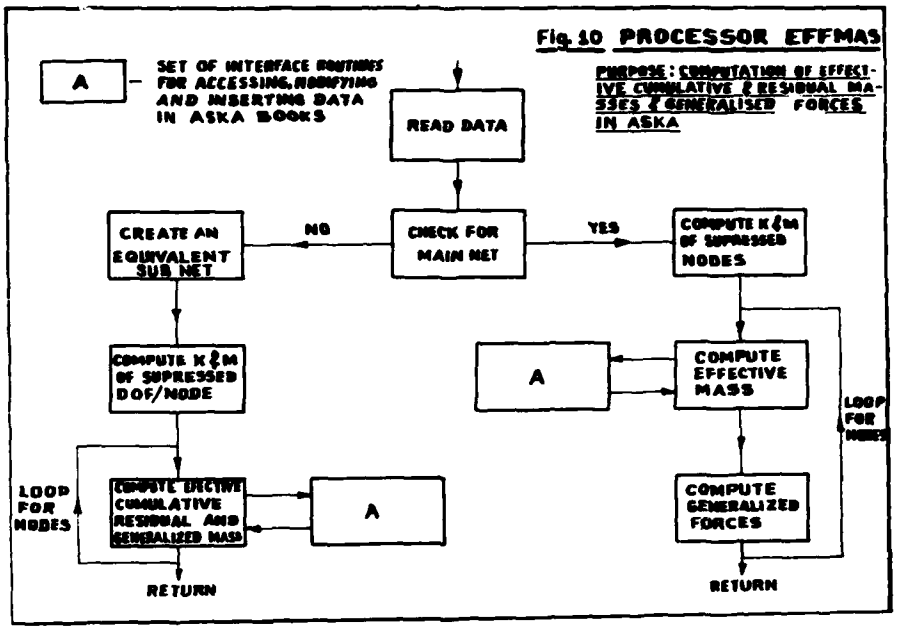
Fig.10 PROCESSOR EFFMAS
A
SET OF INTERFACE ROUTINES FOR ACCESSING, MODIFYING AND INSERTING DATA IN ASKA BOOKS
PURPOSE: COMPUTATION OF EFFECTIVE CUMULATIVE & RESIDUAL MASSES & GENERALISED FORCES IN ASKA
READ DATA
CHECK FOR MAIN NET
NO
YES
CREATE AN EQUIVALENT SUB NET
COMPUTE K&M OF SUPRESSED NODES
COMPUTE K&M OF SUPRESSED DOF/NODE
A
COMPUTE EFFECTIVE MASS
LOOP FOR NODES
LOOP FOR NODES
COMPUTE EFFECTIVE CUMULATIVE RESIDUAL AND GENERALIZED MASS
A
COMPUTE GENERALIZED FORCES
RETURN
RETURN

A DIRECT METHOD FOR ESTIMATING LOWER AND UPPER BOUNDS OF THE FUNDAMENTAL FREQUENCY

Dewen Jin
Visiting Scholar at the University of Virginia
Lecturer, Department of Precision Instruments
Tsinghua University
Beijing, China

Walter D. Pilkey
Professor
Department of Mechanical and Aerospace Engineering
University of Virginia
Charlottesville, Virginia 22901

B. P. Wang
Associate Professor
Department of Mechanical Engineering
University of Texas at Arlington
Arlington, Texas 76019

Yohji Okada
Associate Professor
Department of Mechanical Engineering
Ibaraki University
Hitachi, Japan 316

When studying or designing a vibrating system, it is useful to have a quick estimate of frequencies, especially the fundamental frequency. The lower and upper bounds of the fundamental frequency provide the approximation and range of this frequency. This paper presents a direct method to get the lower and upper bounds of a fundamental frequency. In contrast to currently used approaches, the lower and upper bounds can be obtained simultaneously by this method. The method is applicable to discrete and continuous systems. For discrete systems this procedure involves substituting an assumed mode shape into the equations of motion, and then the bounds of the fundamental frequency are obtained by the enclosure theorem. For continuous systems, an initial distributed load is assumed instead of an initial modeshape. A simple formula for estimating the bounds of the fundamental frequency of a continuous beam is derived in this paper. This technique is especially appropriate for a system having a first modeshape which is easy to estimate. Several examples are presented to illustrate the method.

INTRODUCTION

It is commonly accepted that the lower bound of the fundamental frequency of a vibrating system can be obtained using Dunkerley's Method [1] and the upper bound can be found by means of Rayleigh's Method [1]. Since the results calculated using these methods are sometimes not sufficiently accurate, both improved Dunkerley's and Rayleigh's methods have been developed [2], [3], [4], [5]. In general, these improved methods involve iterative procedures. The original Dunkerley's or Rayleigh's relations usually serve as the first step of the iterative procedure.

The direct method presented here involves substituting an assumed modeshape of a discrete system or an initial distributed load acting on a continuous system into equations of motion. The lower bound and upper bound for an eigenvalue can then be obtained at the same time. These bounds for the fundamental frequency are calculated using an iterative procedure and their accuracy can also be improved, as long as

the initially assumed modeshape is not orthogonal to the first mode of the vibrating system. This method is quite efficient for a vibrating discrete system when a rough estimate of the first modeshape is available. For a continuous mass system where a distributed load is assumed, a simple and useful formula for estimating the lower bound of the fundamental frequency is obtained in the latter part of this paper. Examples are presented to illustrate this direct method.

NOMENCLATURE

- M - mass matrix
- K - stiffness matrix
- α - flexibility (influence coefficient) matrix
- D - dynamic matrix
- X_i - eigenvector in iteration procedure
- $\underline{X}_i$ - actual modeshape for discrete system
- $Y_i(x)$ - actual modeshape for continuous systems
- $y(x)$ - modeshape for continuous system in iteration procedure
- λ - eigenvalue, the frequency parameter
- λ_1 - fundamental frequency parameter
- λ_u - upper bound of λ_1
- λ_L - lower bound of λ_1
- λ_R - Rayleigh's quotient
- λ_T - Timoshenko's quotient
- λ_D - lower bound of λ_1 using Dunkerley's formula
- λ_{ID} - lower bound of λ_1 using improved Dunkerley's formula
- $\alpha(x,u)$ - Green's function
- E - Young's modulus
- I - moment of inertia of beams
- $m(x)$ - mass of beams with variable cross section
- ρ - mass per unit length of uniform beams
- $q(x)$ - distributed load acting on beams
- f - fundamental frequency

ITERATION TECHNIQUES AND IMPROVED RALEIGH'S AND DUNKERLEY'S METHODS

The Inverse Iteration Procedure

The natural frequencies of a vibrating system can be found by solving the eigenvalue problem

$$Kx = \lambda Mx \tag{1}$$

or, equivalently,

$$x = \lambda \alpha Mx \tag{2}$$

where:

K = stiffness matrix

M = mass matrix

x = eigenvectors

α = influence coefficient (flexibility) matrix

$\lambda = \omega^2$, the frequency parameter.

An inverse iteration procedure using an assumed eigenvector $x^{(o)}$ would be

$$x^{(1)} = \alpha M x^{(o)} \tag{3a}$$

$$x^{(2)} = \alpha M x^{(1)} \tag{3b}$$

$$\vdots$$

$$x^{(k)} = \alpha M x^{(k-1)} \tag{3c}$$

For the first mode, $x^{(k)}$ will approach the first modeshape, and the ratio of corresponding elements of $x^{(k)}$ to $x^{(k-1)}$ will approach the first eigenvalue λ_1 [6], provided that $x^{(o)}$ is not orthogonal to the first modeshape.

From a physical point of view, the iteration procedure seeks the displacements of the vibrating system due to the inertia force generated by the motion of the system in an assumed modeshape. Thus, a modeshape is approached step by step finding the kth displacements due to the inertia force associated with the (k-1) displacements.

The Improved Rayleigh's Method

The improved Rayleigh's formula for the fundamental frequency is [3] [8]

$$\lambda_u = \frac{x^T k x}{x^T M x} \tag{4}$$

where x is $x^{(k)}$ obtained by the iteration procedure. Thus

$$\lambda_u^{(k)} = \frac{[x^{(k)}]^T K[x^{(k)}]}{[x^{(k)}]^T M[x^{(k)}]} \qquad (5)$$

When k = 0 in Eq. (5), $\lambda_u^{(o)}$ is the usual Rayleigh's quotient λ_R.

With increasing k, $x^{(k)}$ approaches the first modeshape, and $\lambda_u^{(k)}$ should approach the fundamental frequency. Since Eq. (4) is based on a particular energy principle, $\lambda_u^{(k)}$, approaches λ_1 from the high side. It is an upper bound.

Timoshenko's quotient λ_T [7] [8] is slightly different from $\lambda_u^{(1)}$. In this quotient the $x^{(o)}$ is used for computing the maximum kinetic energy and $x^{(1)}$ is used to compute the potential energy [4]. This leads to

$$\lambda_R > \lambda_T > \lambda_u^{(1)} \qquad (6)$$

Then the result from Eq. (5) is closer to λ_1 than Timoshenko's quotient.

The Improved Dunkerley's Method

Dunkerley's formula is usually derived from

$$Dx - \frac{1}{\lambda} x = 0 \qquad (7)$$

with D = αM, the dynamic matrix. The characteristic equation is the polynomial

$$\left| Dx - \frac{1}{\lambda} I \right| = 0$$

From the theory of equations,

$$\lambda_D = \frac{1}{\sum_{i=1}^{n} D_{ii}} \qquad (8)$$

where

D_{ii} = diagonal elements of matrix D

λ_D = lower bound from Dunkerley's formula.

The improved Dunkerley's formula presented in [2] [5] can be also derived from an iteration procedure. Set

$$x^{(k)} = D^k x^{(o)} \qquad (9)$$

substitute $x^{(k)}$ into Eq. (7)

$$Dx^{(k)} - \frac{1}{\lambda} x^{(k)} = 0 \qquad (10)$$

In Eq. (10), $x^{(k)}$ should be closer to the first modeshape and λ should be closer to the fundamental eigenvalue λ_1 with increasing k. From Eqs. (7) and (9)

$$Dx^{(o)} = \frac{1}{\lambda} x(o)$$

$$x^{(2)} = D^2 x^{(o)} = D \cdot Dx^{(o)} = D \frac{1}{\lambda} x^{(o)} = \frac{1}{\lambda^2} x^{(o)}$$

Then

$$x^{(k+1)} = D^{k+1} x^{(o)} = \frac{1}{\lambda^{k+1}} x^{(o)}$$

$$D^{k+1} x^{(o)} - \frac{1}{\lambda^{k+1}} x^{(o)} = 0 \qquad (11)$$

so that

$$\left| D^{k+1} - \frac{1}{\lambda^{k+1}} I \right| = 0 \qquad (12)$$

and

$$\lambda_{ID}^{k+1} = \left(\sum_{i=1}^{n} D_{ii}^{k+1} \right)^{-1} \qquad (13)$$

where λ_{ID} is th eigenvalue from the improved Dunkerley's method.

With an increase in k, λ_{ID} will approach λ_1, *but from below. It is a lower bound.*

The improved Rayleigh's and Dunkerley's methods are approximate methods for computing the fundamental frequency. The exact value is approached from the higher and lower sides, respectively. For large systems, the computation involved in Dunkerley's method makes it impractical. An alternative, efficient method to obtain the lower bound is desirable.

It can be shown that lower and upper bounds can be derived from the iteration procedure itself. This method for computing both the lower and upper bounds directly from the iteration procedure will be referred to here as the direct method. It is also an approximate method. The exact value of λ_1 is approached from both the higher side and lower side rather than just from one side.

DIRECT METHOD FOR DISCRETE SYSTEMS

In the direct method, the eigenvalue bounds are computed directly from Eqs. (2) and (3). Begin with an assumed initial eigenvector $x^{(o)}$ and substitute it into Eq. (2)

$$x^{(o)} = \lambda \alpha M x^{(o)} \qquad (14)$$

Define a vector $\lambda^{(o)}$ with elements $\lambda_j^{(o)}$

$$\lambda^{(o)} = \begin{bmatrix} \lambda_1^{(o)} \\ \lambda_2^{(o)} \\ . \\ . \\ . \\ \lambda_j^{(o)} \\ . \\ . \\ . \\ \lambda_n^{(o)} \end{bmatrix}$$

$$\lambda_j^{(o)} = \frac{x_j^{(o)}}{[\alpha M x^{(o)}]_j} = \frac{x_j^{(o)}}{x_j^{(1)}} \qquad (15)$$

$$j = 1, 2 \ldots n$$

So that the $\lambda_j^{(o)}$ is the ratio of the corresponding elements of vectors $x^{(o)}$ and $x^{(1)}$.

If $x^{(o)}$ is an actual eigenvector $\underline{X}_i$, then all of the $\lambda_j^{(o)}$ in the vector $\lambda^{(o)}$ will be the same. That is,

$$\lambda_1^{(o)} = \lambda_2^{(o)} = \ldots = \lambda_n^{(o)} = \lambda_i$$

where λ_i is the i th eigenvalue.

In practice, $x^{(o)}$ will only approximate an eigenvector and the $\lambda_j^{(o)}$'s will differ. According to the enclosure theorem [3], when M is a diagonal matrix with positive elements, there will be a true eigenvalue λ that satisfies

$$\lambda_{min}^{(o)} < \lambda < \lambda_{max}^{(o)}$$

where $\lambda_{min}^{(o)}$ and $\lambda_{max}^{(o)}$ are the smallest and largest elements of the vector $\lambda^{(o)}$, respectively.

When the iteration procedure is employed, we can get a series of $\lambda^{(k)}$

$$\lambda_j^{(k)} = \frac{x_j^{(k)}}{x_j^{(k+1)}} \qquad (17)$$

$$k = 1, 2, \ldots$$

and

$$\lambda_{min}^{(k)} \leq \lambda_1 \leq \lambda_{max}^{(k)} \qquad (18)$$

with $\lambda_{min}^{(k)}$ and $\lambda_{max}^{(k)}$ the lower and upper bounds of the fundamental frequency, respectively. The spread between $\lambda_{min}^{(k)}$ and $\lambda_{max}^{(k)}$ will decrease with increasing k and, hopefully, will approach zero. One important implication of the results is that both the upper and lower bounds of an eigenvalue can be obtained during each step of the inverse iteration procedure for computing eigenvalues. This fact does not appear to have been used in eigenvalue solution routines.

Applications and Comparisons With Other Methods

The direct method for discrete systems will be demonstrated and compared with the other methods considered previously.

Example 1. Shown in Fig. 1 is a 3DOF system. There are three concentrated masses connected by springs. The masses and stiffnesses are indicated on Figure 1. The matrices M, K, and α are

$$M = m \begin{bmatrix} 1 & 0 & 0 \\ 0 & 2 & 0 \\ 0 & 0 & 3 \end{bmatrix}$$

$$K = k \begin{bmatrix} 5 & -2 & 0 \\ -2 & 3 & -1 \\ 0 & -1 & 1 \end{bmatrix}$$

$$\alpha = K^{-1} = \frac{1}{6k} \begin{bmatrix} 2 & 2 & 2 \\ 2 & 5 & 5 \\ 2 & 5 & 11 \end{bmatrix}$$

Having assumed

$$x^{(o)} = \begin{bmatrix} 1 \\ 2 \\ 4 \end{bmatrix}$$

the upper bound, 0.176 k/m, and lower bound, 0.1463 k/m, of λ_1 are obtained for this system using Eq. (15). The results improved greatly with the next iteration step (k = 1). See Table 1. The results obtained by using Dunkerley's and Rayleigh's methods are also listed in Table 1. The initial vector used in Rayleigh's method is the same as in the direct method. All the results improve when k = 1.

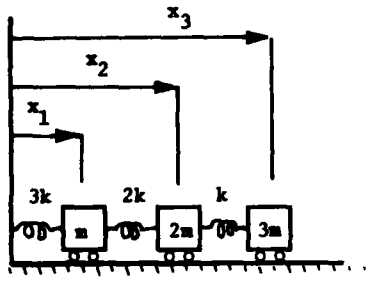

Fig. 1 - Example 1 3DOF System

Example 2 is a beam with two concentrated masses (Fig. 2). The segments are assumed to be weightless. The results obtained by using the three methods are shown in Table 2.

Looking at only the accuracy, by comparing the results in Tables 1 and 2, would make it difficult to choose the superior method. For example, the accuracy of the lower bound derived by Dunkerley's method depends on a property of the vibrating system, the spread of the fundamental frequency λ_1 and the next frequency λ_2. Also, the choice of the initial vector $x^{(o)}$ affects the bounds derived by Rayleigh's method and the direct method. However, the direct method has the characteristic that both bounds are found in the same step. This is its advantage.

When the initial estimated eigenvector does not have elements that are opposite in sign to the corresponding elements of the first modeshape, then both the lower and upper bounds can be obtained by the direct method in the initial step (k = 0). Otherwise, the lower bound becomes negative when k = 0, which is not useful. However, the upper bound can always be derived, and a useful lower bound can be calculated with a larger k, except when the approximate vector is orthogonal to the fundamental eigenvector. We do not need the lower bound in this case, since this occurs when it is exactly the same as the actual eigenvector.

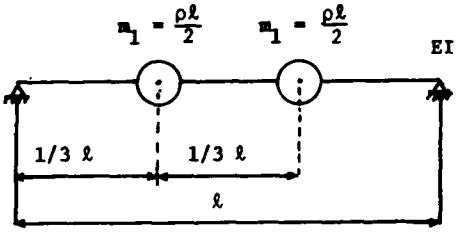

Fig. 2 - Example 2 2DOF Beam

The Effect of Initially Assumed Eigenvectors

An assumed initial vector can be expanded in the actual modeshapes $\underline{X}_1, \underline{X}_2 \ldots \underline{X}_n$

$$x^{(o)} = c_1 \underline{X}_1 + c_2 \underline{X}_2 + \ldots + c_n \underline{X}_n$$

$$= \begin{bmatrix} x_{11} & x_{12} \ldots x_{1n} \\ x_{21} & x_{22} \ldots x_{2n} \\ \cdot & \\ \cdot & \\ \cdot & \\ x_{n1} & x_{n2} \ldots x_{nn} \end{bmatrix} \begin{bmatrix} c_1 \\ c_2 \\ \cdot \\ \cdot \\ \cdot \\ c_n \end{bmatrix} \tag{19}$$

where $\underline{X}_1 = [x_{11}\ x_{21} \ldots x_{n1}]^T$. $\underline{X}_2 = [x_{12}\ x_{22} \ldots x_{n2}]^T$ and x_{ij} is the displacement at point i of the jth modeshape. Therefore, the displacement at point i of the initial vector $x_i^{(o)}$ is

$$x_i^{(o)} = \sum_{j=1}^{n} c_j x_{ij} \tag{20}$$

Substitute (19) and (20) into Eq. (3) to get

Table 1 - Lower and Upper Bounds of Fundamental Frequency of the 3DOF System Shown in Fig. 1

Number of iteration	Lower bound of λ_1		Upper bound of λ_1		Exact value of λ_1
	Dunkerley's Method	Direct Method	Direct Method	Rayleigh's Method	
k = 0	$0.1333 \frac{k}{m}$	$0.1463 \frac{k}{m}$	$0.176 \frac{k}{m}$	$0.1579 \frac{k}{m}$	$0.1546 \frac{k}{m}$
Deviation	-13.7%	-5.4%	13.8%	2.1%	
k = 1	$0.1532 \frac{k}{m}$	$0.1540 \frac{k}{m}$	$0.1548 \frac{k}{m}$	$0.1546 \frac{k}{m}$	$0.1546 \frac{k}{m}$
Deviation	-0.9%	-0.38%	0.13%	0.00%	

$$x_i^{(1)} = \sum_{j=1}^{n} D_{ij} \; c_j \; x_{ij} \qquad (21)$$

If every element of vector $x^{(1)}$ has the same sign as the corresponding element of vector $x^{(o)}$, the ratio $x_i^{(1)}/x_i^{(o)}$ should be greater than 0. Then, from Eqs. (20) and (21), the following inequality should be satisfied

$$\frac{x_i^{(o)}}{x_i^{(1)}} = \frac{\sum_{j=1}^{n} c_j \; x_{ij}}{\sum_{j=1}^{n} D_{ij} \; c_j \; x_{ij}} > 0 \qquad (22)$$

The inequality of Eq. (22) indicates that $x^{(o)}$ is near a modeshape. The next iterative step will indicate if $x^{(o)}$ is near the first modeshape by using the inequality

$$\lambda_{max}^{(1)} - \lambda_{min}^{(1)} < \lambda_{max}^{(o)} - \lambda_{min}^{(o)} \qquad (23)$$

If Eq. (23) is not satisfied, the iteration procedure should continue until

$$\lambda_{max}^{(k)} - \lambda_{min}^{(k)} < \lambda_{max}^{(k-1)} - \lambda_{min}^{(k-1)} \qquad (24)$$

Generally, Eq. (23) is easily satisfied. For the beam shown in Example 2, when $c_1/c_2 >$ 6.6%, the inequality of Eq. (23) is satisfied. This conclusion comes from Eq. (22), by letting the numerator and denominator be greater (and less) than zero at the same time. There will always be some negative elements in the higher modeshape; therefore, the coefficient of c_1 is much larger than the coefficients of c_2, c_3.... It can be seen that D_{ij} in Eq. (22) affects the ratio c_1/c_2. When the diagonal elements D_{ii} are much greater than the other elements, the ratio c_1/c_2 will increase.

DIRECT METHOD FOR CONTINUOUS SYSTEMS

The direct method can be applied to continuous systems. The beam in Fig. 3, which has a continuous mass, will be used to demonstrate this.

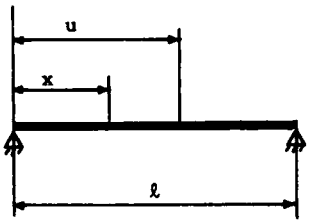

Fig. 3

The equation of motion of this beam is

$$y(x,t) = -\int_o^{\ell} \alpha(x,u)\ddot{y}(u,t)\, m(x)\, du \qquad (25)$$

where $\alpha(x,u)$ is Green's function.

Assume $\quad y(u,t) = y(u) \sin \omega t \qquad (26)$

Then $\quad y(x) = \lambda \int_o^{\ell} \alpha(x,u)\, y(u)\, m(u)\, du \qquad (27)$

Once an initial function $y_o(x)$ is assumed, the iteration procedure appears as

$$y_1(x) = \int_o^{\ell} \alpha(x,u)\, y_o(u)\, m(u)\, du$$

$$y_2(x) = \int_o^{\ell} \alpha(x,u)\, y_1(u)\, m(u)\, du$$

$$\vdots$$

$$y_k(x) = \int_o^{\ell} \alpha(x,u)\, y_{k-1}(u)\, m(u)\, du \qquad (28)$$

Table 2 - Lower and Upper Bounds of Fundamental Frequency of the 2DOF System shown in Fig. 2

Number of iteration	Lower bound of ω_1		Upper bound of ω_1		Exact value of ω_1
	Dunkerley's Method	Direct Method	Direct Method	Rayleigh's Method	
k = 0	7.7942 b	6.647 b	9.165 b	12.47 b	8.0498 b
Deviation	-3.2%	-20.2%	13.85%	54.9%	
k = 1	8.04096 b	7.966 b	8.1327 b	8.0776 b	8.0498 b
Deviation	-0.1%	-1.04%	1.03%	0.35%	

$$b = \frac{1}{\ell^2}\sqrt{\frac{EI}{\rho}} \qquad b = \frac{1}{\ell^2}\,\frac{EI}{\rho}$$

It can be proved (Appendix) that

$$\lim_{k\to\infty} y_k(x) = Y_1(x) \qquad (29)$$

$$\lim_{k\to\infty} \frac{y_{k-1}(x)}{y_k(x)} = \lambda_1 \qquad (30)$$

During the iteration procedure, $\lambda_1^{(k)}(x)$ is a function of x rather than a constant. According to the enclosure theorem

$$\min\ [\lambda_1^{(k)}(x)] < \lambda_1 < \max\ [\lambda^{(k)}(x)] \qquad (31)$$

Since Green's function $\alpha(x,u)$ and its integral are difficult to compute, the following procedure will be used. For a beam with variable cross sections the differential equation of motion is

$$\frac{d^2}{dx^2}\left[\ EI\ \frac{d^2y}{dx^2}\ \right] = \lambda\ m(x)\ y \qquad (32)$$

Although an initial $y_o(x)$ can be assumed and substituted into Eq. (32) to get $\lambda^{(o)}(x)$, it is more convenient to begin with an assumed initial distributed load $q^{(o)}(x)$.

$$q^o(x) = \frac{d^2}{dx^2}\ [EI\ \frac{d^2y}{dx^2}\ ] \qquad (33)$$

and from Eq. (32)

$$\lambda^{(o)}(x) = \frac{q^{(o)}(x)}{m(x)\ y_o(x)} \qquad (34)$$

where $y_o(x)$ is the deflection of the beam due to the load $q^{(o)}(x)$.

The next step is to let the distributed load $q^{(1)}(x)$ be $m(x)\ y_o(x)$

$$q^{(1)}(x) = m(x)\ y_o(x) \qquad (35)$$

Then $$\lambda^{(1)}(x) = \frac{q^{(1)}(x)}{m(x)y_1(x)} = \frac{y_o(x)}{y_1(x)}$$

$$\lambda^{(2)}(x) = \frac{y_1(x)}{y_2(x)} \qquad (36)$$

$$\lambda^{(k)}(x) = \frac{y_{k-1}(x)}{y_k(x)}$$

After k iterative steps, λ_1 should satisfy

$$\min[\lambda^{(k)}(x)] < \lambda_1 < \max[\lambda^{(k)}(x)]$$

Applications

The application of the direct method for continuous systems will be demonstrated in the next three examples. The simple beam with a uniform cross section used in the next example is shown in Fig. 4. Since it is a uniform beam, the initial load is assumed to be uniform.

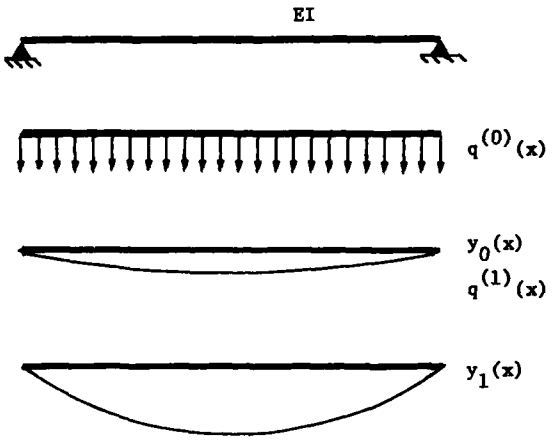

Fig. 4

$q^{(o)}(x) = q$ = constant

Then $y_o(x) = \frac{q}{24EI}\ (\ell^3x - 2\ell x^3 + x^4)$

Substitute $y_o(x)$ into Eq. (34)

$$\lambda^{(o)}(x) = \frac{q^{(o)}(x)}{\rho y_o(x)} = \frac{24EI}{\rho(\ell^3x - 2\ell x^3 + x^4)}$$

where E - Young's modulus

I - moment of inertia

ρ - mass per unit length

From Eq (31).

$$76.8\ \frac{EI}{\rho\ell^4} < \lambda_1 < \infty$$

In the next step, let $q^{(1)}(x)$ be proportional to $y_o(x)$

$$q^{(1)}(x) = \rho\ y_o(x) = \frac{\rho q}{24EI}\ (\ell^3x - 2\ell x^3 + x^4)$$

$$y_1(x) = \frac{q\ x\ \rho}{24E^2I^2\ 60}\ (\frac{x^7}{28} - \frac{\ell\ x^6}{7} + \tfrac{1}{2}\ \ell^3x^4 - \ell^5x^2 + \frac{17}{28}\ \ell^7)$$

$$\lambda^{(1)}(x) = \frac{y_o(x)}{y_1(x)}$$

$$= \frac{60EI}{\rho} \quad \frac{\ell^3 - 2\ell x^2 + x^3}{\frac{x^7}{28} - \frac{\ell x^6}{7} + \frac{\ell x^3}{2}^4 - \ell^5 x^2 + \frac{17}{28}\ell^7}$$

$$\lambda^{(1)}_{max} = 98.8235 \frac{EI}{\rho \ell^4}$$

$$\lambda^{(1)}_{min} = 96.55 \frac{EI}{\rho \ell^4}$$

$$96.55 \frac{EI}{\rho \ell^4} < \lambda_1 < 98.8235 \frac{EI}{\rho \ell^4}$$

The exact value of λ_1 of the beam is $97.4091 \frac{EI}{\rho \ell^4}$

The lower and upper bounds of the fundamental frequency and their deviations are listed in Table 3. It should be noted that since there are rigid supports in this example, the upper bound obtained in the first step is ∞. This is not the case when the beam is supported on elastic supports.

The next example is a beam with a variable cross section which is supported on three elastic supports. The initial load is assumed to be proportional to the mass, as shown in Fig. 5(b).

$$q^{(o)}(x) = \begin{cases} 1 \text{ N/m} & 0 \le x \le 5 \\ 1.45 \text{ N/m} & 5 \le x \le 7.5 \end{cases}$$

The deflection of the beam shown in Fig. 5(c) was derived by using a computer program. The maximum deflection is

$$[y_o(x)]_{max} = 0.1049 \times 10^{-3} \text{ m}$$

$$\lambda^{(o)}_{Lower} = \left[\frac{q^{(o)}(x)}{m(x)\, y_o(x)} \right]_{min} = 4271.712 \text{ (Rad/sec)}^2$$

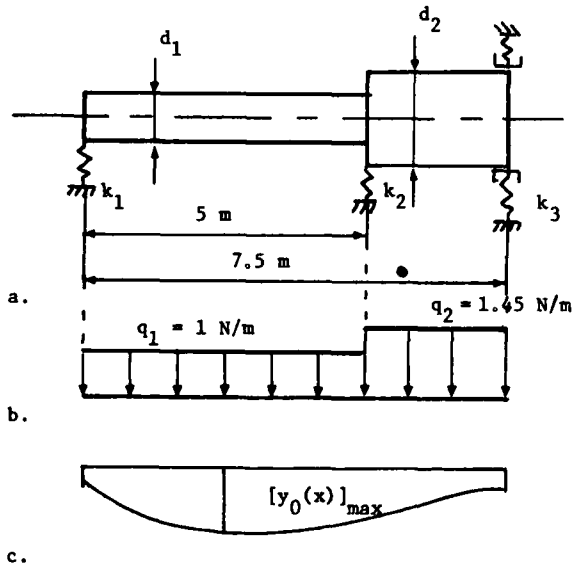

$d_1 = 6 \times 10^{-2}$ m
$d_2 = 7 \times 10^{-2}$ m
$\rho_1 = 21.87$ kg/m
$\rho_2 = 31.67$ kg/m
$M_1 = 154.9$ kg
$M_2 = 100$ kg
$k_1 = 3.5 \times 10^4$ N/m
$k_2 = 3.5 \times 10^4$ N/m
$k_3 = 4 \times 10^4$ N/m
$E = 2 \times 10^{11}$ N/m

Fig. 5 - A Beam with Three Elastic Supports and Variable Cross

Table 3 - The Lower and Upper Bounds of the Fundamental Frequency of the Beam of Fig. 4

Frequency f_1 cycles/second			Deviations	
f_{1L}	f_{1L} exact	f_{1V}	f_{1L}	f_{1U}
$1.5638\sqrt{\frac{EI}{\rho\ell^4}}$	$1.5708\sqrt{\frac{EI}{\rho\ell^4}}$	$1.5822\sqrt{\frac{EI}{\rho\ell^4}}$	0.45%	0.73%

$$f^{(o)}_{lower} = 10.4 \text{ cycles/sec.}$$

$$\lambda^{(o)}_{upper} = \left[\frac{q^{(o)}(x)}{m(x)\, y_o(x)} \right]_{max} = 8724.254 \text{ (Rad/sec)}^2$$

$$f^{(o)}_{upper} = 14.864 \text{ cycles/sec}$$

$$10.4 < f_1 < 14.864 \text{ cycles/sec}$$

The exact value of f_1 is 11.58 cycles/sec as calculated by a transfer matrix program. In this example both lower and upper bounds of the fundamental frequency are obtained in the first step.

When the beams have concentrated masses, the initial load should be assumed to be made of not only a distributed load, which is proportional to the continuous mass, but also concentrated loads which are proportional to the concentrated masses.

The next example is a beam with two concentrated masses as shown in Fig. 6. The deflection of this beam due to its initial load was derived with a beam analysis program and the lower and upper bounds of the fundamental frequency found using Eq. (31) are

$$\lambda^{(o)}_L = \left(\frac{q^{(o)}(x)}{m(x)\, y_{(o)}(x)} \right)_{min} = \frac{9.8 \times 10^3}{0.4313 \times 21.87}$$

$$= 1040.368 \text{ (Rad/sec)}^2$$

$$f_L = 5.128 \text{ cycles/sec}$$

$$\lambda^{(o)}_u = \left(\frac{q^{(o)}(x)}{m(x)\, y_o(x)} \right)_{max} = \frac{9.8 \times 10^3}{0.5229 \times 31.67}$$

$$= 591.7789 \text{ (Rad/sec)}^2$$

$$f_u = 12.459 \text{ cycles/sec}$$

Thus

$$5.128 < f_1 < 12.459 \text{ cycles/sec.}$$

The exact value of f_1 can be computed to be 5.978 cycles/sec.

The Effect of the Initial Load

It is evident that the closer the initial assumed load $q^{(o)}(x)$ is to the actual inertia force generated by the first mode, the better the results. When there are no in-span supports, there should not be any nodes in the first modeshape. Therefore, we can assume that $q^{(o)}(x)$ remains in the same direction and the magnitude is proportional to the mass of the beam. In this case, the lower and upper bound of the fundamental frequency can be derived by using only Eq. (34) and inequality (37), where k is equal to zero.

For a beam with more than two elastic supports, the $q^{(o)}(x)$ can be assumed as was described above. But, it should be noted that when the stiffness of the in-span supports increases, the deflection, due to $q^{(o)}(x)$ for which all loads are in the same direction, can be in opposite directions on some parts of the beam. In this case, the lower bound will be negative when k is zero. Of course, the

Table 4 - The Lower and Upper Bounds of the Fundamental Frequency of the Beam of Fig. 5 from 1st Step

Frequency f_1 cycles/second			Deviation	
f_{1L}	f_{1} exact	f_{1U}	f_{1L}	f_{1U}
10.4	11.58	14.864	-10%	+28%

Table 5 - The Lower and Upper Bounds of the Fundamental Frequency of the Beam in Fig. 6

Frequency f_1 cycles/second			Deviation	
f_{1L}	f_{1} exact	f_{1U}	f_{1L}	f_{1U}
5.128	5.978	12.459	-14.2%	+108%

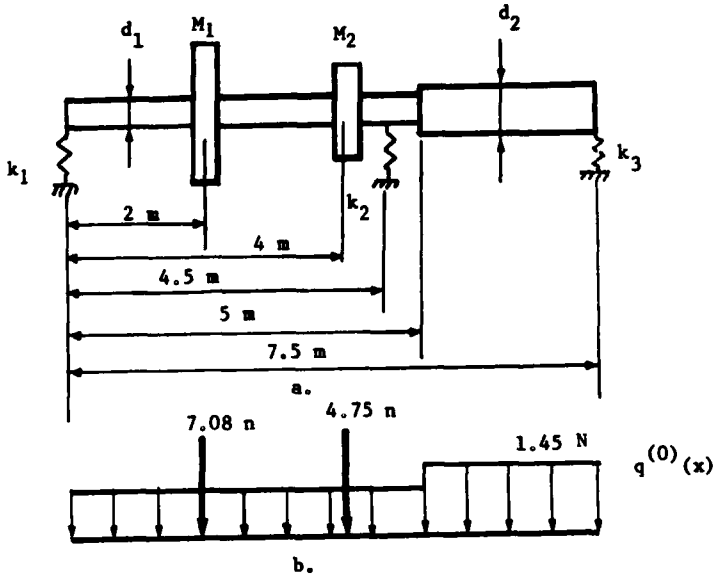

$d_1 = 5.9 \times 10^{-2}$ m
$d_2 = 7.1 \times 10^{-2}$ m
$k_1 = 3.5 \times 10^4$ N/m
$k_2 = 7 \times 10^4$ N/m
$k_3 = 3.5 \times 10^4$ N/m
$\rho_1 = 21.87$ kg/m
$\rho_2 = 31.67$ kg/m
$E = 2 \times 10^{11}$ N/m

Fig. 6 - A Beam with Concentrated Masses

positive bound can be obtained using the iteration procedure (Eqs. (35) and (36)), but it is much better to change the assumed load $q^{(o)}(x)$ into a load containing components in different directions. This is illustrated by the example in Table 6, which uses a beam which is similar to that in Fig. 5. The deflection of the beam changes with increasing stiffness k_2 of the in-span support. When $k_2 = 5 \times 10^6$ N/m, as shown on the last line of Table 6, the deflection $y_o(x)$ near the in-span support is in

TABLE 6 The Influence of the inspan support Stiffness on the Initial Load

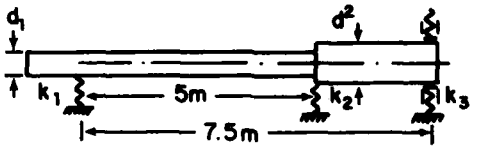

$d = 5.9 \times 10^{-2}$m
$d = 7.1 \times 10^{-2}$m
$P_1 = 21.87$ Kg/m
$P_2 = 31.67$ Kg/m
$k_1 = k_3 = 4.5 \times 10^4$ N/m

k_2 N/m	$q_0(x)$ Assumed load N/m	$y_0(x)$ Deflection m	f Frequency cycles/sec.			Error of f_{lower}
			f_{lower}	f_{exact}	f_{upper}	
7×10^4	1 1.45	0.149×10^{-3}	10.40	11.580	14.864	-10.2%
3×10^5		0.7063×10^{-4}	12.675	13.151	25.908	- 3.6%
4×10^6		0.5981×10^{-4}	13.774	14.835	203.45	- 7.2%
5×10^6	1 1.45	0.8151×10^{-4}	11.808	13.492	∞	-21.5%
5×10^6	1 1.45		-∞	14.823	∞	

the opposite direction; then the lower and upper bounds become indefinite. But, when the initial load changes as shown on the fourth line of Table 6, the lower bound is derived when k is zero. The upper bound will be obtained in next step, when k = 1, as mentioned in the simple beam example.

From all the examples of the continuous system, the lower bounds of the fundamental frequency obtained in the first step of the direct method are much better than the upper bounds.

CONCLUSIONS

All the methods discussed here - Rayleigh's and improved Rayleigh's methods, Dunkerley's and improved Dunkerley's methods, and the direct method - involve iteration procedures. The direct method is a technique by which both lower and upper bounds can be derived by the iteration procedure itself.

The direct method appears to be an effective method for estimating the bounds of the fundamental frequency of a vibrating system. The advantages of this method are that both bounds can be obtained at the same time. The direct method is more efficient for a system for which a rough estimate of the first modeshape is available. Since many modern eigenvalue extraction routines use some form of the inverse iteration procedure, an important implication of the direct method is that both upper and lower bounds can be obtained during the iteration process. Existing routines can take advantage of this fact.

For continuous systems it is more convenient to assume an initial load instead of an initial modeshape, and the bounds can be derived by computing the deflection due to the load. The lower bound for beams derived in the first step of the direct method seems much better than the upper bound.

ACKNOWLEDGEMENT

The work of W. Pilkey was supported by the Office of Naval Research, Arlington, Virginia.

REFERENCES

1. William T. Thomson, Theory of Vibrations with Applications, Prentice-Hall, Inc., Englewood Cliffs, NJ, 1981.
2. A. Rutenberg, "Dunkerley's Formula and Alternative Approximations," Journal of Sound and Vibration, 1975, Vol. 39(4), 530-531.
3. S. Crandall, Engineering Analysis, McGraw-Hill, New York, NY, 1956.
4. Ray W. Clough and Joseph Penzien, Dynamics of Structures, McGraw-Hill, New York, NY, 1975.
5. L. S. Jacobson and R. S. Ayre, Engineering Vibrations, McGraw-Hill, New York, NY, 1958.
6. Zheng Zhaochang, Mechanical Vibrations (in Chinese), Publishing House of Mechanical Industry, Beijing, China, Second Edition, 1982.
7. C. H. Popelar, "Lower Bound for the Buckling Load and the Fundamental Frequency of Elastic Bodies," Journal of Applied Mechanics, Vol. 41, 151-154, 1974.
8. A. B. Ku, "Upper and Lower Bound Eigenvalues of a Conservative Discrete System," Journal of Sound and Vibration, Vol. 53(2), 183-187, 1977.
9. Stephen Timoshenko and J. M. Gere, Theory of Elastic Stability, McGraw-Hill, New York, NY, Second Edition, 1961.

APPENDIX

An assumed initial modeshape $y_o(u)$ can be expanded in the actual modeshapes Y_1, Y_2 ... Y_i...

$$y_o(u) = \sum_{i=i}^{\infty} c_i Y_i \qquad (1)$$

When the iteration procedure is employed, the modeshape in the kth step will be

$$y_k(x) = \int_o^{\ell} \alpha\,(x,u)\; y_{k-1}(u)\; m(u)\; du \qquad (2)$$

Substitute (1) into (2); when k = 1

$$Y_1(x) = \sum_{i=1}^{\infty} \int_o^{\ell} \alpha(x,u)\; c_i Y_i(u)\; m(u)\; du \qquad (3)$$

and

$$Y_i(x) = \lambda_i \int_o^{\ell} \alpha(x,u)\; Y_i(u)\; m(u)\; du \qquad (4)$$

Substitute (4) into (3)

$$Y_1(x) = \sum_{i=1}^{\infty} \frac{c_i}{\lambda_i}\; Y_i(x) \qquad (5)$$

The next iteration step will be

$$y_2(x) = \int_o^{\ell} \alpha\,(x,u)\; y_1(u)\; m(u)\; du$$

$$= \int_0^{\ell} \alpha(x,u) \sum_{j=1}^{\infty} \frac{Y_i(u)\, c_i}{\lambda_i}\, m(u)\, du$$

$$= \sum_{i=1}^{\infty} \int_0^{\ell} \alpha(x,u)\, \frac{Y_i(u)\, c_i}{\lambda_i}\, m(u)\, du$$

$$= \sum_{i=1}^{\infty} \frac{Y_i(x)}{\lambda_i^2}\, c_i \qquad (6)$$

.
.
.

$$y_k(x) = \sum_{j=1}^{\infty} \frac{Y_i(x)}{\lambda_i^k}\, c_i$$

$$= \frac{1}{\lambda^k} \left[c_1 Y_1(x) + c_2 \left(\frac{\lambda_1}{\lambda_2} \right)^k Y_2(x) + \ldots \right]$$

Then

$$\frac{y_{k-1}(x)}{y_k(x)} =$$

$$\frac{\lambda_1^k}{\lambda_1^{k-1}} \quad \frac{c_1 Y_1(x) + c_2 \left(\frac{\lambda_1}{\lambda_2} \right)^{k-1} Y_2(x) + \ldots.}{c_1 Y_1(x) + c_2 \left(\frac{\lambda_1}{\lambda_2} \right)^k Y_2(x)\ (+)\ \cdots} \qquad (7)$$

Since

$$\lambda_1 < \lambda_2 < \lambda_3 \ldots$$

$$\lim_{k \to \infty} y_k(x) \to Y_1(x) \qquad (8)$$

$$\lim_{k \to \infty} \frac{y_{k-1}(x)}{y_k(x)} = \lambda_1 \qquad (9)$$

APPROXIMATING DYNAMIC RESPONSE IN SMALL ARRAYS USING POLYNOMIAL PARAMETERIZATIONS AND RESPONSE SURFACE METHODOLOGY

K. P. White, Jr., H. C. Gabler, III, and W. D. Pilkey
School of Engineering and Applied Science
University of Virginia
Charlottesville, Virginia

This paper describes a method for deriving an approximate algebraic model which defines the performance of a dynamic system as a function of its response parameters. The method extracts essential response information from large amounts of test data or simulation output and stores this information in a single, small, two-dimensional array. This data compression provides for highly efficient storage of essential information in a form which is especially convenient for subsequent use in analysis, experimentation, model validation, or design optimisation. The method is illustrated by an application to passenger-vehicle crashworthiness design optimisation.

INTRODUCTION

Managing the large volume of experimental and/or simulation data required for design studies is a significant problem in many applications. This paper describes a method for dealing with such problems that has proven successful in vehicle collision research. The method involves (1) characterising the continuous response of a dynamic system in terms of manageable set of performance measures and (2) deriving an approximate algebraic model which defines each of these performance measures as a function of selected design parameters. In this way, essential design information can be extracted from large amounts of data and represented as a single, small, two-dimensional array. The resulting compression permits the efficient management and storage of essential design information in a form which is especially convenient for subsequent use in analysis, experimentation, model validation, or design optimisation.

In the following sections, we first define the problem addressed in this paper. Second, we describe the general method for developing polynomial parameterisations of deceleration time histories and demonstrate the application of this method in vehicle collision research. Next, we describe the general response surface method and its application in passenger vehicle design optimisation studies.

NOMENCLATURE

$a(t)$: simulated vehicle acceleration
a_i : polynomial coefficient
b_0 : polynomial coefficient
b_j : polynomial coefficient
b_{jk} : polynomial coefficient
b_{jkl} : polynomial coefficient
f_i : i-th response surface component
$\mathbf{f}$: vector-valued response surface
$p^{(2)}(t)$: approximated vehicle deceleration
$p^{(1)}(t)$: approximated vehicle velocity
$p(t)$: approximated vehicle displacement
t_c : time to deceleration centroid
t_m : time to maximum crush
v_m : velocity at maximum crush
v_r : rebound velocity
v_0 : initial velocity
x_j : j-th predictor variable
$\mathbf{x}$: vector of predictor variables
$x^{(2)}(t)$: actual vehicle acceleration
$x^{(1)}(t)$: actual vehicle velocity
$x(t)$: actual vehicle position
y_i : i-th response variable
$\mathbf{y}$: vector of response variables

Problem Definition

The specific application considered in this paper and used to demonstrate the general method arises in passenger-vehicle collision research. The basic problem is that of summarising information which defines the dependence of the dynamic response of a vehicle during a barrier collision on the levels of a set of structural response parameters. In this paper it assumed that complete information on the significant structural behavior of a vehicle, in terms of the impact of that behavior upon occupant dynamics, is contained in the deceleration time history or *crash signature* of the vehicle occupant compartment. This assumption is generally accepted and, indeed, it is standard practice to describe the dynamic response of a vehicle in laboratory crash tests by the deceleration of a fixed point on the vehicle. While the ultimate relationship between vehicle deceleration and occupant injuries in actual highway accidents is impossible to prove (or disprove), good correlation can be shown between deceleration and standard occupant dynamic response measures in both laboratory tests and computer simulations. In addition, other correlates with occupant response measures (such as impact velocity, absolute velocity change, and vehicle crush) can be derived from the vehicle deceleration profile. See for example White, *et. al.* [1], for an correlation analysis of vehicle and dummy response measures using test data for twenty 1982 Citations; Huang, *et. al.* [2], for an analysis of relationship between vehicle deceleration and simulated occupant responses; and Langwieder, *et. al* [3], for a comparison of passenger injuries in frontal collisions with dummy loadings in equivalent simulations.

Data implicitly describing the relationship between crash signatures and selected vehicle response parameters can be derived from computer simulations of collisions under a range of different crash conditions. Data from several hundred computer simulation runs are required to complete the simulation experiment design, however, in order to insure that the relationship is adequately defined. For the current application, a compact representation of the information contained in these data is required for efficient storage and retrieval. In addition, the relationship defined by these data must be stored in an explicit form which is convenient for use in subsequent design optimization studies.

The original design/response data for each simulation run include the simulation input parameters defining the value of each collision parameter and each design parameter and the corresponding (digitized) occupant compartment deceleration profile derived from the simulation output. Initial compression of the data is achieved by replacing the 4000 or more [a(t),t] data pairs (where a(t) is the acceleration of the vehicle occupant compartment) defining the complete simulated deceleration profile with only two parameters. These two parameters, together with the collision conditions, define a polynomial approximation of the original waveform and represent summary performance measures for the complete vehicle dynamic response.

The implicit relationship contained in the summary design/response data from this initial step is subsequently converted into an explicit model of the relationship by applying response surface methodology. For each of the vehicle response parameters, a polynomial approximating function is developed by stepwise, multiple, linear regression on the design/results data. While the purpose of this step is to derive an explicit relationship convenient for optimization studies, a second and equally significant compression of the data is also achieved.

The end result of this two-step procedure is a single, two-dimensional array containing the desired information from a large number of vehicle crash simulations. Each row of the array corresponds to one of the parameters of the polynomial approximation of the original crash signatures. Two columns are required for each parameter of the polynomial approximation of the corresponding row parameter, one for the coefficent value of the regression equation and a second for the code identifying the corresponding predictor. This convenient compression of the data represents, in effect, a simple algebraic model relating the collision response of the vehicle to its structural design.

Parameterisation of Dynamic Response using Polynomial Approximations

To apply the method described in this paper, the continuous response of a dynamic system must first be characterised in terms of a manageable set of parameters. This is a universal problem in experimentation and simulation. Parametric representations of continuous time histories are commonly used as time-domain performance measures and in establishing time-domain performance specifications. Such characterisations are also essential for the statistical analysis of experimental data and simulation output, for empirical and model-based sensitivity analysis, and for experimental and simulation optimisation. Moreover, such simplified descriptions of the dynamic response permit the efficient storage of large amounts of test data or simulation output for subsequent use in experimentation, modeling, analysis, validation, or design optimisation.

Although there are many means available for achieving the desired parameterization, a general approach is to use the coefficients of a polynomial-in-time which has been fit to the actual dynamic *reponse variable (here, the crash signature a(t))*. This parameterization permits the results a single laboratory experiment or computer simulation to be stored in a single vector of dimension (p+n), where (p-2) is the order of the approximating polynomial and n is the number of control variables of the simulation (or, equivalently, the number of experimental treatments). The results of multiple simulations can be stored in m such vectors, or in an array of dimension [m x (p+n)], where m is the the number of simulation runs with different combinations of control variable settings (or, equivalently, the number of experimental observations with different treatments).

Polynomial Parameterisations of Crash Signatures Although approximating a continuous function with a polynomial fit is a standard practice, the parameterisation of vehicle crash signatures using polynomials-in-time appears to have been studied originally by Huang, *et al*. The general problem considered was that of approximating an arbitrary continous vehicle deceleration profile $x^{[2]}(t)$ with an nth-order polynomial in time

$$p^{[2]}(t) = \sum_{i=0}^{n} a_i t^i$$

over the time interval $(t_m>t>0)$ in the least squares sense

$$\min_{a_i} \int_0^{t_m} [x^{[2]}(t) - p^{[2]}(t)]^2 dt$$

subject to the equality of the initial conditions on velocity

$$p^{[1]}(0) = x^{[1]}(0)$$

and position

$$p(0) = x(0).$$

Huang, *et al*, showed that the least squares criterion, together with the specified initial conditions, implies the following (equivalent) conditions

o the equality of the first n area moments of $p^{[2]}(t)$ and $x^{[2]}(t)$

o the equality of the corresponding definite integrals from 0 to t_m of $p^{[2]}(t)$ and $x^{[2]}(t)$ up to and including order n+1

o the equality of the centroid times t_c of the corresponding integrals of $p^{[2]}(t)$ and $x^{[2]}(t)$ up to and including order n-1

The TESW Approximation *The simplest polynomial* approximation of the crushing phase of the vehicle deceleration profile is a linear or first-order approximation. When combined with a second linear segment to account for the rebound phase of the deceleration, the result is the piecewise linear TESW (tipped equivalent square wave), shown in Fig. 1.

With the general equivalence conditions specified above, and with the final time of the collision t_f selected to insure the equality of the actual and approximated rebound velocities, the TESW for a collision can be completely specified by four parameters

o t_m, the time to maximum total dynamic crush

o t_c, the time to the centroid of deceleration

o v_r, the rebound velocity

o v_m, the change in velocity at the time of maximum crush

While specification of the TESW requires four parameters, for barrier collisions two of these four parameters are redundant, since v_m equals the initial vehicle velocity v_0 (which is the collision parameter) and since t_c can be calculated directly from t_m and v_0. Thus the entire crash pulse can be specified with only two parameters, t_m and v_r.

Figures 1, 2, and 3 show the measured deceleration, velocity, and position time-histories of a 1982 Chevrolet Citation during a 35mph frontal-barrier crash test, together with the corresponding TESW approximations. Note that the TESW deceleration profile in effect smooths the raw accelerometer data such that successive integrations of the TESW show generally excellent correlation with the corresponding integrations of the actual accelerometer data (particularly during the crushing phase).

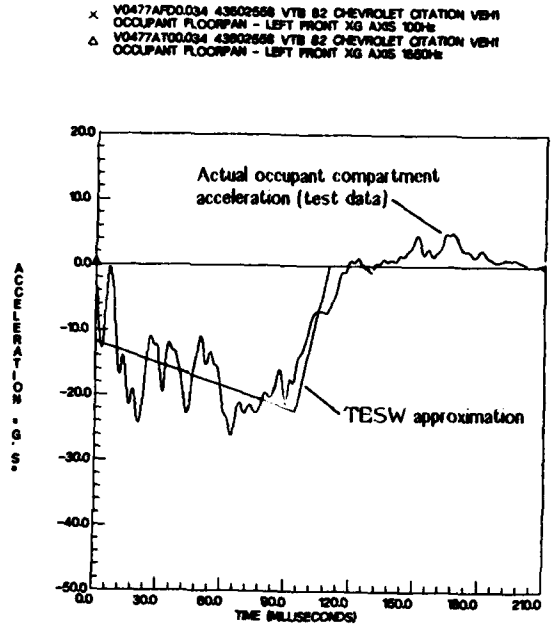

Fig. 1–Actual and TESW approximation of occupant compartment acceleration during a barrier collision

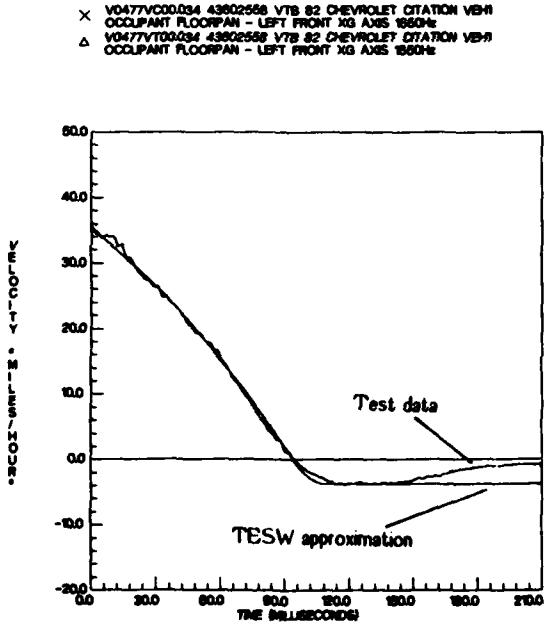

Fig. 2–Actual and TESW approximation of occupant compartment velocity during a barrier collision

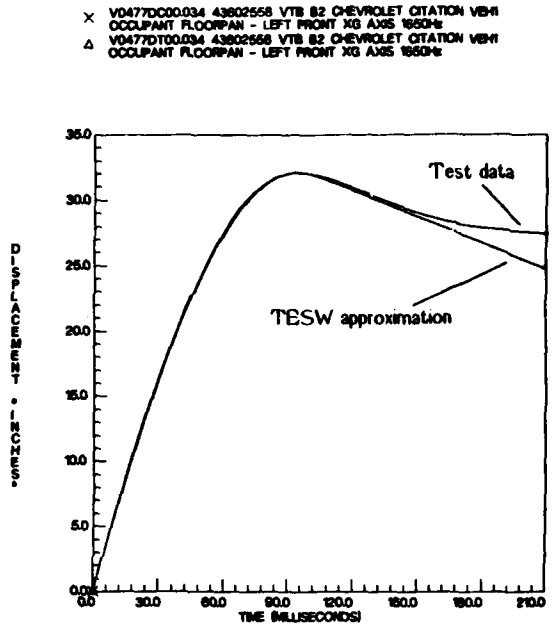

Fig. 3–Actual and TESW approximation of occupant compartment position during a barrier collision

In validation studies, the TESW approximation has proven to be remarkably successful in capturing the essence of vehicle collision response, at least insofar as this response determines simulated occupant dynamics. Huang, *et al.*, report differences in simulated occupant head and chest decelerations of less than 7%, when using complete deceleration data and the corresponding TESW approximation. In work currently in progress, the authors preliminarily have found differences in HIC (head injury criterion) and CSI (chest severity index) of less than 10% in similar tests, although this work has not yet been verified.

Response Surface Methodology

A response surface is a mathematical representation of the relationship between a dependent or response variable and a set of independent or predictor variables. Response surface methodology (RSM) refers to the unique synthesis of otherwise standard statistical techniques which are used to develop response surfaces for experimental or simulated data. The general issue of RSM is considered by Myers [4] Box, Hunter, and Hunter [5], and Box and Draper [6], among others. The specific application of RSM to computer simulation experiments is considered by Fishman [6] and Naylor, *et al.* [8]. Biles and Swain [9] provide an excellent description of RSM in

the context of industrial experimentation and optimization.

The primary objective of RSM is determining a relationship of the form

$$y = f(x)$$

from the experimentally determined n-tuples (y,x) where y is the vector of response variables y_i, x is the vector of predictor variables x_j, and f is the vector-valued function representing the response surface. This relationship is not intended to be a causally correct representation of the underlying process, such as one would seek in developing a dynamic simulation based upon differential or difference equations. Rather, the response surface is intended to be a statistically optimal summary of the data (usually in the least squares sense), which provides a parsimonious and explicit representation of the observed but otherwise implicit input/output relationship between predictor and response variables. The resulting response surface typically is used for (1) investigating the relationship of the response to the predictor variables, in order to determine sensitivities or to evaluate the underlying process mechanism, and (2) determining the combination of predictor variables for which the response is optimized.

RSM concerns itself with the four steps of developing and using response surfaces. These are

Step 1. Determining the appropriate number and choice of response and predictor variables y_i and x_j.

Step 2. Designing an experiment to generate the predictor/response data (y,x).

Step 3. Deriving the response surface $y=f(x)$ from the predictor/response data.

Step 4. Applying the response surface for analysis and/or optimization.

Details of each of these steps for general applications can be found in the RSM literature previously cited. In the following, we outline the first three of these steps as these apply to the application under consideration.

TESW Crash Signature Response Surface In the application described, we seek to develop a response surface which defines the relationship between the summary parameters of the crash signature of a passenger vehicle and a set of vehicle structural design variables. The broader context of this application, in which the resulting response surface is used in determining optimal vehicle designs for occupant protection (at step 4), is described by White, *et al.* [10,11,12]. Here we limit our attention to the form of the model developed and its implications for data storage and retrieval.

Step 1. The response variables selected for this application are the two nonredundant TESW parameters, t_m and v_r, which (together with the collision parameter v_0) characterise the vehicle deceleration profile during a barrier crash. The predictor variables are selected physical properties of structural components of the front structure of the design vehicle, together with the parameter defining the collision type. The structural design parameters are

x_1 = constant collapse force of the foreframe
x_2 = constant collapse force of the aftframe
x_3 = constant collapse force of the sheetmetal
x_4 = available crush length of the foreframe
x_5 = available crush length of the aftframe

as shown in the one-dimensional lumped-mass model of a vehicle during front-to-fixed-object collisions depicted in Fig. 4. For the initial study, the predictor or design variables were chosen based upon engineering judgement. Subsequent sensitivity analysis using the response surface developed by the method described here provides an ultimate test of this judgement (see [12]).

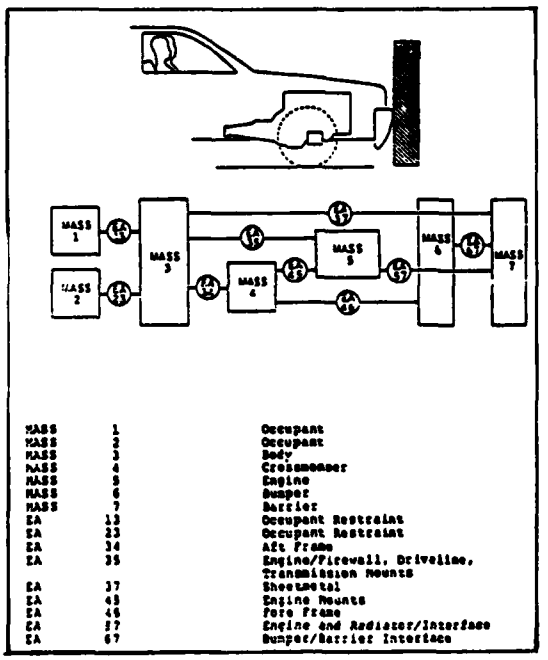

Fig. 4-One-dimensional lumped-mass model of a vehicle during a barrier collison

Step 2. Data defining the implicit relationship between the design variables and the TESW response parameters were generated by completing 128 computer simulation runs using the CRUSH [13] vehicle simulator. Each run corresponds to one of the combinations of design parameter values and collision condition defined by an experiment design developed specifically for this application (see Ford [14]). The occupant compartment deceleration profile obtained from each run was postprocessed to determine the corresponding TESW parameters. The design/response data for all the simulation runs was concatinated into a single design/results file---an array of dimension (128 x 8).

Step 3. A response surface typically is derived by multiple, linear, least-squares regression of a polynomial in the (perhaps coded) predictor variables on the predictor/response data for each of the (perhaps transformed) response variables. First- and second-order polynomial response surfaces are reported almost exclusively in the literature. In the current application, however, significant fits could not be achieved for the design/response data using either first- or second-order approximating functions. A third-order polynomial approximating function of the form

$$y_i = b_0 + \sum_{p=1}^{k} b_p x_p + \sum_{p=1}^{k}\sum_{q=1}^{k} b_{pq} x_p x_q + \sum_{p=1}^{k}\sum_{q=1}^{k}\sum_{r=1}^{k} b_{pqr} x_p x_q x_r$$

was required for each component f_i, i=1,2, of the response surface f. Stepwise, multiple, linear, least-squares regression was applied to minimize the number of terms in the regression equations. In this way, significant fits (r^2>0.95) were obtained with 17 terms in each case. The response surface representing an explicit model of the design information derived from the simulation runs can then be stored in a single file---an array of dimension (2 x 34).

CONCLUSIONS

In this paper we have illustrated a general method for approximating performance of a dynamic system as a function of its design parameters, by reference to a specific application of this method in conjunction with passenger-vehicle crashworthiness design optimization. In the general case, we have shown that if an adequate parameterisation of a continuous dynamic reponse in p parameters can be achieved, this parameterization permits the results of a single laboratory experiment or computer simulation run to be stored in a vector of dimension (p+n), where n is the number of control variables of the simulation (or, equivalently, the number of experimental treatments). We have suggested that a polynomial in time of order (p-2) is a suitable candidate for achieving the desired parameterisation. Similarly, we have shown that the results of multiple experiments or simulations can be stored in a single array of dimension [m x (p+n)], where m is the the number of simulation runs with different combinations of control variable settings (or, equivalently, the number of experimental observations with different treatments).

We have also shown in the general case that a model of the data can be achieved through the application of response surface methodology, which further compresses the original data. In the general case, we have shown that the data in the [m x (p+n)] dimensional array can be modeled by the coefficients of p polynomials in the experiment or simulation control variables. We have suggested that stepwise, multiple, least-squares, linear regression is an appropriate candidate means for specifiying these approximating polynomials. As a consequence of this modeling, the results of the entire simulation study are summarized by a global response surface, which can be stored in an array of dimension (p x 2q), where q is the maximum number of terms in any of the approximating polynomial regression equations. Each row of the array corresponds to one of the summarising parameters of the dynamic response variable. Two columns are required for each parameter of the polynomial approximation of the corresponding row parameter, one for the coefficient value and a second for the code identifying the corresponding predictor.

For the specific vehicle collision problem described in this paper, we have shown that the deceleration time history or crash signature of the vehicle can be characterized by the coefficients of a low-order polynomial approximation. Specifically, we indicated that the barrier crash signature can be approximated by the piecewise linear TESW approximation, involving only two parameters which are distinct from the collision condition specified in the simulation input. This parameterization permits the results of a single laboratory or computer simulation, consisting of a minimum of 8000 data elements, to be summarized by only 8 data elements. Similarly, the results of 128 multiple simulations, consisting of a total of more that a million individual data elements, can be stored in a single array of dimension (128 x 8), with only 1024 data elements. Thus the original data storage requirements are compressed by three orders of magnitude.

For the vehicle collision problem described in this paper, we also have shown that the data in the (128 x 8) array achieved after parameterisation can be modeled by a third-order global response surface.

This response surface can be characterized by 17 coefficients terms, permitting the results of the entire simulation study to be stored in an array of dimension (2 x 34). Each row of the array corresponds to one of the two nonredundant parameters of the TESW approximation of the crash signature. Seventeen paired columns are required for the *response-surface coefficents*, one for the coefficient value and a second for the three-digit integer code identifying the corresponding predictor. Thus the thousand-plus nonzero data elements obtained through the initial parameterization, corresponding to the original million-plus nonzero data elements associated with the simulation study, are compressed into the 68 elements defining response surface.

The end result of this method is a small array representing an approximate closed-form solution for the dynamic response of a vehicle during barrier collisions as a function of its design variables. Approximations of the this relationship have been achieved with only 68 individual data elements, resulting in a reduction of data storage requirements by almost seven orders of magnitute. This approximation has been used with success in subsequent design optimization studies.

REFERENCES

1. White, K.P., Jr., Gabler, H.C., III, and Pilkey, W.D., Limiting Performance Approach to Systems Design: Refinements to the Safety Systems Optimization Model, Report UVA/529361/MAE85/102 University of Virginia, September 1984.

2. Huang, M., Lawson, G.P., Powell, B.K., and Walker, J.H., "Characterization of vehicle deceleration time histories in the analysis of impact dynamics," SAE paper no. 770013, 1977.

3. Langwieder, K., Danner, M., Schmelzing, W., Appel, H., Kramer, F., and Hofmann, J., "Comparison of passenger injuries in frontal car collisions with dummy loadings in equivalent simulations," 23rd Stapp Car Crash Conference, October 1979, pp. 201-231.

4. Myers, R.H., Response Surface Methodology, Allyn-Bacon, 1971.

5. Box, G.E.P., Hunter, W.G., and Hunter, J.S., Statistics for Experimenters, Wiley, 1978.

6. Box, G.E.P., and Draper, N.R., Evolutionary Operation: A Statistical Method for Process Improvement, Wiley, 1969.

7. Fishman, G., Concepts and Methods in Discrete Event Digital Simulation, Wiley, 1973.

8. Naylor, T., Balintfy, J., Burdick, D., and Chu, K., Computer Simulation Techniques, Wiley, 1966.

9. Biles, W.E., and Swain, J.J., Optimization and Industrial Experimentation, Wiley, 1980.

10. White, K.P., Jr., Pilkey, W.D., Gabler, H.C., and Hollowell, W.T., "A computer-aided design tool for automobile crashworthiness: overview of the system model," Large Scale Systems, Vol. 4, No. 4, November 1983, pp. 245-262.

11. White, K.P., Jr., Pilkey, W.D., Gabler, H.C., and Hollowell, W.T., "Optimizing design parameters for highway vehicle safety," International Journal of Vehicle Design, Vol. 4, No. 6, November 1983, pp.618-632.

12. White, K.P., Jr., Pilkey, W.D., Gabler, H.C., and Hollowell, W.T., "Minimizing injuries in frontal collisions using the SSOM optimization technique," International Conference on Structural Impact and Crashworthiness, Vol. II, July 1984.

13. Ford Motor Company, Crash Reproduction Using Static History (CRUSH) Reference Guide II, March 1975.

14. Ford Motor Company, Safety Systems Optimization Model, Final Report, in 3 volumes, U.S. Department of Transportation, report under contract DOT HS-6-01446, November 1978.

*U.S. GOVERNMENT PRINTING OFFICE: 1985-461-639:20008